UNIVERSITÀ
DEGLI STUDI
DI PADOVA

Head Office: Università degli Studi di Padova
Centro di Ateneo di Studi e Attività Spaziali "Giuseppe Colombo" – CISAS

Ph.D. COURSE IN: SCIENZE, TECNOLOGIE E MISURE SPAZIALI
CURRICULUM: SCIENZE E TECNOLOGIE PER APPLICAZIONI SATELLITARI E AERONAUTICHE
SERIES XXXV

CHARACTERIZATION AND CALIBRATION OF VIS CAMERAS FOR SPACE APPLICATIONS – JANUS AND HYPSOS SYSTEMS

Coordinator: Prof. Francesco Picano
Supervisor: Prof. Gabriele Cremonese
Co-Supervisor: Ch.mo Prof. Giampiero Naletto
Dr. Alice Lucchetti

Ph.D. student : Livio Agostini

Ringraziamenti

Mi sono sempre piaciute le pagine di ringraziamento; quando leggo una tesi è la prima pagina che vado a sfogliare. In qualche modo ti proietta nel mondo dell'autore, ti lascia immaginare anche la parte di relazione con gli altri che è tanto importante quanto spesso trascurata nella stesura di una tesi. Mi è sempre piaciuta anche l'idea di scrivere questa pagina in particolare, perchè in qualche modo segna la fine di un percorso importante e permette anche a me di lasciar trasparire un pò del mondo di persone che ho avuto il piacere di conoscere e che in qualche modo hanno contribuito sia alla mia formazione che ad arrivare in fondo al tunnel e vedere la luce.

Non posso quindi non ringraziare:

i miei supervisori, Gabriele Cremonese, Giampiero Naletto e Alice Lucchetti per avermi guidato in questi anni e avermi dato l'occasione di poter lavorare su due progetti incredibili, poter osservare allo stesso tempo due attività diverse e in qualche modo complementari mi ha dato una nuova luce sull'argomento.

Maurizio Pajola_ per aver creduto in me, una parola è poca, due sono troppe.

i colleghi che con me hanno condiviso gioie e dolori al banco ottico di HYPSOS, benchè in momenti differenti: Francesca Brotto, Andrea Meneguzzo ed Emanuele Desirò. Partire da un banco vuoto e arrivare ai primi dati è stato un percorso incredibile, non sempre facile ma sicuramente stimolante!

Matteo Faccioni, per la disponibilità, per le birre dopo il lavoro e per avermi ospitato quando ne avevo bisogno!

Alain J. Corso, per tutte le discussioni, i caffè (e i cappuccini), i suggerimenti e per i pezzi!

Giovanni Santi, per le pause caffè alla macchinetta del LUXOR.

Alessio Aboudan, per avermi fatto vedere davvero come si scrive un codice pulito e per il supporto alla scrittura dei codici per il quick look durante le calibrazioni di JANUS.

Cecilia Tubiana, per la grande disponibilità mostrata nei miei confronti e per avermi mostrato quanto è fondamentale essere organizzati nella gestione delle informazioni sui dati e come si fa un log impeccabile!

Emanuele Simioni, per la stima, il supporto nella calibrazione geometrica e l'estrema disponibilità. Avere feedback da una persona cosi competente è stato un vero onore.

Pasquale Palumbo, per la fiducia che ha sempre riposto in me, per i commenti sempre pertinenti e dritti al punto sulle mie analisi su JANUS. La competenza e la grande umanità sono per me motivo di ammirazione.

la mia famiglia, che sempre ha creduto in me.

Anna Homberg, se ora sono relativamente tranquillo sul divano a scrivere questa pagina, lo devo a te.

L'ultimo ringraziamento ha per me un significato particolare. Sono stati tre anni difficili, abbiamo abitato lontano centinaia di chilometri e spesso il lavoro ha condizionato le nostre giornate. Nonostante questo, mi ha sempre spronato a dare il massimo, a credere in me soprattutto quando io non lo facevo, mi ha ascoltato, pianto e gioito con me. Se fosse solo questo sarebbe però un pò opportunista da parte mia. Ha invece preteso la mia

parte migliore e se sono riuscito a scrivere questa tesi e a realizzarmi come persona (e come ricercatore) è solo merito suo, mi ha dato più di quanto potrei mai chiedere. Questo lavoro è dedicato a te, Cristina, ora come allora, compagna preziosa e insostituibile

Riassunto

La strumentazione ottica costituisce attualmente una componente fondamentale delle missioni spaziali per l'esplorazione del Sistema Solare. Le declinazioni possono essere molteplici sia in termini di regioni di spettro magnetico osservato che in termini di tipologia di strumento. Tutti però hanno un denominatore comune: *devono essere calibrati e caratterizzati*. Gli strumenti a bordo di sonde spaziali operano in ambienti molto ostili e sono soggetti a ripetuti sforzi termomeccanici dovendo comunque garantire le loro capacità. Il processo di calibrazione consente di avere una mappatura tra il mondo esterno e il dato prodotto dallo strumento, fornendo dati in unità fisiche. Il processo di caratterizzazione consente di avere conoscenza del comportamento di singoli componenti o dell'insieme, ampliando la comprensione dello strumento. Uno strumento ben caratterizzato e calibrato fornirà dati più attendibili, sarà più facile prevederne il comportamento e capire l'origine di eventuali problematiche durante la vita operativa.

Nella tesi questa tematica è applicata a due diversi strumenti, ciascuno a differenti livelli di sviluppo: JANUS (Jovis Amorum ac Natorum Undique Scrutator), una camera ad alta risoluzione in programma di essere lanciata verso il sistema gioviano in Aprile 2023 a bordo della missione ESA JUICE (JUpiter ICy moons Explorer) e HYPSOS (HYPerspectral Stereo Observing System), uno stereo spettrometro ad immagine sviluppato a livello di laboratorio per validare un nuovo concetto di strumento.

La prima metà della tesi è dedicata alle attività svolte su JANUS, in particolare sull'analisi dei dati di calibrazione a terra.

Nel Capitolo 1 viene descritta brevemente la missione JUICE, JANUS e gli obiettivi scientifici, fornendo il contesto generale per i capitolo 2 e 3.

Il Capitolo 2 descrive le metodologie applicate per l'analisi dei dati di calibrazione, la discussione e i risultati ottenuti nel caso della calibrazione radiometrica, spettrale e geometrica. E' inoltre presentata un'analisi delle prestazioni del rivelatore (ad esempio, stabilità dell'offset, dark current, readout noise) e di un effetto inatteso osservato sui dati.

Il Capitolo 3 riporta un'analisi volta ad evidenziare possibili candidati scientificamente interessanti (Targets of Opportunity) che JUICE (in particolare JANUS) potrebbe osservare durante la lunga fase di crociera interplanetaria verso il sistema gioviano.

I restanti Capitoli sono invece dedicati alle attività svolte nello sviluppo, caratterizzazione e integrazione di HYPSOS sul banco ottico presso il CNR-IFN di Padova.

Il Capitolo 4 descrive l'esperimento, lo strumento e il principio di funzionamento e il contesto per i successivi Capitolo 5, 6, 7.

Il Capitolo 5 è dedicato alle attività di caratterizzazione dei due specchi asferici off-axis di HYPSOS e del reticolo di diffrazione.

Il Capitolo 6 descrive le soluzioni adottate sul banco ottico da un punto di vista optomeccanico e di software di gestione del setup e dell'acquisizione.

Il Capitolo 7 descrive le attività di caratterizzazione svolte sullo spettrometro (inclusa un calibrazione spettrale preliminare) e le metodologie di allineamento del reticolo nello spettrometro e del telescopio (Three Mirror Anastigmat) di HYPSOS.

Abstract

Optical instruments are fundamental tools of the space missions for Solar System exploration. They can differ both for the observed region of electromagnetic spectrum and for the type of instrument. However, they all have a common denominator: *must be calibrated and characterized*. Instruments on board space missions operate in harsh environments and suffer from thermomechanical stresses, but they must guarantee their capabilities. The *calibration* process allows to have a mapping between the external ambient and the data generated by the instrument observing it, providing information in physical units. The *characterization* process allows to have an understanding of how the single components work and of the whole system, improving the comprehension of the instrument itself. A well characterized and calibrated instrument will provide more reliable data, its behaviour will be more predictable and it allows to identify possible problems during its operative lifetime.

This thesis applies this theme to different types of instrument, and in different development phase: JANUS (Jovis Amorum ac Natorum Undique Scrutator), a high-resolution camera ready to be launched towards the Jovian system in April 2023 on board the ESA JUICE (JUpiter ICy moons Explorer), and HYPSOS (HYPerspectral Stereo Observing System), a stereo imaging spectrometer which has been realized in laboratory as a prototype with the goal to validate a new concept of instrument.

The first part of the thesis is dedicated to the activities conducted on JANUS, in particular about the analysis of the on ground calibrations data.

In Chapter 1 the JUICE mission, JANUS, its scientific objectives and technical solutions are described. It provides the context for the Chapter 2 and 3.

In Chapter 2 the methodologies applied for the analysis of the calibrationd data, discussion and results for radiometric, spectral and geometrical calibrations are presented. There is also an analysis of the detector performances (such as, offset stability, dark current, readout noise) and of an unexpected effect observed directly on the data.

Chapter 3 shows an analysis performed to identify scientifical interesting targets (Targets of Opportunity) potentially observable by JUICE (and in particular JANUS during the long interplanetary cruise toward the Jovian System.

The remaining Chapters describe the activities performed at CNR-IFN in Padua, to develop, to characterize and to integrate HYPSOS and the setup in the optical bench.

Chapter 4 describes the experiment, the instrument design and its working principle. Moreover, it provides the context for the following Chapters (5,6,7).

Chapter 5 is dedicated to the characterization activities performed on the two aspheric off-axis mirrros composing the HYPSOS' telescope, and on the selected diffraction grating.

Chapter 6 describes the adopted solutions on the optical bench for the experimental setup both in terms of optomechanical and control software.

Finally, Chapter 7 describes the characterization activities on the spectrometer (including a preliminar spectral calibration) and the methodologies used for the alignment of both the diffraction grating on the spectrometer and Three Mirror Anastigmat telescope of the instrument.

Contents

List of Figures

List of Tables

Part I

JANUS (Jovis Amorum ac Natorum Undique Scrutator)

Chapter 1

JANUS experiment

1.1 JUpiter ICy moons Explorer (JUICE)

1.1.1 Introduction

JUICE (JUpiter ICy moons Explorer) is the first large (L1) mission of the European Space Agency (ESA) in the framework of the Cosmic Vision 2015-2025 programme.

The program was the result of the interaction among scientists, in response to an ESA call for themes opened in April 2004. It was the natural evolution of previous plans (Horizon 2000, Horizon 2000 Plus) and of the idea that successful missions need a long-range space science plan (ESA 2005).

Four main Themes emerged from the scientific community as higher priority topics to be addressed in (at that time) future missions.

- *What are the conditions for planet formation and the emergence of life?*
- *How does the Solar System works?*
- *What are the fundamental physical laws of the Universe?*
- *How did the Universe originate and what is made of?*

The JUICE mission has been conceived to answer to the questions posed by Themes 1 and 2, exploring the Jovian system as whole (Jupiter, its icy moons and their interactions) (Figure 1.1).

The mission was selected in May 2012, adopted in November 2014 and the industrial implementation started in July 2015 (Witasse et al. 2019).

Originally planned to be launched in 2022, it has been currently postponed to April 2023.

1.1.2 Scientific objectives

The main objective of the mission (as detailed in ESA JUICE definition study report/Red Book 2014 and Grasset et al. 2013) is the investigation of the habitable worlds around the gas giant exploiting two themes:

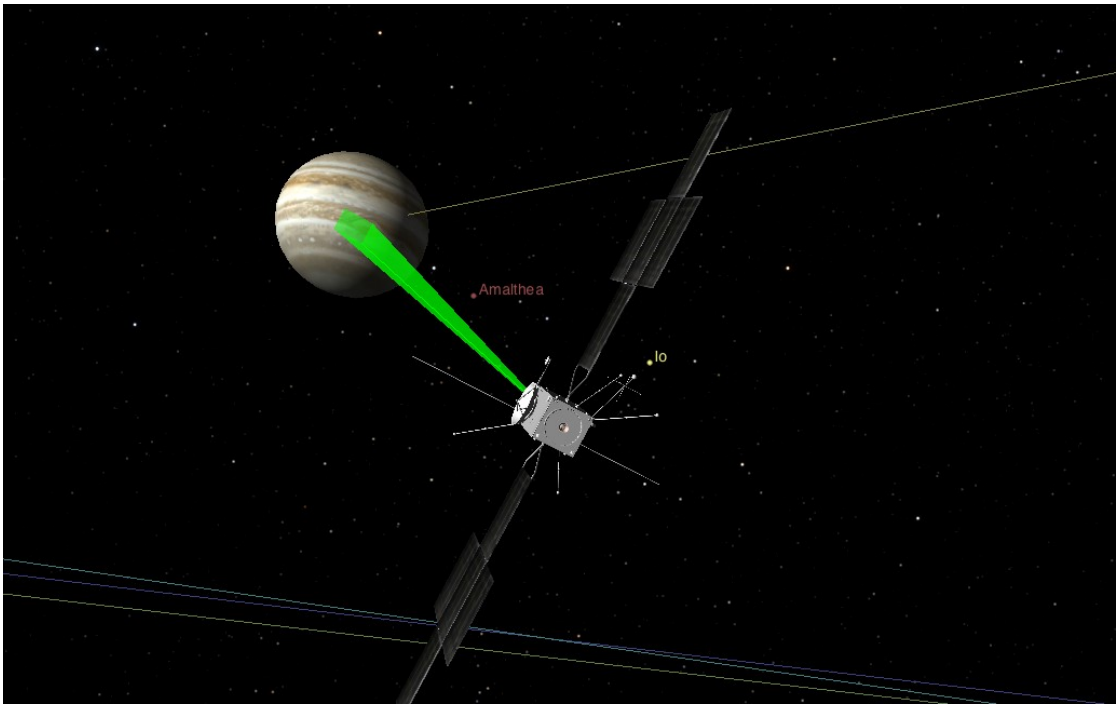

Figure 1.1: A pictorial representation of JUICE exploring Jupiter. In green, the FOV of JANUS, the high-resolution camera on board the mission. Image from Cosmographia

- Characterize Ganymede, Europa and Callisto as planetary objects and potential habitats
- Explore the Jupiter system as an archetype for gas giant

By now it is commonly accepted that the possibility to have *habitable* environments is no more restricted to places located into the habitable zone of a stellar system. The habitable zone is where liquid water is possible on the surface of a planet. Thanks to the probes Galileo on Jupiter and Cassini on the saturnian system it was clear that liquid oceans are also possible under the surfaces of the icy moons. The liquid water is a fundamental block for the presence of life and this justifies the deep interest in finding liquid reservoirs. However, it is not the only one. To sustain life, according to the actual knowledge: liquid water, energy, nutrients (in particular C, H, O, N, P, S to drive biochemical reactions) and time stability (Grasset et al. 2013,Nimmo et al. 2016) are required. Icy moons as Ganymede and Europa are excellent candidates.

A generic icy satellite consists of an H_2O layer sitting atop a silicate core (Nimmo et al. 2016). For largest icy satellites as Ganymede (the main objective of the JUICE mission) the situation is more complex due to iron core, high pressures and internal heat sources (Hussmann et al. 2015). The plausible structure of Ganymede is shown in Figure 1.2. The moon surface is covered by a layer of ice-I. Ice shows a large number of possible structure depending on the temperature and pressure conditions and Ice-I (Ih, hexagonal

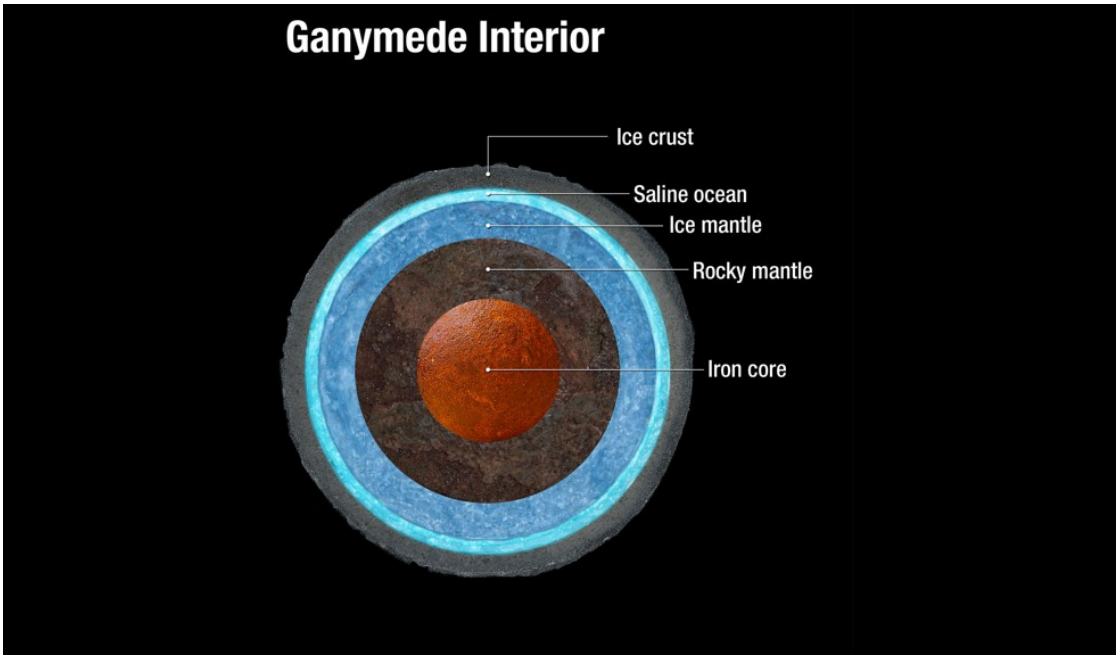

Figure 1.2: Interior model of Ganymede. Credits: NASA, ESA, A. Feild (STScI- Space Telescope Science Institute)

structure) is a stable phase of Ice sharing a phase boundary with the liquid water (Hansen 2021). Ice-I melting temperature decreases with increasing pressures allowing the have a saline liquid ocean between the Ice-I and high-pressure ice phases. Underneath that layer, there is, probably, a rocky mantle differentiated from the iron core, interpretation supported by the self-sustained magnetic field of the satellite (Hussmann et al. 2015). The ocean is probably maintained liquid thanks to a combination of radiogenic heating, tidal heating and the presence of antifreezing chemical species (Nimmo et al. 2016). The reason because Ganymede has been selected as the main focus of the mission, is well resumed by a sentence of the RedBook-Definition study report (ESA JUICE definition study report/Red Book 2014):

Ganymede is identified for investigation because it provides a natural laboratory for analysis of the nature, evolution and potential habitability of icy worlds but also because the role it plays within the system of Galilean satellites and its unique magnetic and plasma interactions with the surroundings Jovian environment.

1.1.3 Mission scenario

After a long interplanetary cruise (about 8.5 years), JUICE will arrive at Jupiter in 2031 and it will spend at least four years in the Jovian system (Witasse et al. 2022). The mission timeline is subdivided into three main phases:

- Cruise

- Jovian Tour
- Ganymede Tour

The launch is planned for April 2023 and the trajectory structured in three main phases: the cruise phase, the Jupiter tour beginning with the Jupiter Orbit Insertion (JOI) in July 2031 and the Ganymede phase with the Ganymede orbit insertion (GOI) occurring in December 2034 and ending in September 2035. In particular, the cruise phase lasted about 8 years and foresaw one Moon-Earth flyby (August 2024), two Earth flybys (September 2026 and January 2029) and one Venus flyby (August 2025) before the JOI (figure 1.3).

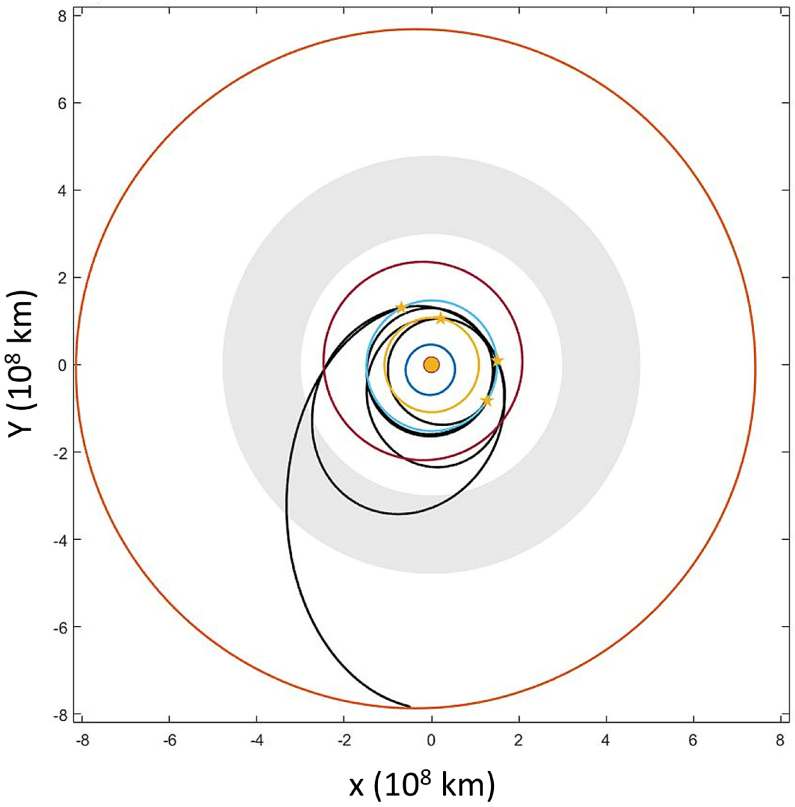

Figure 1.3: The baseline orbit of the JUICE mission before entering orbit around Jupiter. The yellow stars show the four Earth gravity assists (including the Moon-Earth one) and one Venus flyby. The grey circular band shows the asteroid Main Belt extension.

During the cruise there will be instrument calibration and check out operations; nevertheless, other scientific opportunities have also been considered, including one or multiple asteroids flyby (Witasse et al. 2021).

During the *Jovian Tour* the spacecraft will investigate Jupiter, its atmosphere, magnetosphere and dynamics at different elevations up to 30°, taking advantage of multiple Callisto flybys (figure 1.4). In this phase Callisto will be studied and also the polar region of Jupiter, difficult to observe from ground.

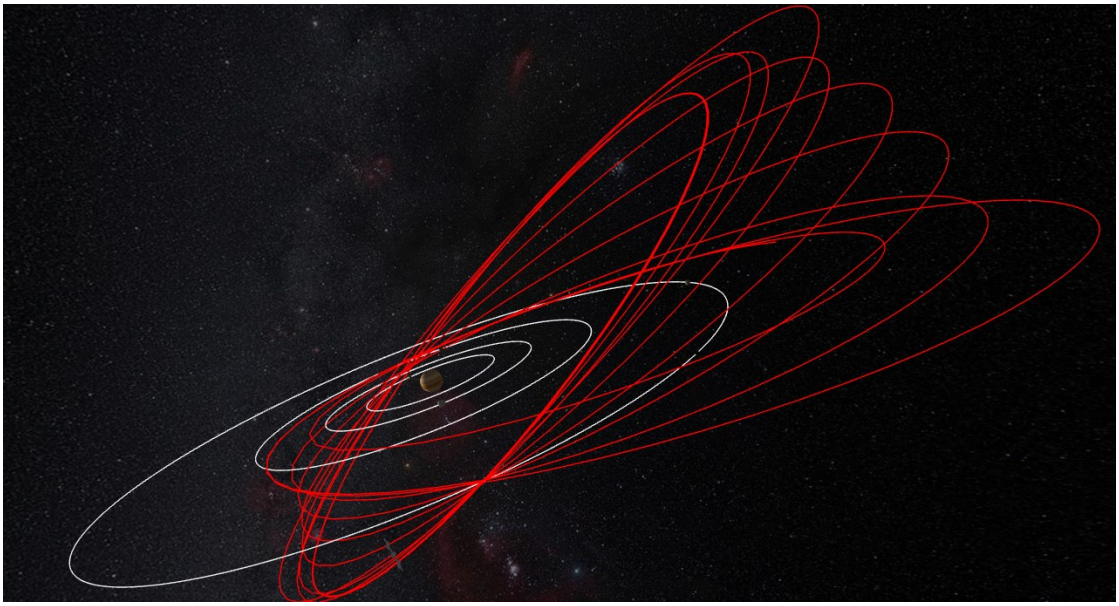

Figure 1.4: JUICE high altitude orbit phase. Image from ESA website tool: "Where is Juice?". Credit: ESA

Moreover, JUICE will also make two Europa flybys in order to study the composition of non-water-ice material, organic chemistry, tenuous atmosphere, surface geological features, induced magnetic field, the top ice layer and, including the first subsurface observation of an icy moon (Grasset et al. 2013).

The last mission phase, the *Ganymede tour*, will be entirely devoted to the study of the icy moons, which will be exploited in four subsequent phases: elliptical orbit, high altitude circular orbit at 5000 km (namely *GCO5000*), elliptical orbit and low altitude circular orbit (namely *GCO500*). Actually, also a fifth phase is possible, a circular orbit at 200 km.

1.1.4 Spacecraft and instrumental suite

JUICE is equipped with 10 instruments designed to answer the broad range of scientific questions posed by the mission's objectives. The instruments are conceptually divided into three categories: remote sensing, geophysical and in-situ. A summary of the instruments and their scientific support to the mission is provided in Table 1.1. JANUS, the high-resolution camera, which is one of the main topics of this Thesis will be described deeply in the following chapters.

JUICE instrumental suite

Instrument	*Type*	*Mission contribution*
	Remote sensing	
JANUS	Imager	Moons geologic process and morphology of surfaces, Jupiter atmosphere and dynamics, physical and dynamical properties of minor moons and rings, auroras, plumes torus and exospheres
MAJIS	Vis-IR imaging spectrometer	Moons surface composition and Jupiter atmosphere
UVS	UV imaging spectrometer	Moons exospheres and interaction with Jovian magnetosphere and plasma tori. Jupiter auroras
SWI	Sub-millimetre wave spectrometer	Composition and structure of moons exosphere, Jupiter's stratosphere dynamics, winds speed and temperature
	Geophysical	
GALA	Laser altimeter	Moons topography and tidal deformations
RIME	sub-surface sounding radar	Moons subsurface structure. Search for ice/water interface
3GM	Radio science experiment	Interior state of Ganymede and presence of deep water. Moons surface properties. Atmospheric science at Jupiter and moons, rings
	In-situ	
JMAG	Magnetometer	Induced magnetic field of moons, Ganymede intrinsic magnetic field and interactions
PEP	Particle environment package	Plasma composition and distribution. Jovian magnetosphere interaction. Energetic Neutral Atom imaging of neutral and plasma tori. Composition and structure of exospheres and ionospheres of the moons
RPWI	Radio and Plasma wave instrument	Exospheres, magnetospheres, magnetic fields and interactions
	Virtual	
PRIDE	Very-long baseline interferometry	Moons ephemerides and gravity fields

Table 1.1: JUICE payload. The *virtual* instrument is not physically on board and will make use of the antenna and radio stations. Adapted from ESA JUICE definition study report/Red Book 2014 and Plaut et al. 2014

JUICE is a solar-powered three-axis stabilized spacecraft. The solar panels, composed by triple-junctions cells (Khorenko et al. 2017), are able to provide 730 W (end of life, EOL) thanks to 85 m^2 of array surface.

JUICE is never operated in direct commanding (except in LEOP, "Launch and Early Orbit Phase") and, apart 8 hours ground-station pass of nominal science operations, the spacecraft is fully autonomous (Ecale et al. 2018). The operations out-of-visibility are executed inserting the telecommands in the Mission Time Line with a time tag (Ecale et al. 2018).

The remote sensing suite, GALA, STR-OH (Start TRacker Optical Head) and the Navigation Cameras required to be co-aligned and are mounted on the so-called *Optical bench* with the boresights pointing towards the +Z axis of the spacecraft. The Optical bench is made of Carbon Fiber Reinforced Polymer (CFRP) and all the instruments are radiatively and conductively decoupled from the bench in order to reduce thermo-elastic disturbances to the other instruments line of sight (Peyrou-Lauga et al. 2018).

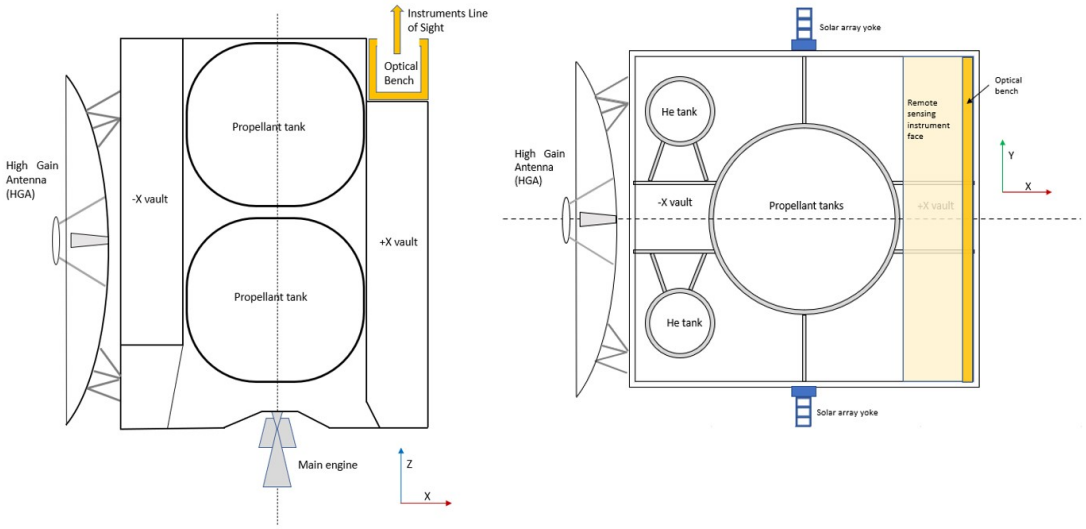

Figure 1.5: Sketch of the JUICE spacecraft body cross-section. The drawing is not in scale. The JUICE reference system is shown. Adapted from Peyrou-Lauga et al. 2018

Figure 1.5 shows a sketch of the S/C body cross-sections; in yellow it is highlighted where the Optical bench is located on the spacecraft and where the boresights overlook.

As much as possible, the electronics (of the S/C and of the instruments) are located inside two lead reinforced vaults (-X and +X vaults) which offer protection from the harsh Jovian radiation environment.

As described in Peyrou-Lauga et al. 2018 and Peyrou-Lauga et al. 2019, the thermal control is based on a passive approach supported by active heating. The thermal units are organized in 5 (actually 6, but Category 6 is never used) units:

- Category 1: Conductively controlled by S/C
- Category 2: Radiatively controlled by S/C
- Category 3: Thermally decoupled from S/C
- Category 4: Thermally decoupled from S/C with a separate radiator
- Category 5: Thermally decoupled from S/C but requiring a cold finger

Concerning JANUS, the instrument parts are included in Categories 1 and 5. In particular, the Main Electronic (Category 1 - collectively controlled) is controlled along with the other units in the vault in a *collectively* fashion. The conductive coupling is performed using a network of heat pipes (Peyrou-Lauga et al. 2019). The Proximity Electronic (Category 1 - individually controlled) is mounted on a dedicated bracket, coupled to its own radiator by means of flexible high conductance thermal straps and actively controlled with a dedicated heating line (Peyrou-Lauga et al. 2019). The optical head (Category 5), is mounted on the Optical bench and thermally decoupled from it; it requires a cold finger for the detector (Peyrou-Lauga et al. 2019)

1.2 JANUS Instrument

1.2.1 Instrument configuration

JANUS (Jovis Amorum Ac Natorum Undique Scrutator) is the high-resolution camera selected for the JUICE mission. The instrument has been developed by an international consortium having Italy as leader both for scientific (INAF - National Institute of Astrophysics) and industrial (Leonardo S.p.A) parts and composed by the German Aerospace Center - Planetary Research Institute (DLR) which provided the Electronics and the Focal Plane Module, the Instituto de Astrofisica de Andalucia (IAA) in charge of the Filter Wheel, CEI-Open University, which provided the detector, and CISAS-University of Padua which contributed with the Cover Module.

Its development has been influenced by the great variability of observing conditions for several objects of the Jovian system, allowing orders-of-magnitude steps ahead in terms of coverage and/or resolutions and/or time evolution on many targets (Palumbo et al. 2014).

The instrument is composed by three main functional blocks, shown in Figure 1.6: the Optical Head Unit (OHU), the Main Electronics Unit (MEU) and the Proximity Electronics Unit (PEU).

The MEU includes the Power Supply Module (PSM) and the Data Processing Module (DPM) and it is organized in a fully cold-redundant configuration with the main function to interface the instrument to the spacecraft and control the instrument itself. (Della Corte et al. 2014).

The PEU electronic box is devoted to the communication from/to the detector and in general to low-level detector management and digitization (ADC 14 bit). It is located

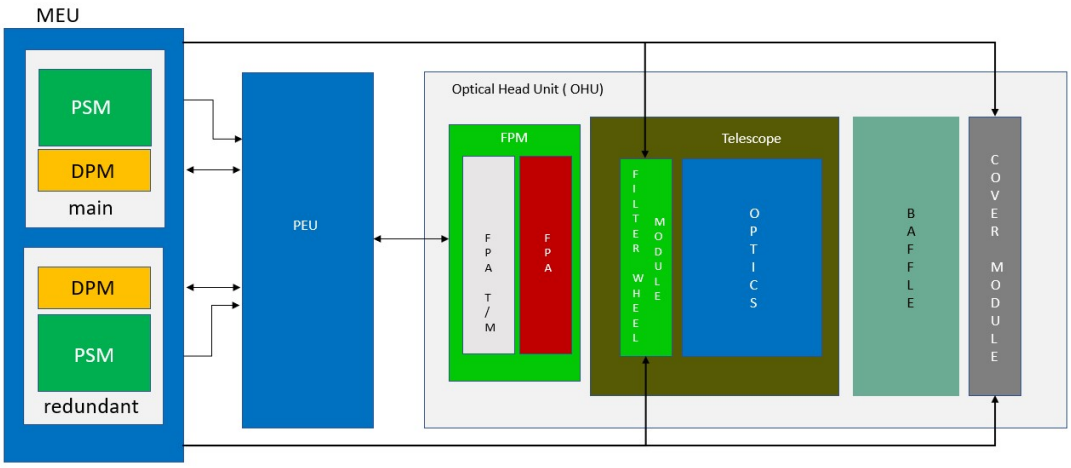

Figure 1.6: JANUS functional blocks diagram. Adapted from Della Corte et al. 2019

near the FPM (Focal Plane Module) in order to reduce the noise and in general the electrical path between the image sensor and its readout circuit (Della Corte et al. 2014).

The OHU section includes the telescope, the baffle, the FPM, the Filter Wheel Module (FWM) and the Cover Module (COM). The FWH and the COM have the strong heritage from OSIRIS instrument on board Rosetta mission (Keller et al. 2007). The OHU houses all the optical-mechanical components of the instrument.

The telescope is supported by the Optical Wall, together with the FWM from one side and the FPM on the other side. The Baffle Wall supports the long external baffle in front of the telescope. These mechanical structures are made in Invar36 (Della Corte et al. 2019).

The preliminary design of the instrument was a TMA (Three Mirrors Anastigmat) telescope (Greggio et al. 2014) which eventually moves towards a two-mirrors telescope configuration (modified Ritchey-Chretien, RC) (Greggio et al. 2016). Although the TMA configuration offered better performances in terms of MTF (due to the unobstructed FOV) and straylight control with respect to the RC one, the latter has been preferred mainly due to stringent requirement from the spacecraft in terms of mass (the RC is a more compact solution) and also for ease of alignment and manufacturability of the components (Greggio et al. 2016).

Figure 1.7 shows a sketch of the optical design of the instrument. The baseline optical design is Ritchey-Chretien (with the strong heritage from HRIC/SIMBIO-SYS (Cremonese et al. 2020), but the mirrors feature an aspherical 10th order shape rather than pure hyperboloid, with the primary mirror (M1) made by Fused Silica and the secondary mirror (M2) made by Zerodur (Della Corte et al. 2019). The RC is coupled to a dioptric corrector composed by three spherical lenses in fused silica (Della Corte et al. 2019). The instrument has also multispectral capabilities thanks to the Filter Wheel housing 13 filters with an overal spectral range from the 350 nm to the 1100 nm.

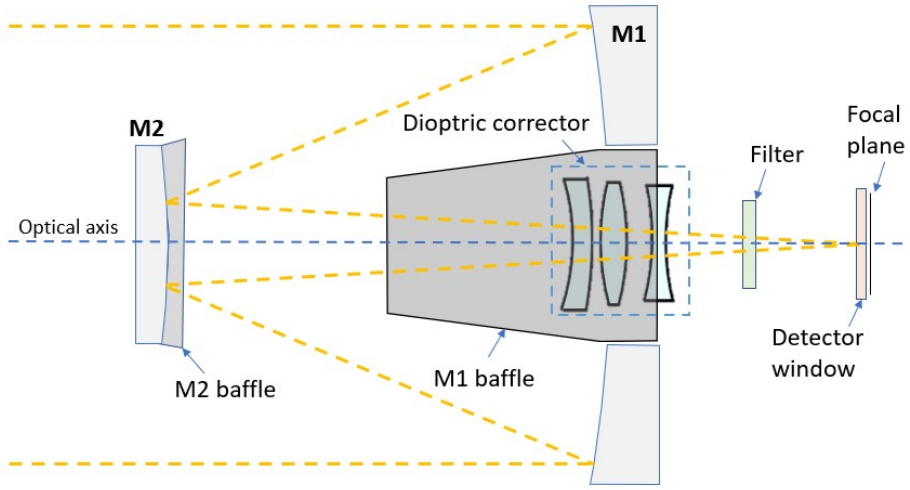

Figure 1.7: Sketch of the JANUS optical design

The filters are located, in the optical path, after the dioptric corrector with the beam being convergent towards the detector. Figure 1.8 shows a pictorial representation of the spectral coverage offered by JANUS with its filters. Table 1.2 resumes the principal nominal characteristics of the filters and their purposes.

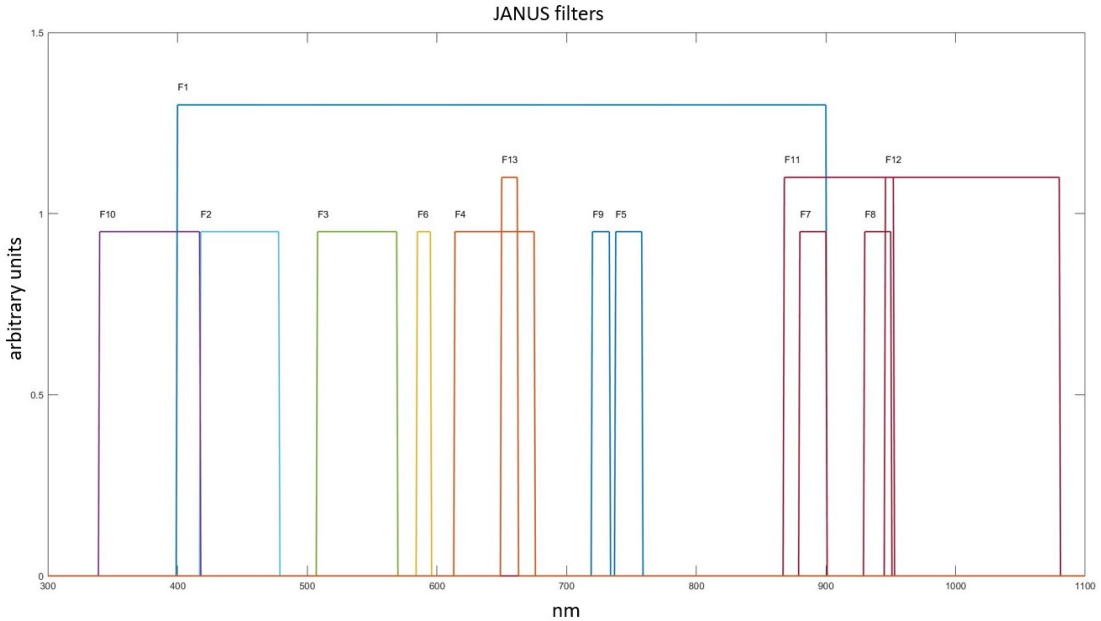

Figure 1.8: JANUS filters position in the spectrum along with their nominal bandpass. The height of the filters has no significance, and it is used only for visual purposes.

JANUS filters			
Filter ID	Center (nm)/ FWHM (nm)	Name	Note
F1	650/500	Panchromatic	
F2	450/60	Blue	satellite colours
F3	540/60	Green	satellite colours - background for Na
F4	646/60	Red	satellite colours- background for $H\alpha$
F5	750/20	CMT Medium	continuum for strong Jovian methane band, geology
F6	590/10	Na	Sodium D-lines in exospheres
F7	889/20	MT strong	strong Jovian methane band
F8	940/20	CMT strong	Continuum for medium Jovian methane band, Fe^{2+}
F9	727/10	MT medium	medium Jovian methane band
F10	380/80	Violet	UV slope
F11	910/80	NIR1	Fe^{2+}, Io lava spots
F12	1015/130	NIR2	Fe^{2+}, Io lava spots, GALA laser altimeter footprint
F13	656/10	$H\alpha$	$H\alpha$ line for aurorae and lightning

Table 1.2: JANUS filters nominal characteristics. Adapted from Della Corte et al. 2019

The last optical element before the focal plane is a transparent window, his function is to protect the detector. JANUS makes use of CMOS detector (Soman et al. 2014), the CIS115 designed by e2v (now Teledyne e2v). The detector is back-illuminated, providing 100% fill factor. It features 2000x1504 pixels of $7\mu m$ pitch size, subdivided into four zones (2000x376 pixels) which are simultaneously read in rolling shutter mode. In the context of this work, they will be named *Tiles*. The pixels feature a 4T structure (pinned photodiode) and each of the four zones has its own signal line and reference line which are used to implement a CDS (Correlated Double Sampling) readout. The detector has been deeply characterized in terms of response to radiation (Winstone et al. 2015, Crews et al. 2020, Crews et al. 2019, Lofthouse-Smith et al. 2018b, Soman et al. 2015b, Soman et al. 2016), image lag (Lofthouse-Smith et al. 2018a) and non-linear responsivity (Soman et al. 2015a). The baffle scheme is composed by the external baffle, characterized by vanes to block first order straylight paths from the baffle itself, an extension baffle between M1 and M2, a baffle on M1 (supporting also the catadioptric corrector), a baffle on M2 and a detector baffle (Greggio et al. 2018).

1.2.2 Science Objectives

JANUS will provide a tremendous support to the overall mission science objectives both as primary and support instrument, providing also a context for other instruments such as GALA (the laser altimeter). A list of topics of interest for JANUS is:

- Geology of the icy moons Ganymede, Callisto and Europa (study of tectonics, mass wasting, cryovolcanism, craters, colours characteristics)
- orbit, rotation status and interiors of icy moons
- Io volcanic activity
- Jupiter's atmosphere and magnetosphere (troposphere, dynamical processing, clouds, vortices, stratospheric variations, lightning, auroral and interaction)
- satellites exospheres
- Jupiter's ring
- Jupiter's irregular satellites

JANUS will perform a global coverage of Ganymede at 400 m/pix and of Callisto at $<$ 2 km/pix, Europa's surface will be covered at 55% at $<$ 3km/pix and the instrument footprint on Io will range from 5 to 20 km/pix. On Ganymede, the sampling will be improved thanks to the passage from the GCO5000 to the GCO500 and, if possible, to GCO200. The improvement in terms of Ganymede coverage (for each ground sampling distance, GSD) with respect to that offered by Galileo mission is 50 times higher. For specific targets the GSD will reach, on Ganymede up to 3 m/pix. Moreover, JANUS will provide Digital Terrain Models (DTM) for selected targets combing nadir and off-nadir images.

Chapter 2

Targets of Opportunity

2.1 Introduction

In this section the analysis carried out to identify possible targets of opportunity for the JUICE mission and in particular for the JANUS instrument, during the long cruise phase is described.

The analysis (Agostini et al. 2022) made use of the latest mission trajectory available at time (Consolidated Report on Mission Analysis (CReMA 5.0b23), meta-kernel: *juice_crema_5_0b23_1.tm*). Recently, a new set of SPICE kernels have been released and in principle the analysis should be updated. However, it will be clear in the following sections that the flexibility of the approach allows a relatively fast re-application of the method in every phase of the JUICE mission and also for other missions. Updating the results is planned in the next future.

2.2 Scientific rationale

Figure 2.1 shows the heliocentric distance of the JUICE spacecraft during the cruise phase, together with the limits (in astronomical units, AU) of the asteroid Main Belt (MB) region. The spacecraft will cross this region twice, providing a solid possibility to observe one or more Solar System's small bodies.

Asteroids play a fundamental role in the comprehension of the Solar System and planetary systems at large (Michel et al. 2015; Morbidelli et al. 2015). The observation of possible targets of opportunity (ToO) for the the JUICE mission would maximise the scientific return of the entire mission (addressing two Cosmic Vision's main themes: *What are the conditions for planet formation and the emergence of life?* and *How does the Solar System work?*) and would enrich the knowledge of the Main Belts itself, as it occurred with the Rosetta mission on asteroids (2867) Steins (Schulz 2010; Keller et al. 2010) and (21) Lutetia (Schulz et al. 2012; Sierks et al. 2011) while en route to comet 67P/Churyumov-Gerasimenko (Taylor et al. 2017).

This work has been structured having in mind the JANUS high-resolution camera capabilities to observe these bodies. JANUS could provide data useful for rotational curve

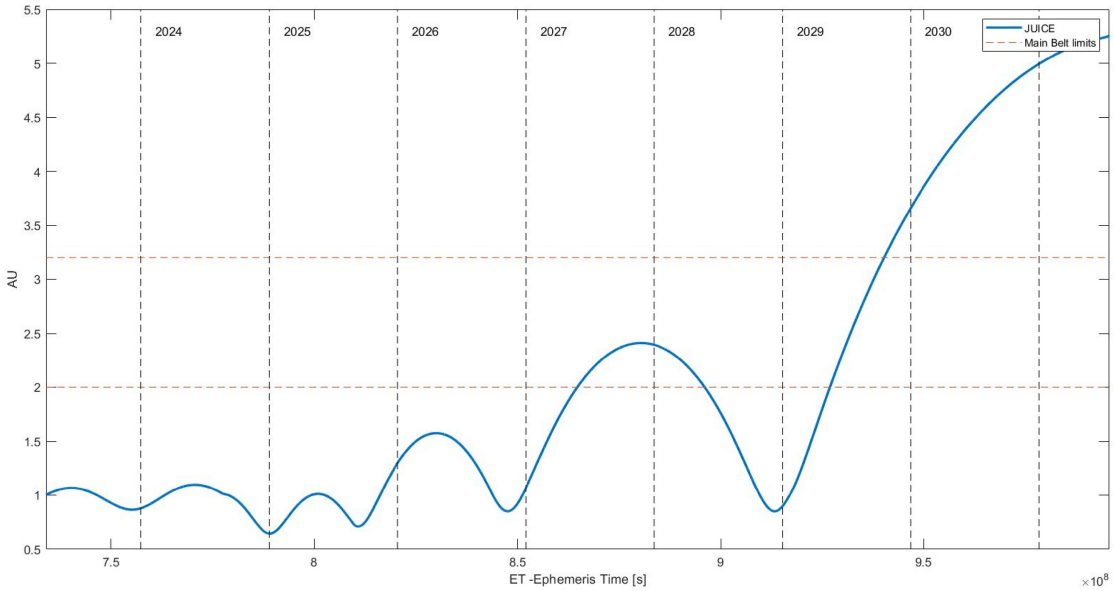

Figure 2.1: Heliocentric distance of JUICE S/C. Starting point is April 2023 and ending point is July 2031. The x-axis is the Ephemeris Time (seconds past J2000).

analysis and multi-wavelength photometry (e.g., Lamy et al. 2010)

2.3 Methodology and dataset

The analysis has been developed making intensive use of the SPICE system, since both the JUICE spacecraft kernels[1] and the asteroids ones[2] are publicly available. The asteroids SPK are retrieved from the JPL HORIZONS system (Acton 1996). It is, therefore, possible to evaluate the distance between the spacecraft and each selected asteroid, and, in turn, how the latter would appear on the focal plane of the JANUS camera. A similar methodology has been proposed in the context of a mission study to an Ice Giant planet with the objective to prove that this type of analysis is feasible and useful to optimise the trajectory design and the target selection process for flyby opportunities (Costa Sitjà et al. 2020).

The procedure marks an asteroid as a target of opportunity according to both the following criteria:

- spacecraft-target distance
- pixel fraction on the JANUS focal plane

The pixel fraction, that is how many pixels on the camera focal plane are covered by

[1] ESA SPICE Service, https://doi.org/10.5270/esa-ybmj68p
[2] https://ssd.jpl.nasa.gov/horizons/

the diameter of the target body, is calculated according to:

$$PixFrac = \frac{D_{body}}{R} \cdot \frac{f_{janus}}{pix_{janus}} \tag{2.1}$$

where $PixFrac$ is the pixel fraction, D_{body} is the diameter of the target, R is the minimum range between the spacecraft and the target over the all trajectory, f_{janus} and pix_{janus} are the nominal focal length and pixel size of JANUS, respectively.

Starting from an extremely large dataset of asteroids, the analysis has been limited to those with reported diameter (or retrievable from albedo e magnitude), that is about 140000 possible targets. This choice reduces the computational effort and makes it possible to use both the selected criteria already mentioned.

The used methodology allows to split the problem of ToO identification in a sequence of consecutive steps. The first step reduces the initial dataset to a limited number of targets by selecting suitable thresholds for distance and pixel fraction. A second step consists in the evaluation of other geometrical information (such as the solar phase angle) on the reduced dataset and after that a selection is performed on the basis of physical properties (such as known/unknown taxonomic classification, diameter size) and "observational status" (already observed/not observed in situ).

2.4 Automatic Asteroid Search Toolkit

In order to perform this analysis, a dedicated software tool has been developed, called Automatic Asteroid Search Toolkit, A^2ST (Agostini et al. 2022). It it composed by two main parts:

- SPK downloader
- distance and pixel fraction calculation

The SPK downloader part is a Python script able to automatically download the binary SPK kernel from HORIZONS. The input is a list of asteroid SPICE IDs in a form of text list. The output is a single spk kernel for each ID. The script also provides two text files which could be used as a log of the session. The first text includes all the downloaded targets, the second one a list with the failed IDs. The text file with the failed calls to HORIZONS can be used as a new input file since generally the download fails due to a temporary problem in the communication with HORIZONS.

The core of the python script is the *smb_spk* function (provided by NASA), written in Expect/Tcl language. It has been found easier to manage it in a linux-based environment, which is therefore used during the download of the dataset.

It should be highlighted that after the development of the presented tool, Horizons system has done a major update to its interface providing an easier to handle method for retrieving the SPK files[3]. The new API does not make use of the smb_spk function

[3] https://ssd-api.jpl.nasa.gov/doc/horizons.html

and could be managed in a simple way in different operative systems using the provided examples (with very small modifications to adapt it to the tool structure). This could allow to include all the pipeline in a unique MatLab environment, hence simplifying the usage of the tool (Agostini et al. 2022).

Figure 2.2 shows the workflow of the data elaboration to retrieve the distance and the pixel fraction. This part of the toolkit is written in MatLab and takes advantage of MICE, which is the MatLab implementation of the SPICE toolkit. The analysis is performed in a Windows 10 environment.

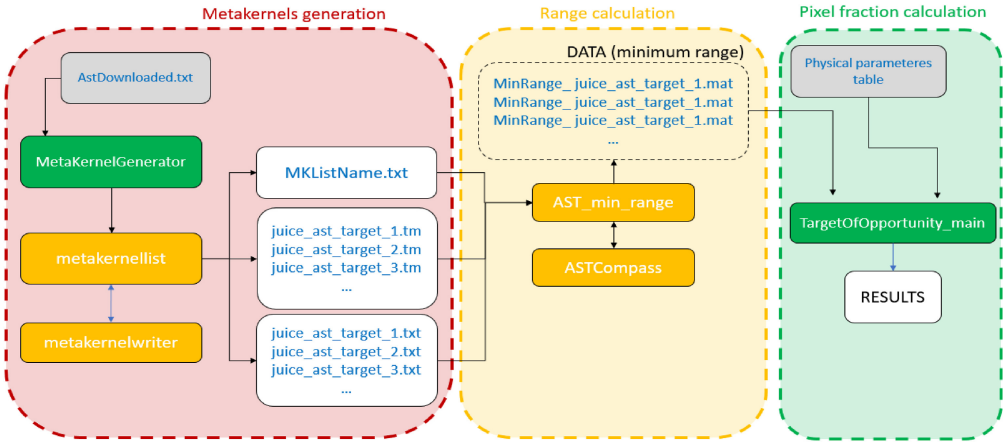

Figure 2.2: Workflow of data elaboration. The selected targets are saved in a .txt file. Meta-kernels generation: *metakernelwriter.m* writes the single metakernel using the selected JUICE meta-kernel as baseline, *metakernellist.m* divides the targets in "elaboration nuclei" and manages *metakernelwriter.m*. Range calculation: *ASTCompass.m* implements the SPICE function used. *AST_min_range.m* generates data compatible with the pixel fraction calculation section and manages *ASTCompass.m*. Pixel fraction calculation: *TargetOfOpportunity_main.m* loads the data generated by the previous step and the physical parameters related to the target, providing the target list of possible targets of opportunity.

The process develops in three phases (Figure 2.2) with the addition of a preliminary phase. The preliminary phase is required to verify the consistency between the names and IDs from different sources. If the ID used in the download step ("external") is different from the ID inside the comment section of the kernel ("internal") both the IDs are considered valid to search the small body in the physical parameters table but the "external" ID is used in the SPICE functions.

The global dataset is subdivided into groups of maximum 2000 asteroids, which IDs are added to the baseline JUICE meta-kernel generating a new meta-kernel. To maintain the JUICE kernels to the highest priority, the asteroid SPK kernels are loaded first. The whole process is repeated until all the available targets are terminated (Agostini et al. 2022).

For each newly generated meta-kernel, the algorithm loads the meta-kernel, calculates

SPKPOS parameters	
Frame	ECLIPJ2000
Aberration correction	LT+S (light time + stellar aberration)
Observer	JUICE
Date Start	2023 APR 06 00:00:00 UTC
Date End	2031 JUL 21 00:00:00 UTC
Time resolution	1h

Table 2.1: Parameters used as input for SPICE function SPKPOS

the minimum JUICE-target distance for each asteroid in the meta-kernel and at the end unloads the meta-kernel itself. The distance is calculated using the SPICE function cspice_spkpos[4] which allows to calculate the position vector of the selected target in the JUICE reference frame, eventually corrected for light time and stellar aberration for each date defined by the user. The time window considered includes the entire trajectory. The used settings for the SPKPOS function are summarised in Table 2.1. Since, the idea is to just set up a threshold condition no attention is paid to the attitude of the spacecraft (that is, if the asteroid is actually in the FOV of the JANUS camera). In this context "threshold condition" means that if the pixel fraction is too small or the distance extremely high, the target is not observable or a possible flyby could not be a feasible solution (Agostini et al. 2022).

Finally the pixel fraction is evaluated using equation 2.1 and the asteroid physical parameters from a file.

It is possible, for a very few cases, that the asteroid diameter is not explicitly reported but geometric albedo and absolute magnitude are instead available. In this case the diameter information is derived from the equation (Bowell et al. 1989; Harris et al. 1997):

$$D_{body} = \frac{1329.23 \cdot 10^{-0.2H}}{\sqrt{a}} \tag{2.2}$$

where H is the absolute magnitude and a is the geometric albedo. The diameter estimation based on this formula could have a large error[5] leading to a wrong estimation of the pixel fraction. For this reason, the tool flags the solutions retrieved in this way allowing the user to verify the used assumptions. Nevertheless, the code still provides the results sorted both for pixel fraction/distance and only distance, so a flagged solution could still be taken into account considering the distance-sorted solution (Agostini et al. 2022).

Table 2.2 provides a list of potentially interesting targets, resulting from the searching procedure. The first 100 targets with the higher pixel fraction are then sorted according to increasing distance from JUICE, up to a threshold value of $500 \cdot 10^5$ km, resulting in a selection of 71 asteroids.

[4] https://naif.jpl.nasa.gov/pub/naif/toolkit_docs/MATLAB/mice/cspice_spkpos.html
[5] https://cneos.jpl.nasa.gov/tools/ast_size_est.html

TargetID	Distance [10^5 Km]	Diameter [km]	Pixel Fraction	SMASSII	Tholen	Absolute Magnitude	Albedo	Rotation Period	BV	UB
2229179	3.13	3.05	0.65			16.54	0.05	-	-	-
2052073	3.24	2.67	0.55			15.48	0.14	-	-	-
2350979	7.28	1.6	0.15			17.88	0.06	-	-	-
2053982	10.33	6.83	0.44			14.83	0.06	36.38	-	-
2195434	11.02	2.49	0.15			16.83	0.07	-	-	-
2010650	13.77	2.15	0.1			15.45	0.32	33.9	-	-
2012327	14.27	5.96	0.28			15.51	0.03	-	-	-
2055438	14.54	3.06	0.14			15.23	0.14	20.34	-	-
2086362	15.77	4.22	0.18			15.78	0.05	-	-	-
2038547	19.53	6.95	0.24			14.24	0.08	-	-	-
2016511	19.96	3	0.1			14.93	0.26	7	-	-
2031661	20.47	2.97	0.1			14.55	0.38	-	-	-
2108093	20.73	3.43	0.11			15.17	0.18	-	-	-
2011741	20.89	6.01	0.19			13.56	0.21	-	-	-
2107764	24.62	3.62	0.1			16.56	0.03	-	-	-
2012191	25.81	4.92	0.13			13.39	0.38	-	-	-
2116035	26.62	6.88	0.17			14.99	0.04	-	-	-
2014679	27.08	4.04	0.1			15.7	0.06	-	-	-
2024188	27.16	3.83	0.09			14.32	0.25	70.54	-	-
2016044	27.39	4.24	0.1			13.88	0.33	-	-	-
2014051	28.36	4.1	0.1			14.6	0.26	5.54	-	-
2003940	31.99	5.08	0.11			12.86	0.57	84	-	-
2021923	34.8	8.37	0.16			12.79	0.21	-	-	-
2041508	36.28	5.01	0.09			14.27	0.13	0.72	-	-
2009559	36.43	14.23	0.26			13.38	0.05	203.26	-	-
2067083	36.82	12.43	0.23			13.72	0.05	-	-	-
2008861	37.67	14	0.25			13.13	0.04	-	-	-
2001650	**38.83**	**30.2**	**0.52**		**F**	**11.64**	**0.05**	**14.89**	**0.64**	**0.2**
2000223	**42.71**	**79.81**	**1.25**		**X**	**9.9**	**0.02**	**20.28**	**0.71**	**0.28**
2067100	44.64	15.27	0.23			13.57	0.04	-	-	-
2029372	45.04	5.98	0.09			14.08	0.2	-	-	-
2004016	45.48	8.31	0.12			14.14	0.06	-	-	-
2002139	47.4	17.24	0.24		F	12.92	0.04	11.98	0.65	0.23
2020210	50.87	19.7	0.26			12.47	0.06	10.33	-	-
2017534	52.44	8.91	0.11			14.2	0.04	-	-	-
2010944	57.06	14.66	0.17			12.95	0.05	12.58	-	-
2054750	60.78	10.52	0.12			13.36	0.11	-	-	-
2005706	61.55	14.45	0.16			12.87	0.07	8.25	-	-
2002505	67.79	22.29	0.22			11.71	0.09	-	-	-
2000673	69.88	37.62	0.36	S	S	10.08	0.09	22.34	0.78	0.43
2012317	73.19	13.1	0.12			13.6	0.05	7.26	-	-
2001088	77.68	15.14	0.13	S	S	11.38	0.17	3.04	0.95	0.59
2017617	77.88	10.51	0.09			12.57	0.21	-	-	-
2003652	78.03	12.65	0.11			13.36	0.04	-	-	-
2000461	80.1	43.6	0.36		FCX	10.54	0.06	7.35	0.61	0.31
2030787	81.13	10.57	0.09			13.7	0.06	-	-	-
2003601	95.76	13.46	0.09			12.77	0.12	12.12	-	-
2001257	112.89	21.39	0.13			12.2	0.05	5.29	0.63	0.32
2001044	124.69	17.51	0.09			10.87	0.25	3.15	-	-
2003325	152.02	28.24	0.12			11.55	0.07	11.57	-	-
2001295	163.79	47.41	0.19			10.73	0.05	14.64	-	-
2005852	177.67	23.74	0.09			12.18	0.04	5.61	-	-
2000821	193.29	28.86	0.1	Ch	C	11.83	0.03	236.6	0.71	0.32
2002524	194.04	32.68	0.11			11.21	0.07	10.08	-	-
2000580	200.72	48.2	0.16			10.28	0.08	9.47	-	-
2000066	210.42	71.82	0.23	Ch	C	9.54	0.02	9.74	0.7	0.36
2000510	229.61	60.45	0.18		PD	9.78	0.06	19.4	0.73	0.3
2000042	230.83	111	0.32	L	S	7.58	0.14	13.59	0.87	0.46
2000080	235.9	68.56	0.19	S	S	8.07	0.21	14.03	0.9	0.52
2000169	281.22	37.52	0.09	Sl	S	9.52	0.19	14.54	0.85	0.46
2000397	288.89	49.03	0.11	K	S	9.43	0.14	15.48	0.82	0.36
2001574	342.34	57.78	0.11			9.95	0.04	12.64	-	-
2000393	351.07	116.19	0.22	Xc	C	8.4	0.02	38.45	0.74	0.32
2001424	380.32	64.69	0.11	X		9.96	0.03	93.73	-	-
2000051	382.25	138.16	0.24	Ch	CU	7.59	0.1	7.78	0.79	0.48
2000392	404.2	60.75	0.1	Ch		9.8	0.17	13.06	-	-
2000043	422.77	71.34	0.11	Sk	S	8.03	0.23	5.76	0.86	0.49
2001042	425.72	63.92	0.1			9.97	0.05	540	-	-
2000045	444.95	202.33	0.3	C	FC	7.62	0.04	5.7	0.68	0.27
2000640	450.11	62.67	0.09		G	9.23	0.06	7.77	0.75	0.47
2000335	485.86	97.11	0.13	B	FP	9.09	0.05	12.05	0.62	0.23

Table 2.2: The 71 asteroids with the larger pixel fraction ordered according to target-spacecraft distance. For each asteroid is indicated (from left to right): SPICE ID number, the S/C – target distance corrected for light time and stellar aberration, the diameter of the asteroid, SMASSII (Bus et al. 2002 and Tholen taxonomical classifications (Tholen 1989; Tholen et al. 1989), the absolute magnitude, the albedo, the rotation period, the colour index B–V magnitude difference (BV), the colour index U–B magnitude difference (UB). Asteroids (1650) Heckmann and (223) Rosa are in bold.

Figure 2.3 (A) shows the distribution of the minimum distance JUICE-target for all the considered dataset. Figure 2.3 (B) shows the closest approach for the targets of Table 2.2 in the ecliptic plane.

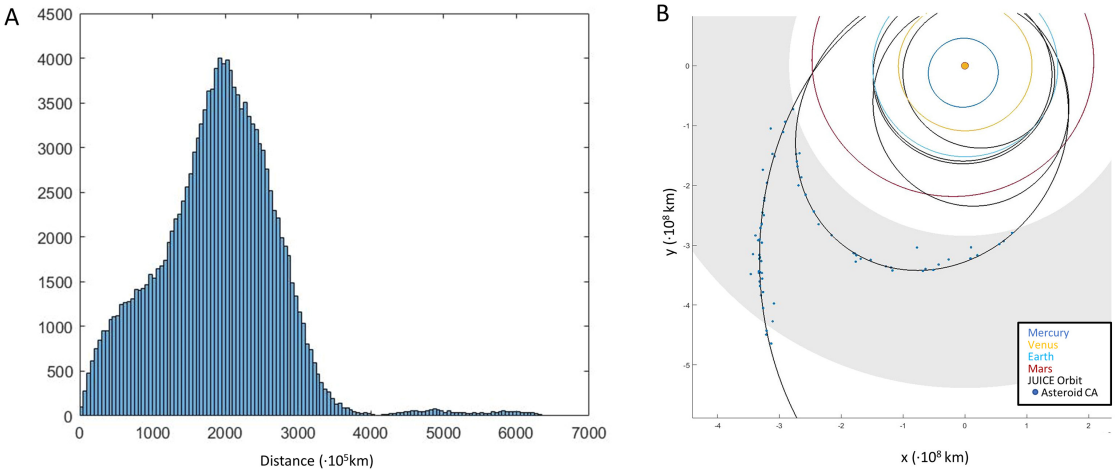

Figure 2.3: A) The distribution of the spacecraft/asteroid distance. The few solutions with distance larger than $7 \cdot 10^8$ km are not shown for better visualization. B) The position (blue points) at the closest approach of each of the 71 asteroids of Table 2.2

2.5 Results

Table 2.2 shows that only asteroid 2000223 ((223) Rosa)), could be observed by JANUS with a pixel fraction higher than 1. It is therefore important to highlight that a trajectory change is necessary to reduce the minimum distance between the spacecraft and the target, allowing to determine the actual target shape, the presence and quantity of craters, the boulders size-frequency distribution, the occurrence of fractures, as well as any possible mineralogical variegation (Marchi et al. 2015; Scheeres et al. 2015; Murdoch et al. 2015).

From Table 2.2, two asteroids have been selected as scientifically compelling targets: (1650) Heckmann and (223) Rosa. The choice has been limited to targets with known classification type and with mineralogical composition (Reddy et al. 2015), photometry (J. Li et al. 2015) and thermophysical properties (Delbo et al. 2015) not yet observed in situ before (Agostini et al. 2022). The asteroids visited by a spacecraft still today are summarised in Table 2.3, along with their classification type.

Figure 2.4 shows for both (223) Rosa and (1650) Heckmann, the trajectory and the closest approach to JUICE. Table 2.4 summarises the main characteristics of an observation at the closest approach.

It should be also considered that other targets closer to JUICE (from 3.13 to $37.67 \cdot 10^5$km, Table 2.2) are not spectroscopically characterised and have small diameters, therefore ground based observation at support to in situ observation are more difficult.

Asteroid	Classification	Reference
(951) Gaspra	S	Belton et al. 1992
(243) Ida	S	Veverka et al. 1996
(433) Eros	S	Veverka et al. 2000
(5535) Annefrank	S	Duxbury et al. 2004
(25143) Itokawa	S	Fujiwara et al. 2006
(4179) Toutatis	S	Huang et al. 2013
(253) Mathilde	C	Veverka et al. 1997
(1) Ceres	C	Russell et al. 2016
(162173) Ruygu	C	Watanabe et al. 2019
(21) Lutetia	M	Sierks et al. 2011
(2867) Steins	E	Keller et al. 2010
(4) Vesta	V	Russell et al. 2012
(101955) Bennu	B	Lauretta et al. 2019

Table 2.3: Asteroids visited by a spacecraft.

Asteroid name	CA Date	Pixel fraction	Minimum distance (aberration corrected)	Apparent solar phase angle
1650 Heckmann	2027 JUN 29 01:30:37	0.52	$38.830 \cdot 10^5$ km	103.15°
223 Rosa	2029 OCT 15 20:01:44	1.25	$42.711 \cdot 10^5$ km	80.07°

Table 2.4: The main characteristic of the CA of both (1650) Heckmann and (223) Rosa. Time resolution for closest approach evaluation is 1 s.

2.5.1 (1650) Heckmann

Asteroid (1650) Heckmann is a member of the Polana family (Pinilla-Alonso et al. 2016), a dark objects subgroup of the Nysa-Polana complex. According to Tholen classification (Tholen et al. 1989), it is an F-type asteroid, classification type not yet in situ observed (Table 2.3). F-type objects generally present spectra that are similar to those of the B-type, but lack the $\sim 3\ \mu m$ hydrated mineral feature, while the UV side of the spectrum $< 0.4\ \mu m$ shows a different absorption intensity (Bus et al. 2002), therefore a dedicated close-observation by JANUS/JUICE could provide valuable insights into the difference of this object type among the C–B–F-G dark asteroid complex and how the Polana family have formed and evolved (Agostini et al. 2022).

2.5.2 (223) Rosa

(223) Rosa is a very compelling scientific target of opportunity. Despite its large size, it has been previously not well studied, the observations made at different epochs, phase angles and the resulting classifications differ in their results (Avdellidou et al. 2021).

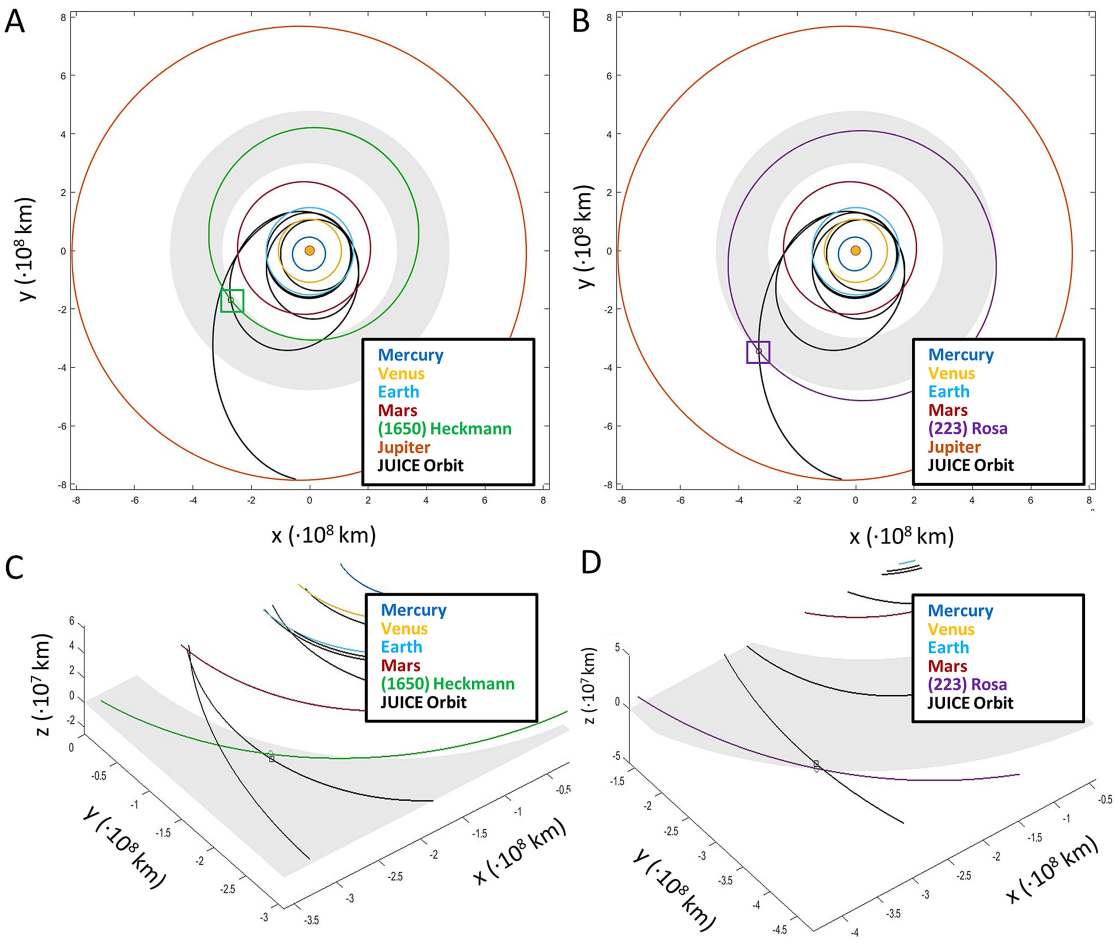

Figure 2.4: A and B) The JUICE orbit (in black) in ecliptic plane together with the asteroid trajectory are reported for both (1650) Heckmann and (223) Rosa (in green and purple, respectively). The green and purple boxes represent the locations of the JUICE-asteroid close encounter. C and D) For each considered asteroid, it is reported a trajectory close up of the closest approach time window.

Although it is considered as a member of the Themis family (Licandro et al. 2012), recent observations (Avdellidou et al. 2021) suggest a different interpretation about the origin of (223) Rosa. The Themis family is composed of fragments of the remaining core of an icy 400 km size protoplanet broken apart by impacts about 1.0–2.5 Gyrs ago (Landis et al. 2020). According to Avdellidou et al. 2021:

- the mean spectrum of Rosa defines the asteroid as a X-type in the BusDeMeo classification (or P in Tholen classification), having a different spectrum with respect to the majority of the studied members of the Themis family (and the Beagle one)

- the average albedo is marginally consistent with the albedo of the family
- the position of (223) Rosa in the parameters space (a_p (proper semimajor axis), 1/Diameter) is outside of the V-shaped formation (typical for the member of a asteroid family)

suggesting that (223) Rosa is not a family member but an original planetesimal formed in the Outer Solar System. Its close flyby would help to solve the issue of whether this asteroid is a Themistian collisional member characterised by water-ice exposed on a generally dark surface or a dark primitive planetesimal (Agostini et al. 2022). Moreover, the observation of dark primitive bodies (Jupiter Trojans) by the NASA Lucy mission (Levison et al. 2021) is a very promising opportunity to perform comparative studies.

Chapter 3

On Ground Calibrations

3.1 Setup

3.1.1 Description

The on-ground calibrations of JANUS has been performed at Leonardo Company S.p.A. at Campi Bisenzio (FI) which is also the industrial prime in charge of the development of the instrument. The figure 3.1 shows the schematics of the calibration setup.

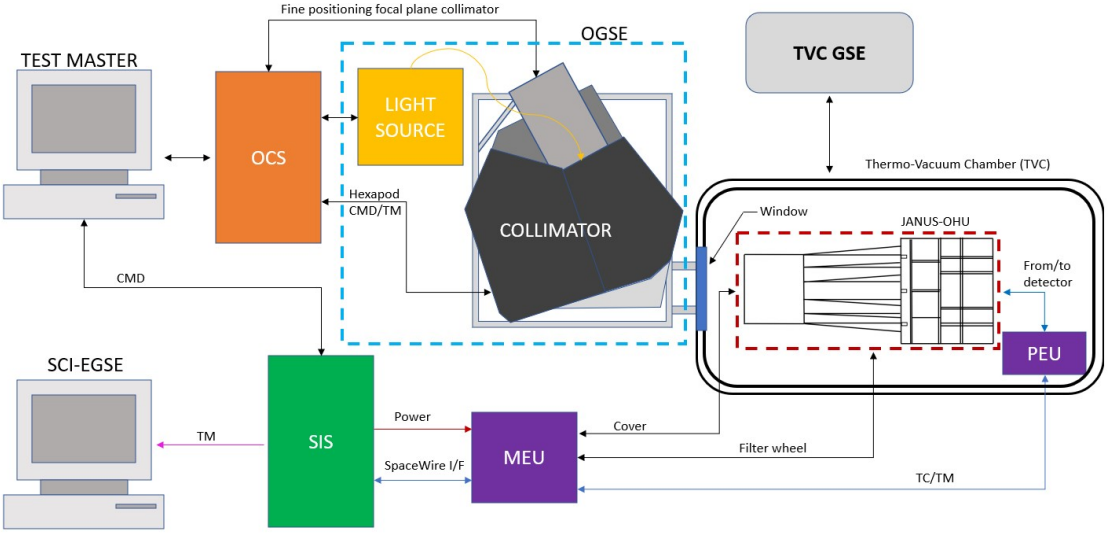

Figure 3.1: Calibration setup schematics

The setup, tailored on JANUS, is able to manage both the instrument itself and the devices needed to characterize it.

In the Thermo-Vacuum Chamber (TVC), specifically developed for the JANUS project, the instrument Optical Head Unit (OHU) is located over a baseplate (see figure 3.2) along with the Proximity Electronics Unit (PEU).

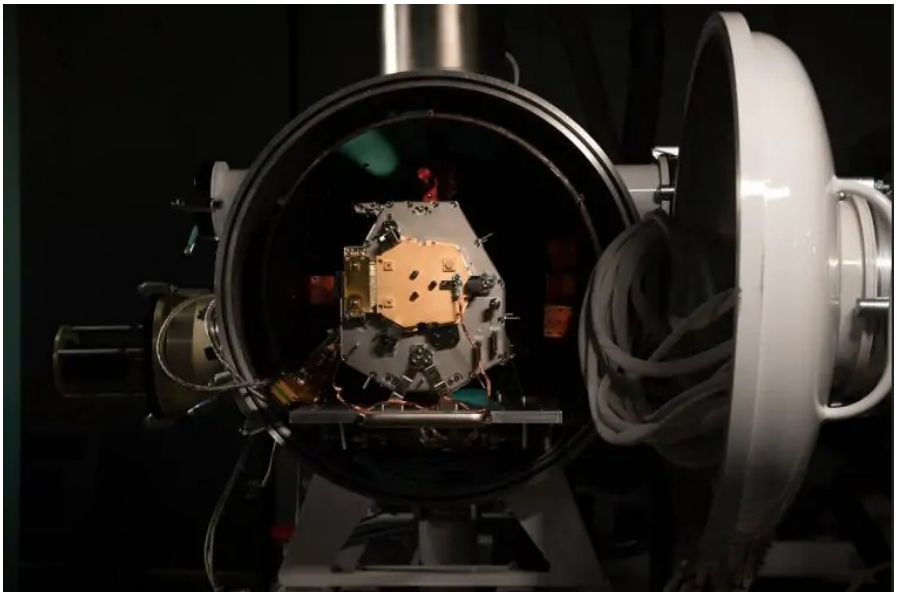

Figure 3.2: JANUS inside the TVC. Courtesy of Leonardo Company S.p.A.

The TVC has all the interfaces needed to connect JANUS to the setup. A dedicated GSE (Ground Support Equipment) monitors and manages temperatures and pressure of the TVC and of the instrument. Thermal straps are connected to specific parts of the instrument allowing to change the thermal set point exploiting during the calibration the operative condition of the JUICE mission. The TVC control, moreover, manages the heat lines under the responsibility of the S/C (the survival heaters). The TVC has a Fused Silica window required to allow an optical stimulus to reach the instrument. The optical stimulus is provided by an Optical Ground Support Equipment (OGSE) (Figure 3.3) selectable on the basis of the specific measurement.

In particular two different OGSE devices can be used:

- Collimated beam
- Non Collimated beam

The communication between the instrument and the user is instead managed by the *Spacecraft Interface Simulator* (SIS) which simulates the interfaces between the instrument and the spacecraft. The SIS provides to JANUS the power and the SpaceWire connection for the Telemetry and Telecommand channel. The SIS communicates directly with the Main Electronic Unit (MEU) (Figure 3.4), which in turn manages the Cover mechanism, the Filter Wheel and data exchange with the PEU (data from the detector). The images and housekeepings during the session can be monitored in quasi-real time on a dedicated computer upon which the Scientific-Electric Ground Support Equipment, a software specifically developed to read and interpret the data from JANUS, is installed. Finally, the operator can develop an automatic procedure (named *Automatic Test Procedure*

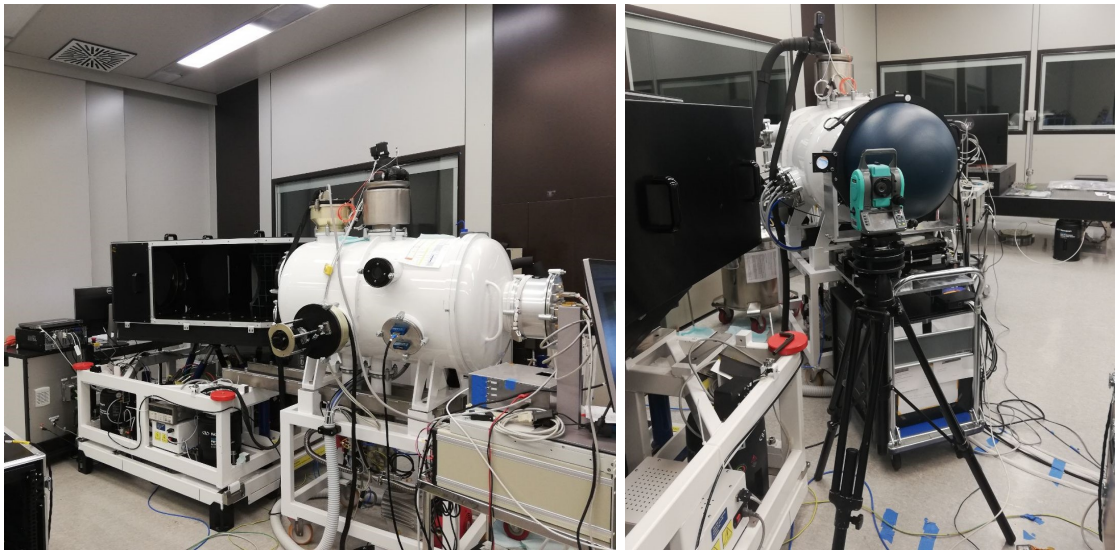

(a) (b)

Figure 3.3: Setup during the calibration sessions at Leonardo Company S.p.A., Campi Bisenzio (FI). (a): collimated beam setup. It is possible to see the TVC (in white), the collimator and on the rear side the Test Master. (b): non collimated beam setup with the integrating sphere couple to the TVC.

(ATP)) which is interpreted by the Test Master and can send telecommands both to the OGSE devices and to the instrument.

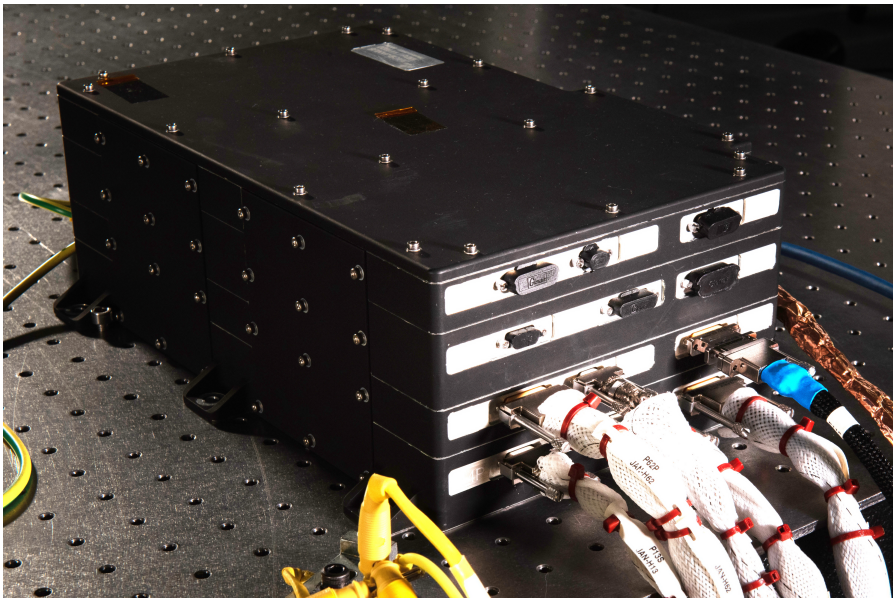

Figure 3.4: Flight model of Main Electronic Unit (MEU). Courtesy of Leonardo S.p.A.

Integrating sphere characteristics	
Sphere diameter	20 inch
Exit port diameter	8 inch
Internal coating	Spectraflect
Coating reflectance	98%
Lamp configuration	three 35W
	one 100W + shutter
Lamp type	Tungsten Halogen
Color temperature	3000 K
Monitoring photodiode	Silicon detector

Table 3.1: Characteristics of the integrating sphere used in the NCB-OGSE.

The devices composing the OGSE are managed by the OGSE Control System (OCS).

Non collimated beam OGSE

The non collimated beams OGSE (NCB-OGSE) is a integrating sphere (IS), Labsphere USS-2000C. A comprehensive characterization of the sphere has been made during SIMBIO-SYS calibration campaign (Da Deppo et al. 2014). The sphere can be illuminated by four lamps (three 35W plus one 100W) which can be independently powered on and off. For the setup only the 100W lamp is used (namely "Lamp3"). The IS has its own power source with the main objective to feed the lamp with a constant and stable current in order to provide a stable colour temperature (and therefore spectral radiance). The Lamp3 is equipped with a mechanical shutter in order to provide a variable level of radiance. A summary of the IS characteristics is presented in Table 3.1.

Collimated beam OGSE

The fundamental device of the collimated beam OGSE (CB-OGSE) is an unobscured four mirrors collimator designed by Selex Galileo (now Leonardo S.p.A.), as a solution adopted for the OGSE of HRIC/SIMBIO-SYS (Barilli et al. 2012). The collimator has a Brunn configuration with a nominal focal length of 3000 mm (actually measured as 3090 mm) and nominal F# of 13.6 (Barilli et al. 2012). The collimator is mounted over an hexapod, a device able to provide 6 degrees of freedom movements. The user has, also, the possibility to accurately locate a target holder with respect to the collimator focal plane using motorized linear stages. The collimator is illuminated by a light source coming from a monochromator coupled with a small teflon integrating sphere. This produces a spatially flat input on the test target (which can be selected between pinholes, slits, etc...) whose wavelength can be selected remotely. This is extremely useful for JANUS, which has multispectral capabilities thanks to the 13 filters mounted on the Filter Wheel. The monochromator source is a Quartz Tungsten Halogen (QTH) lamp: selecting the zero

Naming convention	
Type	Subtype
Radiometric	ITF_RAD, ITF_TEXP
Full Performance	SRF (*Spectral Response Function*), USAF, LOS (*Line Of Sight*), MTF (*Modulation Transfer Function*), BS (*Boresight*), SL (StrayLight)
TempName	perfHot (MIDDLE), perfSuperHot (HOT), perfCold (COLD)

Table 3.2: Calibration sessions naming convention

order of the monochromator the output is a continuous spectrum, otherwise a spectral scan allows to evaluate the spectral performance of JANUS.

3.1.2 Naming convention

For the characterization of the instrument, the calibrations are subdivided into two main logical groups:

- Radiometric
- Full Performance

based on what type of OGSE is used.

The Full Performance group includes a broad range of instrument aspects such as the spatial capabilities (MTF), the spectral capabilities (SRF), straylight, etc. (see Table 3.2).

The name convention used for the calibration sessions is:

nnn_Type_Subtype{_XXX}_FF{-FF}_TempName

where *nnn* is a progressive index, *Type* is the main type of the session (*Radiometric* or *FullPerformance*), *Subtype* is used to discriminate between the different types of measurements, *FXX* is the filter number (for example: F1, F10) and *TempName* defines the temperature set point. The curly brackets indicate optional text: *XXX* is an additive part to further characterize the session and {-FXX} is instead added if multiple filters are acquired, repeated as many times as the number of filters acquired (for example: F1-F2-F3).

3.2 Detector

3.2.1 Introduction

The performance of the detector and the readout chain have been determined by analysing the data acquired in dedicated sessions planned during the calibration activity. Several aspects have been considered including dark current rate, offset (the so called "FPN",Fixed Pattern Noise), repetition time, image deformation induced by the rolling shutter readout, image lag, unexpected effects, binning, windowing, cropping and compression (in particular, the combination of them). In this section only part of these have been considered.

For this measurement, the baffle cover (COM) is closed in order to prevent possible external light and the exposure time is set according to table 3.3.

Dark current session							
$t_{int}[ms]$	0.2215	0.886	9.9675	99.8965	999.851	9999.839	99999.9405
Number	50	50	50	50	50	10	9
Temperature							
Cold	-43.1 °C ± 0.1 °C						
Middle	-38.3 °C ± 0.1 °C						
Hot	-37.40 °C ± 0.04 °C						
Ambient	21 °C ± 0.01 °C						

Table 3.3: Exposure time range used for the evaluation of the offset and the dark current. It is also reported the number of images acquired for each exposure step. The averaged temperature of the focal plane is shown with its standard deviation.

3.2.2 Offset (FPN) and Readout Noise (RoN)

The value of 221.5 μs is the shortest exposure time which was possible to command to the instrument at the time of the calibrations. For this reason it is considered for the purpose of this analysis as a "virtual zero" and used for retrieving the offset and the readout noise. This assumption is reasonable due to the very low dark current rate shown by this detector. The measurement has been repeated at three different temperatures (Table 3.3 reports the temperature of the focal plane array) in the thermo-vacuum chamber plus one session in air (inside the thermo-vacuum chamber) and ambient temperature. As previously said, the first point of the sequence is assumed to be the *offset* (often called Fixed Pattern Noise; in this Thesis the term *offset* is preferred because *noise* is reserved to a stochastic mechanism). The dark current in principle is negligible and then the frames are representative of the readout chain.

Figure 3.5 shows the time-averaged offset frames (over 50 repetitions) for the considered temperature conditions, that is:

$$\overline{DN}_{ij} = \frac{1}{N}\sum_{k=1}^{N} DN_{ijk} \tag{3.1}$$

Offset averaged values [DN]					
Temperature	Tile 1	Tile 2	Tile 3	Tile 4	All
COLD	503	517	549	551	530
MIDDLE	502	516	548	550	529
HOT	502	516	549	551	530
AMBIENT	492	506	545	544	522

Table 3.4: Averaged values of the offset in DN units. Two cases are considered, tile-basis (each tile is 2000 rows x 376 columns) and all-frame-basis

where i stands for row index, j stands for column index and k stands for image number index of the stack.

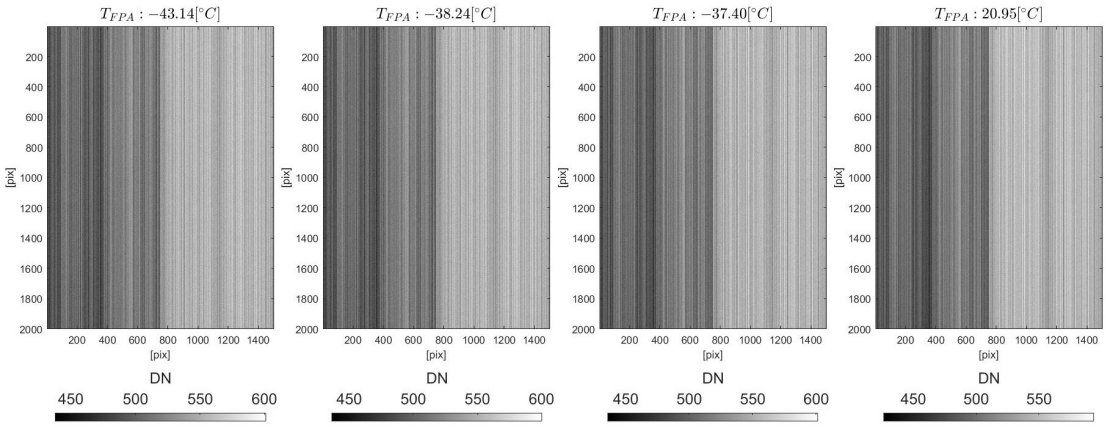

Figure 3.5: averaged offset frames over 50 repetitions for four temperature conditions.

It is possible to observe four main different sections (tiles) of size 2000 rows x 376 columns which correspond to four different electronic chains used for reading out the overall detector photosites. The analysis is performed considering the tiles as separated entities due to the fact that they are read using different amplifiers.

Figure 3.6 shows the distribution of the offset for each tile separately. The tiles are shown from the left to the right starting from 1 to the number 4. Different colours indicate different temperatures (with the exclusion of the ambient temperature for clarity). A quantitative analysis is reported in Table 3.4. It seems that there is not a well defined trend depending on the temperature, with a difference of the average less than 1.5 DN and no significant variation of the distribution.

The same image sequence is used for evaluating the readout noise (hereafter RoN), defined as the temporal standard deviation at zero exposure time (on pixel-per-pixel basis):

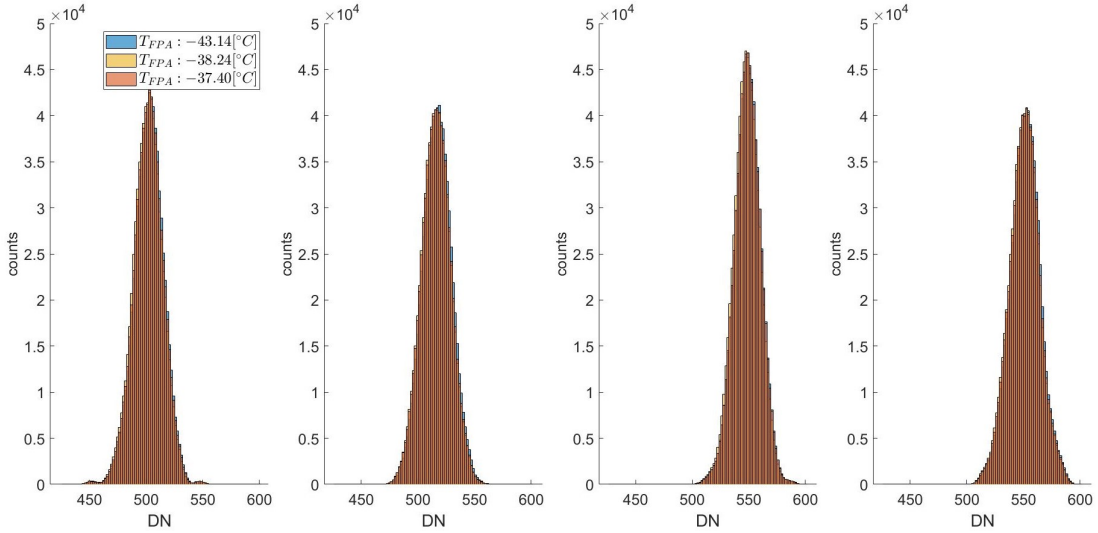

Figure 3.6: Histograms of the offset distribution (in DN). Each subfigure shows a different tile, each colour a temperature case according to the legend. The bins are the same for each tile and temperature case. The histogram for the ambient temperature is not shown for clarity.

ReadOut Noise [DN]					
Temperature	Tile 1	Tile 2	Tile 3	Tile 4	All
COLD	2.50	2.55	2.57	2.61	2.55
MIDDLE	2.51	2.55	2.57	2.61	2.56
HOT	2.52	2.56	2.58	2.62	2.57
AMBIENT	2.50	2.54	2.56	2.60	2.55

Table 3.5: Readout noise (mean of the temporal standard deviation frame) in DN. Two cases are considered, tile-base and all-frame-base

$$RoN_{ij} = \sqrt{\frac{1}{N-1}\sum_{k=1}^{N}(DN_{ijk} - \overline{DN}_{ij})^2} \tag{3.2}$$

the indexes are the same as equation 3.1. The produced map describes the fluctuation of the readout process (fig 3.7) and related histograms (fig 3.8), organized with the tile-base subdivision. The average values of the 3.2 are reported in Table 3.5. Considering a conversion factor of 2.1 e^-/DN, the RoN is less than 5.3 e^-.

3.2.3 Dark Signal Non Uniformity /Dark Current Non Uniformity

Table 3.6 shows the DSNU calculated for all the exposure times available for this measurement. In this context DSNU is defined as the spatial standard deviation of a *dark*

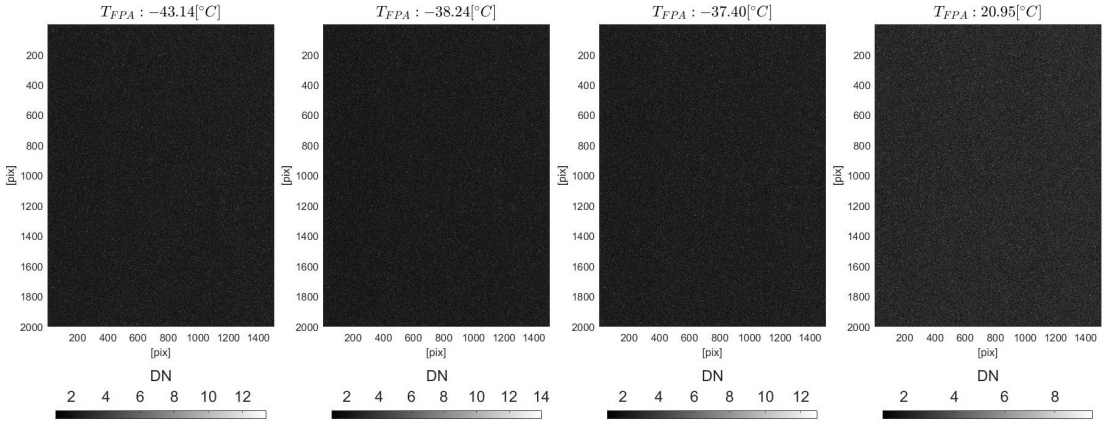

Figure 3.7: Readout noise map [DN] at various temperatures

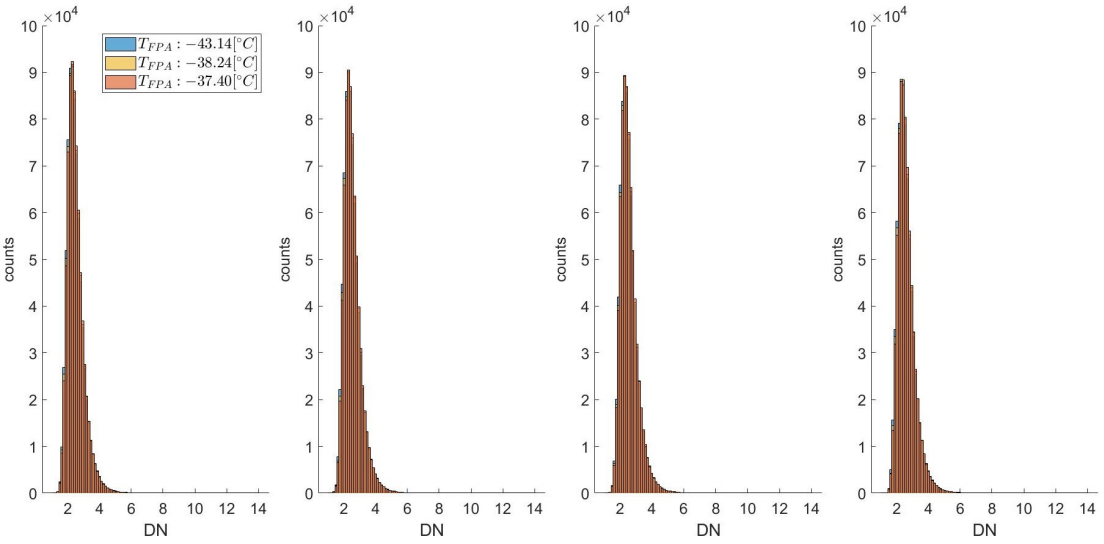

Figure 3.8: Readout noise distributions shown as histograms at various temperatures. The respective maps are shown in Figure 3.7

image, where *dark* means *without illumination*. Each dark image is the average of a stack of dark images all with the same exposure time. The averaging process reduces the temporal noises leaving the spatial non-uniformities of the offset plus that coming from the different pixel-to-pixel dark current generation. Sometimes it is also defined as DCNU (although here the contribution of the spatial variance of the offset is included). Excluding the *AMBIENT* condition, clearly not possible for the JANUS experiment, the results indicate a very low contribution of the dark current. If a more classical definition of the DSNU is considered, the values to be considered are referred to the first column of the table (virtual zero exposure time).

Due to the different electronic chains the DSNU is different among the tiles. In

DSNU - Dark Signal Non Uniformity [DN]

$Temp_{FPA}/t_{int}$	221.5 μs	886 μs	10 ms	100 ms	1 s	10 s	100 s
			Tile 1				
COLD	13.03	13.03	13.04	13.05	13.04	13.12	17.34
MIDDLE	13.05	13.05	13.05	13.05	13.05	13.13	17.57
HOT	13.04	13.05	13.05	13.05	13.05	13.12	17.61
AMBIENT	13.26	13.26	13.26	13.27	15.90	79.48	331.96
			Tile 2				
COLD	12.80	12.81	12.81	12.81	12.80	12.86	15.09
MIDDLE	12.78	12.79	12.79	12.79	12.79	12.85	15.29
HOT	12.78	12.79	12.79	12.80	12.79	12.85	15.33
AMBIENT	12.70	12.70	12.70	12.72	15.01	78.19	330.96
			Tile 3				
COLD	11.76	11.76	11.76	11.77	11.76	11.81	14.15
MIDDLE	11.73	11.73	11.73	11.73	11.73	11.79	14.35
HOT	11.72	11.73	11.73	11.73	11.72	11.78	14.38
AMBIENT	11.41	11.41	11.41	11.43	13.96	77.46	328.49
			Tile 4				
COLD	13.40	13.41	13.41	13.41	13.40	13.45	15.18
MIDDLE	13.40	13.41	13.41	13.41	13.41	13.45	15.40
HOT	13.39	13.40	13.40	13.41	13.41	13.45	15.43
AMBIENT	13.39	13.39	13.39	13.41	16.00	81.75	329.50
			All				
COLD	24.44	24.39	24.40	24.30	24.38	24.34	25.83
MIDDLE	24.51	24.59	24.53	24.44	24.50	24.58	26.24
HOT	24.54	24.59	24.56	24.56	24.62	24.61	26.24
AMBIENT	26.43	26.38	26.36	26.45	28.16	84.63	343.51

Table 3.6: Dark signal non uniformity (standard deviation of the temporal average frame). Two cases are considered, tile-base and all-frame-base

summary, DSNU is less than 18 DN if the tiles are considered separately and less than 27 DN if the all detector is considered, independent of temperature and exposure time.

3.2.4 Dark Current

To evaluate the dark current rate, the same sessions are considered, plotting the (spatially) averaged-values with respect to the exposure time. For each temperature setpoint the respective mean offset frame has been subtracted on a pixel basis before to compute the average value. As usual in this context the analysis is performed considering the tiles separately.

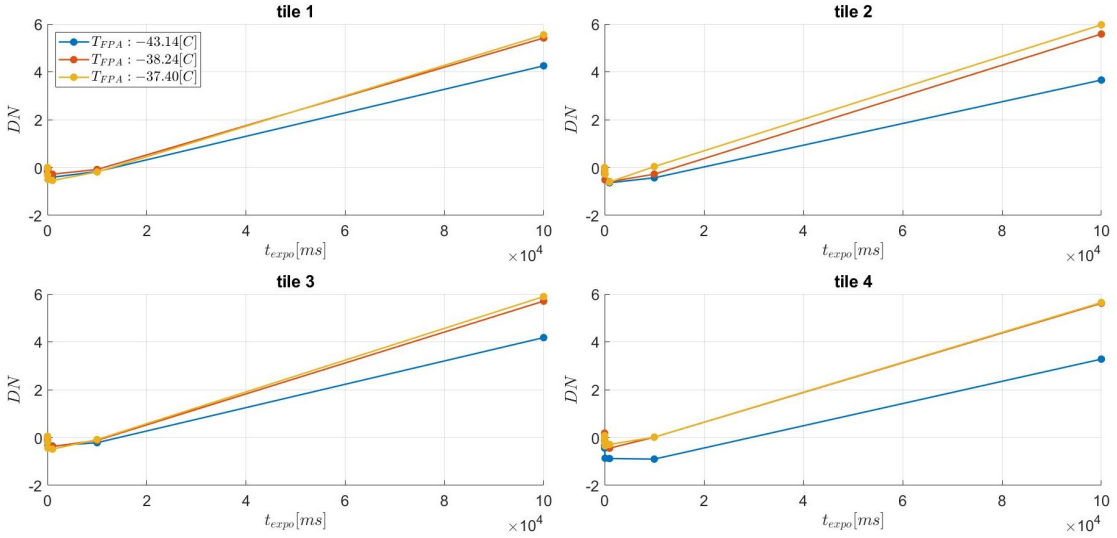

Figure 3.9: Average dark current. For each temperature the offset has been subtracted

Figure 3.9 shows the average dark current rate up to 100 s for the TVC setpoint conditions. The maximum DN value at 100 s is 6 DN (about 12 e-). Below 10 s, the rate appears to be negative and it is supposed to be due to the CDS (the subtraction between the signal line and the reference line).

Figure 3.10 shows the dark current rate up to 1 s. In general, the electron generation is very low and negligible for a broad range of applications. This measure has been replicated also at ambient temperature (see Figure 3.11) providing an estimation of about 40 e-/s which is twice the expected value.

3.3 Radiometric calibrations

The objective of the radiometric calibration activity is to determine a bijective function able to retrieve the radiant quantity of interest from the instrument output (Wyatt 1978). For an imager, as JANUS, the interest is focused on the radiance, a quantity useful in the description of extended sources. The final product of the activity should be then

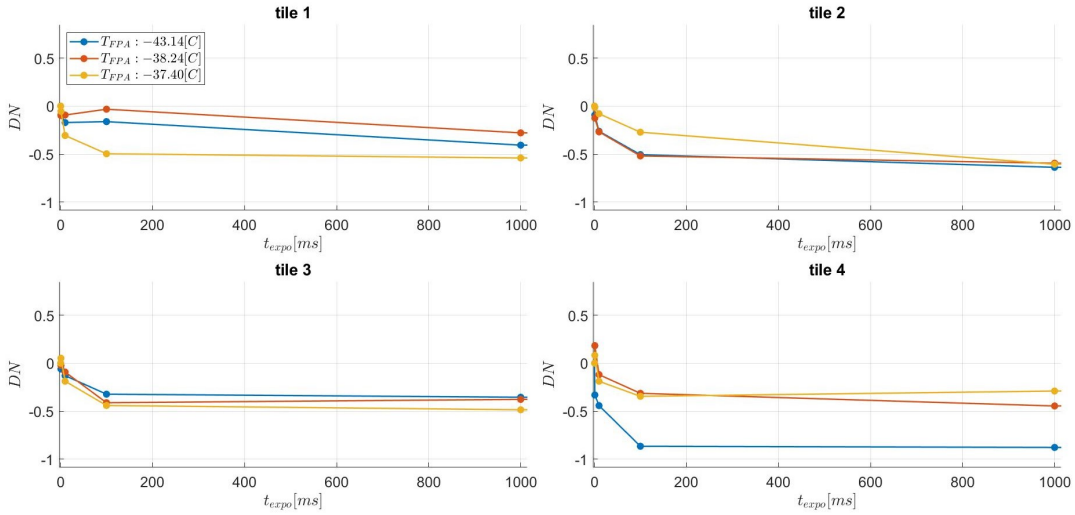

Figure 3.10: Particular of Figure 3.9. The exposure time, here, is limited to 1 s

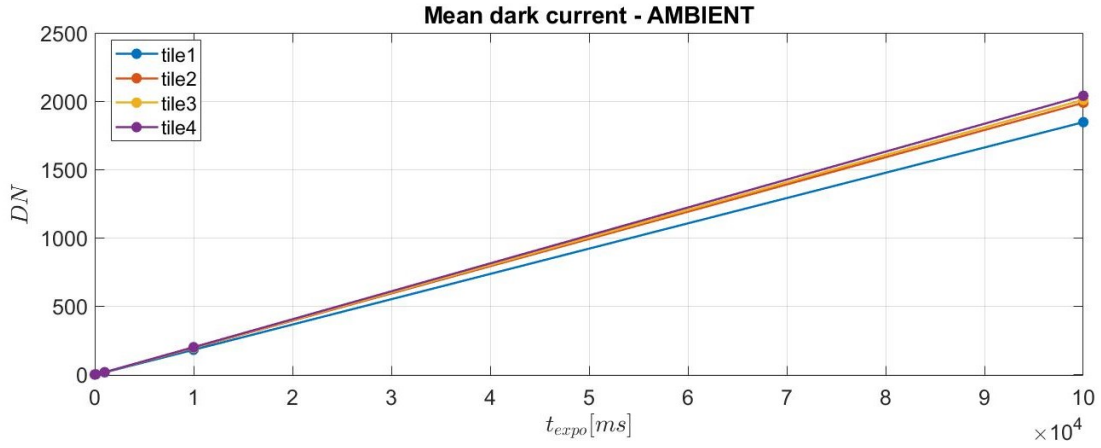

Figure 3.11: Dark current rate at ambient temperature. The FPA temperature is 21°C

an *Instrument Transfer Function* (ITF) for each pixel. This ensemble of ITFs will be then inserted in a dedicated pipeline for the conversion of the raw images (with arbitrary units) into calibrated images (with physical units).

As summarized by Table 3.7 two type of measurements have been planned for the radiometric calibration of JANUS:

- Fixed exposure time and variable radiance level
- fixed radiance level and variable exposure time

The used setup is described in section 3.1.

Radiometric calibration measurements				
Type	KDP	Points	Temperature	Notes
ITF vs radiance	Absolute (ITF) and relative (FF) radiometric response, bad pixels	21/52/17 shutter positions* (including shutter closed)	MIDDLE (Hot), HOT (SuperHot), COLD (Cold)	Fixed exposure time
ITF vs exposure time	Absolute (ITF) and relative (FF) radiometric response, bad pixels	24/30 exposure times* (including minimum allowable exposure time)	MIDDLE, HOT	Fixed shutter position

Table 3.7: Summary of the radiometric calibration measurement approach considered for JANUS. The *KDP (Key Data Parameters)* column lists the parameters which are expected from the analysis. The *Points* column gives the number of samples acquired for a specific session (and type). The *Temperature* column describes in which of the three temperature set-points of the thermo-vacuum cycling performed during the calibration campaign the measurement has been acquired. Denominations inside the brackets refer to an alternative nomenclature which is maintained in the naming of the calibration dataset. *The different sessions have different sampling in order to optimize the measurement. The numbers refer to a summary of what is available (not necessary for all filters)

3.3.1 Radiometric model

During the calibration sessions, there was the need to develop a radiometric model of the instrument and to perform a comparison with the data acquired in clean room. The goal is to develop a model able to convert a suitable source input to DN (digital number) (Da Deppo et al. 2016), which is the output of the instrument and is provided in arbitrary units. The equation describing this process is (Da Deppo et al. 2016,Zusi 2009):

$$DN = \int_{\lambda_i}^{\lambda_f} L(\lambda) \cdot A\Omega \cdot T(\lambda) \cdot QE(\lambda) \cdot \frac{\lambda}{hc} \cdot \frac{1}{g} \cdot t_{expo} \cdot d\lambda \tag{3.3}$$

In this model the light source is considered *extended* and it is assumed the spectral radiance ($L(\lambda)$) as input. The output is the mean value of a single illuminated pixel.

A corresponds to the area of the entrance pupil. In JANUS the aperture stop is the primary mirror (M1) that corresponds also to the entrance pupil (EP). The instrument is based on a Ritchey-Chretien design and therefore the effective collection area should consider the central obscuration. It is possible to express the *equivalent* entrance aperture diameter as

Radiometric model input		
Parameter	Symbol	Reference
M1 reflectance	$\rho_{M1}(\lambda)$	*Flight mirror reflectivity.xlsx* provided by Leonardo S.p.A.
M2 reflectance	$\rho_{M2}(\lambda)$	*Flight mirror reflectivity.xlsx* provided by Leonardo S.p.A.
Lens transmittance	$\tau_{lens}(\lambda)$	*Report JANUS lenses.xlsx* provided by Leonardo S.p.A.
Detector window transmittance	$\tau_{detector}(\lambda)$	*PFM FPM Windows Transmission v1.xlsx* provided by DLR
Filter transmittance	$\tau_{filter}(\lambda)$	*JANUS_spektral Daten_selection_Leonardo.xlsx* provided by Balzers
Quantum efficiency	$QE(\lambda)$	*detector_QE.xlsx* provided by Open University
Gain	g	provided by DLR
Optical parameters (focal length, EP maximum diameter, EP minimum diameter)	f, $D_{M1,max}$, $D_{M1,min}$	*Janus optical model.zmx* provided by Leonardo S.p.A.

Table 3.8: Symbols and references of the radiometric model components

$$D_{EP} = \sqrt{D_{M1,max}^2 - D_{M1,min}^2} \tag{3.4}$$

which is 103.59 mm for JANUS. The effective (radiometric) F# is therefore 4.5081.
The Ω parameter is the solid angle subtended by the pixel and it can be estimated as:

$$\Omega = IFOV^2 \tag{3.5}$$

where the IFOV (Instantaneous Field of View) is:

$$IFOV = \frac{pix}{f} \tag{3.6}$$

where pix is the pixel pitch and f is the focal length of the instrument, assumed to be nominal (467 mm).

$A\Omega$ (sometimes called Etendue or Throughput) is a factor describing the geometrical parameters of the acceptance of the instrument.

$T(\lambda)$ is the spectral transmittance/reflectivity of the optical elements:

$$T(\lambda) = \rho_{M1}(\lambda) \cdot \rho_{M2}(\lambda) \cdot \tau_{lens}^3(\lambda) \cdot \tau_{filter}(\lambda) \cdot \tau_{detector}(\lambda) \tag{3.7}$$

which includes:

- reflection from M1 (primary mirror)
- reflection from M2 (secondary mirror)
- transmission of the corrector barrel (composed by three elements)
- transmission of the selected filter (F1 - F13)
- transmission of the detector window

The reflection and transmission parameters and their references are listed in following Table 3.8.

$T(\lambda)$ is shown in figure 3.12.

The other parameters are $\frac{\lambda}{hc}$ (which is the inverse of the photon energy and converts from input energy to number of photons), the quantum efficiency of the detector $QE(\lambda)$ (which converts from photons impinging on the detector in photoelectrons), the gain g (which converts from photoelectrons to DN) and the exposure time t_{expo}. The Fill Factor, which indicates the fraction of the active area of the photosite with respect to the whole pixel area, is not included in the equation because it is 100% due to the back-illuminated design of the detector.

The *Instrument Transfer Function* (ITF) (Da Deppo et al. 2016) is then:

$$ITF(\lambda) = A\Omega \cdot T(\lambda) \cdot QE(\lambda) \cdot \frac{\lambda}{hc} \tag{3.8}$$

and it is shown in Figure 3.13.

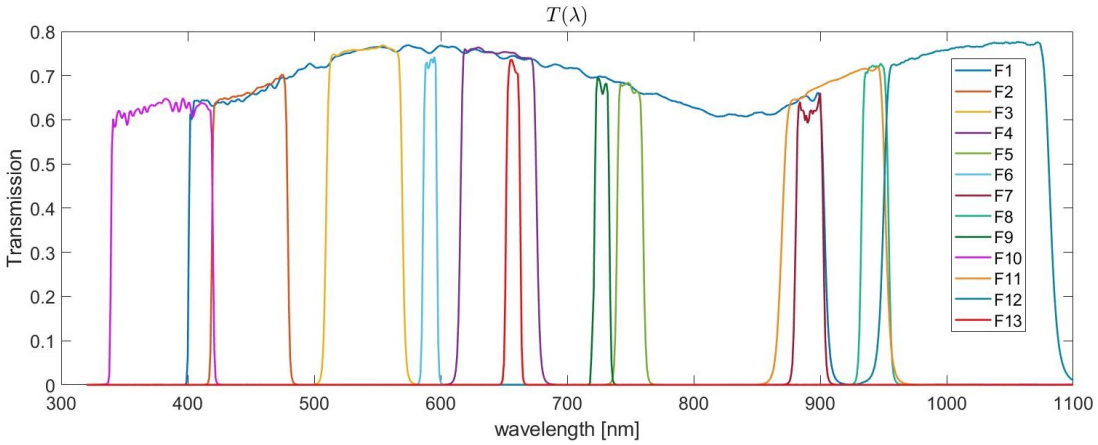

Figure 3.12: JANUS transmission curves. They are described by equation 3.7

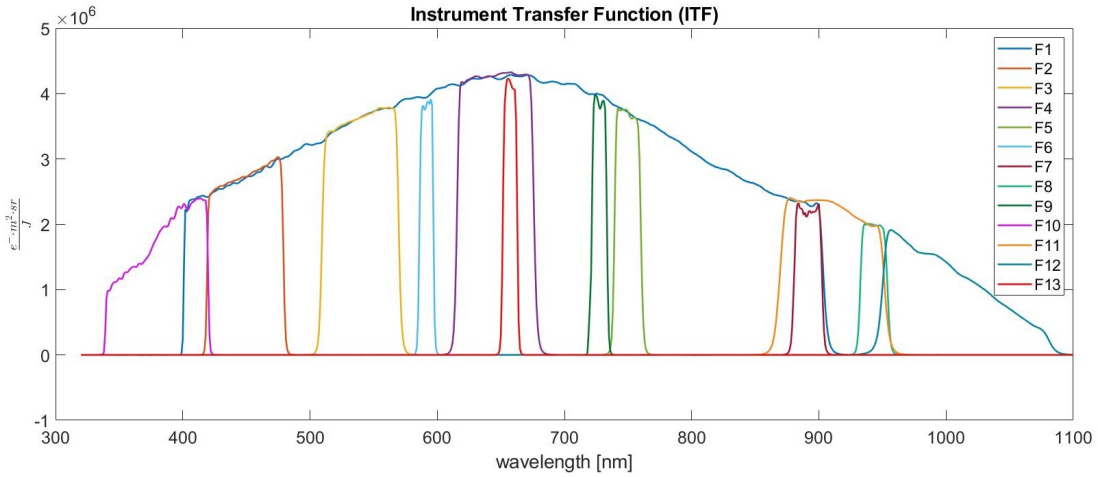

Figure 3.13: JANUS ITF for each filter. They are described by equation 3.8

The references for used parameters are listed in Table 3.8.

The nominal QE (included also in figure 3.13) has been measured at room temperature. In order to be more in line with the calibration session data, the QE should be evaluated at operative temperature. A correction factor has therefore been included in the simulation. The estimation of the correction factor is based on the predicted QE performance for the JANUS detector presented in Soman et al. 2014, where the curve is simulated for 20° and -40°, the last temperature assumed as operative for the instrument (see figure 3.14).

A correction factor could be estimated considering the ratio between the -40° QE and 20° QE of figure 3.14 and assuming that it could also be applied to the QE measured for JANUS. Figure 3.15 shows the correction factor.

The QE in operative condition is then:

Constants	
Parameter	Value
Focal length	$f = 467$ mm
Gain	$g = 2.1$ e-/DN
Effective Entrance Pupil diameter	103.59 mm
F# (radiometric)	4.5081
Pixel pitch	$7\mu m$
Spectral range	350-1100 nm

Table 3.9: Simulation constants

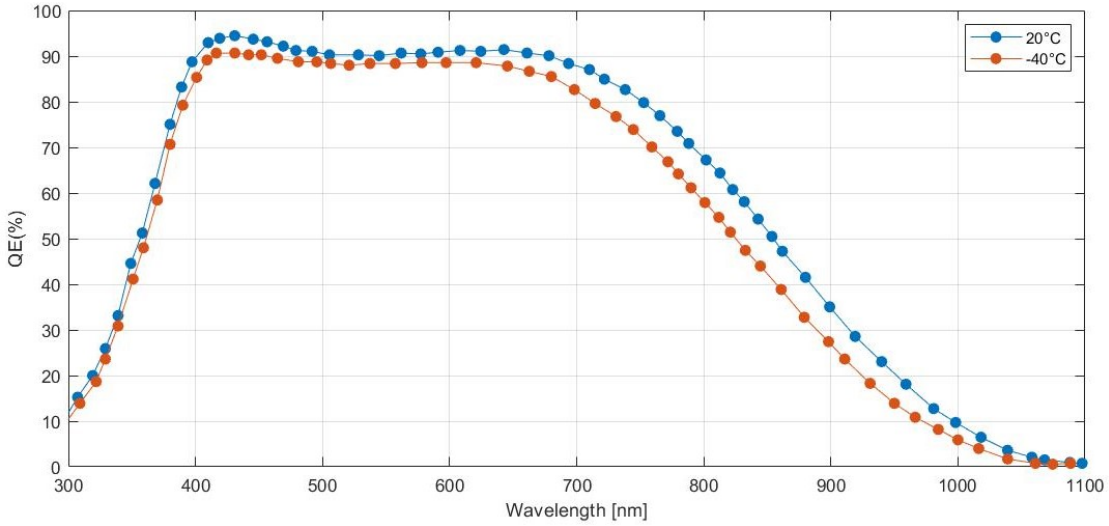

Figure 3.14: QE for back-illuminated CIS115 coated with e2v Multilayer-2 anti-reflective coating. Adapted from Soman et al. 2014

$$QE_{TVC} = cf \cdot QE_{Ambient} \tag{3.9}$$

The simulation is compared then to the data from the radiometric calibration sessions. In this configuration the selected OGSE is the NCB-OGSE (see section 3.1 for a detailed description), the exit port of the integrating sphere is coupled with the window of the TVC. This allows also to highlight the congruence of the function generating the spectral radiance.

The spectral radiance, which is the energy input of the model (equation 3.3), is derived directly from the calibration session: from the log of the session, the monitoring photodiode (MPD) current is read and the spectral radiance is extracted with a linear interpolation over the calibration data of the integrating sphere, because the relationship

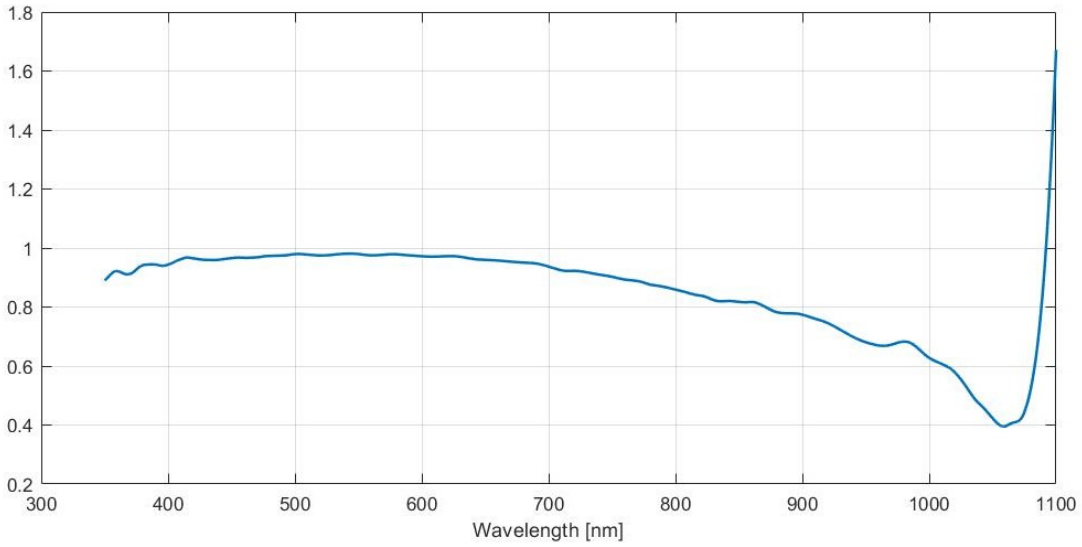

Figure 3.15: Correction curve for QE. This is the ratio between predicted -40° QE and predicted 20° QE. The curve beyond about 1080 nm is no reliable due to the fact the curves go to zero and the ratio is more unstable

between MPD current and spectral radiance is available only at limited values and the shutter does not provide enough reliability (as will be shown in Section 3.3.2).

It should be highlighted that the considered spectral radiance already includes the transmittance of the TVC window:

$$L(\lambda) = L_{IS}(\lambda) \cdot \tau_{TVC} \tag{3.10}$$

The radiance (resulting from the integration of the spectral radiance with respect to the wavelength) is obtained considering only the energy entering in the spectral range of the selected filter. Since in this context the radiometric model is used as a comparison with the data observed experimentally, the exposure time is usually extracted from the housekeepings of the images.

Figure 3.16 shows graphically this process.

3.3.2 Analysis of radiometric data

In order to provide the bijective function described before, it is necessary to have the input source (in this case the integrating sphere) calibrated with respect to a traceable standard. For this reason the radiance coming out from the IS has been measured with a calibrated FieldSpec spectrophotometer for all the levels set by the motorized shutter (hereafter VA or *variable attenuation*). The monitoring photodiode current is also registered along with corresponding VA values. It should be highlighted that the VA value is not the percentage

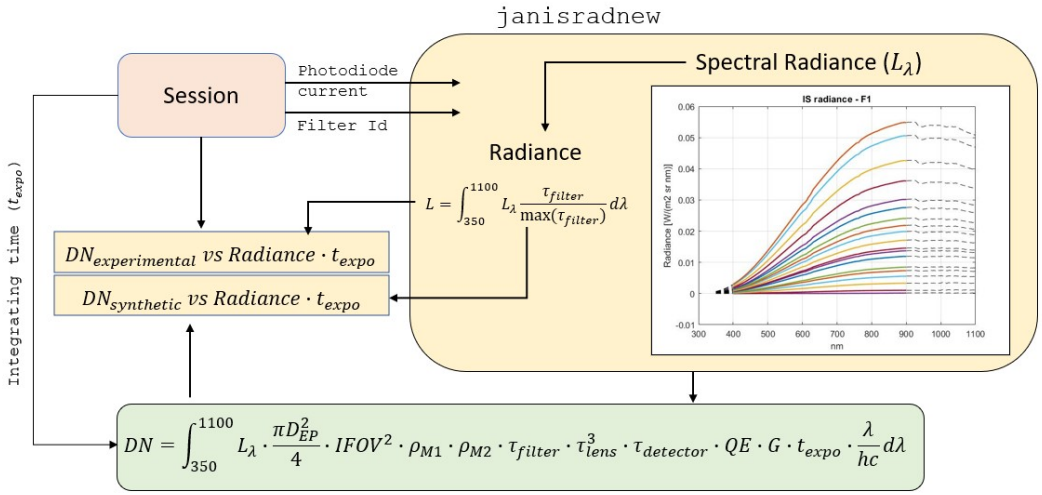

Figure 3.16: Graphical description of how the synthetic signal is generated from the radiometric model and compared with experimental calibration data. Radiometric data are analysed by a MatLab script. From the specific session log the current of the MPD is read and passed to a custom function (*janisradnew* in the image) which generates both the spectral radiance and radiance. The spectral radiance then is passed to another function (*janfastradmod*) which calculates the equation 3.3

radiance with respect to the maximum achievable but it indicates a percentage value of the shutter position with respect to the overall full range of the shutter rail.

In this section it will be shown that only the use of the photodiode current is reliable and should be considered for the radiometric calibration of the instrument.

Analysis of temperature dependence

In this section the response of the instrument at different (thermal) operative conditions will be compared. The temperatures of the components are resumed in Table 3.10 retrieved by JANUS image ancillary data.

Temperatures					
	Hot	Middle	Cold	$\Delta_{hot/middle}$	$\Delta_{middle/cold}$
FPA	-36°	-37.7°	-42.6°	1.7°	4.9°
CWS	-15°	-21.7°	-28°	6.7°	6.3°
Optical Wall	-13.85°	-24.8°	-31.1°	10.95°	6.3°
PEU	28.1°	5.24°	-0.73°	22.86°	5.97°

Table 3.10: Averaged temperatures for some instrument components during the *ITF vs radiance* test for F1 filter.

For this analysis only data for the panchromatic filter (F1) are considered because it has the photodiode current correctly registered for all the temperature cases.

First the DN response is evaluated with respect to the commanded step position (or VA) (Figure 3.17). The DN value in this analysis is simply the spatial average of a background-subtracted frame. The data come from *ITF vs radiance* sessions and therefore are illuminated with a lambertian surface which provides homogeneous illumination on the focal plane. The used background is the first image of the sequence (shutter virtually closed) and the average is performed on a tile-base. The step is retrieved from the log of the session.

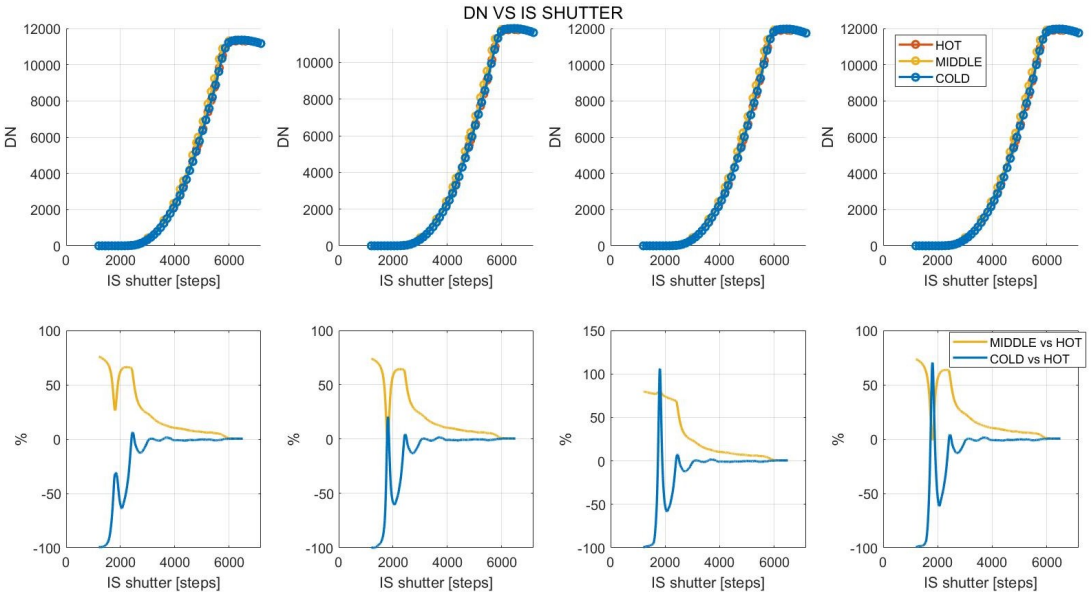

Figure 3.17: *Top*: Panchromatic filter response (in DN) with respect to the commanded step. Each column is a different tile. *Bottom*: percentage relative deviation of the response. The Hot case has been selected as reference.

Each curve has been interpolated using a piecewise cubic hermite interpolating polynomial (pchip) in manner to respect the monotonicity; the interpolation is used to evaluate the percentage relative deviation of the response in the middle and cold case with respect to the hot one (figure 3.17, bottom). Data with steps less than about 3000 are excluded by this consideration due to very low SNR which make the data not reliable. However for steps greater than 3000 it is possible to observe a very high variation of the response in the middle case with respect to the hot. The hot and the cold case, instead, appear to be closely related with a percentage deviation no more than 1-2%. It is difficult to attribute this variation to a temperature change in particular considering the small difference in response between the hot and cold case. Therefore the cause has been identified in insufficient stability and repeatability of the illumination of the sphere.

The analysis has been repeated avoiding the use of the VA parameter and instead considering the monitoring photodiode current of the IS as a valid parameter. In order to use the photodiode current, a dedicated function interpolates the spectral radiance values with respect to the photodiode current both coming from the IS calibration. Therefore for each acquisition the photodiode current has been read and the function used to generate the related level of spectral radiance. To generate the (integrated) radiance, the spectral radiance is multiplied by a window function and integrated over the JANUS spectral range. The used window function is the filter transmittance normalized to the peak value.

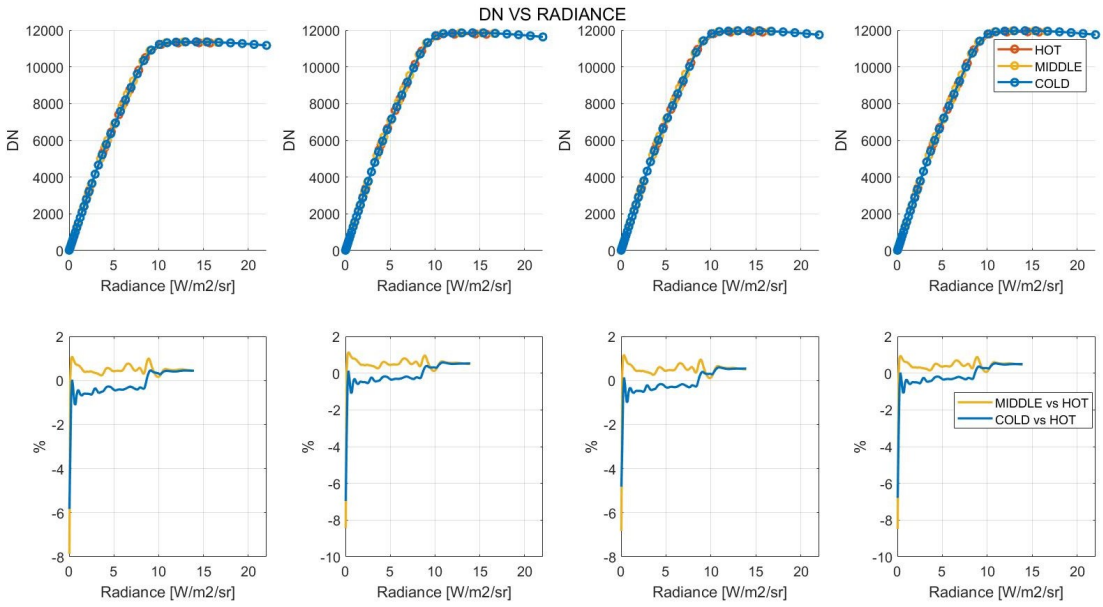

Figure 3.18: Analogous analysis of Figure 3.17. The x-axis is the radiance in order to include the photodiode response

The result of this operation is reported in Figure 3.18. The x-axis is the radiance, which is calculated every time on the base of the photodiode response.

Considering that the filter is the same for all the temperatures a first consideration is that the VA values should not be considered appropriate for radiometric calibration purposes. The repeatability of the command seems to be not guaranteed enough for the capability of JANUS. Instead, the photodiode response seems to provide reliable results. Another consideration is that, considering the variation of the integrating sphere output implicitly included in the interpolation process, and that the temperature variation between the Hot and Cold case is considerable, it is plausible that the variation of the JANUS response in the assumed temperature range is less than 2%

Radiometric curve

In this section it will be presented the most recent status on development of the radiometric calibration for JANUS. Besides these results, the main idea is to have an ITF for each pixel instead of calibrating using a flat-fielding approach. The selected strategy has been considered more reasonable because, at the end, each pixel is a separated detector with its own properties. Moreover, the detector is a CMOS with known non-linearities (Soman et al. 2015a) which in principle makes the use of flat-field less reliable.

This analysis is limited to the verification of the approach and makes use of the (spatial) averages instead of considering the response for each pixel. The extension to each pixel is a second-level step and also requires defining a functional shape to fit the data.

In the same way for all the analyses related to radiometry, each of the four tiles of the detector is considered separately, because pixels in each zone share more similar readout properties.

The on-ground calibration allows two variables to be used to generate DNs: the radiance level and the exposure time. Broadly speaking, this is similar to the in-flight condition where the radiance depends on the different targets and the exposure time is selected accordingly to a desired level of signal-to-noise ratio. Following this consideration and what has been done on previous instruments such as STC (Slemer et al. 2019) and HRIC (Cremonese et al. 2020), a preliminary attempt to produce a mapping for absolute radiometric has been done considering the DN with respect to the product of radiance and exposure time. Using this approach, it is possible to combine in a single graph the ITFvsRadiance, the ITFvsTexpo (Table 3.7) and the radiometric model. Considering the different conditions on the parameter space (which are radiance and exposure time), to verify that all the measurements collapse on a single curve could be a good indicator that the right strategy has been considered.

The dataset used for this analysis is reported in Table 3.11. The dataset is very broad and includes data with different temperature conditions, different ranges of exposure times and input radiance.

Each frame is loaded, background-subtracted, subdivided into the four tiles and spatially averaged. From the session log the photodiode current is extracted and used to derive the spectral radiance and the radiance following the strategy already outlined in Section 3.3.2. The spectral radiance is then also used as input for the radiometric model (Section 3.3.1) to derive a theoretical curve which is superimposed on the experimental ones as comparison.

The selected background frame is common to all the sessions and is a frame selected to be potentially used as on-board background image in the early mission phase. This is because the dark current is negligible for the exposure time ranges used in these measurements. This will be shown in Section 3.2.4.

To compare the different curves, the ITFvsRadiance (MIDDLE) has been selected as reference and for all the others the percentage deviation evaluated. This requires evaluating the curves to common points. For this reason, the curve under analysis is interpolated and evaluated in a range of values common both to the reference and the

Radiometric calibration used dataset	
Session Type	*Filters*
ITFvsRadiance (MIDDLE)	F1 (0.89 ms), F2(35 ms), F3(11 ms), F4 (4.9 ms), F5(14 ms), F6 (35.9 ms), F7 (20 ms), F8 (22 ms), F9 (24 ms), F10 (109.9 ms), F11 (4.9 ms), F12 (8 ms), F13 (26.8 ms)
ITFvsTexpo (MIDDLE)	F2-F3-F4-F5-F6-F7-F8-F9-F10-F11-F12
ITFvsTexpo (HOT)	F1-F13
ITFvsTexpo (HOT) - SpecialFilters	F5-F6-F7-F8-F9
ITFvsRadiance (COLD)	F1 (0.89ms,16 ms)-F4 (4.9ms, 80ms)-F9 (24 ms, 384 ms)
Range of t_{expo}	
ITFvsTexpo	0.2215 ms - 43 ms
F5 SpecialFilters	0.2215 ms - 719 ms
F6 SpecialFilters	0.2215 ms - 2188 ms
F7 SpecialFilters	0.2215 ms - 968.84 ms
F8 SpecialFilters	0.2215 ms - 227.92 ms
F9 SpecialFilters	0.2215 ms - 1250 ms

Table 3.11: Summary of the dataset used for each filter. The keywords *SpecialFilters* means that the radiance level has been optimized to simulate the expected one in-flight. For the COLD sessions the radiance sampling is improved considerably.

selected curve. In this way there is no extrapolation which could potentially introduce erroneous results. The curves are reported in Appendix A, together with the output of the radiometric model superimposed to the experimental curves.

Results and discussion

In general a good agreement can be observed between the different types of sessions for almost all filters, having limited percentage variations between them with the exception of values at low fluxes where the noise probably affects the measure. It confirmed the stability of the system at various temperatures, in particular observing the filters acquired both at HOT and COLD. The "SpecialFilters" sessions seem to show a lower deviation with respect to the others also at low abscissa values. For those sessions it is also observable a systematic deviation in F7 and F8; instead, F5, F9 and F6 do not show that systematic error.

The larger deviation in F6 is due to a not yet explained different value of saturation in the respective ITFvsRadiance reference; the two plateaus have different levels and it is not due to the background subtraction because the same background image has been

used. In fact, the SpecialFilter session is consistent with the ITFvsTexpo around the saturation zone and this confirms that the problem is limited to the ITFvsRadiance.

F1 shows quite large deviations although the same types of acquisitions have similar behaviours. Looking at how the radiometric model simulates the other filters, it seems that the ITFvsRadiance sessions of F1 have a higher signal with respect to what is expected considering the parameters of the specific acquisition (that is the exposure time and spectral radiance). Figure 3.19 shows a comparison of the Tile3 for F1, F4 and

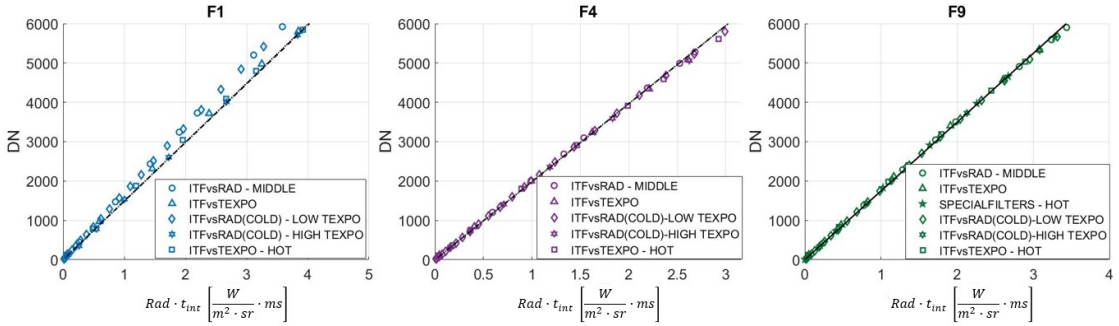

Figure 3.19: Particular of radiometric curves for selected filters. The black dotted lines are the radiometric model output

F9. F4 and F9 are selected for comparison because F9 has the largest number of points but it is a narrow band, instead F4 is a broadband filter. The Figure shows that the radiometric model, for F4 and F9, is capable of reproducing the experimental data, but for F1 this capability is limited to the ITFvsTexpo measurement types. The spectral radiance is estimated by interpolation but the same procedure is used for all the other filters, some having also the same level of radiance used for F1. The exposure time, instead, is quite different because F1 has the largest bandpass and the smallest used exposure time.The reasons why the difference is present is currently under study but preliminary consideration suggests a dependence by (low) exposure time.

3.4 Spectral calibrations

Some sessions have been dedicated to the evaluation of the relative Spectral Response Function (SRF) of each filter. The measurement has been performed using the CB-OGSE. A pinhole of $300\mu m$ is located on the focal plane of the collimator, illuminated by a small integrating sphere fed by a monochromator which is used to perform a spectral scan. To have enough SRN, the edges and the plateau of each filter have been acquired with different exposure times.

The main objective is the verification of the central wavelength and the bandpass and, in general, shape of the filter.

Figure 3.20 shows the strategy used to perform a preliminary evaluation of the SRF. From the session, the images are loaded, background-subtracted and normalized over the

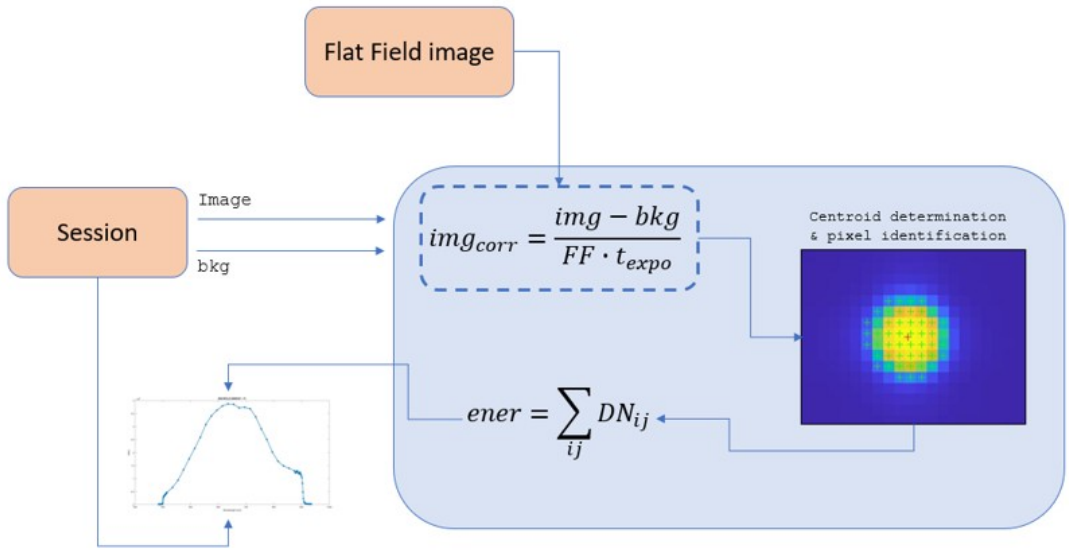

Figure 3.20: Strategy for the preliminary evaluation of the SRF

exposure time and the preliminary flat-field. A centroid algorithm detects the centroid of the spot and the pixels in a defined radius are summed. In this analysis the selected radius is 4 pixels. This process generates a set of curves which contain the lamp spectrum.

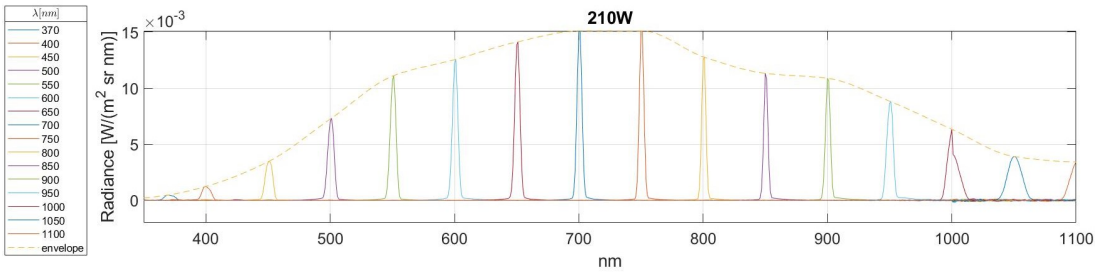

Figure 3.21: Spectral radiance of the source used for SRF measurement.

Figure 3.21 shows the spectral radiance of the source used for the SRF measurement measured by a FieldSpec spectrophotometer, for a set of wavelengths selected on the monochromator (displayed in the legend of the figure). In order to remove the lamp contribution from the measurement, the envelope of the peaks has been spline-interpolated to generate a curve usable for normalizing the results.

$$SRF_{unnormalize} = \frac{ener}{Lamp \cdot \tau_{coll+TVCwindow}} \tag{3.11}$$

$$SRF = \frac{SRF_{unnormalize}}{max(SRF_{unnormalize})} \tag{3.12}$$

where *ener* is the variable in output from the algorithm and $\tau_{coll+TVCwindow}$ is the transmission of the collimator plus the window of the thermo-vacuum chamber.

The results are plotted against the simulated ITF (Eq: 3.8) normalized to their peaks. Figure 3.22 shows the curves after normalization.

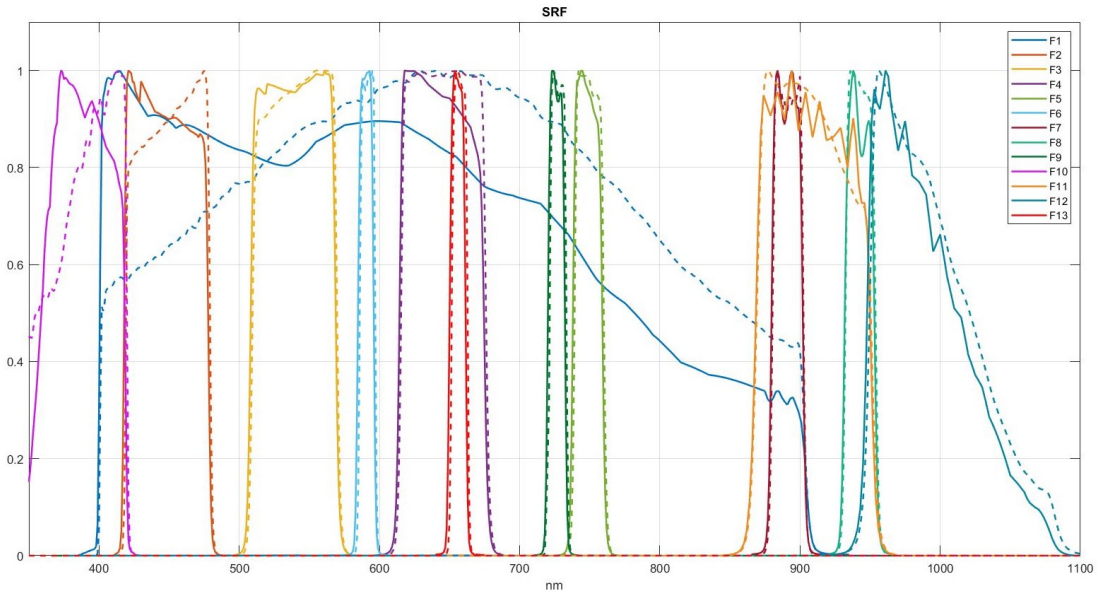

Figure 3.22: Spectral Response Functions of JANUS filters. Experimental data are in continuous curve, shape from the radiometric model are dotted curve

Results and discussion

A clear result is that the bandpasses of the filters are in general in line with the expected ones and the same is possible to see for the central wavelength, although a more precise definition of how these quantities should be evaluated is ongoing. An unexpected shape is present for filters with response lower than 600 nm of the spectrum (F1,F2,F3,F10). It is supposed to be something related to how the normalization is performed. In fact, the curves seem to have the same slope but with a different inclination with respect to the expected ones (dotted curves in Fig. 3.22), in a very systematic manner.

If the data are plotted with a different normalization, using the maximum value of the *ener* variable for F1 (which should be about the maximum point both for the ITF and the lamp), the situation changes with interesting results, shown in Fig 3.23.

The envelope is clearly different due to contribution given by the shape of the lamp, but it is possible to appreciate how the measurements are consistent among themself for both the experimental (solid lines) and synthetic (dotted lines).

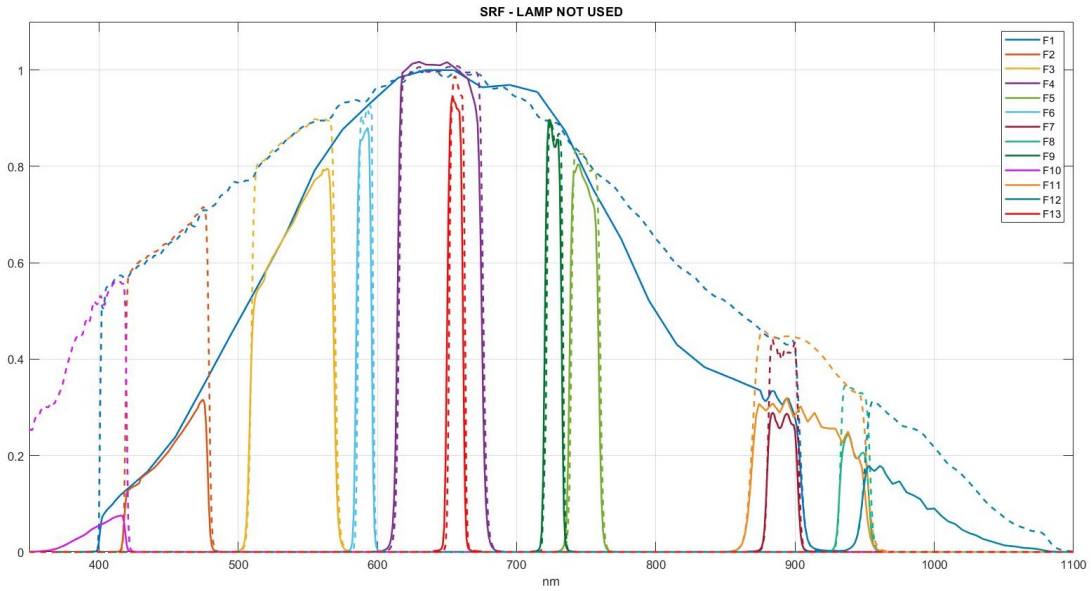

Figure 3.23: Spectral Response Functions not normalized using the lamp but using the maximum value of F1. The ITFs from the model are normalized in the same manner

3.5 Geometrical calibrations

The aim of the geometrical calibrations is to provide a convenient description of the instrument response in the spatial domain and, in particular, of its *geometrical* properties (such as the focal length, the IFOV and the FOV). All these parameters, in fact, are related to a paraxial description of the telescope and allow to obtain a mapping between the real world (or object space) and the image (or image space). This mapping provides a suitable description for a broad range of analyses (for example the determination of the libration period of Ganymede (Aboudan et al. 2019)

Table 3.12 summarizes the measurements planned for JANUS in the framework of the geometrical calibration: Boresight (BS) and Line Of Sight (LOS). Due to time schedule limitation, the LOS approach which is, in principle, by far the most complete strategy, has been considered only for an intermediate temperature case study. In fact, from the LOS it is possible, in principle, to extract the paraxial properties of the instrument and the distortion map, providing also a description of the deviations from the simple mapping available using only the paraxial properties.

It should be highlighted that a complete characterization of the instrument response in the spatial domain should also include a measurement of the MTF (Modulation Transfer Function) and/or the PSF (Point Spread Function) which effectively describe the spatial response. These two measurements are not described in this section and have been estimated by the industrial prime (Sarti et al. 2022).

Geometrical calibration measurements				
Type	Expected outputs	Points	Temperature	Note
Boresight (**BS**)	Variation induced by changing the filter, temperature variation of boresight	1	HOT (superHot), COLD (Cold)	Static measurement, small time interval between filters
Line of Sight (**LOS**)	focal length, IFOV, FOV, boresight direction (for each filter frame), distortion map	63 (9x7)	MIDDLE (Hot)	"Dynamic" measurement, time demanding test

Table 3.12: Summary of the geometrical calibration measurement approach considered for JANUS. The *Expected outputs* column lists the parameters which are expected from the analysis. The *Points* column gives the number of spatial points in the instrument FOV. The *Temperature* column describes in which of the three temperature set-points of the thermo-vacuum cycling performed during the calibration campaign the measurement has been acquired. Denominations inside the brackets refer to an alternative nomenclature which is maintained in the naming of the calibration dataset.

3.5.1 Reference systems

In this section the reference systems adopted to define the relative attitude of the instrument with respect to the setup are described. This measurement requires the collimator in order to produce collimated beams to simulate a source at infinity. The collimator is mounted on a Syrius hexapod produced by Symetrie. In this way it is possible to exploit a FOV large enough to cover the JANUS one. The hexapod has four reference systems which are required to define its movement: Machine frame, Platform frame, Object frame and User frame. The Machine frame is fixed and it is defined by its mechanical structure. The Platform frame is fixed with respect to the platform but mobile with respect to the Machine frame. The User and Object frame are two systems defined by the user and correspond to a reference frame at the beginning and at the end (respectively) of the roto-traslation movement. When a movement is commanded, the Object frame moves with respect to the User frame (Symetrie 2020). In the ATP there is always a setting of the Object and User frames. They differ only in a rotation which is what the ATP commands during the calibration session. In order to completely describe the OGSE-JANUS interaction, five reference systems are required, as shown in Figure 3.24:

- **URF (Unit Reference Frame)**: it defines the mechanical reference frame. The

system is co-aligned with the JUICE reference frame (see Fig: 3.24)

- **UARF (Unit Alignment Reference Frame)**. It is a reference frame defined by the faces of the reference cube and it is virtually aligned with the URF except for a (known) rotation. (see Fig: 3.24)

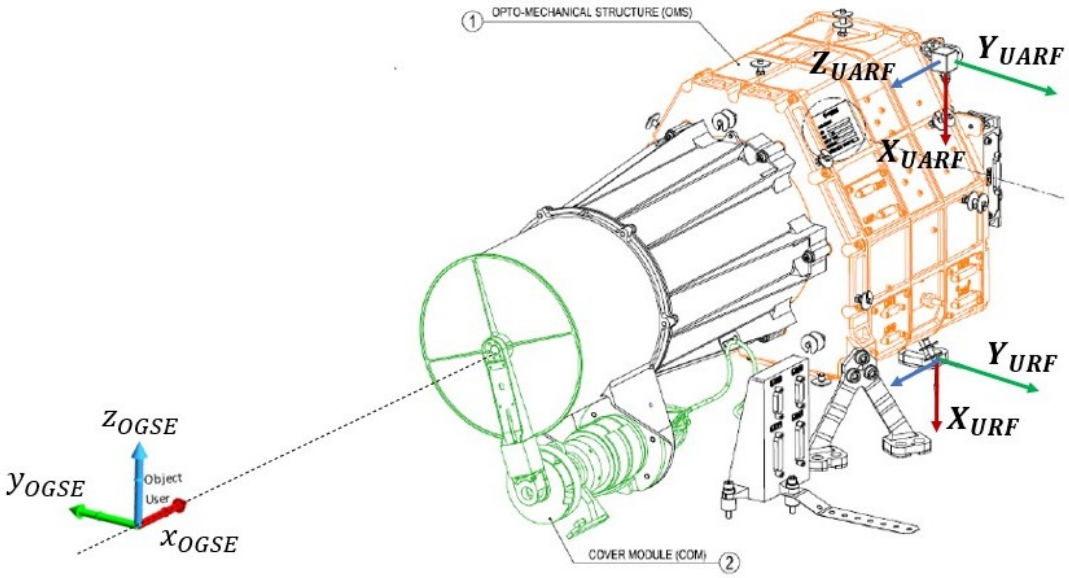

Figure 3.24: Reference frames for JANUS and OGSE. The Object and User reference frames have fixed origins in space and are located on the collimator exit port. The image shows the *Zero* with the OGSE x-axis along the URF z-axis. URF and UARF are related by a rotation matrix provided by Leonardo S.p.A. Courtesy of Leonardo S.p.A. for JANUS draw

- **OGSE**: This reference frame defines the hexapod in *zero configuration* (hereafter in this section simply *Zero*) with the collimated beam along the x-axis of this reference system. It is assumed to be fixed in space and it is defined when the Object frame and the User frame are set in the ATP. The x-axis is aligned with the z-axis of the URF. Actually it is aligned with the z-axis of the UARF and then with the z-axis of the URF with a known rotation from UARF to URF (Sarti 2021), because the URF is not physically materialized. (see Fig: 3.24)

- **ILS (Instrument Line of Sight)**: It is a reference frame with z-axis oriented along the boresight direction (defined by the pixel with row 1000 and column 752) and the x and y-axes oriented (but not aligned) with the columns and rows of the detector maintaining a right-handed reference system. One of the objectives of the analysis of this section is to provide the rotation matrix from URF to ILS.

- **DET (Detector Reference)**: The reference frame of the detector. The y-axis is parallel to the rows of the detector and the x-axis is along the columns. (see Fig: 3.25)

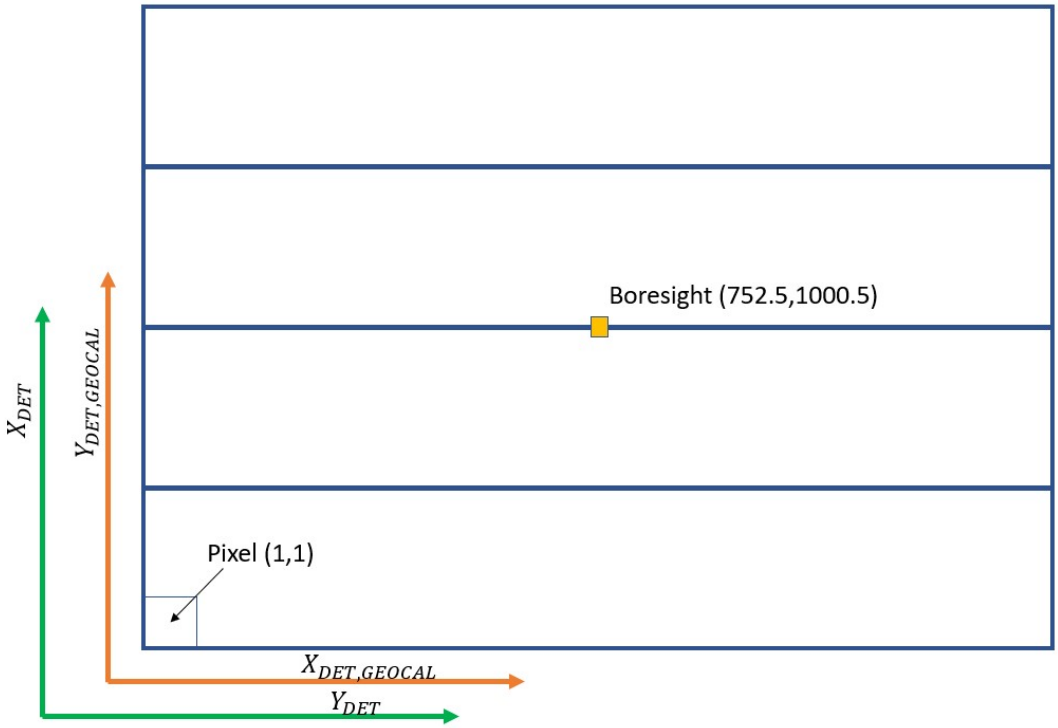

Figure 3.25: Detector reference frame. In green the detector reference frame according to instrument User Manual. In orange the detector reference frame used in this chapter. The reference pixel and the boresight are reported in classical image (Y,X) coordinates.

According to Symetrie 2020 the rotation matrix for the hexapod which describes the orientation of the Object frame with respect to User frame is $R_{hexapod}$, described by:

$$[\mathbf{x'}]_{OGSE} = R_{hexapod}(\angle RX, \angle RY, \angle RZ)[\mathbf{x}]_{OGSE} \tag{3.13}$$

$$R_{hexapod}(\angle RX, \angle RY, \angle RZ) = \begin{bmatrix} cos(RZ) & -sin(RZ) & 0 \\ sin(RZ) & cos(RZ) & 0 \\ 0 & 0 & 1 \end{bmatrix} \begin{bmatrix} cos(RY) & 0 & sin(RY) \\ 0 & 1 & 0 \\ -sin(RY) & 0 & cos(RY) \end{bmatrix} \begin{bmatrix} 1 & 0 & 0 \\ 0 & cos(RX) & -sin(RX) \\ 0 & sin(RX) & cos(RX) \end{bmatrix} \tag{3.14}$$

It is an *alibi* rotation moving the vector $\mathbf{x}$ in the OGSE reference system. The rotation described by the equation is performed along the axis of the fixed OGSE reference system in the sequence $\angle$ RX, $\angle$ RY, $\angle$ RZ. These rotation angles are defined in the ATP. For the specific case of the collimator system, the $\angle$ RX rotation is always set to 0 due to the fact that in zero configuration the collimated beam is aligned with the x-axis and a rotation around this axis produces no effect.

Using an *alias* interpretation of the rotation matrix, a vector in the OGSE reference system can be expressed in the URF one (as shown in Equations 3.15, 3.16). It should be underlined that the OGSE and URF are aligned at ambient temperature and for this reason the subscript *air* will be added in order to make it evident.

$$[\mathbf{x}]_{URF,air} = R_{OGSE2URFAIR}[\mathbf{x}]_{OGSE} = R_{O2U}[\mathbf{x}]_{OGSE} \tag{3.15}$$

$$R_{OGSE2URFAIR} = \begin{bmatrix} cos\gamma & sin\gamma & 0 \\ -sin\gamma & cos\gamma & 0 \\ 0 & 0 & 1 \end{bmatrix} \begin{bmatrix} cos\beta & 0 & -sin\beta \\ 0 & 1 & 0 \\ sin\beta & 0 & cos\beta \end{bmatrix} \tag{3.16}$$
$$\beta = -90°, \gamma = 180°$$

3.5.2 Boresight (BS)

The collimator is oriented with the hexapod in the $R_{hexapod}(0,0,0)$ direction (which corresponds to the *Zero*). A set of 30 images is acquired and the procedure is iterated over each filter. After covering the source the sequence is repeated to make the relative background.

Figure 3.26 shows the logical timeline in which the data have been acquired. The yellow objects indicate the sequence commanded by the ATP, the transition from COLD to HOT is also shown. In the COLD case, when the ATP sends the command with all the parameters ∠RX, ∠RY, ∠RZ null, there is an effective movement of the hexapod platform in order to reset to zero the position from the previous calibration session. In the HOT case, the movement of the hexapod is probably not executed because it is already in position (from the log of the hexapod the angles are in fact always the same for all the timestamps before and after the setting of the *Zero*).

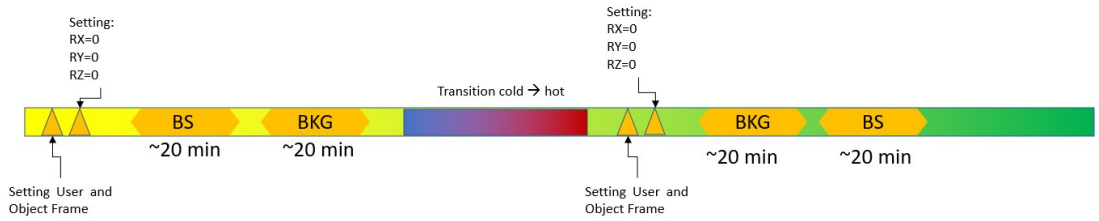

Figure 3.26: Logical timeline in which the two boresight measurements have been acquired. In yellow there are the commands from the ATP. In blue/red the transition from a Cold temperature to the Hot case is shown.

The image is corrected with its background and with a preliminary flat field image. A simple centroid algorithm is applied on the resulting image with a threshold level of 200 DN with respect to about 5000/6000 DN of the spot peak. This threshold level is useful to avoid in the detection to take advantage of the base of the centroid where a spurious

effect was measured (see for example Figures 3.27b, 3.27d). This procedure is applied on each image of the sequence. The spot centroid and its uncertainties are evaluated as the mean and standard deviation over the 30 images.

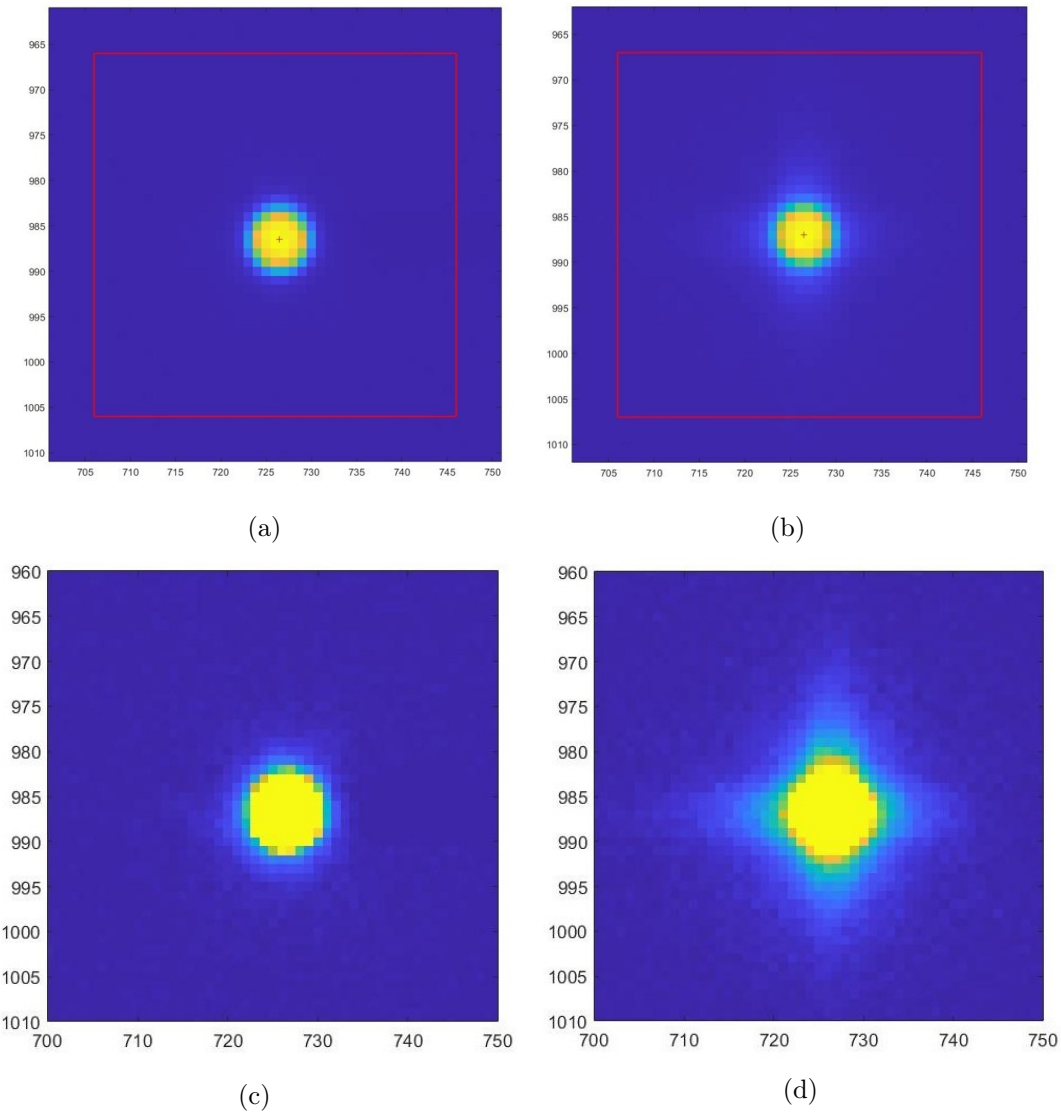

Figure 3.27: Examples of spots. The red cross is the estimated centroid. (a): F1. (b): F8. (c) and (d): Same of (a) and (b) respectively but the range is limited to [0 500] DN to better visualize the spurious signal

In Figures 3.27b and 3.27d) a spurious effect is observable. The signal is not localized in the spot but it is distributed in a cross-shaped pattern. It has also been observed with other target (slits) and we supposed it is due to some diffusion effect at detector level. It appears to be more evident in filters F7, F8, F11 and F12 which are localized in

the RED/IR side of the instrument spectral range. Figure 3.28 shows the results of the estimation.

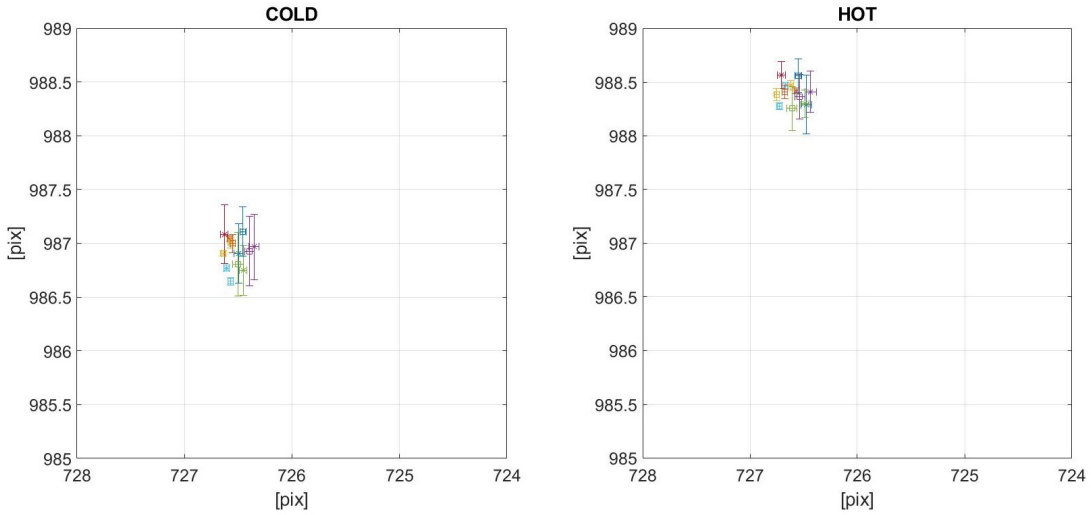

Figure 3.28: Average centroids with related standard deviations for all the 13 filters. The legend is avoided because not necessary. *left*: COLD case, *HOT* case.

It is possible to appreciate the very low dispersion of the various filters with respect to the F1 (the panchromatic) for each considered temperature set point (HOT and COLD, Table 3.12). The maximum standard deviation is 0.055 pixels in column direction and 0.3225 pixels in row direction. Inside the measurement session the OGSE is not moving (with the exception of the residual oscillations). Possible errors include a sub-optimal centroid algorithm selection and the previous cited oscillations.

Figure 3.29 shows the coordinates difference of the centroids between the HOT case and the COLD one for each filter. The difference is mainly in the row direction, with a magnitude of about 1.5 pixels.

3.5.3 Line Of Sight (LOS)

In the LOS measurement, the hexapod is used to span the instrument FoV generating a virtual matrix of 63 points. *Virtual* in the sense that there is one image for each angular direction (and therefore for each spot). An example of the matrix can be seen in figure 3.30a. The ATP is set to iterate over the ∠RZ and ∠RY rotation of the hexapod. Table 3.13 shows visually the angles (∠RY,∠RZ) commanded to the hexapod in a way coherent with the image 3.30a, so, for example the point 57 of figure 3.30a corresponds to the couple (∠RY=-0.8°,∠RZ=+0.57°) of Table 3.13. For each (∠RZ,∠RY), 30 images are acquired. The whole sequence is then repeated for all the filters. The signal has been optimized for each filter in order to provide a response in the about half of the dynamic range.

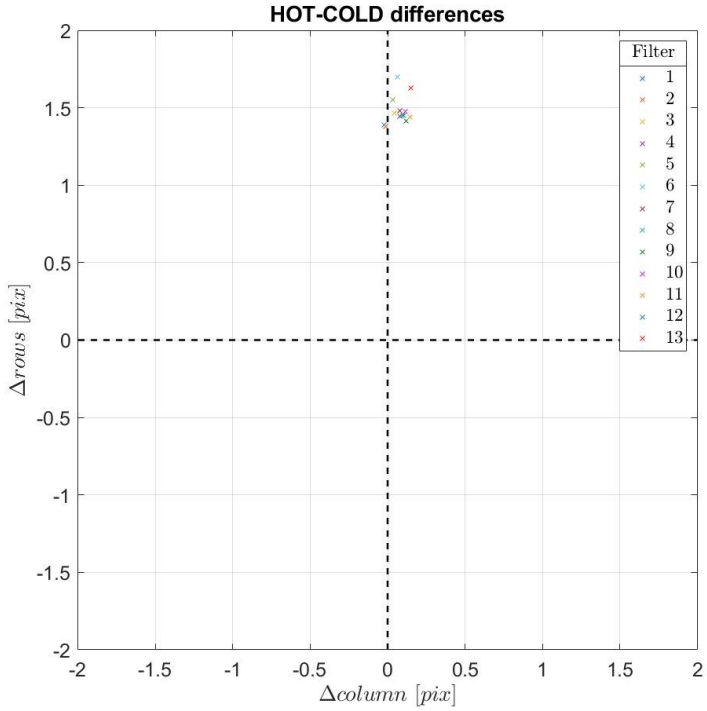

Figure 3.29: Difference map of centroid positions in hot condition with respect to cold. Each filter is considered separately.

The LOS measurements provide potentially a large amount of information (as already summarized in Table 3.12).

The tested strategy is similar to that used for the geometrical calibration of SIMBIO-SYS/STC (Simioni et al. 2016, Simioni et al. 2019 and Simioni et al. 2018) and can be resumed by the flowchart in figure 3.31.

The method has three main steps:

- Mapping points determination
- ideal model
- distortion

In the first step 63 world-image correspondences $\{\overline{X}_i \rightarrow \overline{x}_i\}$ are generated. They are used, in the second step, to perform an estimation of the first order geometrical parameters, which describe the main geometrical properties of the instrument such as the focal length and the orientation of the boresight direction. The deviations from the ideal model are usually ascribed to the distortion (intended in the sense of geometrical aberration) and its removal is performed devising a proper function which relocates the distorted points

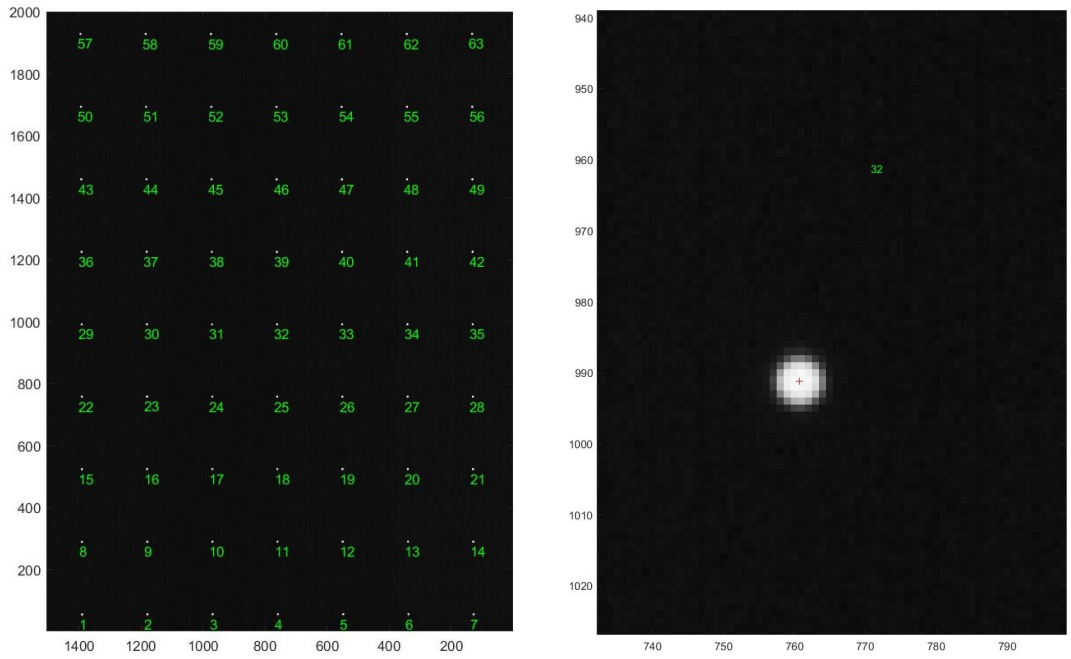

(a) (b)

Figure 3.30: Example of the resulting spot matrix from a Line Of Sight measurement. In (a) all the 63 points are shown. The image is simply the sum of 63 averaged images each with a different point. The enumeration indicates the order of acquisition in the angle scan sequence and therefore shows the movement direction of the hexapod. The image axis direction is consistent with how the detector is physically mounted looking from the z axis of the URF reference system. The pixel (0,0) (or (1,1) depending on the reference definition) is in the bottom right side of the image. In (b): point 32 (about middle FOV) along with the estimated centroid (red cross)

towards the corresponding undistorted points defined by the ideal model (Da Deppo et al. 2015). The last operation is potentially executed the step three.

Mapping points determination

From this section two outputs are expected: the 2D pixel coordinates of the centroids and the corresponding 3D coordinates in the world reference system.

For each of the 63 directions the acquisition is repeated 30 times. Due to the fact that during the analysis of the calibration data it was understood that vibrations and drifting were sometimes present during the acquisitions, the images have not been averaged together. Instead, each one is background subtracted, flat-field corrected using

Elevation/Azimuth commanded rotation angles (∠RY [°],∠RZ [°])						
(-0.8,+0.57)	(-0.8,+0.39)	(-0.8,+0.21)	(-0.8,+0.03)	(-0.8,-0.15)	(-0.8,-0.33)	(-0.8,-0.51)
(-0.6,+0.57)	(-0.6,+0.39)	(-0.6,+0.21)	(-0.6,+0.03)	(-0.6,-0.15)	(-0.6,-0.33)	(-0.6,-0.51)
(-0.4,+0.57)	(-0.4,+0.39)	(-0.4,+0.21)	(-0.4,+0.03)	(-0.4,-0.15)	(-0.4,-0.33)	(-0.4,-0.51)
(-0.2,+0.57)	(-0.2,+0.39)	(-0.2,+0.21)	(-0.2,+0.03)	(-0.2,-0.15)	(-0.2,-0.33)	(-0.2,-0.51)
(+0.0,+0.57)	(+0.0,+0.39)	(+0.0,+0.21)	(+0.0,+0.03)	(+0.0,-0.15)	(+0.0,-0.33)	(+0.0,-0.51)
(+0.2,+0.57)	(+0.2,+0.39)	(+0.2,+0.21)	(+0.2,+0.03)	(+0.2,-0.15)	(+0.2,-0.33)	(+0.2,-0.51)
(+0.4,+0.57)	(+0.4,+0.39)	(+0.4,+0.21)	(+0.4,+0.03)	(+0.4,-0.15)	(+0.4,-0.33)	(+0.4,-0.51)
(+0.6,+0.57)	(+0.6,+0.39)	(+0.6,+0.21)	(+0.6,+0.03)	(+0.6,-0.15)	(+0.6,-0.33)	(+0.6,-0.51)
(+0.8,+0.57)	(+0.8,+0.39)	(+0.8,+0.21)	(+0.8,+0.03)	(+0.8,-0.15)	(+0.8,-0.33)	(+0.8,-0.51)

Table 3.13: Rotation commanded to the hexapod in the ATP. The disposal is congruent with the axes of figure 3.30a. For example: (+0.8,+0.57) corresponds to point 1 of Figure 3.30a and (-0.8,-0.51) to point 63.

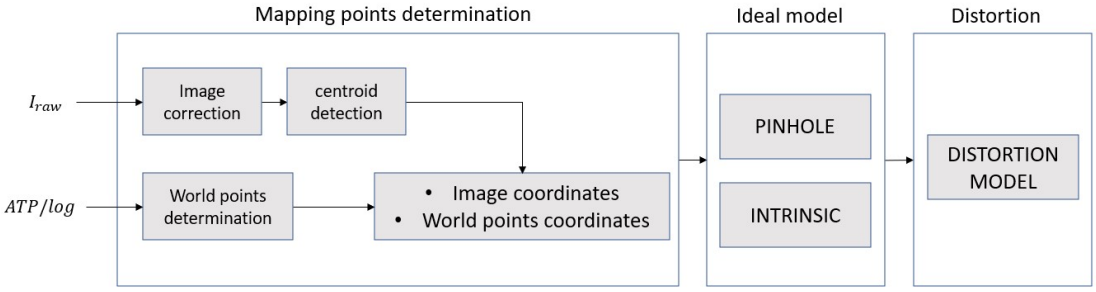

Figure 3.31: Flowchart of the tested geometrical calibration reduction

a preliminary flat field image and then a thresholded centroid algorithm is applied.

The effective centroid is considered to be identified by the average coordinates. Different centroid determination methods have also been considered, including fitting different symmetrical functions such as bidimensional gaussian, super-gaussian, raised cosine, edge detection method and fitting contour ellipses with common centre. They provided very similar results and therefore a more simple and fast centroid algorithm based on intensity barycentre calculation was considered. The procedure has been developed in MatLab environment, where the starting index is 1 (not 0) and therefore the spot coordinates usable by the algorithm are:

$$(i_{DET,geocal}, j_{DET,geocal}) = (i_{DET,geocal} - 1, j_{DET,geocal} - 1)_{MatLab} \tag{3.17}$$

In this section will be used the detector reference system *DET,GEOCAL* as shown in Figure 3.25. The conversion to coordinates in the *DET* reference system (which is the official detector reference system as described in the instrument User Manual) is described

by:

$$X_{DET} = Y_{DET,GEOCAL} \tag{3.18}$$

$$Y_{DET} = X_{DET,GEOCAL} \tag{3.19}$$

To provide the world points coordinates equations 3.13, 3.14, 3.15 and 3.16 are combined:

$$[\mathbf{x}]_{URF,air} = R_{OGSE2URFAIR} R_{hexapod}(RY, RZ)[\mathbf{x}_{ref}]_{OGSE} \tag{3.20}$$

having considered $[\mathbf{x}]_{OGSE} = [\mathbf{x}_{ref}]_{OGSE} = -x$, and the ∠RY, ∠RZ rotations according to Table 3.13. This emulates the physical movement of the collimator. In this way, the rotation generates a new vector in the OGSE reference frame moving the original vector aligned along the -x axis of the OGSE reference frame. This is then interpreted in the URF_{air} frame, where the OGSE x-axis is virtually aligned with the URF z-axis. When the ∠RY=0 and ∠RZ=0 are commanded, the rays coming from the collimator are aligned along the OGSE x-axis and the object virtually is emitting the rays in -x direction.

Ideal model

The imaging geometry of most cameras can be described as a two-stage process: projection of the 3D world onto a unit sphere followed by a projection of the sphere onto the image plane (Da Deppo et al. 2015). Mathematically, this can be expressed, in homogeneous coordinates, in the framework of the projective geometry as (Hartley et al. 2004):

$$[\mathbf{x}]_{img} = K[R \mid \mathbf{t}]\mathbf{X}_{world} \tag{3.21}$$

where K is the *Intrinsic parameters* matrix, R is the rotation matrix from the world reference system to the camera reference system, $\boldsymbol{t}$ is the translation vector which locates the center of the camera system with respect to the world one. Rotation and translation constitutes the *Extrinsic parameters* matrix. The Intrinsic Parameters matrix is:

$$K = \begin{bmatrix} f_x & s & x_p \\ 0 & f_y & y_p \\ 0 & 0 & 1 \end{bmatrix} \tag{3.22}$$

with f_x and f_y the focal lengths in pixel unit, s is the skew factor and (x_p,y_p) the coordinates of the principal point. The skew factor has been set to zero and the principal point coordinates to (999.5,751.5) (in the $DET,GEOCAL$ reference system.). The choice to have a different detector reference system with respect to what is indicated in the User Manual is clear observing figure 3.32. It can be seen that the image plane in *viewing* condition (that is positive focal distance in the camera reference system, which corresponds to the projection of the image plane with respect to camera centre of projection) is coherent with the camera reference system. Considering the high accuracy of the calibration setup, it is expected that the camera reference system is only slightly rotated with respect to the URF_{air} reference system and therefore an iterative procedure is already close to the correct local minimum. It should also be clear that the camera system in this context

corresponds to the ILS (*Instrument Line of Sight*) reference system, because the z-axis of this system is made to be co-aligned with the ray impinging over the pixel defined by (x_p,y_p). It should be underlined that the image plane (and the ILS) is no longer aligned with the actual focal plane defined by using the physical detector (Simioni et al. 2019).

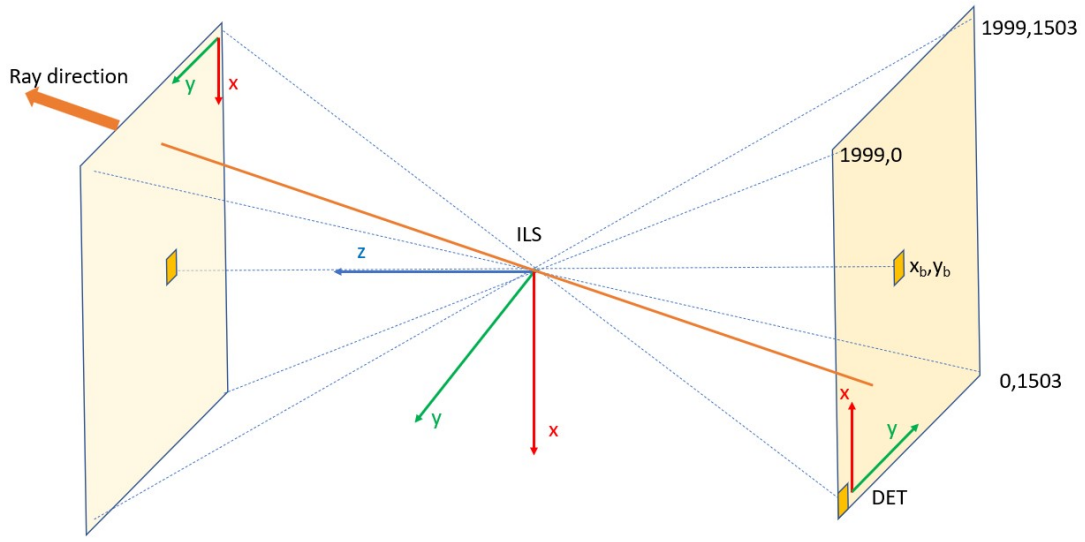

Figure 3.32: Representation of the ILS reference system, the image plane oriented but not aligned with the detector reference frame and its projection in *viewing* configuration

Due to the fact that the objects are located at infinity thanks to the collimator, the extrinsic parameters matrix is reduced to only the rotation part and the projection matrix becomes the *infinite homography* because it maps points from a plane located at infinity to a plane (image) (Hartley et al. 2004).

The equation 3.21 is specialized in this case as:

$$[\mathbf{x}]_{img} = KR_{URF,air2ILS}\ [\mathbf{X}]_{URF,air} \tag{3.23}$$

with the URF_{air} points determined using equation 3.20. The $[\mathbf{X}]_{URF,air}$, due to the fact that the translation is no longer considered in the projective matrix, includes only the euclidean part of the homogeneous vector.

The internal flowchart of the *ideal model* block of figure 3.31 is detailed in figure 3.33. First, the centroid corresponding to ($\angle$RY = 0°,$\angle$RZ = 0°) rotations is estimated using both interpolation and fitting. This in principle provides the projection of the reference vector on the matrix. Then the couple $(\angle RY_{bor},\angle RZ_{bor})$ which should be commanded to the hexapod in order to illuminate the boresight is evaluated. This information is used to provide the initial rotation matrix for the iterative estimation. In particular it is estimated considering that:

$$[\mathbf{x}_{BOR}]_{URF} = R_{O2U} R_{hexapod}(\angle RY_{bor}, \angle RZ_{bor})\ [\mathbf{x}_{ref}]_{OGSE} \tag{3.24}$$

$$[\mathbf{x}_{ref}]_{URF} = R_{O2U}\ [\mathbf{x}_{ref}]_{OGSE} \tag{3.25}$$

$$[\mathbf{x}_{BOR}]_{URF} = R_{O2U} R_{hexapod}(\angle RY_{bor}, \angle RZ_{bor}) R_{O2U}^{T}\ [\mathbf{x}_{ref}]_{URF} \tag{3.26}$$

which corresponds to an *alibi* rotation moving the reference vector towards the boresight in the same reference frame. The rotation matrix required for equation is instead an *alias* rotation which writes the vectors from the URF reference system into the ILS one. This corresponds at the end taking the transpose of the matrix:

$$R_{URF,air2ILS} = [R_{O2U} R_{hexapod}(\angle RY_{bor}, \angle RZ_{bor}) R_{O2U}^{T}]^{T} \tag{3.27}$$

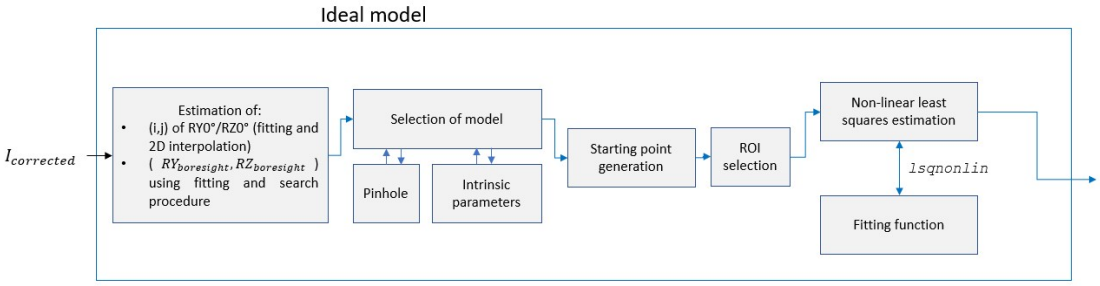

Figure 3.33: Flow chart of the logical operations executed inside the *Ideal model* block of Figure 3.31

Equation 3.27 is then suitable parametrized according to the rotation parametrization selected by the user. It is possible to select several options, including: Rodriguez axis-angle representation, quaternions, Euler angles. If the rotation matrix is already known, the procedure can skip this part and optimize only the focal length(s).

The algorithm allows to select two possible ideal models for the camera:

- pinhole
- intrinsic parameters

The models differ by the possibility to have two focal lengths in the Intrinsic model with respect to a single focal length of the pinhole model. Before starting the non-linear optimization, a ROI can be selected. This allows the user to potentially perform the retrieval only considering certain zones of the detector such as the central one where it is expected that the distortion is low enough to be neglected.

After the camera model has been selected, the initial solution vector can be constructed and passed to the fitting function suitable for the selected strategy. The non-linear least square optimization is performed using the trust-region-reflective algorithm.

Fitting function

The fitting function calculates at every iteration the infinite homography and applies the inverse homogeneous operator to calculate the image coordinates:

$$(x_{det,geocal}, y_{det,geocal}) = hom^{-1}([\mathbf{x}]_{img}) = \left(\frac{[\mathbf{x}]_{img}(1)}{[\mathbf{x}]_{img}(3)}, \frac{[\mathbf{x}]_{img}(2)}{[\mathbf{x}]_{img}(3)}\right) \tag{3.28}$$

Finally the cost function is evaluated:

$$\Phi = \sum d([\mathbf{x}]_{img}, [\mathbf{x}]_{proj}) \tag{3.29}$$

which corresponds to the transfer error, that is the distance between the measured spot and the projected one (Hartley et al. 2004).

FOV, IFOV, boresight and Distortion Map

Once the infinite homography is known, it is possible to determine the FOV directly from the points of the image using the relationships (Hartley et al. 2004):

$$\omega = (KK^T)^{-1} \tag{3.30}$$

$$cos(\theta) = \frac{\mathbf{x}_1^T \omega \mathbf{x}_2^T}{\sqrt{\mathbf{x}_1^T \omega \mathbf{x}_1^T}\sqrt{\mathbf{x}_2^T \omega \mathbf{x}_2^T}} \tag{3.31}$$

with ω the image of the absolute conics (IAC) and $\mathbf{x}_1$, $\mathbf{x}_2$ two image points. The FOV is estimated considering two points at the edges of the image, for both the directions. The IFOV is estimated considering its averaged value:

$$IFOV_x = FOV_x/2000 \tag{3.32}$$

$$IFOV_y = FOV_y/1504 \tag{3.33}$$

the coordinate system refers to the DETGEOCAL detector reference system (in agreement to the procedure implemented).

The direction of the boresight (and also the ILS reference frame) in the URF_{air} reference frame can be evaluated with:

$$Boresight = R'_{URF,air2ILS}[\mathbf{z}]_{URFair} \tag{3.34}$$

The distortion map is the coordinate difference between the ideal model derived and the centroids calculated.

Results and discussion

For this analysis only F1 has been considered in order to evaluate the results of the procedure. The application to all the other filters is, in principle, straightforward, because the process is automatized. Firstly the procedure has been applied directly on the data. The resulting distortion map is shown in Figure 3.34a. The arrows point from the ideal to the real (distorted) values. The increments are multiplied by 100 for visualization. JANUS is an axisymmetric system and thus radial distortion is expected. To better understand, we observed the spots along the two directions (vertical and horizontal). Figure 3.34b shows a zoom on the central column ($\angle$RZ=0.03°), where the spots are displayed along with the centroid determined by the algorithm (red cross). The x/y scales are not the same to improve the visualization. The column seems to be inclined by a certain angle. A rotation around the image normal can be excluded because a similar pattern should also be present in the horizontal direction, and it is not the case.

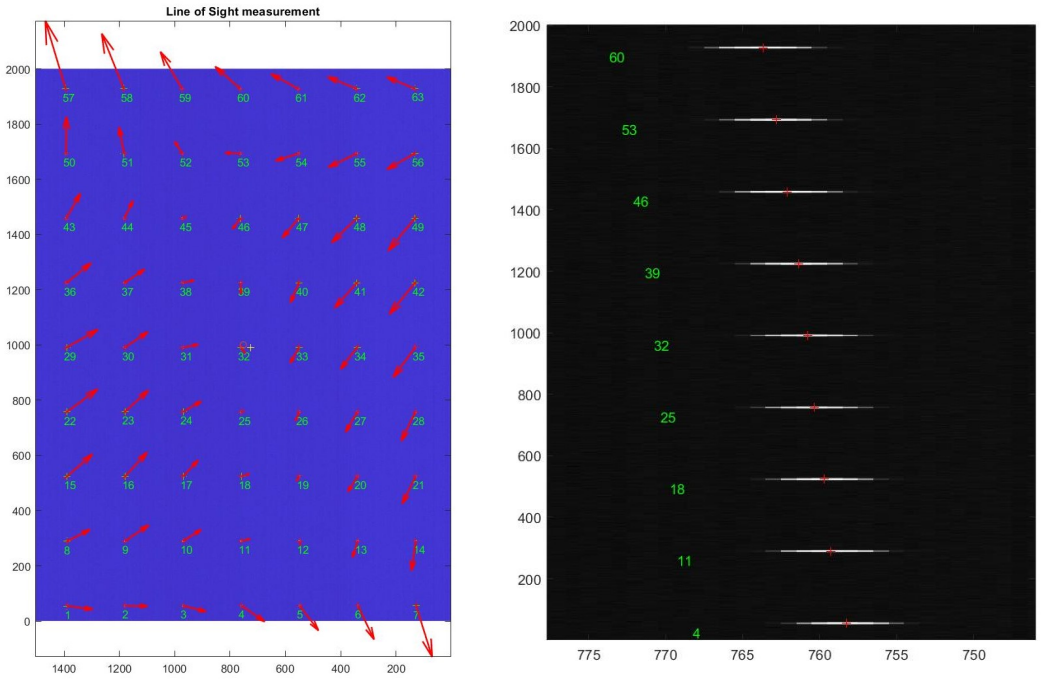

(a) (b)

Figure 3.34: (a): Preliminary definition of the distortion map of F1. axes are in scale. (b). Spots on the central row, corresponding to $\angle$RZ=0.03°. Axes not in scale

The central perspective model is not able to reproduce the pattern probably because it is caused by something not included in the model. The arisen hypothesis is a "drift" induced by the hexapod during the scan of the FOV. To further characterize this behaviour, Figure 3.35 is more explanatory. The Figure 3.35a shows for each column (roughly indicated by the azimuthal angle) how many pixels of variation there are in the column

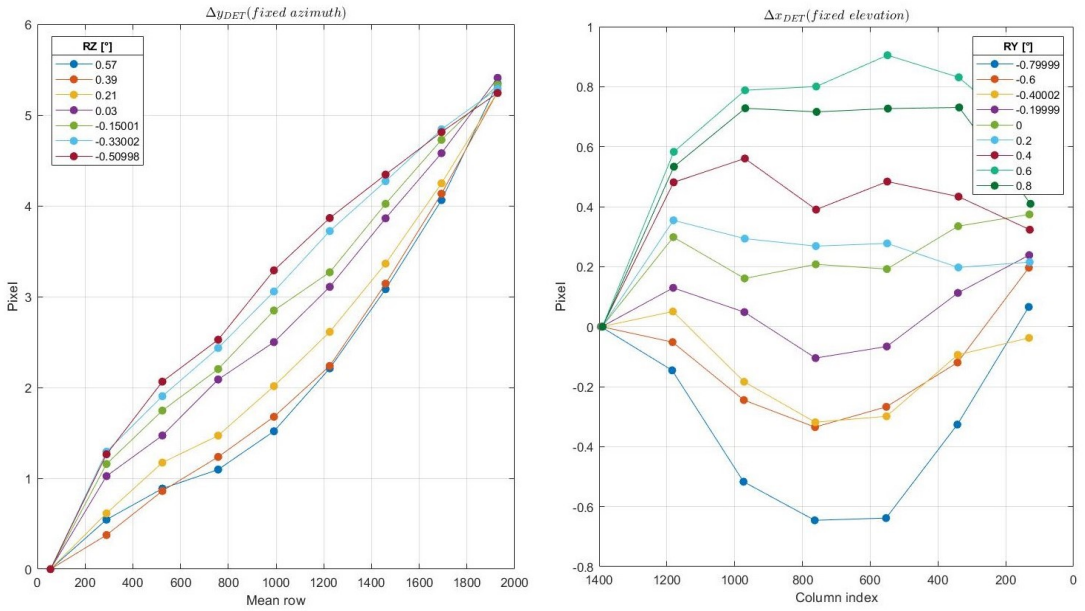

(a) (b)

Figure 3.35: Spots coordinates variation analysis for F1 (panchromatic). (a): Column index variation (in pixels) column-by column. (b): Row index variation (in pixels) row-by-row.

coordinate of the spots with respect to the first point of the column (a measure of what is observed in Figure 3.34b) and, 3.35b, how many pixels of variation there are if the rows are taken singularly and the row coordinate is considered (the reference is the leftmost pixel of each row). According to the optical design (from JANUS zemax model), the instrument suffers from pincushion distortion, thus fixed azimuth points (and varying elevation) should be arranged along vertical arcs with increasing concavities as the azimuthal angle increases. For fixed elevations (and small azimuthal angles) the behaviour is the same but the arcs are horizontal (the system is axisymmetric). Figure 3.35b shows qualitatively this behaviour. A similar behaviour can also be observed in Figure 3.35a but with respect to an oblique line instead the horizontal (horizontal in the plot, where the x-axis represents the average row index). It is not completely clear the reason why the (nominal) $+0.8°$ in Figure 3.35b seems to show lower distortion than the (nominal) $+0.6°$. The overall trend of Figure 3.35 is also observed in the other filters.

According to the commissioning report of the hexapod, when the hexapod performs a RZ rotation from positive to negative the deviation (accuracy measurement) is about + 2.5 arcsec (0.8 pixel). We supposed that it accumulates every time at every elevation angle of the LOS measurement. In fact, the hexapod is commanded to perform scanning from positive to negative $\angle$RZ angles every new RY. Supposing that, the first row has less accumulated error. An estimation of the dRZ accumulated row by row is performed

with a linear interpolation of the curve in Figure 3.35a with ∠RZ=0°. It provides a vector of values of pixel variation, which is converted in angles considering 15 μrad/pixel. These angles are thus added to the nominal angles retrieved from log (but not coherent with the analysis performed) before launching again the algorithm.

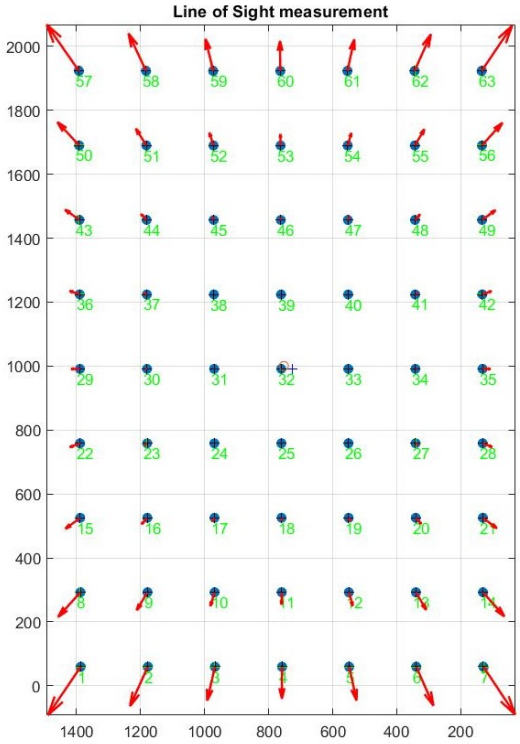

(a)

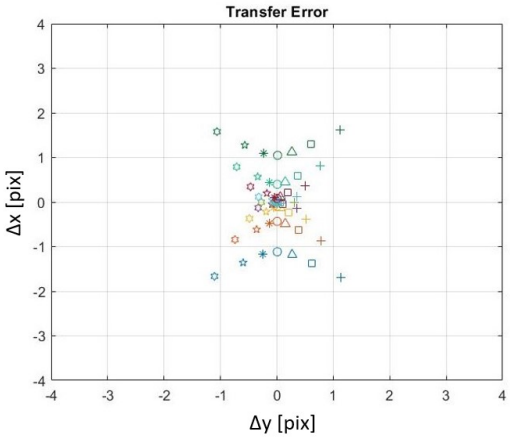

(b)

Figure 3.36: Results of the algorithm applied to a synthetic model of the calibration setup. The dRZ angles are included. The image points are generated from the grid distortion output of the JANUS zemax model. (a): distortion map. The difference between coordinates is multiplied by 100. (b): difference between distorted and ideal model

To compare with the expectations, also a model of the calibration setup has been prepared. From the Zemax optical design, the grid distortion map has been extracted and used to generate the image coordinates by 2D interpolation. The grid distortion includes both the undistorted and the distorted coordinates. The inputs are the RY,RZ rotations commanded to the hexapod which are suitably transformed into the reference frame considered by Zemax. In particular, the elevation angles derived by the hexapod rotation should be converted into the meridian angles accepted by Zemax. The image space of Zemax (output of the interpolation on the grid distortion map) is transformed into the reference system shown in Figure 3.32.

The boresight coordinates are added to the image coordinates (at this stage the

collimator optical axis points towards the pixel (1000.5,752.5)) and finally another fixed offset is added to move the collimator optical axis from the the boresight pixel to where the light actually impinges. This offset is evaluated by means of the algorithm previously described. The same algorithm is also applied to the synthetic model. The results are shown in Figure 3.36. The transfer error shows the difference between the distorted spot and the ideal model calculated by using the estimated homography.

Finally, the algorithm has been applied again to the experimental data after adding the dRZ correction angles derived before. The selected rotation parametrization is Euler angles, the camera model both pinhole and intrinsic (two focal lengths) and the ROI includes only the points closer to the boresight (points: 24, 25, 26, 31, 32, 33, 38, 39, 40). The same ROI selection has also been applied to the synthetic model to have a better comparison. The synthetic model has been analyzed with the intrinsic model and correctly the algorithm provides two almost identical focal lengths (the system is ideally described by a pinhole model). The results on the experimental data are reported in Table 3.14 and shown in Figure 3.37.

Estimated geometrical parameters		
	Pinhole	Intrinsic
f_x	468.34 mm	468.62 mm
f_y	N/A	467.99 mm
FOV_x	1.712°	1.711°
FOV_y	1.287°	1.288°
$IFOV_x$	14.94 μrad	14.93 μrad
$IFOV_y$	14.94 μrad	14.95 μrad

Table 3.14: Results of the non-linear optimization after dRZ angle correction. Panchromatic filter (F1)

Figures 3.37a and 3.37b show the distortion map and the transfer error, respectively, for the case of the pinhole model and Figures 3.37c and 3.37d for the intrinsic model. The angle correction greatly improves the results with respect to that shown in Figure 3.34. The pincushion distortion is now recognizable, in particular in the intrinsic model. The pinhole model appears to show a stretching in row direction. Looking at the transfer error plots, the pinhole model (although more coherent with the axial-symmetry of the instrument) has a larger effect on the y-direction and smaller in x. This is probably due to the fact the algorithm is trying to optimize some residual uncorrected problem in x-direction at the expense of the y-direction. An impression, looking at Figure 3.35b is that there is an asymmetry in x-direction. The distortion should be symmetrical for the first and the last row since they have the same elevation angles, but it is evident that this is not the case. It should be highlighted that no correction has been made in that direction. The reason why the model with two focal flanges seems to show better agreement with the expectation is currently under study. It is possible to approach the same data in a

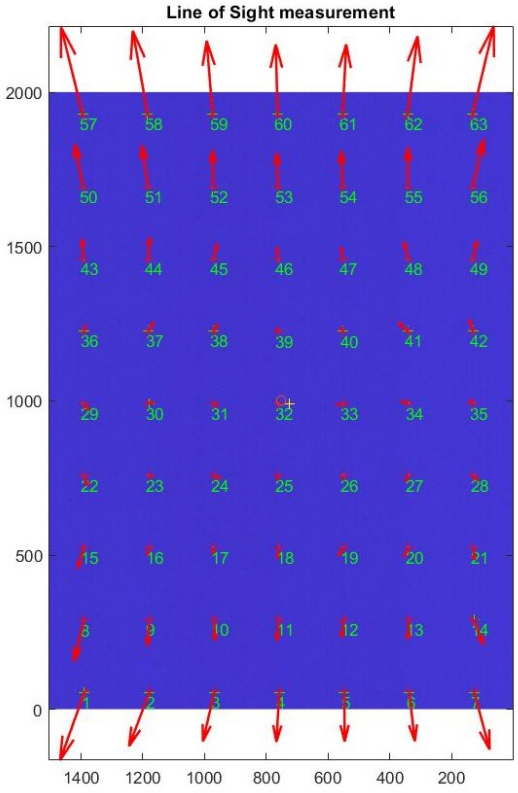

(a)

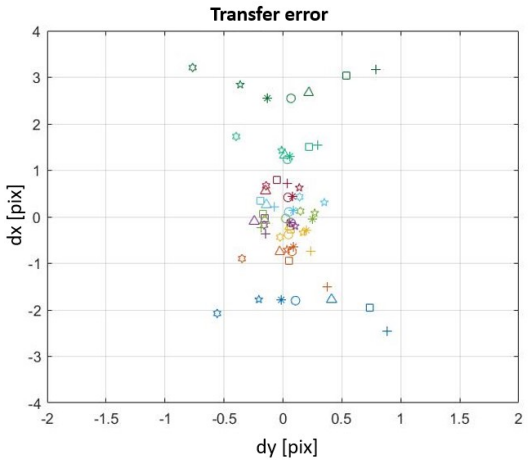

(b)

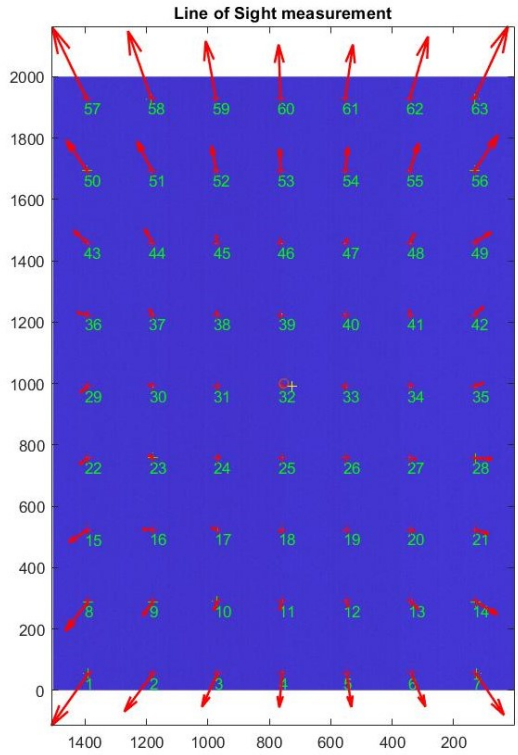

(c)

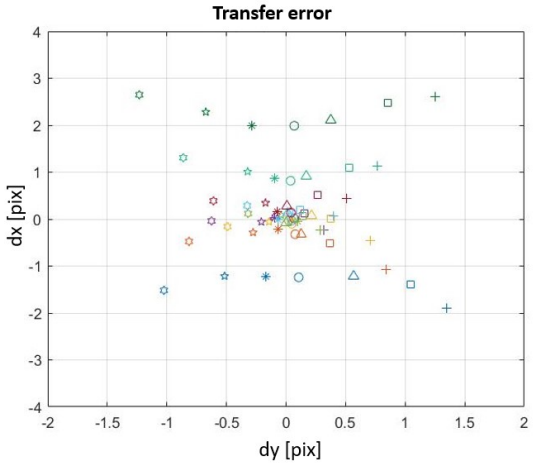

(d)

Figure 3.37: Results of the algorithm applied to the experimental data (F1, panchromatic) after angle correction. (a): distortion map (pinhole). The difference between coordinates is multiplied by 100. (b): difference between distorted and ideal model (pinhole). (c): distortion map (intrinsic). The difference between coordinates is multiplied by 100. (d): difference between distorted and ideal model (intrinsic)

different way. The focal length can be estimated considering the relationship:

$$f = \frac{\Delta i \cdot pix}{\Delta(tan(\theta))} \tag{3.35}$$

where i is the pixel index (row or column according to the desired direction), pix is the JANUS pixel size and θ is the angle from the optical axis. Here, we consider the differences between two consecutive spots having in mind to consider mainly the results in the middle of the field of view, where the distortion is expected to be negligible. Two directions are considered: for each row the y-direction ("horizontal") focal length (note that each row is translated with respect to the other but we made no correction on the angular separation between the spots of each rows) considering the number of pixel in horizontal direction between the spots, and for each column the x-direction ("vertical") focal length considering the number of pixels in vertical direction (note that for each row the row index is almost the same). The angles considered are those from the session logs and are the azimuthal angles in horizontal direction and the elevation angles in vertical direction. The results are arranged in a matrix which recalls to indicate where the estimation is performed in the FOV. The isolines are plotted to better visualize the results (Figure 3.38).

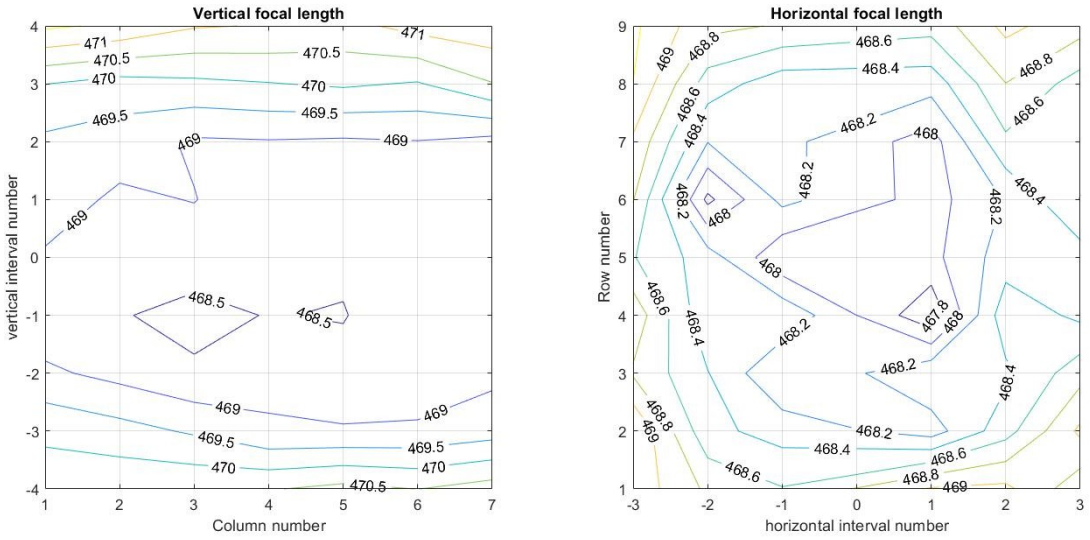

Figure 3.38: Visualization of the Equation 3.35. *left*: vertical focal length (column by column, row index difference of consecutive spots). *right*: horizontal focal length (row by row, column index diffference of consecutive spots)

In Figure 3.38, the *vertical interval number* is the separation/distance in rows from one row the adjacent one (for example: -4 is the difference between rows 290 and 55), Similar consideration applies also for the *horizontal interval number*. Observing the values, in particular in the middle of the FOV (corresponding to the middle of the figure) the

simple calculation performed with Equation 3.35 shows results which are in agreement with the output of the Intrinsic model. From the analysis it appears difficult to use this data for geometrical calibration, being affected by errors of the same order of magnitude as the target of the measurement. This underlines the need of an in-flight geometrical calibration using known stellar fields. Anyway, presuming to have correctly described the shift observed between the rows, the estimated distortion appears to be consistent with the expectation. The reason why two focal lengthes appear should be investigated to verify if it is (or not) due to the instrument. The analysis provides a solid basis for future investigations.

3.5.4 Offset Hollow

This section is intended to report an unexpected behaviour observed in the JANUS data. When the image sensor is illuminated with a source (regardless of its shape) it is possible to note that the signal level outside the image of the source (on focal plane) is to some extent lowered with respect to the expected level. We called this *offset hollow* (Figure 3.39a).

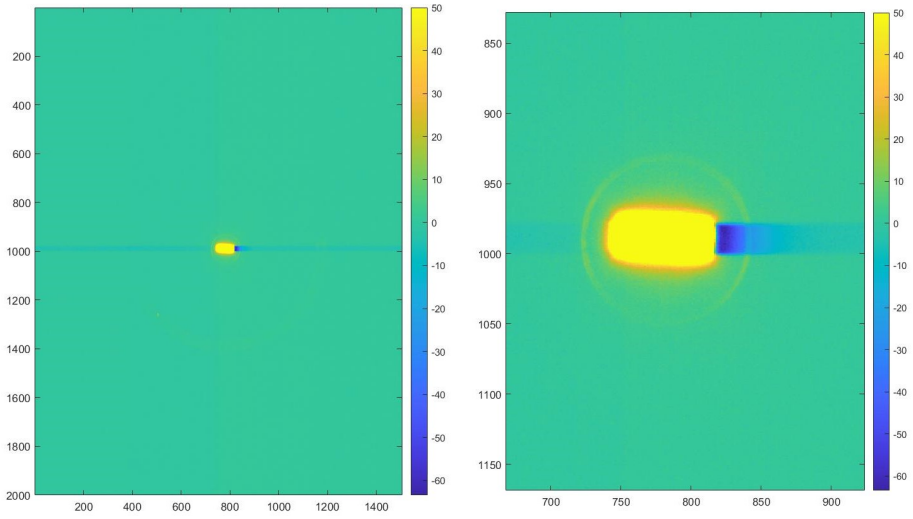

(a) (b)

Figure 3.39: (a): background-subtracted image of a slit. The dynamic range is limited to [-60 50] DN, as shown in the colorbar on the right. The offset hollow is visible as a strip along all the columns having negative DN. (b) Particular of (a). A zone with a steeper hollow is present near the slit. In the image also some spurious signals induced by the setup itself (indicated in the image) are present.

This effect is observable for all the pixels having the same row index of the illuminated ones (Figure 3.39a). The columns with index higher than the illuminated ones seem to

be more responsive to the effect (Figure 3.39b). Hereafter, some case studies will be shown, to observe the response to different shapes and illumination levels. The images and relative background are the result of an average of 50 acquisitions.

The dimension in row direction of the hollow is about the dimension of the source target (but it is not evident due to the mixed combination of spurious signals from OGSE and limitation of dynamic range):

Slit

Figure 3.40 shows images of a test slit, with two different orientations. The images are background-subtracted and plotted in log10 scale to better visualize the effect. Temperature and used exposure time during these measurements are reported in Table 3.15.

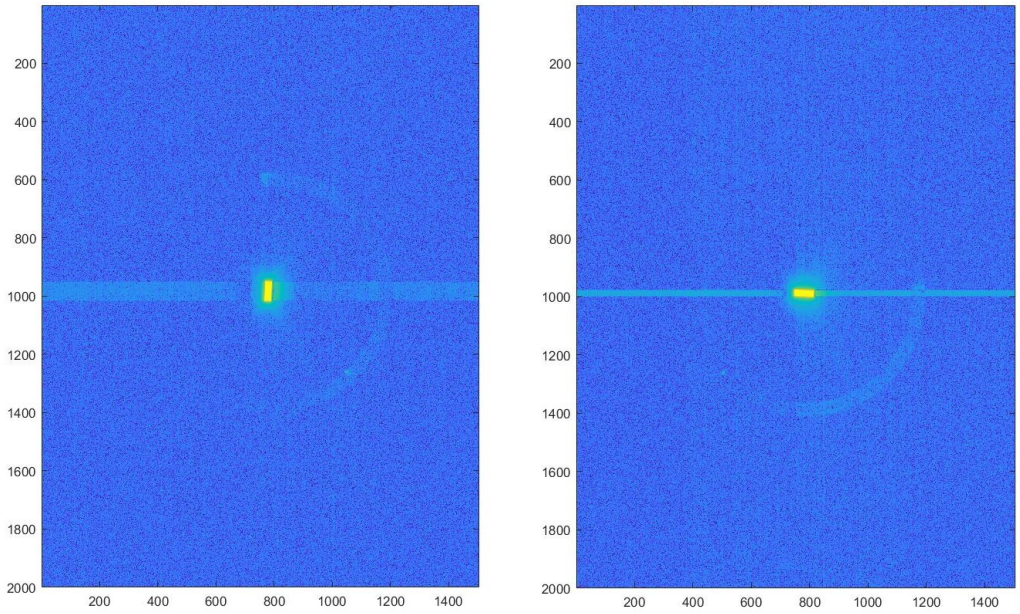

(a) (b)

Figure 3.40: Acquisition of a slit test target ((a): vertical, (b): horizontal). The images are background-subtracted and shown in log10 scale to stretch the dynamic range. Spurious signals from the setup is visible around the slit

Different acquisitions have been realized, with the slit parallel either to the rows or to the columns. Hereafter, in this section, with *vertical* and *horizontal* the orientation of the slit with respect to the sensor coordinates is meant. Actually the target is slightly tilted with respect to the vertical/horizontal directions. A first consideration is that the effect is dependent on the shape of the target. In fact, simply rotating the slit the number of rows

Slit acquisition auxiliary data	
FPA Temperature	-38.3°C
Filter	1
t_{expo}	1 ms

Table 3.15: auxiliary data for offset hollow analysis (slit case)

affected by a signal variation changes accordingly with the target size (Figure 3.40). The signal is also contaminated from spurious signals from the OGSE, due to a non-perfect obscuration of the interfaces between the target holder, the integrating sphere exit port and the TVC window, but these are not considered.

In order to better observe the behaviour of this effect, profiles of different rows crossing the illuminated zone are plotted in Figure 3.41.

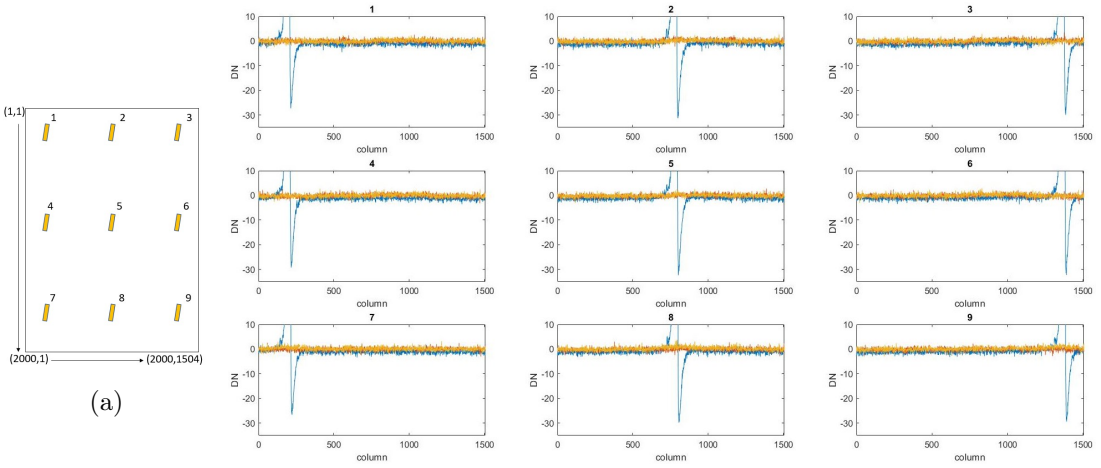

(a)

(b)

Figure 3.41: (a): sketch showing the slit acquisition at different positions in the FOV. The enumeration is used to relate the plots in (b) to FOV position. (b) Row profiles at different FOVs. The data are background-subtracted. The slit direction is vertical. The abscissa coordinates of each figure provide the information about the position on the focal plane. The size of the windows in y direction is the same for each one. The minimum measured signal is about -32 DN.

The selected rows include the middle row of the slit and additional rows far from the illuminated zone as reference (row = 200 and row = 1800). The slit acquisition has been repeated for 9 different view directions to explore the instrument FOV, disposed as a 3x3 grid on the detector (Figure 3.41a). The reference rows are fixed for all the 9 acquisitions, the middle row of the slit is instead identified using a centroid algorithm. This analysis is repeated for all the available viewing directions (Figure 3.41) showing similar responses, suggesting the effect is not depending on the position on the FOV (Figure 3.41b).

The slit test acquisition has been repeated changing the orientation of the slit (from

vertical to horizontal). Figure 3.42 shows a comparison between the horizontal and vertical acquisitions for the position # 5 (see Figure 3.41a). In both cases, the slits have been acquired with a signal of about 5500/6000 DN to have the same dynamic range, avoiding potential influence of non-linearities in the comparison.

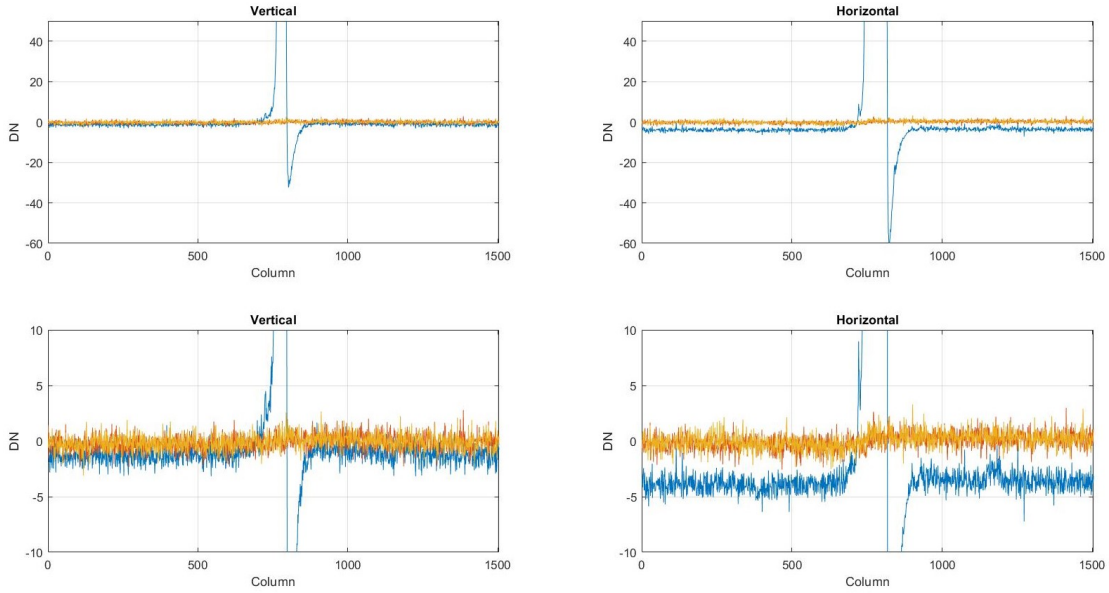

Figure 3.42: Row profiles for vertical and horizontal slit orientation. The selected rows are one in the middle of the slit and two outside for reference (row=200 and row=1800). The position on the FOV is #5 of Figure 3.41a. The *bottom* plots are a zoom of the *top* ones.

The top plots of Figure 3.42 shows that the vertical and horizontal profiles differ in terms of minimum values and offset but the shape seems to be similar. The lowest value in the horizontal case is about -62 DN, about double with respect to the vertical one (-32 DN). The bottom plots of Figure 3.42 better show the difference between the vertical slit and the horizontal one. The signal intensity axis is limited to [-10 10] DN to better visualised the effect. The effect produces a negative offset on all the pixels sharing the same row index of the illuminated zone. Moreover,it is present a small region close to the illuminated zone (higher column indices) showing a deeper slope; after about 50/80 pixels (depending on the acquisition) from the negative peak, the intensity seems to tend to the negative offset (which is -1.5 DN for the vertical slit and -4 DN for the horizontal one). Considering that the intensity of the slit images is quite similar for the considered cases (because the target is illuminated by an integrating sphere), it seems plausible that the amplitude of the hollow depends on the number of illuminated pixels in the row. The global number of illuminated pixels is in fact about the same for both the configurations (the same slit is used, simply rotated), but the rotation varies the number of illuminated pixels in each row. A rude estimation of the illuminated pixel in each row has been

performed considering only pixels with intensity greater than 10 DN after background subtraction. This results in about 45 pixels for the vertical slit (with a negative peak of about -62 DN) and 84 pixels for the horizontal one (with a negative peak of about -32 DN). Currently the cause of this effect is not yet understood, in particular because the detector is actually composed of four blocks of 2000 rows x 376 columns read with four independent lines. An explanation is currently under study.

USAF test chart

In this section the 1951 USAF target is used instead of the slit. Although there are images at different positions of the focal plane, only the middle of the FOV is considered here, due to the fact that the effect seems to be independent of the position on the focal plane.

These data are particularly interesting for two reasons:

- different shape of the target
- different exposure times

The auxiliary information is summarized in Table 3.16.

1951 USAF acquisitions auxiliary information	
FPA Temperature	-43.4°C
Filter	1
t_{expo}	1 ms, 10 ms, 15 ms, 20 ms, 50 ms

Table 3.16: Auxiliary data for offset hollow analysis (1951 USAF target case)

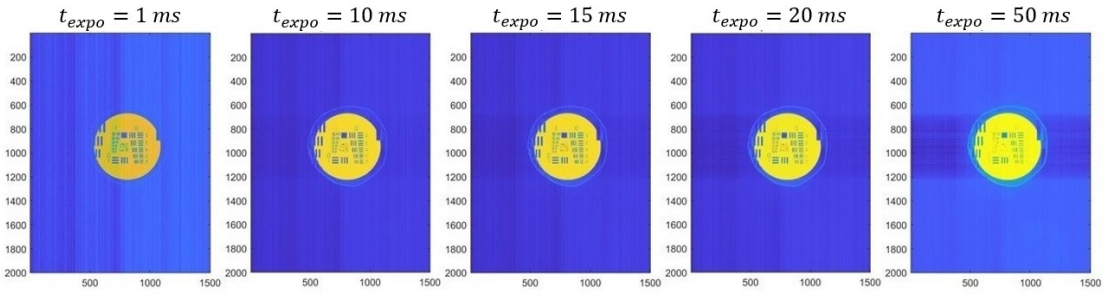

Figure 3.43: Images of USAF resolution chart at different exposure times. The images are not background-subtracted but are in log10 scale

Figure 3.43 shows the acquisition of the USAF chart with different exposure times up about doubling the saturation level. Figure 3.44 shows some profiles for the same images. The selected rows are both inside and outside the USAF chart and the zone of spurious signal coming from the OGSE. The rows outside the illuminated zone can be used as a reference. The presence of the effect is visible also without background removal in both

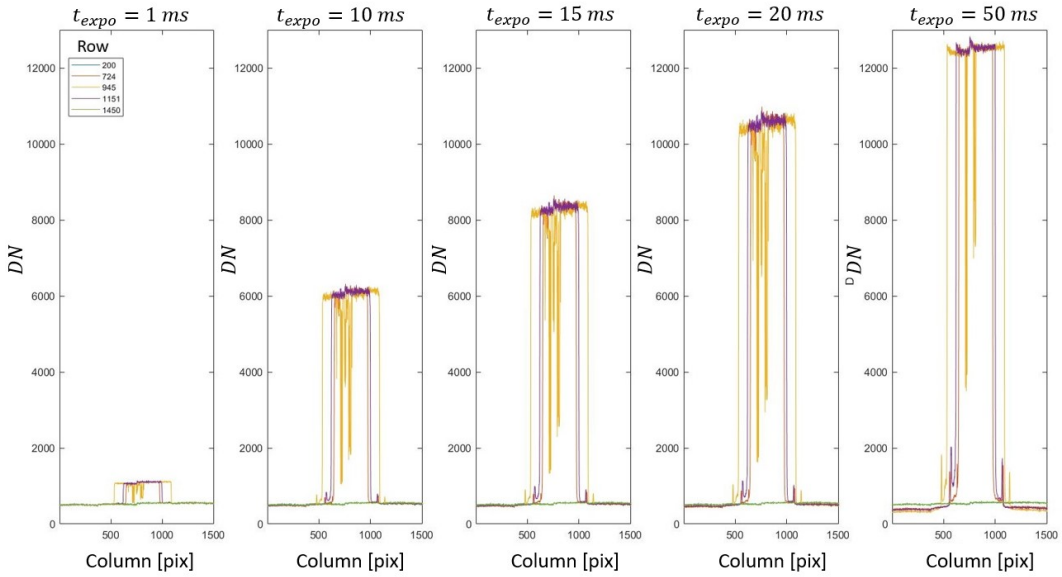

Figure 3.44: Row profiles from images of Figure 3.43, but with linear scale. The selected rows are shown in the legend. The images have not been background subtracted. The rightmost plot shows the case of 2x the saturation level

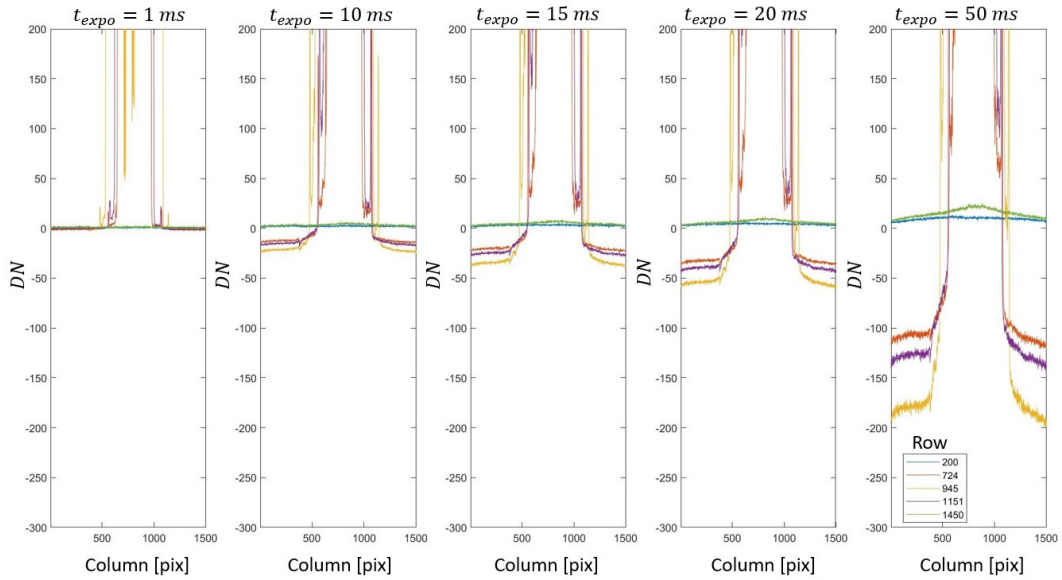

Figure 3.45: Particular of Figure 3.44. In this case the images have been background-subtracted.

the figures. This indicates that the effect is not introduced by the data reduction. The longer the exposure time (or the signal) the larger is the negative offset.

Figure 3.45 allows to better appreciate how the offset hollow effect varies with the signal level. Before extracting the profiles the background has been subtracted. It is possible to see that the "reference" rows show a non-zero level due to a non optimal shielding of the OGSE during the test. Increasing the signal, the constant offset tends to gain a slope.

To perform a comparison with the slit case, the USAF target image acquired with 10 ms of exposure time is considered, because both the acquisitions have similar signals (about 6000 DN). Figure 3.46 shows the selected image along with some rows and their related profiles. The rows differ in the number of illuminated pixels. The response seems to be consistent with the behaviour observed in the slit case. The yellow line, having a higher number of pixels, reaches the lower signal (-20 DN). However, some differences also appear. The deep hollow on the right side of the target is not observable. It is not clear if it is not present at all or if it is masked by a superimposition of spurious signals from the OGSE (for example, a faint *circle* is observable around the resolution chart). The trend of the profile on the right side seems also to be different (different derivative) but the previous consideration is valid also in this case. In the USAF test the negative offset resembles much more a slope as the signal level increase.

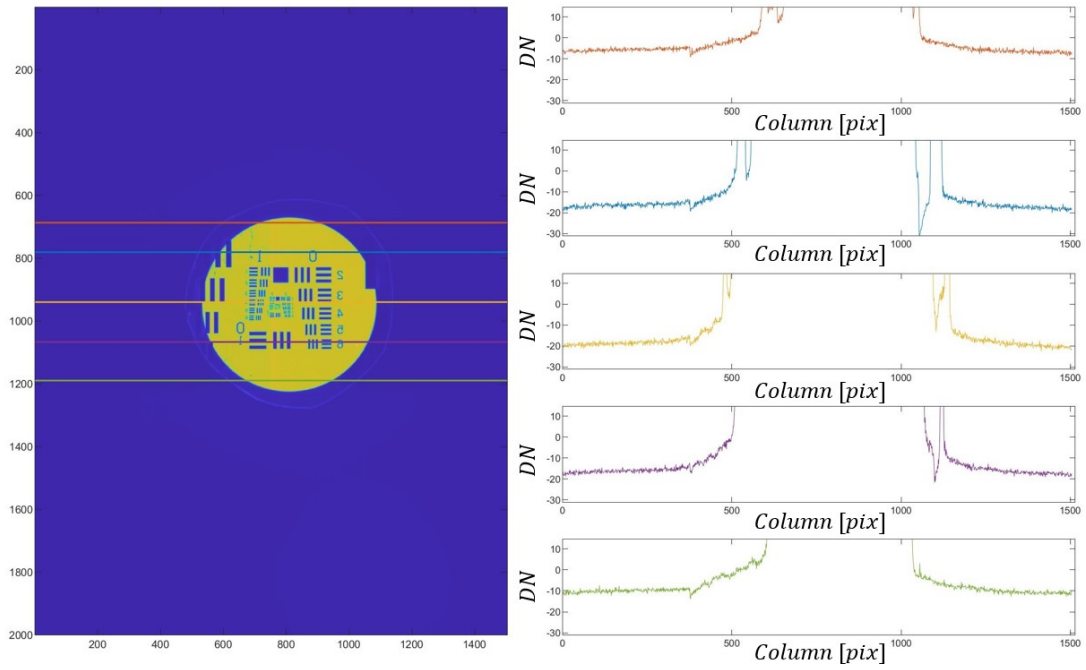

Figure 3.46: USAF image with 10 ms. Coloured lines show the selected rows, displayed also as profiles on the right with the same colour

Conclusions

In summary:

- illuminating the detector generates a lowering of the signal outside the illuminated zone
- the affected area includes all the pixels having the same row index of the illuminated area
- in some cases a deep hollow on the right side near the target is present
- the effect seems to be dependent on the number of illuminated pixels in a row
- the effect seems to be dependent on the the signal level or the exposure time
- it is not induced by the data reduction (background subtraction)

Part II

HYPSOS (HYPerspectral Stereo Observing System)

Chapter 4

The experiment

4.1 Introduction

HYPSOS can be properly described as a stereo imaging spectrometer, since it is able to provide 4D (3 spatial coordinates + 1 spectral information) data as a product of its nominal acquisition mode. HYPSOS acts as two "classical" slit imaging spectrometers in a stereo configuration. The innovative concept stands in collapsing these two instruments in a unique optical design.

HYPSOS has been developed from the heritage of the SIMBIO-SYS suite on board the ESA BepiColombo mission. SIMBIO-SYS is composed by a stereo camera (STC), a high-resolution camera (HRIC) and an imaging spectrometer (VIHI) and it is quite unique in its concept because it is the first time that a planetary mission has three remote sensing instruments integrated in a system sharing hardware components. This configuration allows to simplify the cross-calibration process, the co-registration and data fusion and the science planning (Cremonese et al. 2020).

Stereo imaging is a well consolidated technique in space missions, and often it has been exploited in planetary exploration, making use of images acquired from different perspectives, while the spacecraft hosting the instrument is orbiting around the target. However, this approach could suffer from different illumination conditions and better results could be achieved using specifically designed instruments. Examples of instruments for stereo imaging of planetary surfaces include HRSC/Mars Express (Gwinner et al. 2016), CaSSiS/ExoMars-TGO (N. Thomas et al. 2017), TC/SELENE (Haruyama et al. 2008) and STC-SIMBIO-SYS/BepiColombo (Cremonese et al. 2020). They substantially differ in the stereo acquisition. In HRSC the stereo angle is obtained using the extreme angles of the entire field of view, CaSSiS uses a motor to rotate the telescope and TC has two optical heads properly oriented. The STC design is, instead, composed by two subchannels sharing the majority of the optical elements, with the result to obtain good stereo performances, saving mass, volume and power and reducing the problem of a non-stable stereo angle Da Deppo et al. 2010.

4.2 Design drivers and working concept

The HYPSOS optical design has been conceived considering two design drivers:

- stable stereo angle and channels cross-calibration
- proper telescope/spectrometer pupil matching

The first driver, according to the considerations from the previous Section, is achieved using two sub-apertures of the same telescope. The second one requires the use of a spectrometer with a pupil larger than considering a single channel (Tordi et al. 2020).

Another major improvement comes from the capability to elaborate the two different optical channels in a unique telescope and spectrometer, using the same detector to acquire them. Figure 4.1 describes how this is achieved: two parallel slit-shaped regions of interest (on ground) are rotated of 90° by means of suitable optical elements before being imaged by the telescope, and brought contiguous on the telescope focal plane (with a small separation between the two), to fill in the spectrometer entrance slit.

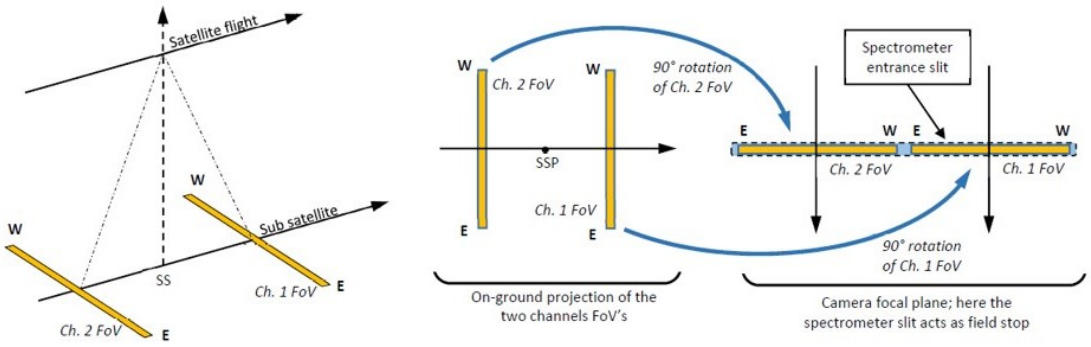

Figure 4.1: HYPSOS working principle. The two projected slits are rotated by 90° before being elaborated by the same spectrometer.

In this way the spectra from the two channels appear on the detector in two adjacent zones avoiding overlaps. Figure 4.2) shows how the focal plane has been designed, with the two spectra embedded in a larger detector array. The central black dead band is helpful to separate the two channels and is due to a physical septum between the two slits, as will be explained in the following pages. This situation, anyway, is not representative of the laboratory implementation of the instrument. In fact, in laboratory the channels are operative one by one and therefore only a single portion of the focal plane is considered; the full frame image will be resized considering a proper region of interest. However, the not illuminated portion of the detector can be used to extract useful information (such as the background level) contextually to the science acquisitions.

The instrument has been designed having in mind its application to the exploration of the Solar System. Although the spectral range of the laboratory prototype includes

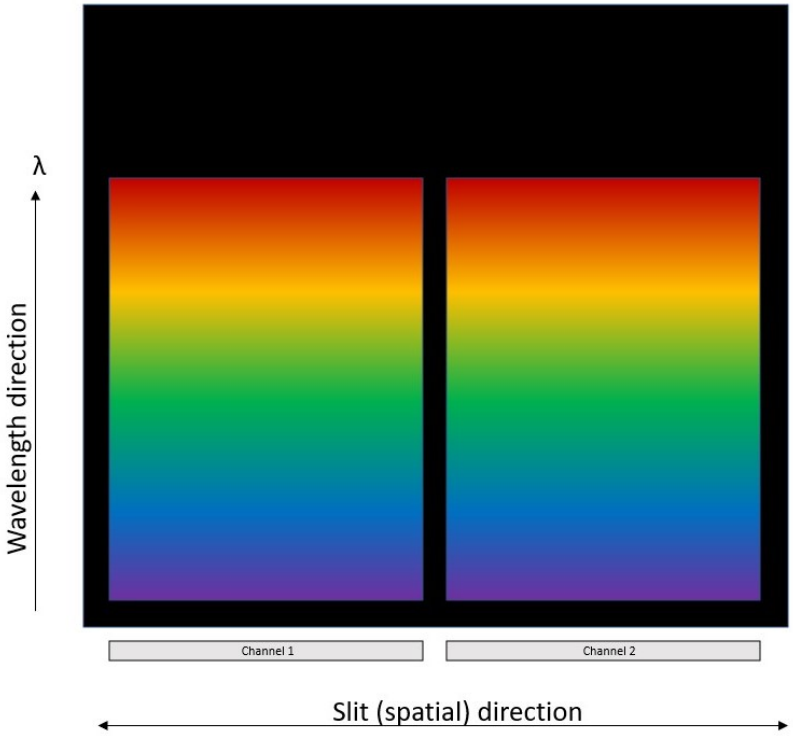

Figure 4.2: Focal plane concept of HYPSOS. Each slit is projected on the focal plane in a separated region of the detector to avoid information mixing.

only the visible part of the spectrum, it could potentially be extended from ultraviolet to mid-infrared without major modifications. The telescope is all reflective and the system can host two spectrometers, each one singularly optimized for a specific spectral range (Naletto et al. 2022), replacing the folding mirror after the telescope with a dichroic. At the same time the rotating device should also be carefully selected according to the application.

The main objective of HYPSOS is to surpass the problems related to the data fusion elaboration currently required to obtain an information which has simultaneously tridimensional (Digital Terrain Model) and spectral characteristics; in fact, different instruments have different pixel size, coverage, calibration and so on, making the generation of this data a very complex task (Naletto et al. 2021).

4.3 Instrument description

In this section the optical design of the instrument is presented. The original optical design was made by EIE Group, but during the development of the project, it underwent some optimizations. It should be highlighted that the development has been influenced by several aspects related to the available COTS (Commercial Off-The-Shelf) components

(e.g. cost, mechanical envelope, etc.), which have been included into the design (the detector and the diffraction grating).

The instrument could be thought of as composed of three main functional sections: the foreoptics, the telescope and the spectrometer (Figure 4.3).

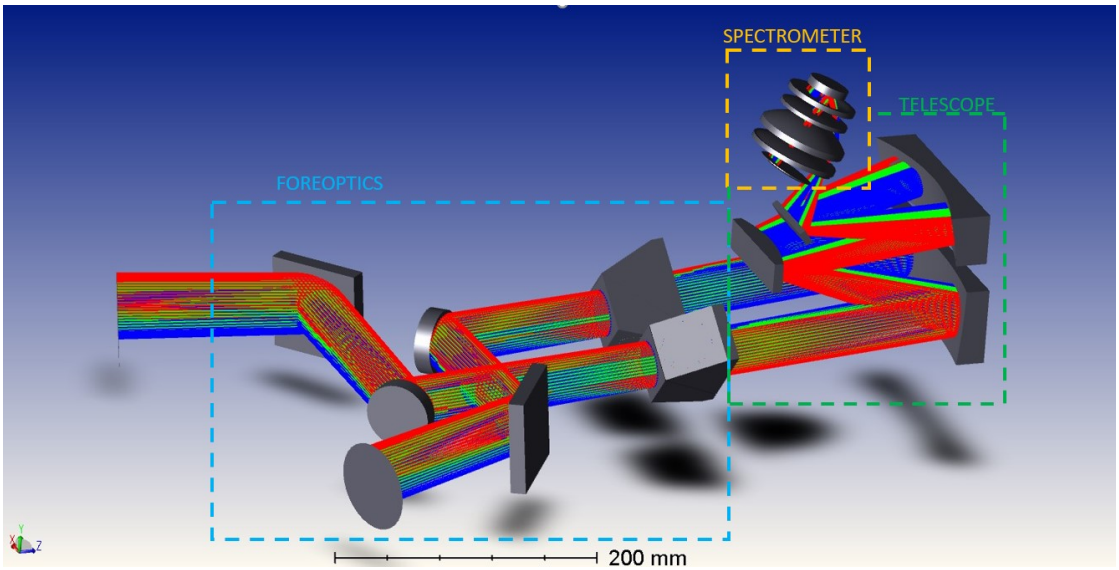

Figure 4.3: HYPSOS optical design. The light blue box shows the foreoptics, the green box shows the telescope and the yellow box the spectrometer. The foreoptics shown here are those foreseen in the original version of the prototype design, currently a different implementation is used (see Section 5.2).

The foreoptics carry out two main functions: folding the paths towards the desired direction (defining the stereo angle) and rotating the field. The first function has been originally assigned to a couple of plane folding mirrors (for each channel, light blue box in Figure 4.3). In a flight model of the instrument, they are required to exploit the stereo angle, because the two channels are identical and work with near-normal rays. The FOV, usually defined in the entrance pupil reference frame, is asymmetric with the extremes fields at 0.125° and 1.8° with respect to the normal of the pupil, in the yz plane. However, for laboratory implementation, the stereo angle selection is performed in a different way and the folding mirrors are used to select the specific channel (see Section 5.2). The second task is exploited with a couple of Pechan prisms mounted in a dedicated 3D-printed custom housing (Figure 4.4).

A Pechan prism is an optical element able to perform a field rotation of a magnitude twice the angle it is rotated. In particular, considering only angular deviations, it behaves like a mirror in one direction and like a thick window in the other direction (Sullivan 1972). Figure 4.4 (top right) shows the field rotation. The prisms (inside their custom supports) are illuminated by a horizontal slit (visible on the 3D-printed structure between the channels) and the output is a vertical one (visible after the left prism).

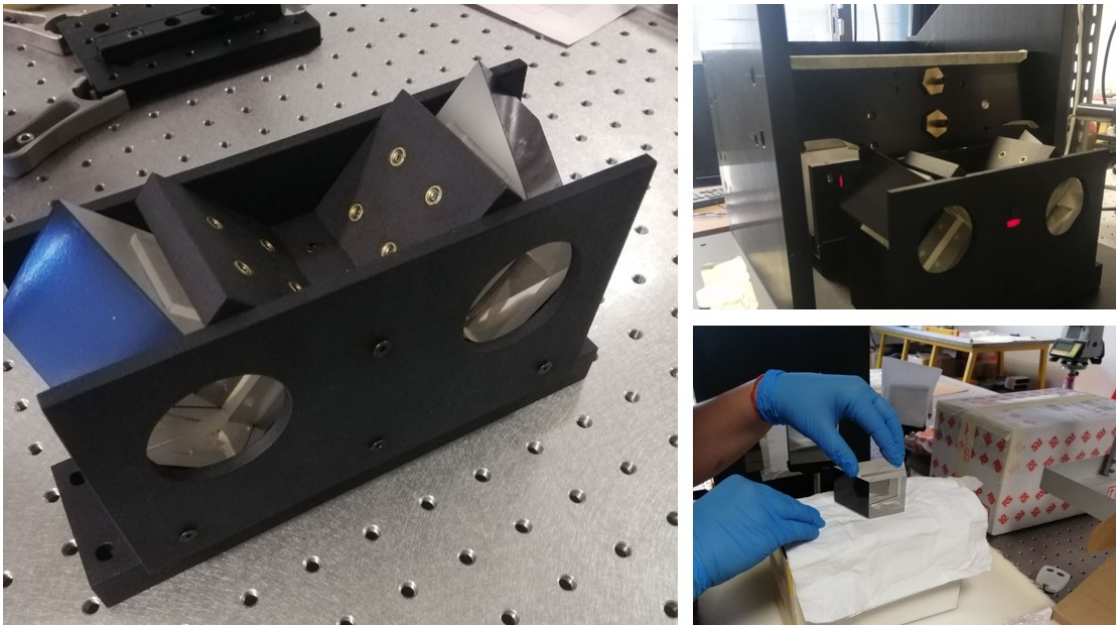

Figure 4.4: HYPSOS pechan prisms and their housing.

The prisms are mounted at ±45° with respect to the symmetry plane dividing the two channels; in this way the rays arriving with the same angles on the prism are directed at ±90° on the telescope depending on the channel. Figure 4.5 better explains the mechanism. The rightmost image of Figure 4.5 shows the footprint on the telescope focal plane for 0°(blue), 1°(green) and 1.875°(red). The same convention is used in the other images of the same Figure. The central rays (in blue), for both the channels, are overlapped because the prisms do not change the angular direction of an axis ray. The axial rays from both the channels are considered, by the telescope, to be part of the same collimated beam and therefore on the focal plane they share the same position.

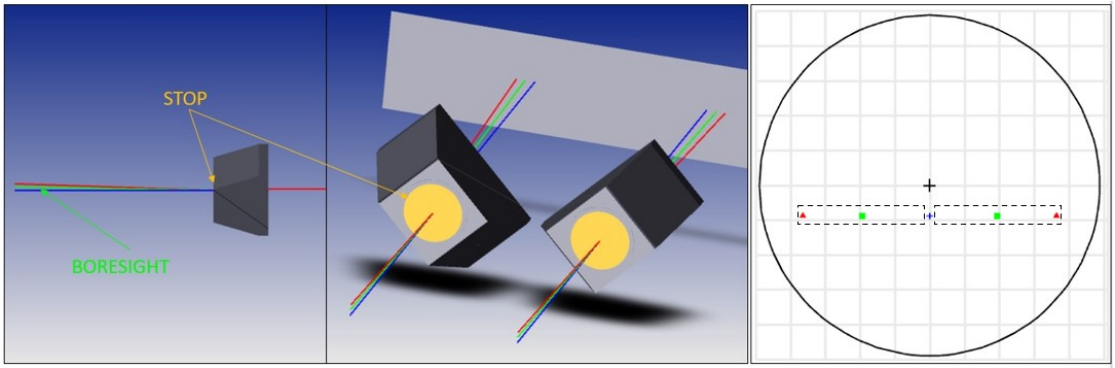

Figure 4.5: Working principle of how the pechan prisms are used on HYPSOS.

The Aperture stop of the system is in front of the Pechan prism and, having no optical

elements with power behind, it is also the entrance pupil of the system. Due to the fact that the 0° generates two overlapping spots, this can not be included in the FOV of the instrument, which is therefore asymmetrical with respect to the entrance pupil normal.

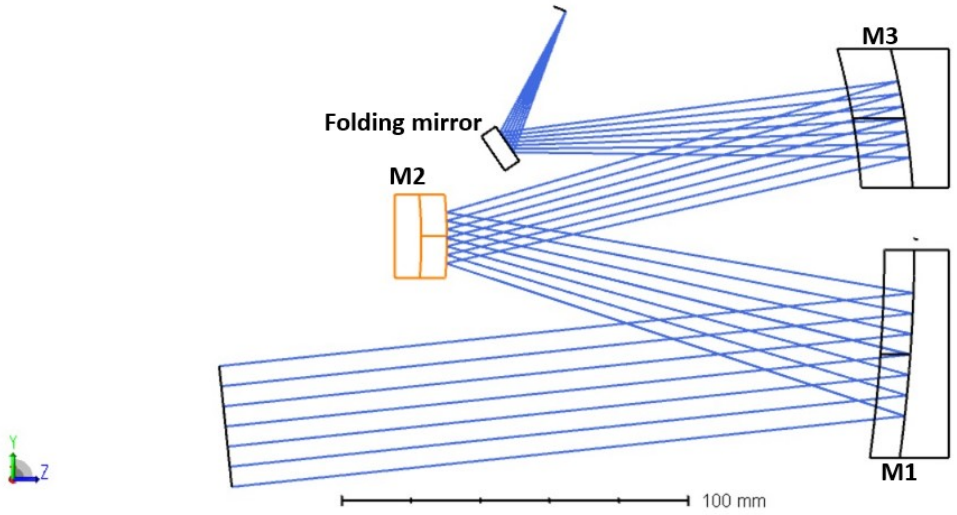

Figure 4.6: HYPSOS Three Mirrors Anastigmat telescope.

HYPSOS features a Three Mirror Anastigmat (TMA) telescope (Figure 4.6), in a configuration which is field-biased and pupil-decentered. The main optical parameters of the mirrors are summarized in Table 4.1.

TMA prescriptions			
Mirror	Curvature radius	K (Conic constant)	Notes
M1	467 mm	-1.474	Concave hyperbolic
M2	141 mm	0	Convex Spherical
M3	225 mm	0.198	Concave oblate ellipsoid

Table 4.1: Mirrors parameters

The field (along track) enters 6°with respect to the optical axis. TMA telescopes are powerful tools for astronomical purposes. Two-mirrors-based telescopes, in fact, can correct only two aberrations, TMA instead have enough degrees of freedom to correct spherical, astigmatism, coma and field curvature (Korsch 1977). The three mirrors share the same optical axis, their centers of curvature all lie on the same line, with M1 and M3 sharing also the same vertex. The optical axis of the telescope assembly could be then considered aligned with the z-direction of Figure 4.6. The optical parameters of the TMA could be resumed in a focal length of 244.5 mm and an entrance aperture diameter of 35 mm.

From a mechanical point of view, the mirrors are located into dedicated aluminium cradles specifically developed for this project (Faccioni 2020), black anodized to reduce possible straylight. Figure 4.7 shows M2 cradle with its mask fastened on it and the springs (4.7a).

(a) (b)

Figure 4.7: a: M2 cradle, with its mask fastened. It is possible to see the springs inside. b: Masks for the three mirrors

The springs are used to keep the mirrors in their nominal position opposing headless screws along the directions parallel to the mirror rear plane and the masks along the direction parallel to the mirror optical axis. This system is used also for fine regulation of the mirror position inside the cradle. The masks (Figure 4.7b) aim to keep the mirrors fixed inside their support, to separate the channels and to limit the mirror aperture for straylight control. The masks have two clear apertures for the channels and a central aperture for alignment purposes (see Section 5.4). The masks are 3D-printed with Selective Laser Sintering (SLS) technique using black loaded nylon.

After M3, the beams are folded toward the spectrometer by means of a plane mirror glued on a 3D-printed support made in the same way as the mirror masks. As previously said, to extend the spectral range of the instrument it is possible to replace this component with a dichroic.

The field stop of the system is the slit located on the telescope focal plane. The slit is realized by CNR-IFN of Rome with a technology already used for the shuttering system of ELENA on board BepiColombo (Naletto et al. 2021, Mattioli et al. 2011). The slit is realized starting from a sandwich of $Si_3N_4 - Si - Si_3N_4$ which undergoes electron beam lithography, dry reactive ion etching and then a KOH (potassium hydroxide) solution to remove the silicon wafer, etching the <1 0 0> planes and leaving the <1 1 1> planes (54.74° with respect to the wafer surface) (Mattioli et al. 2011).

The CNR provided three groups of slits: nominal slits, calibration pinholes slits and

dummy slits (Figure 4.8a).

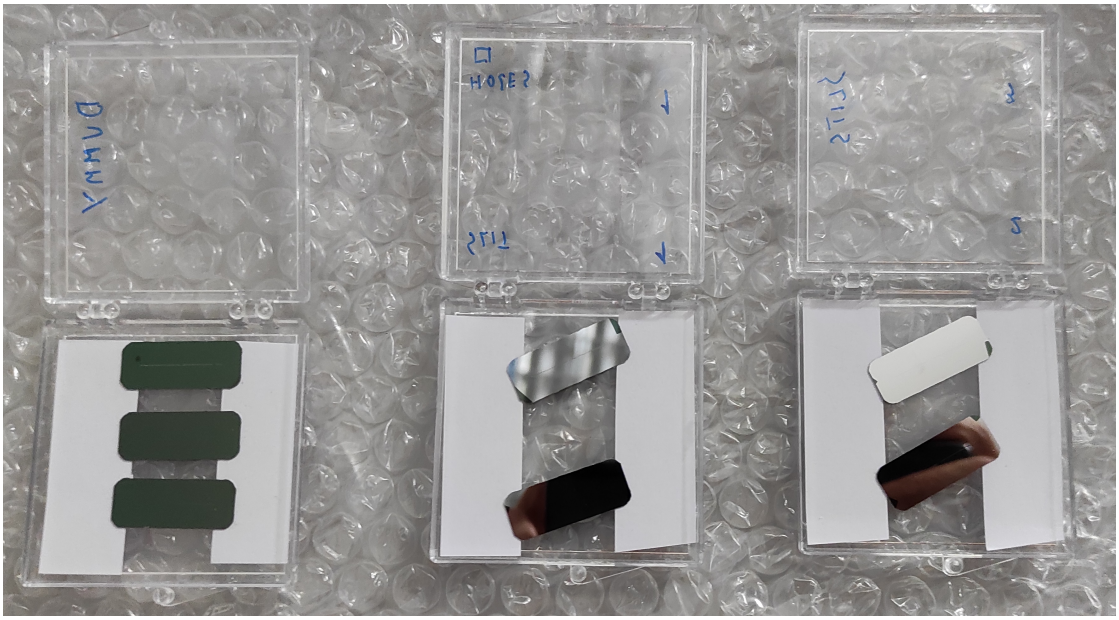

(a)

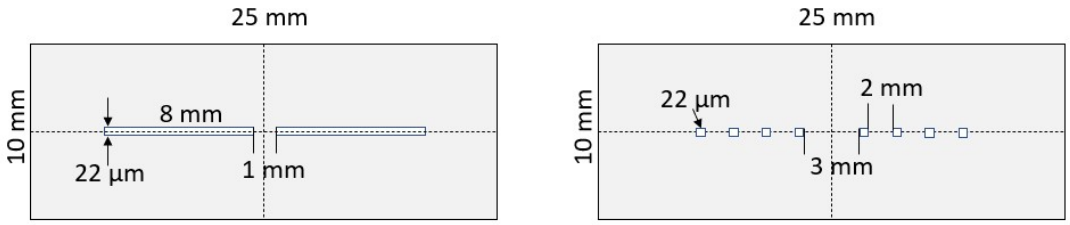

(b)

Figure 4.8: a: Nanotechnology engineered slits for HYPSOS. b: sketch of the slits shape and dimensions.

Figure 4.8b shows a sketch of the shapes and dimensions of the slits. The slit has a nominal width of 22 μm and it is 17 mm long, 8 mm each channel and 1 mm of separation between the slit sub-apertures. In fact, as previously mentioned the 0°angle is not part of the FOV and this septum helps to keep the channels separated. The calibration pinholes slit has four square slits per sub-aperture and has been designed to perform a calibration of the spectrometer distortion and to define the effective spatial resolution of the complete system.

The telescope is coupled to the spectrometer through the slit. The spectrometer is composed of four spherical lenses (Table 4.2) and a concave spherical diffraction grating in a Dyson-like configuration (Figure 4.9a) (nominally about 1:1 magnification). The spectrometer is rotationally symmetric and all the elements are assembled in a cylindrical

aluminium tube internally machined to create the compartments for the lenses. The interface between the metal structure and the glass is realized through O-rings, allowing small differential movements without cracking the glass and helping to maintain the element centering.

Spectrometer prescriptions

Lens	R1	R2	Thickness	Material
L1	84.18 mm	∞	10.5 mm	N-SK5
L2	50.78 mm	∞	19 mm	N-BK7
L3	91.84 mm	∞	7.4 mm	N-BK7
L4	104.4 mm	64.8 mm	3.2 mm	N-BK7

Table 4.2: Lens parameters. R1 and R2 are the curvature radius of the surfaces.

The spectrometer assembly also hosts a couple of annular components with solid circular segments which work spacers as zero-order light trap. Figure 4.9b shows a Zemax (non-sequential) simulation of the effect of the light-trap on the diffraction grating zero-order.

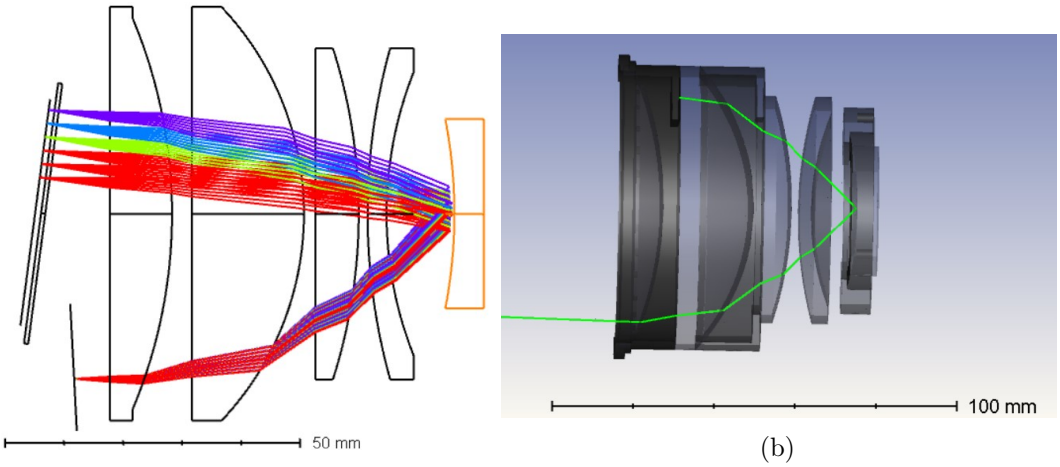

(a) (b)

Figure 4.9: a: optical design of the HYPSOS spectrometer. From left to right: L1, L2, L3, L4 and the concave diffraction grating (in orange). The detector surface is not in scale. b: simulation of the zero-order light trap

The selected diffraction grating is a holographic concave diffraction grating from Richardson Gratings[1]. The main parameters are summarized in Table 4.3. Its selection has been made on the basis of a preliminary version of the optical design, followed by

[1] https://www.gratinglab.com/Products/Product_Tables/Efficiency/Efficiency.aspx?catalog=52088BK-*-257C

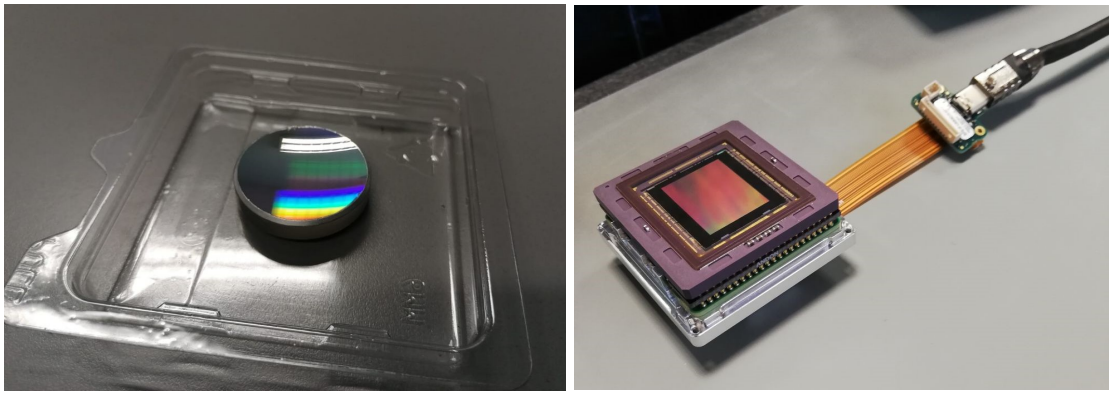

(a) (b)

Figure 4.10: a: HYPSOS diffraction grating. b: HYPSOS detector

research of the commercially available (COTS (Commercial Off-The-Shelf)) diffraction gratings. The optical design has then been re-optimized including the selected grating.

Diffraction grating prescriptions	
Type	Concave for Rowland circle
Producer	Richardson Gratings
Technology	Holographic
Groove density	678 grooves/mm
Radius	83.7 mm
Ruled area	$32mm(\Phi)$
Substrate shape	spherical
Substrate material	BK7
Coating	Al+MgF_2

Table 4.3: Diffraction grating parameters

Detector prescriptions	
Image sensor	Sony IMX342
Pixel Pitch	$3.45\mu m$
Image size	6480x4856 pixels (full frame)
Frame rate	12 fps (streaming)/14.4 (burst) @ full frame
ADC	12 bit
Communication protocol	USB3
Output	Mono8, Mono12 (2 byte), Mono12p

Table 4.4: Detector parameters

The selected detector for the HYPSOS experiment is the MatrixVision BF3-5-0315ZG (Figure 4.10b). The main drivers for its selection were a very large active area, an easy-to-handle communication protocol, a board-level housing and relatively compact mechanical envelope. This results in a CMOS-based camera with an active area of 22.36 x 16.75 mm^2 (6480x4856 pixels) with USB3 communication protocol. The CMOS image sensor is the Sony Pregius IMX342. The sensor can acquire the whole image coming from the optical system and transmit it to the working station without external interfaces (such a frame grabber). The image can be stored in raw format, maintaining the information from the 12-bit ADC either as 2-byte data per pixel or as a bit stream to reduce the data rate. The detector also has different features useful for data volume reduction (Region of Interest and binning). Detector main features are summarized in Table 4.4.

4.4 Channel Crosstalk

In this section the HYPSOS channel crosstalk is described, that is an effect which is intrinsically related to the working principle of the instrument and can be observed directly in Figure 4.11.

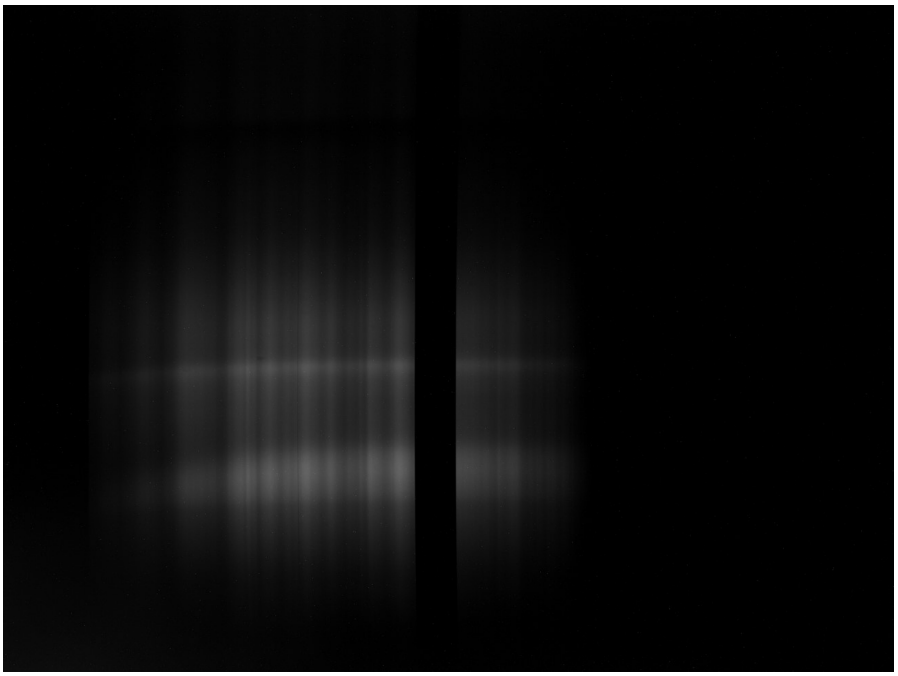

Figure 4.11: Channel crosstalk. Spectrum of concrete. Image reconstructed after pushbroom scanning

Figure 4.11 shows an uncalibrated acquisition of a target (concrete) with one channel of the instrument. A block of concrete has been located on the focal plane of a collimator placed before the HYPSOS telescope to simulate a source at infinity. The same principle

is used also in the experimental setup (as described in Section 5.2). It is possible to see the central dead band due to the septum on the slit separating two zones with spectra. Although similar to Figure 4.2, here, only a single channel is operating and therefore the effective target image is located only on the left side of the dead band. The right side image is also a real spectral image but it is not part of the nominal FOV of the instrument (and it is located in a portion of the detector which is instead dedicated to the other channel).

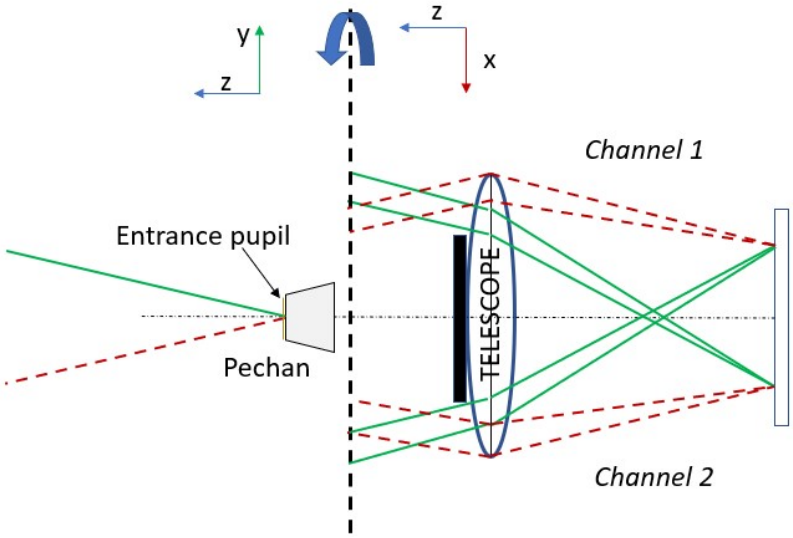

Figure 4.12: Toy model of HYPSOS. The black vertical dotted line indicates that on the left we are observing the system from a lateral point of view (yz plane) and on the right the same system but from above (xz plane). This expedient is used to visualize the effect of the field rotation produced by the prism. The pechan in the image is "symbolic", and it should be considered rotated around the z-axis depending on the specific channel. The black rectangle indicates the masks and the separation between the two channels. The TMA is represented by a lens. Lines with the same colours and style are part of the same beam

Figure 4.12 shows a toy model of HYPSOS, and is helpful to understand how the right-side image of Figure 4.11 is generated (the reader is referred to the caption for an explanation on how the image should be read). Looking at the toy model, rays entering with a given θ angle with respect to the normal (z-axis) of entrance pupil in the yz plane, comes out in the xz plane with a $\pm\theta$ angle with respect to z-axis depending on how the prism is oriented in the channel.

In this way the telescope projects rays from the same directions but collected by the two channels in two different locations. Since we did not foresee along the telescope optical path any physical separation between the two channels (as already mentioned, it is not really necessary, since this lab prototype operates one channel at the time), out-of-field light entering one channel reaches the telescope focal plane and illuminates

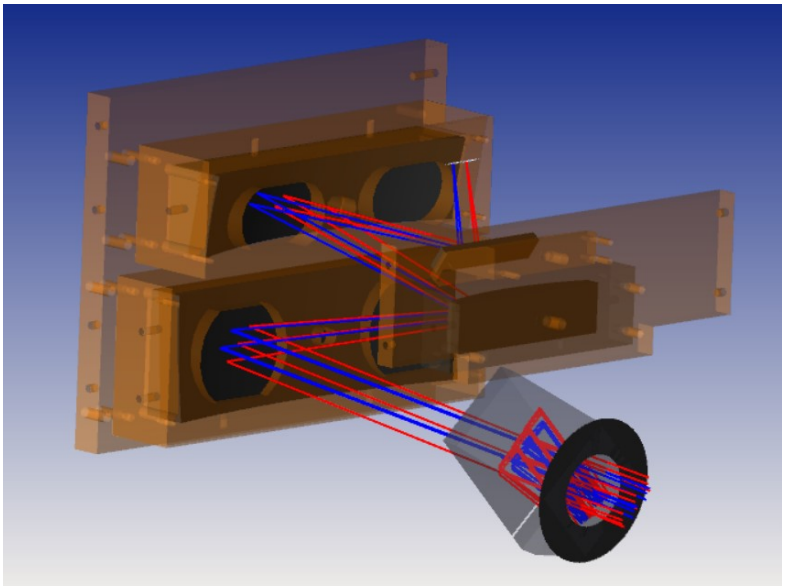

Figure 4.13: Non-sequential simulation with Zemax of the HYPSOS TMA with the masks imported from CAD. Only one channel is operating. The blue rays are part of the nominal FOV, the red rays coming from the opposite angles are not blocked and generate a crosstalk on the other channel

also the entrance slit aperture of the other channel. The effect is an overlap of two different portions of the FOV in the same focal plane location, with the result of an information mixing. For this reason, we called it Channel Crosstalk.

The masks alone are not sufficient to reduce this effect. To better visualize that, a non-sequential simulation in Zemax has been realized (useful also for possible preliminary straylight analysis) to highlight how the masks behave with respect to the crosstalk. Figure 4.13 shows a simulation performed in non-sequential propagation of Zemax; the masks (along with the structure) are imported from the CAD model of the instrument and for simplicity are considered made by absorbing material. The focal plane has been simulated considering two rectangular detectors separated by 1 mm (to simulate the septum). The blue rays belong to the nominal boresight angle of the channel, the red ones, instead, from the opposite angle with respect to the entrance pupil. The clear apertures on the masks are too large to block all the rays. However, this is not an issue for the laboratory prototype. In fact, the channels are operated separately, and the solution stands in considering only the portion of image related to the nominal FOV. Moreover, a windowing is in any case foreseen to reduce the data volume. This effect has definitely been considered for a potential flight model, in which case a suitable baffling system has to be designed. A possible solution to mitigate the crosstalk, would be to locate an absorption stop with a size of 12.3 mm over the folding mirror. To better understand how this stop could work, let's consider Figure 4.14a. The top side of the image shows the footprint coloured by FOV for both the channels and the bottom image the same

FOV but coloured for channel. The three external FoVs provide the whole extension of the channel FoV, so it is evident that the crosstalk happens in the middle of the folding mirror.

Let's consider, for example, the channel one (in blue). The angle -0.125° (blue in the top image) is one extreme of the nominal FoV (moving towards the external side of the mirror). The footprint is almost tangent to the footprint of +1.8° (crosstalk angle) coming from the opposite channel. The same crosstalk angle has been simulated in non-sequential (Figure 4.14b) without considering the obscuration on the folding mirror. The internal side of the M3 mask blocks the rays when the angles are approximately higher than +1.8° , the obscuration on the folding mirror removes the angles from about 0°to about +1.8° in a synergistic way. The septum contributes to this baffling system and could be used to correctly select the size of the obscuration to avoid vignetting of the -0.125° FOV.

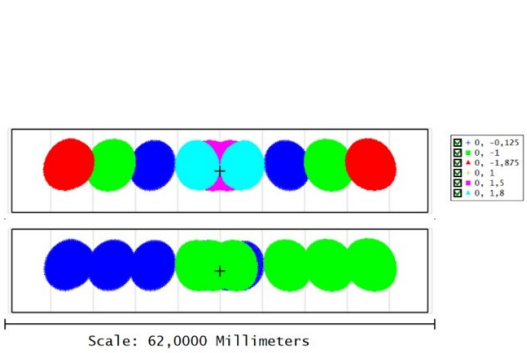

(a)

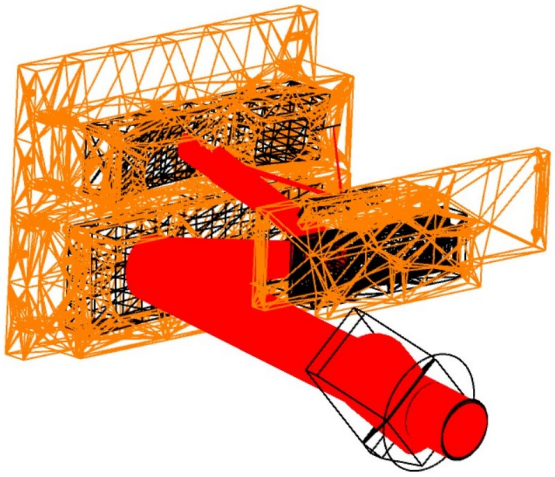

(b)

Figure 4.14: a: Footprints on folding mirrors at various angles. *top*: colour according to field; *bottom*: colour according to channel. b: Non-sequential simulation of +1.8° for the left channel. The larger part of the beam is blocked by the M3 mask. The folding mirror is not centrally obscured.

This analysis is only qualitative and an extensive one is however required. It shows that a possible effective solution resides in a trading-off between the size of the clear aperture on the M3 mask and an obscuration on the folding mirror. However, this is probably not sufficient for the definitive solution of the problem and probably a septum between the two channels is required coupled with a suitable external baffle.

Chapter 5

Setup

5.1 Introduction

In this section the setup prepared in laboratory, on the optical bench for the HYPSOS experiment is described; the objective is to evaluate the capability of the instrument to generate stereo hyperspectral data.

A design driver for the setup development is to provide, as much as possible, an equivalence between the laboratory condition and an in flight.

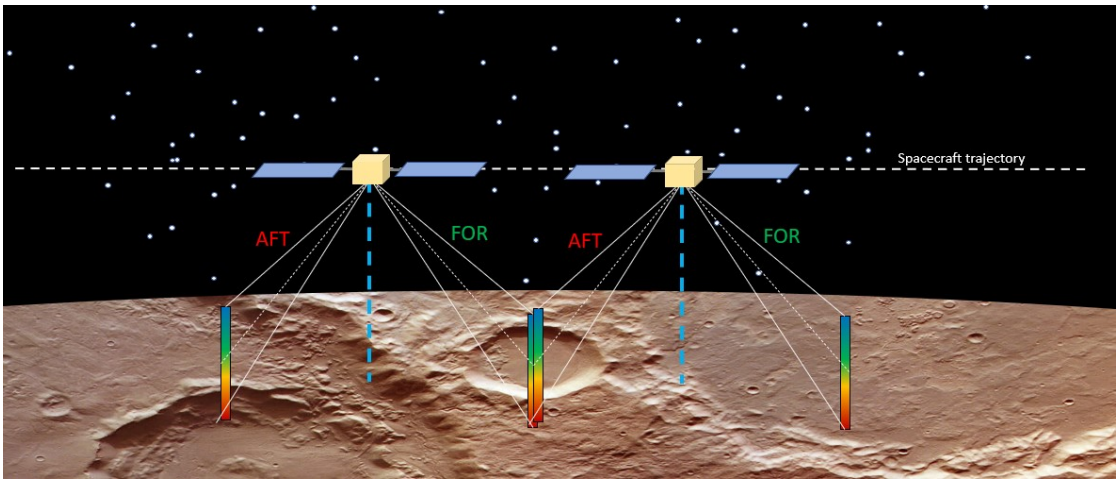

Figure 5.1: Pictorial view of a stereo couple acquisition with HYPSOS in orbit around a planet. The spacecraft moves along the trajectory and the two channels can acquire the same surface portion with different angles. Image credits (original image of Mars): ESA/DLR/FU Berlin

As described in Chapter 4, the stereo camera concept of HYPSOS is inherited from STC/SIMBIO-SYS. STC (and also HYPSOS) generates a stereo couple following the motion of the spacecraft with respect to the surface (see Figure 5.1). The first image is acquired by the forward channel (hereafter *FOR*) and, after a certain amount of time

(depending from orbit, FOV, stereo angle), the backward channel (hereafter *AFT*) acquires the same portion of surface with the opposite angle with respect to nadir. The main difference, in this context, between the two instruments, is how the images are acquired: *push-frame* (STC) and *push-broom*(HYPSOS). STC, in fact, acquires 2D images with each channel; HYPSOS, instead, being a pushbroom (slit) imaging spectrometer, acquires only the portion of surface corresponding to the ground projection of the slit. The 2D images are generated mosaicking several lines.

The setup, therefore, should simulate the fundamental aspects of the instrument and provide to the user a proper stereo couple both for calibration (Re et al. 2022) and for scientific purposes. Then, the acquired data will be used to generate a spectral digital terrain model using an *ad hoc* pipeline derived from 3DPD, a photogrammetric pipeline developed for CaSSIS on board ExoMars TGO (Simioni et al. 2021, Naletto et al. 2021).

5.2 Optomechanical design

The optomechanical setup used for the HYPSOS optical characterization (hereafter named as Stereo Validation Setup or SVS) is a natural evolution of the setup developed for the validation of the stereo capability of STC/SIMBIO-SYS (Naletto et al. 2012,Simioni et al. 2017). Table 5.1 summarizes the main objectives together with the adopted solutions the setup should achieve for the experiment.

Stereo Validation Setup main objectives	
Goal	**Implemented solution**
Source at infinity	Collimator
Stereo observation	rotation stage for target
pushbroom observation	linear stage for target

Table 5.1: Main objectives of the laboratory setup for the HYPSOS experiment along with the adopted solutions.

The first two objectives have already been resolved by the SVS-STC and we maintain the same logical structure for the SVS-HYPSOS. A source at the focal plane of an achromatic doublet (hereafter the *Collimator*) allows to *convert* the finite distance of source on the optical bench into an infinite distance. The stereo observation is simulated by rotating the target by means of a high-precision rotation stage. The fundamental improvement of the SVS-HYPSOS with respect to SVS-STC is the presence of a linear stage between the rotation stage and the target plate (see Figure 5.2). The central hole of the target plate is assumed as a reference point and should correspond to the collimator focal plane.

The Target plate is fastened on the linear stage platform by means of five M6 screws and is moved along the tilted direction to simulate the pushbroom acquisition. The central screw corresponds to the rotation axis of the rotation stage. Calibrated shims are

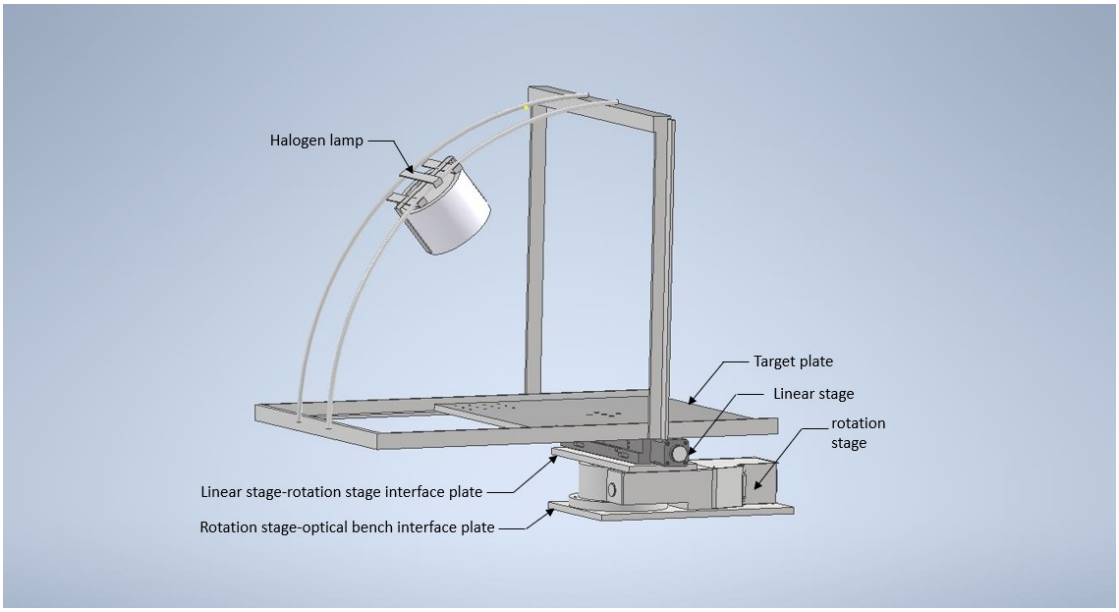

Figure 5.2: Stereo Validation Setup for HYPSOS. A motorized linear stage is used to simulate the pushbroom acquisition mode

inserted in between the linear stage platform and the target plate to avoid mechanical interference with the mechanical structure of the linear stage itself. Since HYPSOS works in pushbroom mode the only zone which is effectively required to be in focus is the rotation stage axis; if this condition is satisfied, when the linear stage moves the Target, the zone related to the rotation axis becomes the observed (and in focus) surface.

Figure 5.3 shows a conceptual schematic of how the optomechanical setup is organized. The upper side of the Figure shows the channel *FOR* of the instrument, the bottom side the channel *AFT*. They share a large part of the setup components, including the collimator and the SVS, reducing the errors induced by assembly and alignment of duplicated elements. With respect to the design proposed in Naletto et al. 2021, the method used to select the instrument channel has been modified. Originally, the whole instrument should have rotated around a carefully selected pivot axis, but then it has been decided to use a simpler three plane mirror system (see Figure 5.3). The main concern is the stability of the optics under a movement of the structure. In fact, during the alignment of the telescope, we tried to rotate the instrument, but it seemed to generate a slight misalignment. We verified the positions on the focal plane of fixed laser rays before and after the movement. Considering that the telescope alignment is a delicate procedure we decided to move towards a more conservative approach. The mirror closer to the collimator can be moved using a linear stage to select one channel or the other. Two nominal positions have been defined for the platform: *home* and 90 mm. The linear stage platform is moved by a step motor driver, in turn commanded by a microcontroller (Arduino Uno). The circuit and control software have been developed in laboratory.

We verified the repeatability using HYPSOS itself. A laser beam has been sent in the instrument using the mirror on the platform and the linear stage commanded in the two nominal positions to select the channel multiple times. Every time, the centroid position has been determined with a 2D gaussian fit and its evolution monitored.

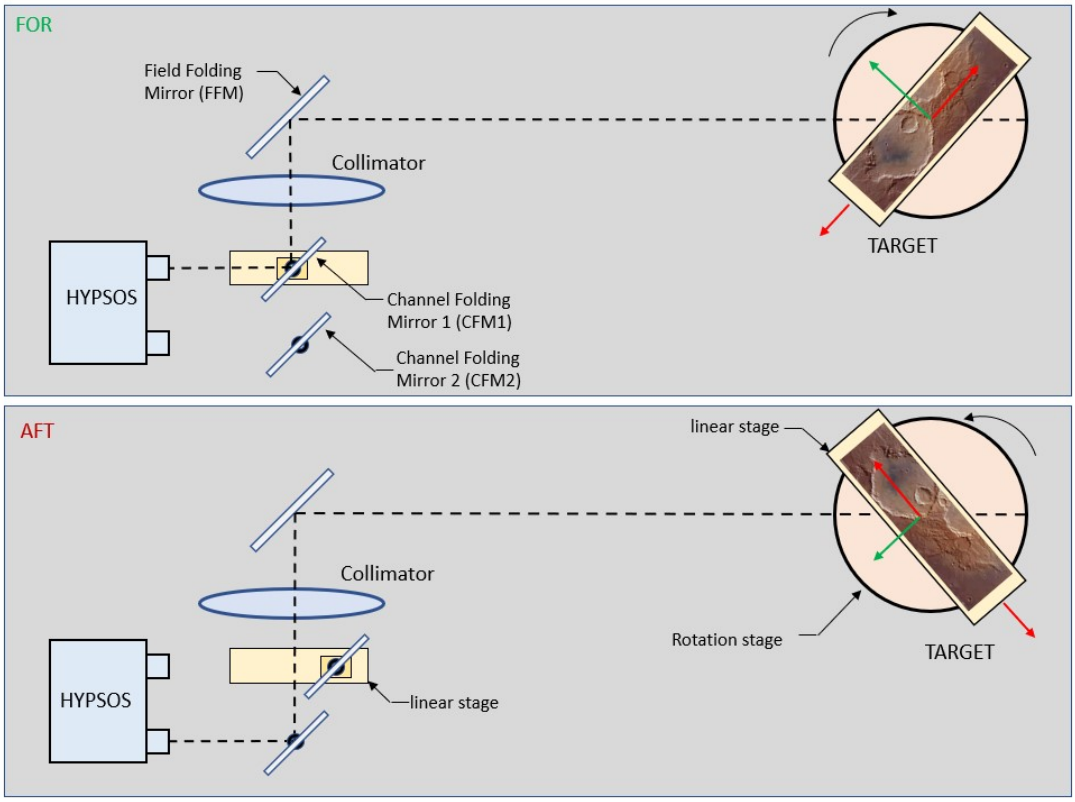

Figure 5.3: Sketch of the setup. All the main optomechanical components are shown. *Top*: Fore channel. *Bottom*: Aft channel. For each channel is displayed also how the rotation should be performed. The red arrow departing from the target linear stage indicates the direction of the translation movement to be consistent with the in-orbit analogue.

Another benefit is the easier foreoptics alignment with respect to the original design, where each channel had a couple of folding mirrors, and one of them with 55° angle of incidence. A drawback of the current configuration is a partial loss of the symmetry between the two channels. In fact, due to different optical paths, for object angles different from the axial one (of the collimator), the wavefront entering in one channel has explored different zones of the collimator with respect to the other one. For HYPSOS, this is the nominal situation because, for simplicity, the collimator is aligned with the instrument entrance pupil normal and (as explained in Section 4.3) the instrument FOV is asymmetric.

5.2.1 Optical element constraints

The optical elements of the setup should be located not to disturb the nominal operation of the instrument. This means that the entrance pupil of each channel should be overfilled for every angle of the nominal FOV of the instrument. The only true constraint on the optical components position (considering the dimensions in Table 5.2) is the distance between the collimator and instrument entrance pupil. For HYPSOS, the entrance pupil is located in front of the pechan prism.

Setup Optical elements			
Element	**Focal length**	**Dimensions**	**Notes**
Collimator	1010 mm	80 mm (diameter)	Achromatic doublet
CFM (1 & 2)	N/A	75 mm x 75 mm	Plane mirror
FFM	N/A	83 mm x 110 mm	Plane mirror

Table 5.2: Optomechanical parameters of the optical elements of the setup. CFM means Channel Folding Mirror, FFM is the Field Folding Mirror, according to Figure 5.3

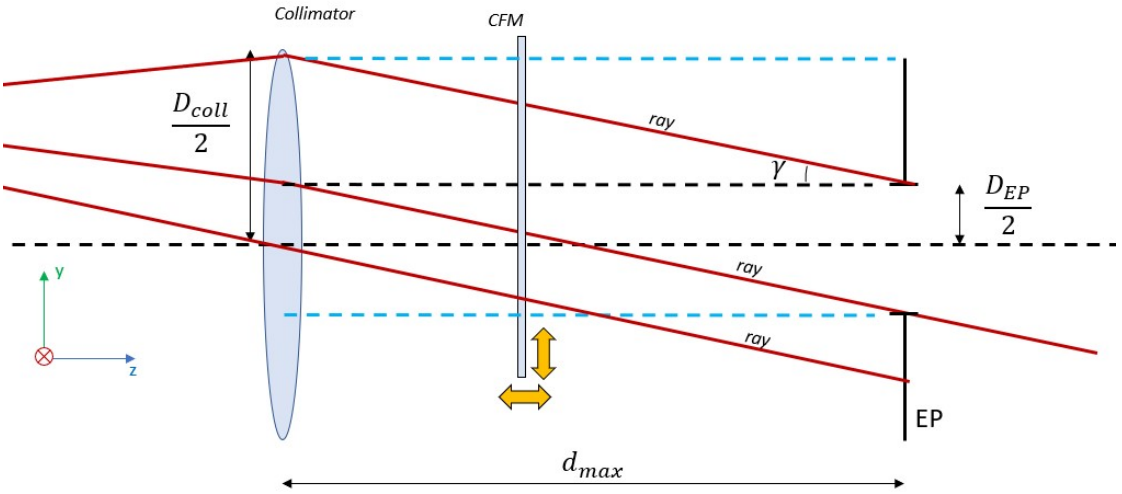

Figure 5.4: Sketch showing the collimator-instrument entrance pupil coupling. EP stands for Entrance Pupil, CFM for Channel Folding Mirror. The yellow arrows show the possible movements of the CFM with respect to the optical path.

Figure 5.4 shows that there is a maximum distance beyond which the entrance pupil (EP) is not completely overfilled and, as a first approximation, it is provided by the equation:

$$d_{max} = \frac{D_{coll} - D_{EP}}{2tan(\gamma)} \tag{5.1}$$

This distance does not depend on the properties of the collimator but only by its size. Considering 80 mm of the collimator diameter, 35 mm of HYPSOS entrance pupil and $\gamma = 2°$, d_{max} is 644 mm. The angle γ corresponds conservatively to the maximum (non-symmetric) FOV of HYPSOS. A folding mirror is inserted in between the collimator and the entrance pupil (indicated in Figure 5.4 as CFM). The position has no particular constraints because, due to the asymmetry of the FOV, it can be decentered in y to cover all the fields. In fact, the maximum size in y direction of the beam is 57.5 mm (40 mm of collimator semi-diameter + 17.5 mm of EP semi-diameter) which is completely covered by the 75 mm of the CFM. In x direction the effective area of the mirror is 53 mm ($75 \cdot cos(45)$) which is larger than the light spot size in that direction (as a first approximation).

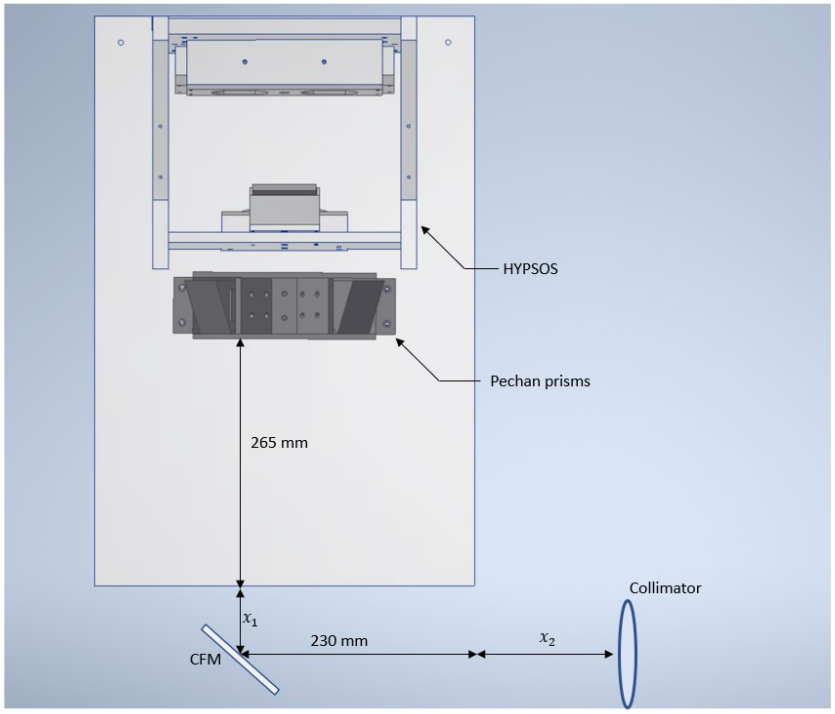

Figure 5.5: Sketch of the distances between optical elements under constraints

Figure also 5.5 shows the HYPSOS structure with its envelope (defined by the aluminium baseplate upon which the mechanical structure is fastened), a single CFM and the collimator. In this case the analysis is limited to the channel more distant from the collimator (CFM2); the other one CFM1) will have the requirements automatically respected.

The free parameters are x_1 and x_2 that can be set according to the relationship:

$$x_1 + x_2 + 495 < 644 \tag{5.2}$$

Similar assumptions could also be applied for the FFM. The length in y direction is 83 mm which is greater than the collimator diameter and the projection in x direction is 77.78 mm with respect to 35 mm of the spot (considering the dimension in x and y decoupled as a first approximation).

A first evaluation of the optimal position of the components and their constraint has been made directly on the optical bench. The second step has been a simulation on Zemax. We estimated, at the end of the assembly phase, that the instrument aluminium baseplate is rotated around the x-axis (see Figure 5.4 for reference frame) of about -0.106°. This rotation has been included in the Zemax model. This rotation has the favorable effect of rotating the boresight of the instrument towards the collimator optical axis.

Measured distances on optical bench	
x_1	110mm
x_2	-25mm

Table 5.3: Distances between optical elements (constrained by analysis) as measured on the optical bench. They refer to Figure 5.5. The negative sign of x_2 indicates that the collimator is more internal than the vertical limit of the instrument optical plate.

Table 5.3 shows the distances measured on the optical bench. The constraint is respected and we expect not to have a vignetting problem induced by the setup. This is also confirmed by the simulation (Figure 5.6).

To recap:

- the distance between collimator and target should be 1010 mm
- the distance between the HYPSOS pupil of AFT channel and the collimator should be at most 644 mm

5.3 Acquisition software

The setup has been conceived to simulate as much as possible the dynamical acquisition of a pushbroom mode instrument. Having in mind this goal, it is mandatory to have a dedicated software able to manage the whole acquisition session.

To generate a single *2D spatial image* a large number of snapshots must be acquired, because each snapshot contains an image of the slit (i.e., intrinsically just 1D spatial information). The size of the scan sets the dimension of the image in the along-track direction and it depends on several factors such as the type of acquisition (calibration gauge, stones) and density of features recognizable by the matching algorithm of the photogrammetric pipeline. On the target, the along-track pixel is about 90 μm on the target, considering a scan of 40 mm, this translates into 444 single snapshots for channel

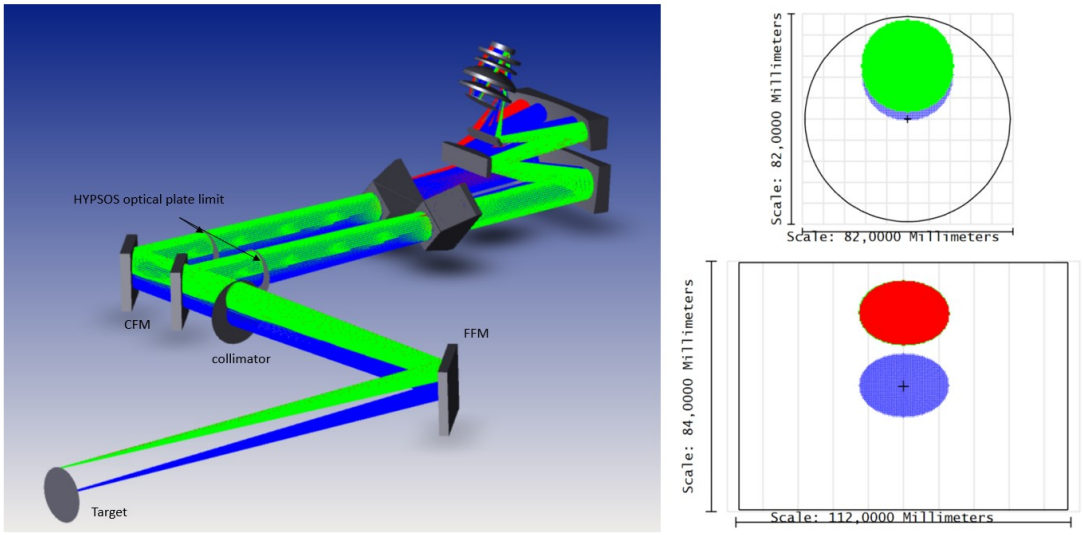

Figure 5.6: Simulation of the experimental setup. The stop is the effective HYPSOS aperture stop. *top right*: footprints on the collimator of 2° for both the channels *bottom right*: footprints on the FFM for on-axis field and 2°.

(thus 888 for stereo couple). An option is to use the graphical user interfaces (GUIs) provided for the hardware by the sellers to manually perform the acquisition previously described, but this mode is extremely prone to errors. and considered not feasible since its complexity. For these reasons, a software able to automate the acquisition process has been developed.

Figure 5.7 shows a sketch of the logical connections of the setup hardware. To manage the system three USB ports plus one USB3 port are required. The only hardware component which is not operated automatically is the halogen lamp. It is possible to include it in the setup after designing a power supply circuit able to dimmer the lamp. The actual power supply has (manual) dimmer capability and it has been decided to manually operate the lamp because typically it requires very low regulations.

The motorized stages in charge of target movement are singularly operated by their dedicated controller. The linear stage dedicated to the channel selection is instead controlled by circuit and software developed in laboratory (as already described in the previous sections).

All the components have Python libraries available in their SDK (*Software Development Kit*). Python has been selected as programming language due its flexibility and the very large community. This translates into a simpler code and to the possibility to find updated and supported libraries and to ease the debugging process.

The first step has been to develop a layer between the hardware (H/W) and a potential *main* code (hereafter in this section, the word *main* in italics is used as in programming to identify the principal code executing all the actions planned by the user). A set of four libraries plus a generic module have been developed:

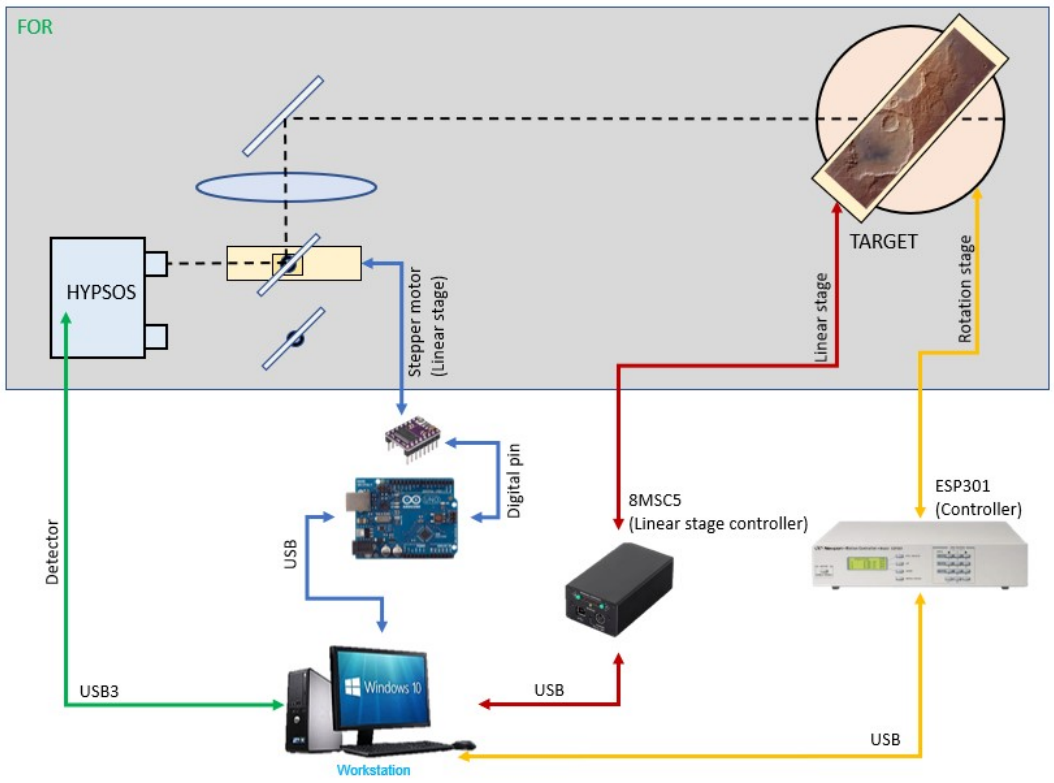

Figure 5.7: Sketch of setup logical connections

- HypsosRotatorsLibrary
- HypsosLinearStageLibrary
- HypsosDetectorLibrary
- HypsosChannelSelector
- HypsosModules

This modular concept of the software allows an easy-to-handle substitution of some components without the need to re-adapt the *main* code to the components. Instead, it is the component library which is *adapted* to the *main*. This allowed us, during the assembly campaign, to test specific aspects of the experiment at intermediate steps (see Section 5.3.1).

The libraries manage specific aspects of each H/W component allowing a more user-friendly communication with them. They manage possible exceptions and adapt the H/W to the requirements of the HYPSOS setup. For example, some functions have been made *blocking* to avoid sending multiple commands simultaneously generating harmful situations.

```python
from HypsosModules import *
import HypsosRotatorsLibrary
import HypsosLinearStageLibrary

AbsAngularPosition1 = 20
AbsAngularPosition2 = -20
AbsPosition = 40

EGSE = HypsosRotatorsLibrary.HypsosEGSE()                                   # EGSE class with common information

ESP301Device = HypsosRotatorsLibrary.HypsosRotatorsOPEN()                   # OPEN the communication with Rotator controller

device_id = HypsosLinearStageLibrary.HypsosLinearStageOPEN()                # OPEN the communication with linear stage controller
userunit = HypsosLinearStageLibrary.HypsosUserUnitdefine()                  # define conversion units between steps and mm

try:
    HypsosRotatorsLibrary.rotMotorOnOff('TARGET','ON',EGSE,ESP301Device)    #Power ON the motor on the selected rotator

    HypsosRotatorsLibrary.HypsosHomeRotator('TARGET',EGSE,ESP301Device)     # Commanding home procedure
    HypsosRotatorsLibrary.HypsosGoToRotator(AbsAngularPosition1,'TARGET',EGSE,ESP301Device)   # Go to AbsAngularPosition1 angle

    HypsosLinearStageLibrary.HypsosHomeLinStage(device_id)                  # Commanding home procedure
    HypsosLinearStageLibrary.HypsosGoToLinStage(AbsPosition,device_id,userunit)             # Move linear stage to AbsPosition (in mm)

    HypsosRotatorsLibrary.HypsosHomeRotator('TARGET',EGSE,ESP301Device)     # Commanding home procedure
    HypsosRotatorsLibrary.HypsosGoToRotator(AbsAngularPosition2,'TARGET',EGSE,ESP301Device)   # Go to AbsAngularPosition2 angle (test negative angles)

    HypsosLinearStageLibrary.HypsosHomeLinStage(device_id)                  # Commanding home procedure
    HypsosLinearStageLibrary.HypsosGoToLinStage(AbsPosition,device_id,userunit)             # Move linear stage to AbsPosition (in mm)

    HypsosRotatorsLibrary.HypsosHomeRotator('TARGET',EGSE,ESP301Device)     # Reset original position for both rotator and linear stage
    HypsosLinearStageLibrary.HypsosHomeLinStage(device_id)

    HypsosLinearStageLibrary.HypsosLinearStageCLOSE(device_id)              # CLOSE communication with linear stage controller
    HypsosRotatorsLibrary.HypsosRotatorsCLOSE(ESP301Device,EGSE)            # CLOSE communication with rotator controller

except:
    HypsosLinearStageLibrary.HypsosLinearStageCLOSE(device_id)              # CLOSE communication with linear stage controller
    HypsosRotatorsLibrary.HypsosRotatorsCLOSE(ESP301Device,EGSE)            # CLOSE communication with rotator controller
```

Figure 5.8: Script used in laboratory to test the libraries and. It shows the fundamental steps to operate the rotator and the linear stage of the target

Figure 5.8 shows a script used in laboratory to test the movement hardware (rotation and linear stages of the target) together. The script simulates the acquisition of a stereo couple (without the detector) and includes all the steps which must be included in the *main* to operate with the movement H/W: to open the communication with the hardware, to give current to the rotator motor, to perform home procedure, to go in specific positions (angular and linear) and to close the communication with the H/W at the end. Although it is a good practice to power off the rotator motor using the specific function (in the script this command is not sent to the rotator controller), the *close* function performs this task anyway after a check of the status of the motor (ON or OFF). The rotator functions require a keyword to address the right rotation axis (the possible choices are *TARGET* or *HYPSOS*). Originally, the setup controlled two rotation stages (the target and the instrument) and this structure has been maintained for legacy. Attention has been paid to name the functions to be as clear as possible describing the task they perform. The acquisition strategy consists in a rotation-translation-rotation-translation sequence which is required to acquire the target at two different perspectives. Before each movement, a home procedure is performed to minimize errors induced by relative movements in which the final error is the result of cumulative errors of each command. For the same reason, relative movements (if not unavoidable) are substituted by absolute movements after a home procedure. The home procedure uses a physical switch to identify the actual position of the platform. The knowledge of that specific position is much higher than the

others.

The module *HypsosModules* includes all the importing calls required to the other libraries to work. In this way all the modules are lighter, avoiding copying large sections of code more times.

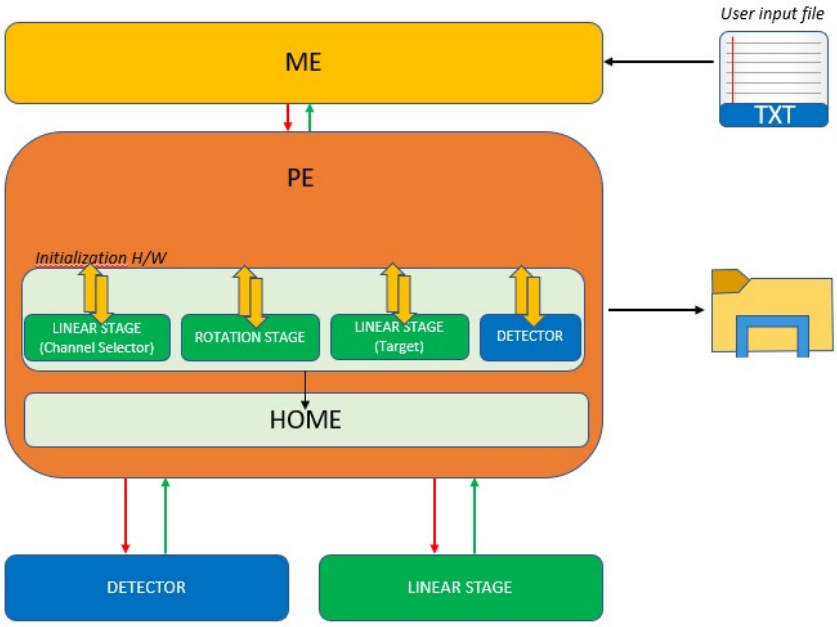

Figure 5.9: Logical blocks of the acquisition software.

Figure 5.9 shows the logical block diagram of the acquisition code. The Main Electronics (ME) block manages the interfaces between the user and the sub-systems. The user can customize the acquisition using a telecommand file which can be written with any text editor. The parameters are recognized by the software by means of specific keywords. The ME loads the file and launches the Proximity Electronics (PE) block. The PE executes all the tasks required for the acquisitions. It is possible to organize the sequence of executed tasks.

First, the code performs two *static* actions (it means that they do not require a synchronization between the components) : *InizializationH/W* and *HOME* (for all the movement stages). They are executed always before all other commands. The first command establishes the connections with all the hardware (movement stages and detector). From this moment the H/W is reachable by the software and the telecommands can be sent. In this phase also all the fixed parameters of the acquisition are loaded and set, such as integration time, detector ROI (region of interest), binning, linear stage velocity. The second command is a general *home* procedure. The movement stages are all sent to their home positions to increase the repeatability of the measurements. At this time the acquisition session could start. Currently, it includes both the channels, thus the sequence is:

- rotation θ
- channel FOR selection
- acquisition
- rotation $-\theta$
- channel AFT selection
- acquisition

Each aspect of the acquisition is managed and properly synchronized using a multi-threaded approach. To have a more accurate reproduction of the pushbroom operative working mode, the acquisition is not organized as a large sequence of (target) movement-then-snapshot but the frame rate is set in agreement with the speed of linear stage. The repetition time (the time interval between two successive acquisitions) is set equal to the dwell time (the time required to scan a single pixel). The frames are saved with a file structure including the binary data, the acquisition time stamp, and the channel name (FOR or AFT).

5.3.1 Preliminary test

The fine alignment phase of the telescope has been performed using a service camera located on the putative focal plane of the TMA. The camera has not been selected with specific performances but only according to the availability in laboratory (with the smallest pixel). The camera is a CMOS detector with 2048x2048 pixels with $5.5\mu m$ pixel pitch. Once the alignment of the TMA has been considered satisfactory, it has been decided to perform a specific test on the acquisition software and on the procedure developed for the stereo reconstruction (Re et al. 2022). The test has been executed performing a very preliminary simulation of the actual configuration of HYPSOS. To simulate the slit, a fixed group of 2048x4 (rows,columns) pixels are extracted from the image. If the Pechan prisms are in the optical path the selected region is 4x2048 pixels. The 2048x4 arrays are (software) binned 4x4, matching exactly the true HYPSOS slit width ($22\mu m$). The columns are first suitably flipped and transposed to obtain the right orientation of the image and then the pixel intensities summed or averaged grouping 4x4 pixels. The order of the operations depends on the channel and on the versus of motion of the linear stage. Finally, the image is reconstructed as a sequence of column vectors each of size 512x1 (Figure 5.10b). The linear stage velocity and the acquisition frame rate have been suitably set up to synchronize the acquisition and the target movement. Each snapshot is triggered every dwell time, that is the time the target moves of 1 pixel. This is calculated for each stereo angle. For this specific test, the integration time is much smaller than the repetition time and therefore the effect of the smearing was not taken into consideration. It should be highlighted that the *main* code used for this test is the same developed for the final experiment, but with a different detector library loaded. This is a further proof of its stability and flexibility.

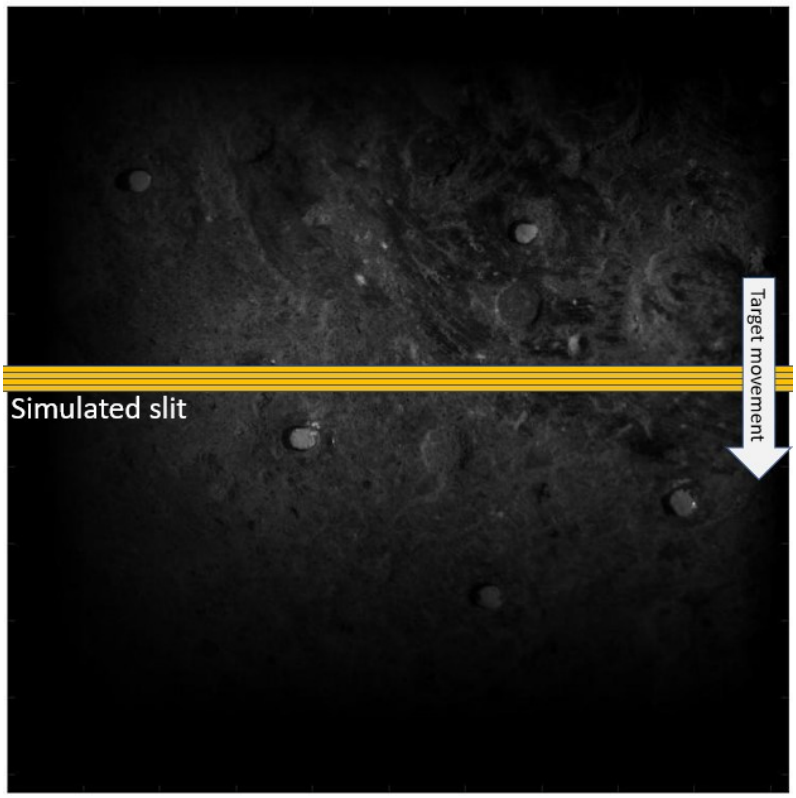

(a)

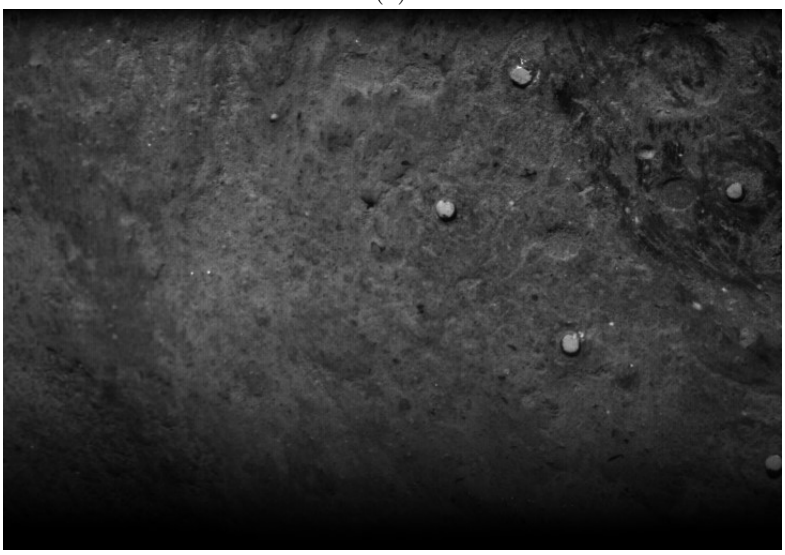

(b)

Figure 5.10: (a): frame (2048x2048 pixels, 5.5μm pixel pitch) extracted from a video acquired with a service camera on the telescope focal plane. The *simulated slit* gives an idea of the fixed group of pixels extracted from the image. The gray arrow indicates the direction of movement of the stone with respect to the slit. (b) is the image reconstructed assembling a sequence of lines extracted from the video mentioned in (a)

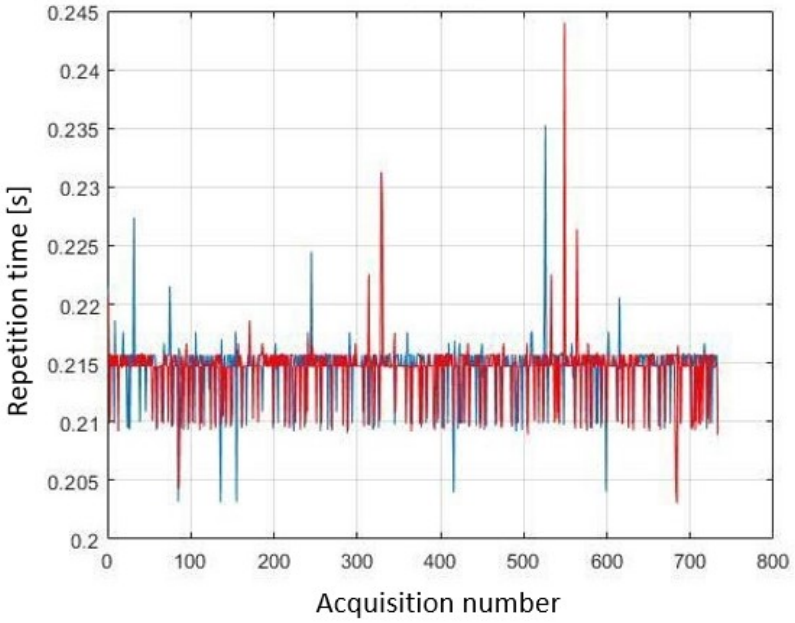

Figure 5.11: Example of repetition time for preliminary pushbroom scanning test. The x-axis is the image index inside the acquisition sequence. The blue curve is the acquisition performed with the first angle, the red one the setup has rotated the target in the opposite direction.

Before providing the data to the team members in charge of the photogrammetric pipeline development, we verified the repetition time stability. This is estimated as the difference between the timestamps of successive acquisition (Figure 5.11). The timestamp is got inside the code after the snapshot function returned the image. It corresponds to the number of seconds from a date.

The first step of the photogrammetric pipeline requires the acquisition of a calibration gauge, in this case a bi-planar chessboard (Figure 5.12). The second step is the acquisition of a target with known topography, at two different angles ($\pm 20°$). The topography has been retrieved with a laser scan and it is used as reference.

The reconstructed images are processed and used to generate a 3D points cloud of the target (Figure 5.13a). The 3D coordinates are aligned to the reference and the differences are calculated. Figure 5.13b shows the reconstructed topography superimposed to the reference one. The colours indicate the amplitude of the differences. Table 5.4 shows the statistics of the comparison. The standard deviation of the differences is 136 μm corresponding to about 1.5 GSD. The result is considered satisfactory, although slightly larger than the expected (about 1 GSD). However, it should be considered that it is a preliminary test, the reference laser scan is probably not enough updated (new topography measurements are currently under elaboration) and the pipeline should be optimized along with the setup parameters.

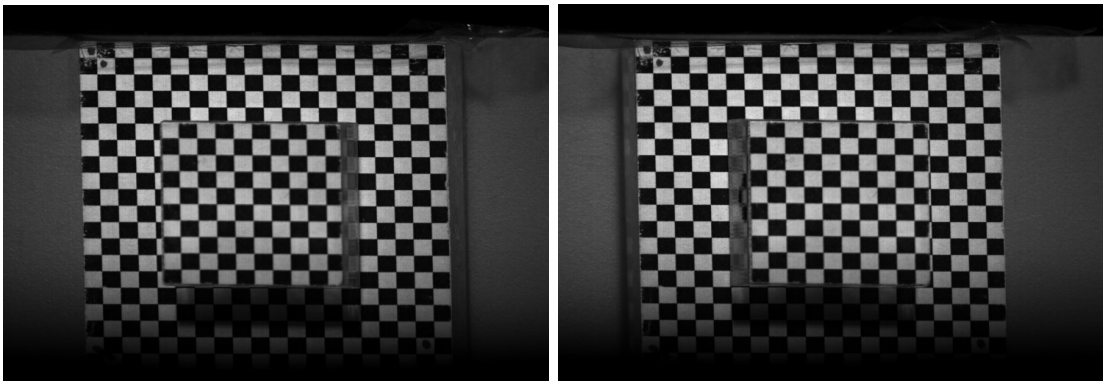

(a) (b)

Figure 5.12: (a): image reconstructed of bi-planar chessboard 20°clockwise-rotated. (b): counter-clockwise-rotated

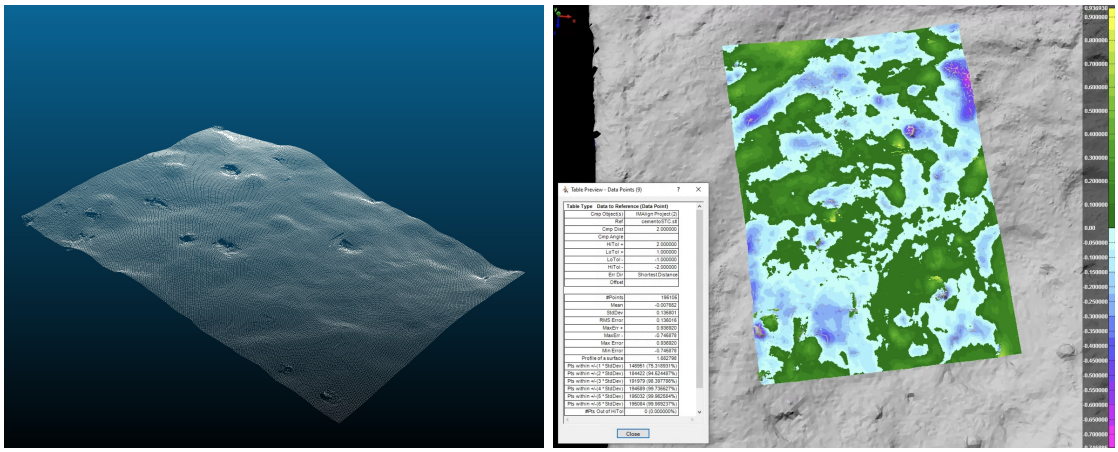

(a) (b)

Figure 5.13: (a): points cloud generated using two reconstructed images, each rotated ±20°with respect to the optical axis of the collimator. (b): alignment between the point cloud and the reference topography. The colours indicate the amplitude of the difference. The table with the statistics is reported in Table 5.4.

5.4 Alignment Tool

In this section the setup used for the alignment of telescope is described.

The FOR and AFT channels are symmetric with respect to the instrument midpoint. They work as separate optical systems but at the same time they share the optical elements, therefore for alignment purposes they could be considered as part of the same telescope.

For this reason, in front of the HYPSOS baseplate, it has been assembled a system

Photogrammetric pipeline output statistics	
# Points	195105
Mean	-0.007652
Standard deviation σ	0.135801
RMS error	0.136016
Max Error +	0.936920
Max Error -	-0.745878
Points within $\pm 1\sigma$	75.32 %
Points within $\pm 2\sigma$	94.52 %
Points within $\pm 3\sigma$	98.49 %

Table 5.4: Results from photogrammetric pipeline. Particular of Table in Figure 5.13b

capable to produce three parallel collimated beams. Two beams illuminates the two HYPSOS channels, the third feeds the midpoint of the telescope (see the central aperture on the mirrors mask, Figure 4.7b). The Alignment Tool (AT) allows to have the same observing direction for both the channels (Figure 5.14).

The AT is composed by two cube beam splitters and two folding mirrors nominally oriented at about 45°. The source is a HeNe laser feeding a 20x beam expander with an iris located at its exit port. During the coarse alignment of the telescope, the iris is partially closed, to simulate a single ray. In the fine alignment phase, the iris is opened up to a diameter of 10 mm: this reduces the diffraction effect with respect to the case of illuminating HYPSOS with the narrow beam of the laser.

However, due to the limited clear apertures of the beam splitters, it is not possible to illuminate the telescope with a larger beam. Actually, this is a potential limitation because with this aperture the system is diffraction limited it is more difficult to evaluate the quality of the alignment from an analysis of the spot diagram.

The beam splitters are 70/30 (Transmission/Reflection) and 50/50; in this way all the laser beams have about the same intensity.

The central ray is assumed to be the absolute reference for the whole experiment. In fact, a beam splitter does not modify the direction of the transmitted ray (the effect is a decenter which is considered negligible in this case). The reflected ray, instead, could suffer of angular variation due to, for example, to temperature gradients or other environmental effects (or misalignment) which change the orientation of the beam splitter. However, it is possible to compensate that using the folding mirror after the reflection. In this sense, it is required an alignment which guarantees:

- collimated beam
- beam parallelism

or, otherwise, the knowledge of the relative directions and a verification system able to monitor such variations. The folding mirrors are held by suitable supports allowing to

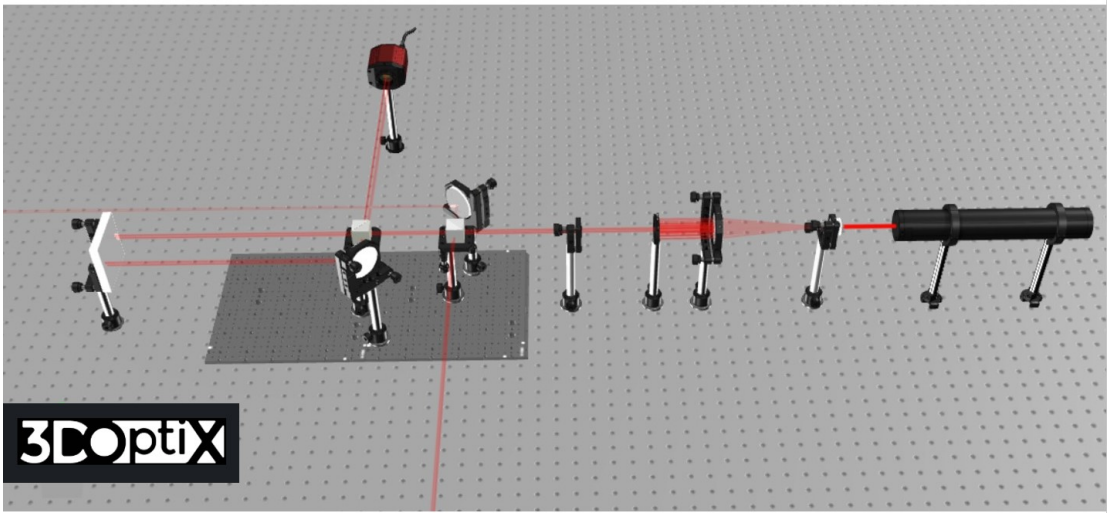

(a)

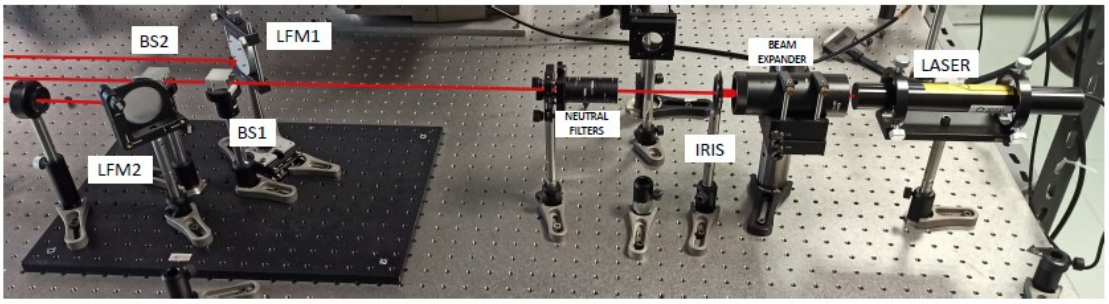

(b)

Figure 5.14: (a): schematic representation of the alignment tool. Image credits: 3DOptix. (b): implementation of the tool on the optical bench. A set of neutral filters has been added to avoid the saturation of the camera.

make small corrections. Originally, both the AT channels had a 2" circular mirror on a 5 DOF (degree of freedom) post-holder. During the alignment of the telescope, one of the mirrors turned out to have had an unacceptable instability probably due to mechanical support. We decided to substitute it, firstly with a 2" mirror on a kinematic mount and finally with a 1" circular mirror.

5.4.1 Setup verification procedure

The fine alignment of the telescope requires a high accuracy of the setup alignment itself. To have an idea about the alignment accuracy required, we can see that the 22 micron slit width corresponds to a projected FoV of about 90 urad, rather difficult to see with "visual" optical tools. Thus, for having good information about the alignment quality, a USB camera with a pixel pitch of 5.5 micron (corresponding to a 22.5 urad IFOV) has

been used on the focal plane of the TMA. Moreover, the procedure is required to be relatively fast because it should be repeated at the beginning of each alignment session (and possibly several times during the day) for stability verification of instrument and setup. Any error in the setup, corrected by the telescope alignment procedure, translates in a misalignment of the telescope itself. The first step is to check the collimation status of the beams, which is performed using a shear plate (Figure 5.15a).

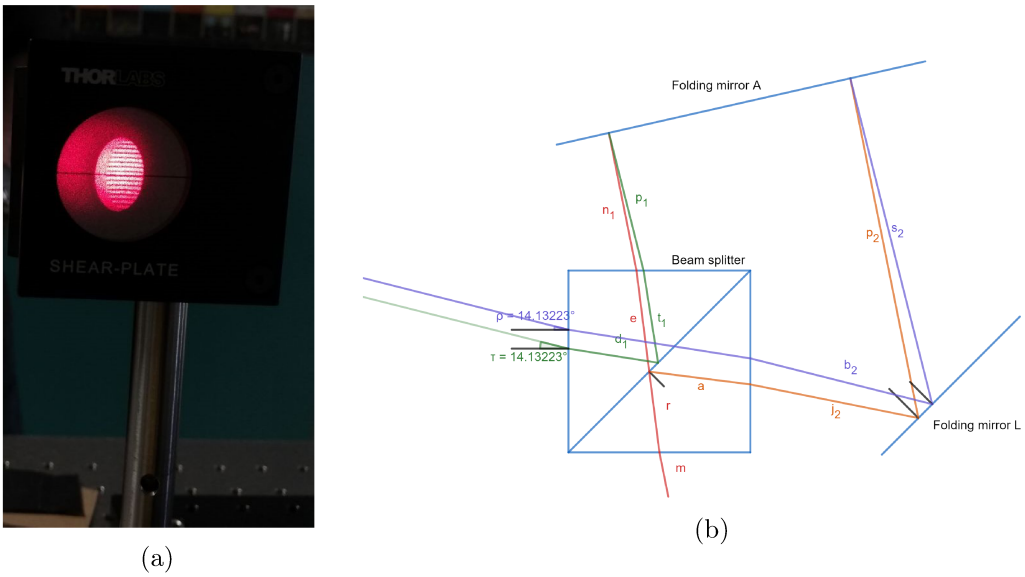

(a) (b)

Figure 5.15: a: test on collimation with the shear plate. b: Toy model of the verification procedure for the Alignment Tool. Here the Folding Mirror A is not in autocollimation with the central ray and the Folding Mirror L is oriented to have the red and orange beams parallel (as required). Made with GeoGebra[1].

The procedure foresees to verify that each lateral beam of the Alignment Tool described in the previous Section is parallel to the central one which is assumed to be the reference. It is performed considering the two couple of rays (the central beam and one of the two channels) separately. The procedure can be better understand observing the Figure 5.15b. A plane mirror (Folding Mirror A) large enough to back reflect the two laser beams from the central channel and one of the lateral channels (as shown in Figure 5.14a) is located after the last beam splitter The two laser beams under test (red and orange) are reflected back from the folding mirror A and go through the beam splitter again, coming out (as rays green and purple respectively) from face opposing the Folding Mirror L where it is easy to locate a device (we selected a CCD camera with 680 x 480 pixels with 10 μm pixel pitch) to verify their relative orientation. The two collimated beams experience an interference that is recorded by the camera as a pattern of fringes. The distance between the crests depends only by the angle between the wave vectors (and the wavelength, but

[1] https://www.geogebra.org/

here it is fixed by the laser) according to the relation (Palmer 2020):

$$d = \frac{\lambda}{2sin(\theta)} \tag{5.3}$$

with θ the half angle between the beams and d the distance between the crests. Due to the limited size of the camera it is not possible to observe fringes that are separated more than the higher dimension of the camera (6.4 mm, that is 640 pixels, 10 μm pixel size). Thus the estimated maximum angular deviation is 100 μrad. The Folding Mirrors L is moved (by means of the kinematic mounts) until the number of fringes is minimized. The same procedure is then replicated with the other beam couple (the central ray and the other lateral channel). This mean that between the two channels the maximum angular deviation is 200 μrad as upper limit. Probably, a higher accuracy is reached, because experimentally it has been observed that, when HYPSOS is illuminated by the Alignment Tool, if the spots on HYPSOS focal plane moved with respect to a reference position (defined from a 2D gaussian fit of the spots) because of the Alignment Tool itself (verified observing the interference fringes on the camera), the described alignment procedure restored the original position (verified acquiring another image and comparing the centroids difference). Another verification strategy can also be implemented, making use of an auxiliary optics with a focal length and pixel size similar to the telescope. The auxiliary optics can be used as alternative to the interferometric verification procedure already described, verifying, this time, that the two beams are converted into two overlapping spots. We used a camera with a standard C-mount and a pixel pitch of 10 μm coupled to an optical tube hosting an achromatic doublet (250 mm focal length, similar to HYPSOS). The optical assembly also includes a threaded part for the fine focus adjustment. Firstly, the optical tube with the lens on is aligned to the central ray of the AT using a combination of autocollimation and back-reflection minimization. After that, a coarse focus has been reached using a Hartmann mask made in laboratory. Finally, the fine focus is reached maximizing the signal intensity around the coarse focus position. In this case, each pixel of the auxiliary optics corresponds to about 2 pixels of the system TMA plus the USB camera with 5.5 μm pixel pitch.

5.4.2 Secondary branch of the setup

Besides the Alignment Tool already described, also a secondary path has been implemented on the optical bench (Figure 5.16a, orange beam).

This has been made to partially cope with the limitation on the beam diameter imposed by the beam splitters clear apertures of the Alignment Tool (10 mm). Another benefit is also to have an aligned path where the SVS-HYPSOS (see Section 5.2) can be positioned to have the correct coupling between the target itself and HYPSOS. It has been decided to bypass the Alignment Tool section (Figure 5.16a, red beam) and to install a secondary beam expander stage composed by two confocal lenses available in laboratory, one of them being the Collimator (see Table 5.2). In this way the Collimator is already located in the right position to exploit its function in the SVS (Section 5.2). This introduces the requirement that the SVS reference hole should be located in the confocal

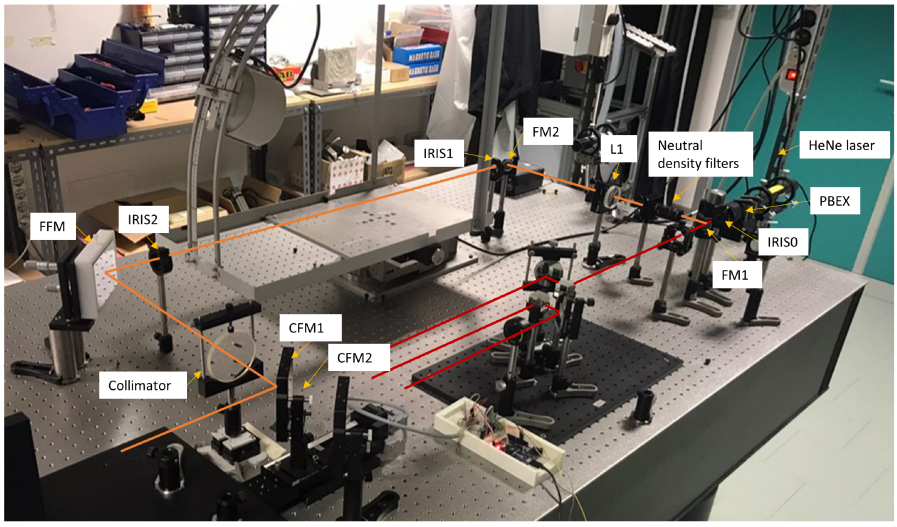

(a)

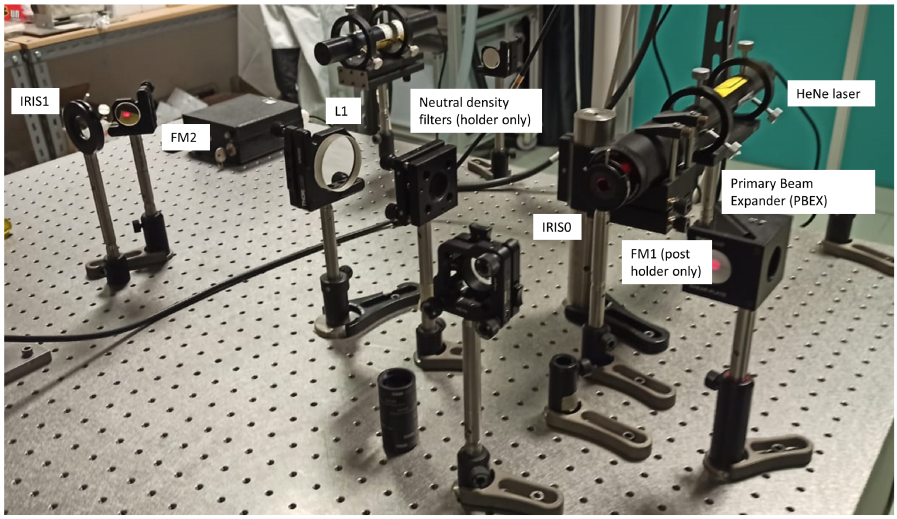

(b)

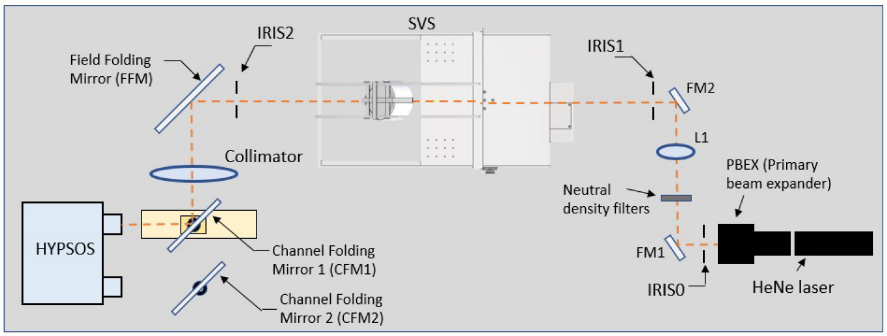

(c)

Figure 5.16: HYPSOS optical bench setup. (a): The two paths are visible: the Alignment Tool in the right side of the image (red) and the Secondary Path (orange) with the SVS structure already located along the path. (b): Particular of the setup. (c): Sketch of the secondary path

point. A 2" achromatic doublet with 750 mm focal length has been selected as second lens achieving a beam expansion of 1.3x. A constraint on the focal length of the latter element is also imposed by the impossibility to fix, on the optical bench, the post-holder in the regions occupied by the SVS. The final beam diameter is not enough to cover the 35 mm entrance pupil diameter of HYPSOS and the system remains diffraction limited but it allows, anyway, to evaluate if the diffraction limited condition is maintained up to the achievable laser beam diameter. The system has been aligned with the following procedure (see Figure 5.16 for the naming convention). Two irises (IRIS1 and IRIS2) are fixed on the optical bench at the same height. They provide a fixed reference for the alignment because the laser beam is constrained to be parallel to the optical bench and aligned its holes. After that, two plane mirrors (FM1 and FM2) are placed in Z-configuration and regulated to have the laser beam from the primary beam expander (PBEX) passing through both the irises. The, the Field Folding Mirror (FFM) is placed and aligned at 45° with respect to the line defined by IRIS1 and IRIS2. This is achieved using another iris (not shown in the figures) at the same height of IRIS1 and IRIS2 and fixed in a hole located at 90° with respect to the reference line. The orthogonality is guarateed by the optical bench. To align the lenses, FM1 is removed from the path and used to illuminate the system in reverse order using one of the Alignment Tool channel. The mirror is aligned taking advantage of IRIS1 and IRIS2 in the same way as before. FM1 is removed with its holder, but its post-holder is kept in position. In this way the mirror can be inserted and aligned in an easy way (using IRIS1 and IRIS2 as reference) each time it is required. This mirror is used to select the Alignment Tool or the secondary path. First, the Collimator is located between this latter mirror and the FFM, and aligned minimizing the back reflection with the constraint to keep the laser beam passing through IRIS1 and IRIS2. The other lens (L1) is aligned in the same way as the Collimator. The collimation is verified with the shear plate (Figure 5.15a). The last step is the alignment of the Channel Folding Mirrors 1 (CFM1) and 2 (CFM2). First, the Alignment Tool (after verifying its alignment, Section 5.4.1) is used to illuminate HYPSOS and the two spots (of the lateral channels) acquired with the USB camera located on the focal plane and used a reference. FM1 is located again in position and aligned. After that, the CFM2 is located along the path after the Collimator, to illuminate HYPSOS. The mirror is then regulated to have the spot overlapped with the corresponding reference spot (from the Alignment Tool). The same procedure is replicated for CFM1.

Chapter 6

Components characterization

6.1 Mirrors

As previously described, the telescope is an unobstructed TMA, which is composed of two off-axis conic surface mirrors and a spherical mirror.

The first step has been a visual inspection (Figures 6.1a,6.1b,6.1c) of the elements, to verify the presence of cosmetic defects or macroscopic problems in manufacturing. After that, the mirrors have been mounted in their custom holders for the alignment process.

However, very soon in the alignment process of the telescope, a major problem appeared and a characterization of the mirrors was required in order to understand the problem. We limited the analysis to M1 and M3, the most probable source of the errors due to their off-axis shape, more difficult to manufacture with respect to M2 which is spherical.

We decided to investigate the goodness of the components manufacturing with a semi-qualitative approach. Each mirror has been singularly illuminated by our telescope alignment tool (AT, Section 5.4) and a "through focus" sequence of images has been acquired. We used a USB camera located on a manual linear stage to acquire the spots projected by the mirror under test. This sequence is then compared with a suitable simulation in ZEMAX. The first step is the identification of a recognizable spot diagram to be used as reference. The simulation and the camera have been therefore set to reproduce the reference spot diagram. Then, systematically, the camera is moved by 0.5 mm by using the linear stage in and out focus. The same procedure is replicated in ZEMAX in order to have a suitable basis for comparison.

6.1.1 M1

Although the measurement strategy is almost the same between M1 and M3, the setup is slightly different. In fact, M1 has been analyzed directly inside its support and located on the instrument mechanical structure (Figure 6.2).

The mirror support is put in "nominal" position by means of two shims 3 mm width inserted between the rear side of the support and mechanical structure. However, some

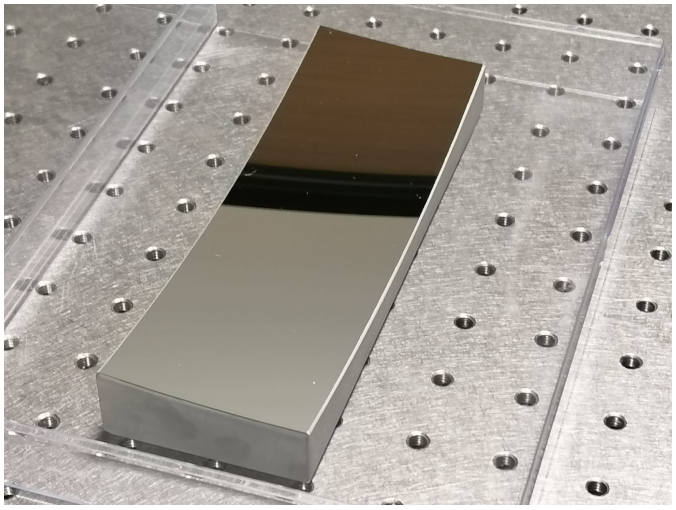

(a) M1

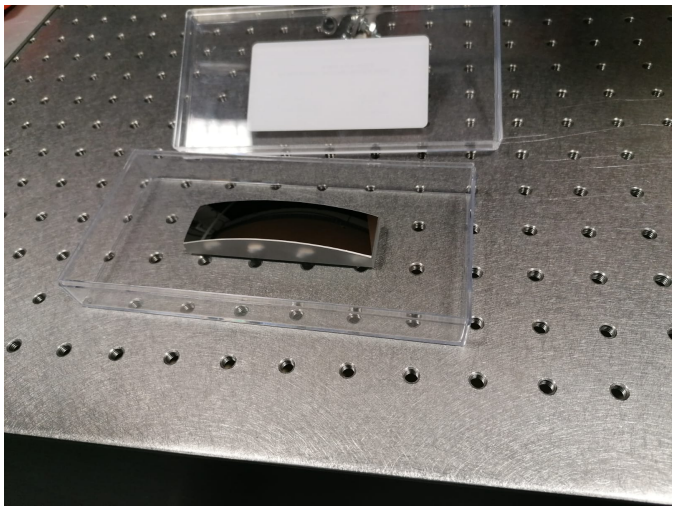

(b) M2

(c) M3

Figure 6.1: HYPSOS telescope mirrors. The images have been acquired during the visual inspection of the components.

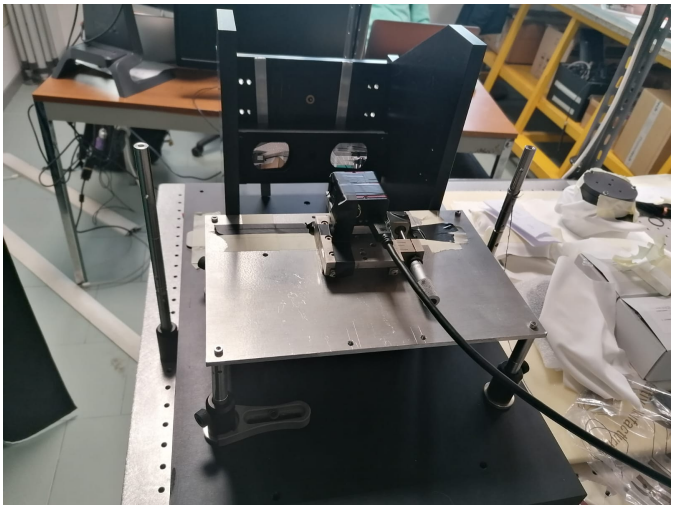

Figure 6.2: Characterization of M1. The mirror is inside its structure and located in "nominal" configuration using two shims with a width of 3 mm.

residual misalignments induced by the position of the mirror with respect to the support itself are possible. In this case the optical axis of the mirror is 6° tilted with respect to the optical bench, due to the telescope configuration.

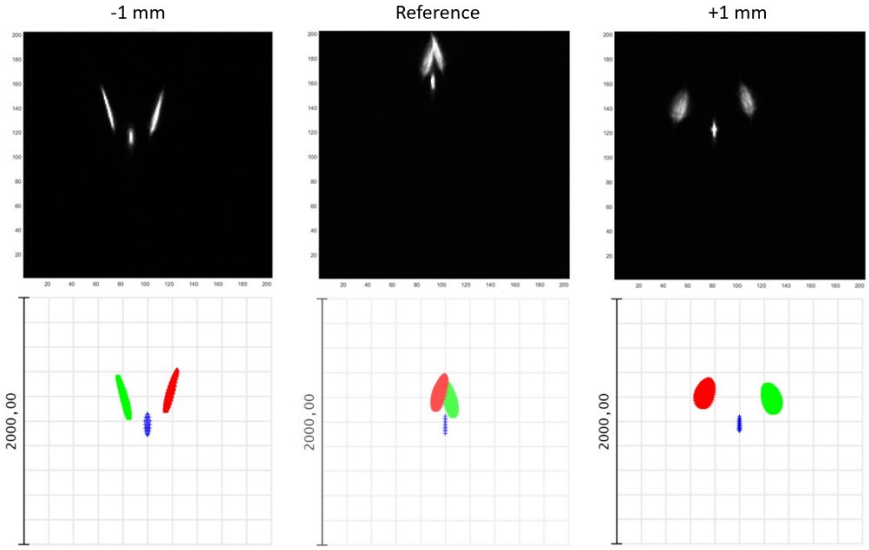

Figure 6.3: Comparison between acquisition and simulation for M1. The top images show the acquired images, the box is 200x200 pixels (2000 μm x 2000μm). The bottom images show the ZEMAX simulation. The colours indicate the three different channels of the alignment tool.

The Figure 6.3 shows the result of the test. The measurements are consistent with

the simulation and so we decided to not proceed further in the analysis.

6.1.2 M3

A first characterization has been done with the mirror mounted in its support. However, the preliminary test seemed to show a large deviation from simulation. To reduce as many uncertainties as possible (the orientation of the mirror with respect to the support), the mirror has been removed from the support and the test repeated. The mirror has been put on a platform aligned to the optical bench with a spirit level (Figure 6.4). The mirror has been oriented around the gravity axis and put in contact with the rear face with a bubble level tangent to a couple of identical post-assemblies directly fastened to the optical bench.

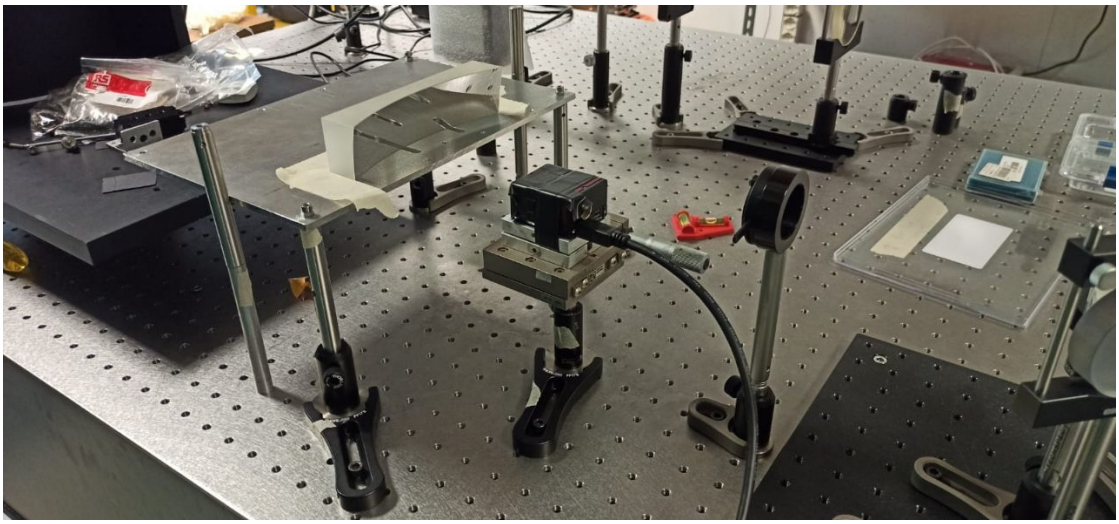

Figure 6.4: Characterization setup for M3.

Figure 6.5 shows the problem encountered with M3. The first column of the Figure shows the "through" reference sequence of images. The middle column shows the output of the Zemax simulation with the nominal parameters of the mirror. The rightmost column shows a modified version of the simulation using the supposed "wrong" parameter (that is a wrong sign of the mirror surface conic constant). All the images have the same scale. It is evident the different size between the acquired images and the simulated nominal spot diagrams (left and central columns). In particular, the measured spot sizes are not consistent with possible misalignment errors (such as laser beam positions on the mirrors, incidence angles, etc...). In this case there is no influence of the mirror positioning inside its mechanical support, therefore the problem has been restricted to a manufacturing error.

During the production of the mirror, the factory required the team to deliver some specific parameters and in particular the sign of the conic constant of M3. The conic

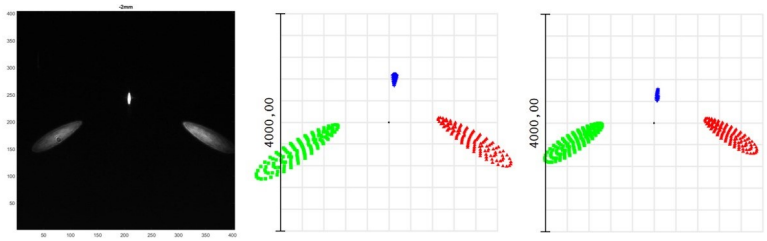

(a) -2mm from reference

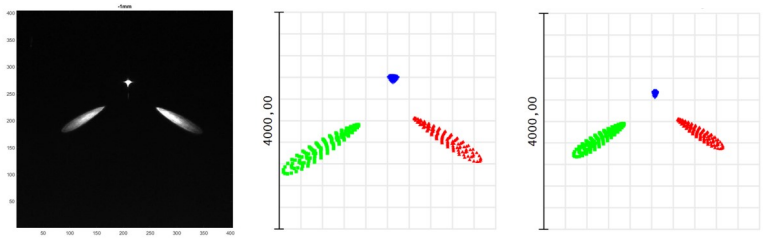

(b) -1 mm from reference

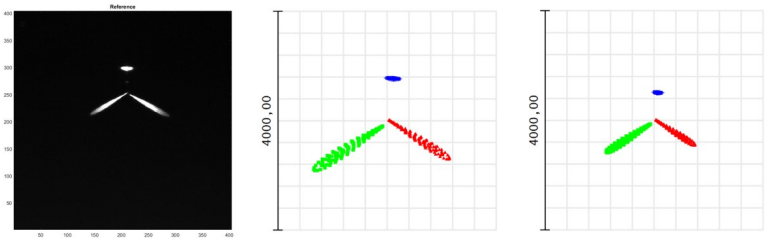

(c) Reference

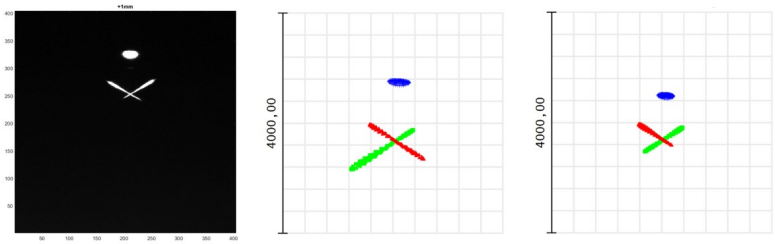

(d) + 1mm from reference

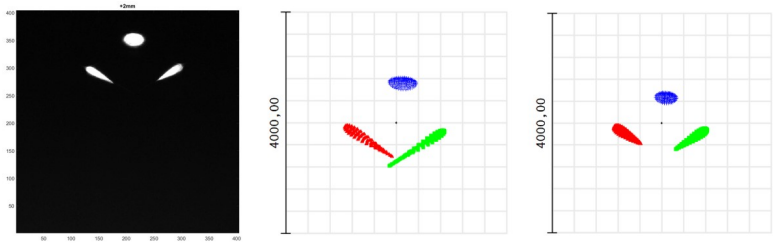

(e) +2 mm from reference

Figure 6.5: Comparison between the acquisition and the simulation. In the leftmost column, images from the camera. The central column is the ZEMAX simulation with a positive conic constant (k>0), the rightmost column is the simulation with negative conic constant (k<0). The colours in the simulations correspond to the three different paths of the telescope alignment tool. The image is 400x400 pixels, corresponding to 4000 μm (ZEMAX simulation). Each row is a different "through reference" position.

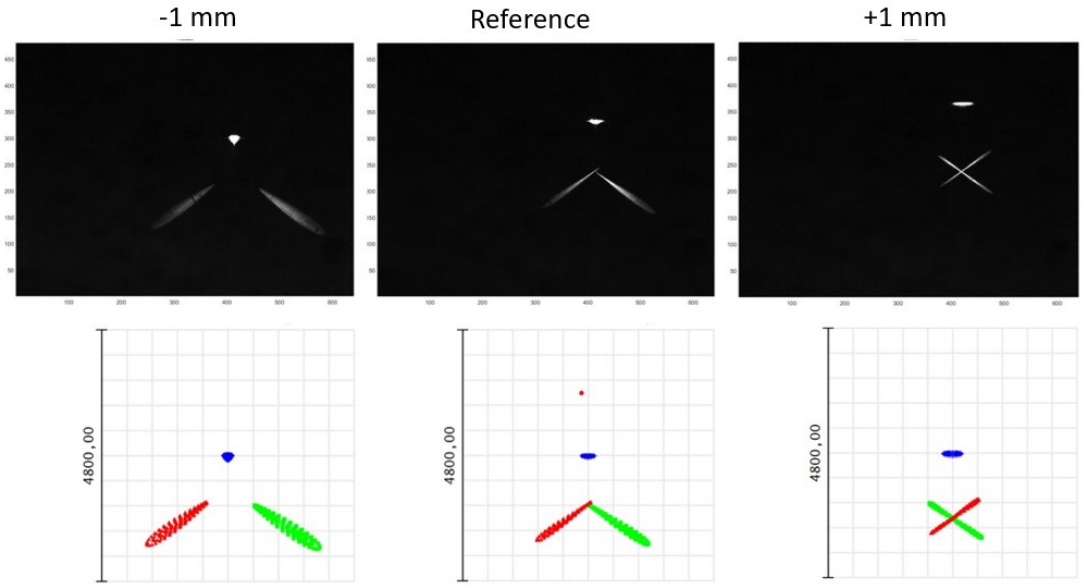

Figure 6.6: Comparison between the acquisition and the simulation for the new and corrected M3 mirror. The image is 480x640 pixels (4800 μm x 6800 μm), the simulation has a box of 4800 μm. The colours indicate the three different path of the alignment tool

constant (K), for a conic surface, indicates the shape of the mirror. M3, in particular, is nominally an oblate ellipsoid (K $>$ 0). To investigate possible manufacturing errors, we took in consideration the possibility that the mirror had the wrong sign of the conic constant.

The rightmost column of Figure 6.5 shows the results obtained changing the sign of the conic constant. It is important to highlight that it is not an "absolute" measure but a relative one: every time the reference point is searched with the linear stage and the same procedure is performed in ZEMAX, images and simulations are affected by a variable relative shift. The simulation appears to be in agreement with the experimental data. After some interactions with the manufacturer, the error has been confirmed and a new mirror has been provided.

The characterization has been replicated with the new mirror before inserting it in the support. Figure 6.6 shows the result of the test, where the acquisitions of the reference point and $\pm$1 mm along the optical axis direction with respect to reference are reported. This time the mirror seems to behave as expected, the simulation is very in line with the data. Probably, the slight difference in data/simulation in Figure 6.5 is due to residual errors in the simulation parameters.

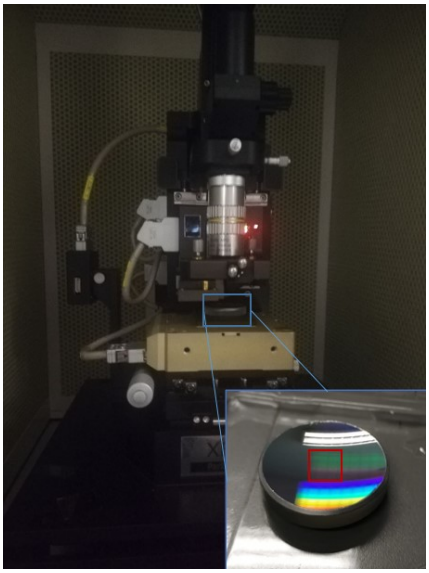

(a)

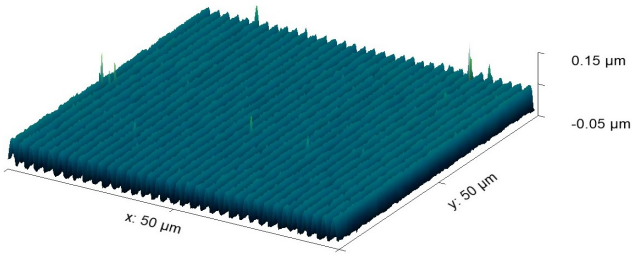

(b)

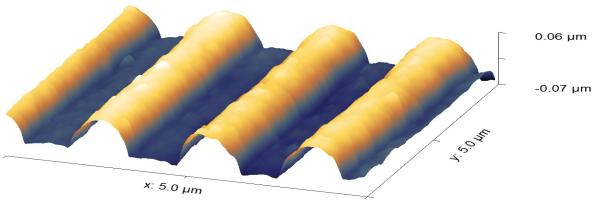

(c)

Figure 6.7: a shows the topography measurement of the diffraction grating (light blue box). The red box on the diffraction grating shows the examined area. b is the result of a $50\mu m$ x $50\mu m$ AFM scan. c shows the grating profile over a $5\mu m$ x $5\mu m$ scan.

6.2 Diffraction Grating

The grating has been characterized both in terms of surface quality and absolute efficiency using facilities available CNR-IFN (LUXOR) in Padua.

Firstly, images of the topography have been acquired with an Atomic Force Microscope (AFM) used in non-contact mode (see Figure 6.7a). The AFM uses a microcantilever with a tip to detect the attractive van der Waals forces acting between the tip and the sample, performing the topographic measurement scanning the tip over the sample (Jalili et al. 2004).

The acquisition has been performed with two different levels of sampling: 195 nm/pix (fig. 6.7b) and 19.5 nm/pix (fig. 6.7c).

Although some cosmetic defects are present, the overall quality of the grating surface is satisfactory.

Figure 6.8a shows three profiles for the topography of Figure 6.7b and three of Figure 6.7c. The profiles are extracted after a polynomial background removal performed using Gwyddion software[1]. It should be highlighted that the three rows of the high-resolution profiles are different from those of low-resolution. The numbers listed in the legends refer simply to the row index of the specific image.

From the profiles it is possible to perform a verification of the groove density. The middle profile of the $50\mu m$ topography is Fourier-transformed to highlight the frequency

[1] http://gwyddion.net/

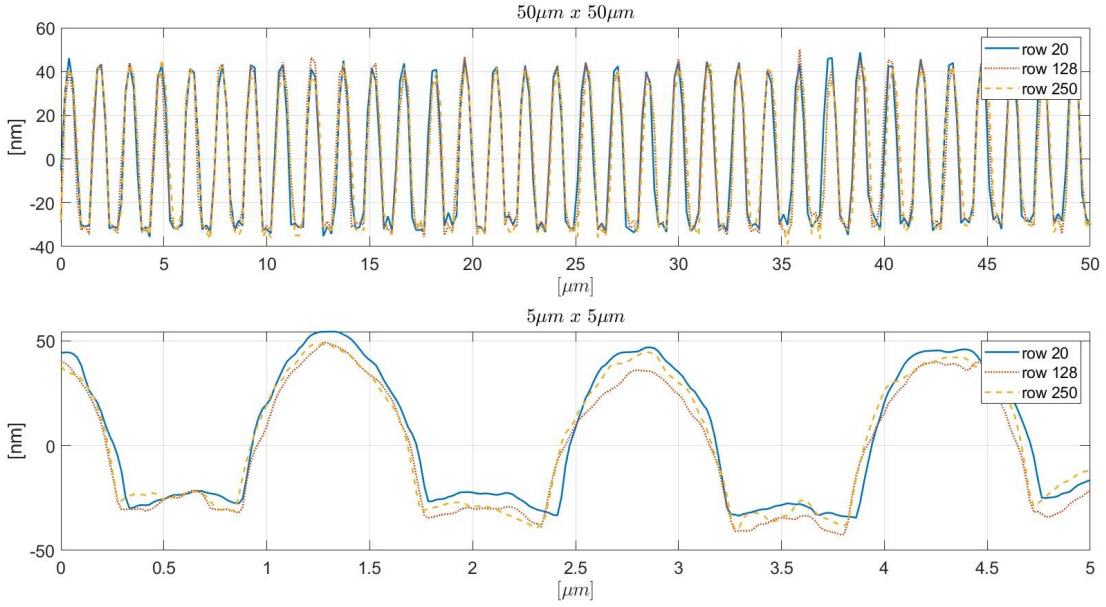

(a)

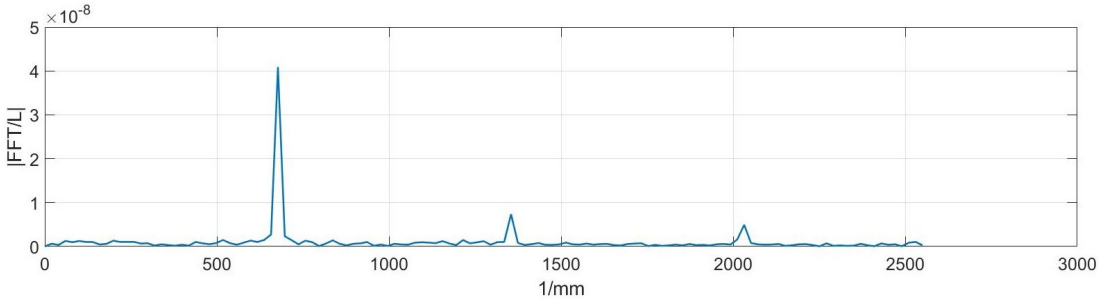

(b)

Figure 6.8: a *top*: Examples of profiles extracted from topography in Fig. b. *bottom*: As *top* but they refer to Fig. c. The legends in the figures indicate the displayed row. b: Fourier transform of the central profile of topography b

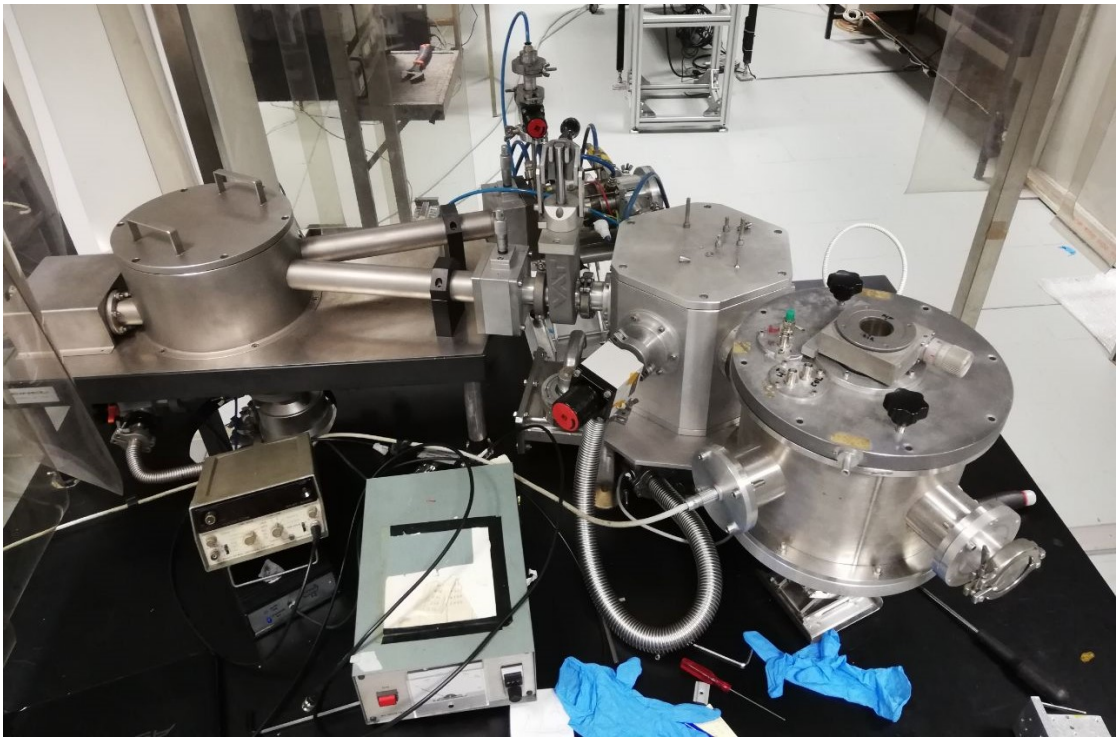

(a)

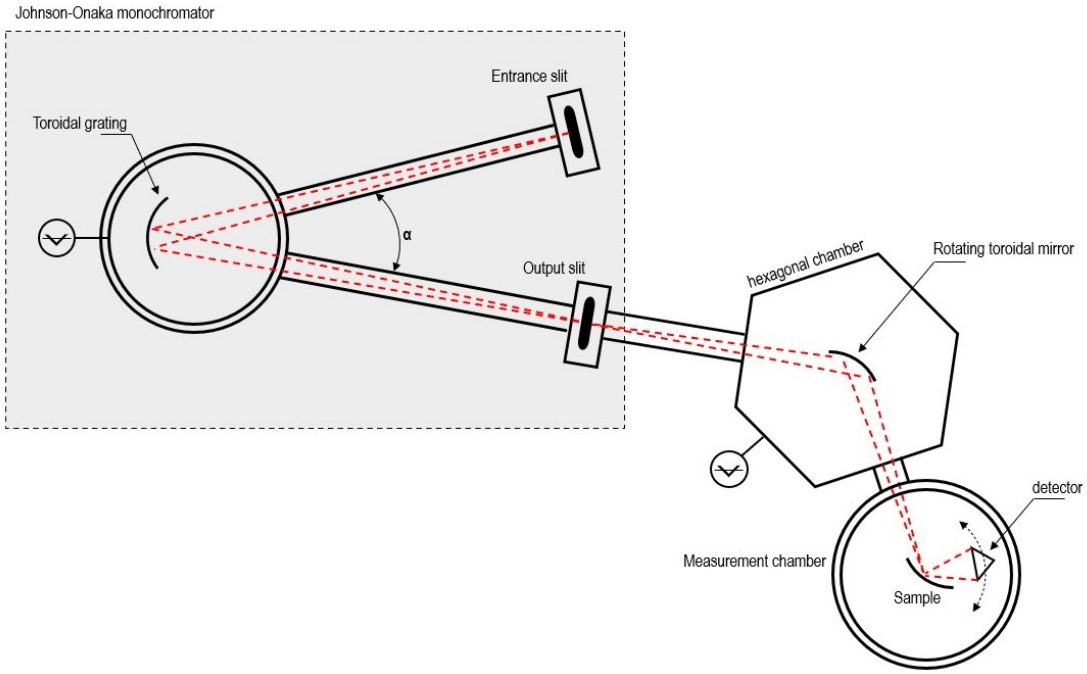

(b)

Figure 6.9: a Reflectometer facility at CNR-IFN LUXOR in Padua. b Sketch of the facility

components (Figure 6.8b). The main peak corresponds to a frequency of 680 grooves/mm, with a frequency resolution of 19.92 grooves/mm. The estimated groove density is consistent with the theoretical one. The other peaks are multiple integers of the fundamental frequency and are probably related to the non-sinusoidal pattern which is possible to observe in the high-resolution profile.

The next step was the evaluation of the diffraction efficiency. The factory, in fact, provides only the relative diffraction efficiency measured in near-Littrow configuration, which is quite different with respect to how the diffraction grating will be used on HYPSOS. Inside the spectrometer each channel illuminates an off-axis portion of the diffraction grating with about fixed angular direction. The experimental results have also been compared with simulations prepared in PcGrate Demo 6.7.1 software. The objective is trying to provide a reliable model for radiometric considerations.

For the experimental measurements, we took advantage of the reflectometer facility at the CNR-IFN in Padua (Figure 6.9). The setup is composed of three sections: a Johnson-Onaka monochromator, an hexagonal chamber and a measurement chamber (Naletto et al. 1995). The Johnson-Onaka monochromator has f/10 aperture and uses a toroidal diffraction grating to separate the spectral components of the light. It has a main curvature radius of 0.5 m and a ruling frequency of 600 l/mm. The hexagonal chamber accommodates a rotating toroidal mirror, able to focus the beam coming from the toroidal grating in different positions. During these measurements the toroidal mirror has been kept fixed with the focal point in the middle of the measurement chamber. The measurement chamber accommodates two co-aligned rotation stages. On one rotation stage it is possible to locate the device under test (DUT) and on the other a suitable detector. The facility has been conceived for UV and it is optimized for a wavelength of about 120 nm, but, actually, it is possible to work also in the visible light (Naletto et al. 1995), of interest for our purposes. The diffraction grating is located in the measurement chamber on a support which can rotate and also translate (Figure 6.10b). The same approach has also been used for the characterization of the diffraction gratings for the PHEBUS instrument on board the BepiColombo mission (Zuppella et al. 2012), in the same facility described here.

We selected as detector two silicon photodiodes with an active area of 1 mm^2 (see Figure 6.10a), disposed to have their normals along opposite directions.

The detectors have been selected with the largest possible area to collect all the radiation coming from the diffraction grating. The beam from the reflectometer is convergent on the gratings and, after that, due to its spherical shape, the beam diverges in the photodiode direction. For this reason the photodiode should be large enough to collect all the energy of the diffracted beam. The detector assembly is arranged on a rotating arm, allowing to measure the input radiation and the diffracted beam with a short time interval between the measurements. This is important in particular because we selected as source a commercially-available halogen lamp which is supposed to not feature a very stable illumination.

The absolute diffraction efficiency is evaluated using the following approach:

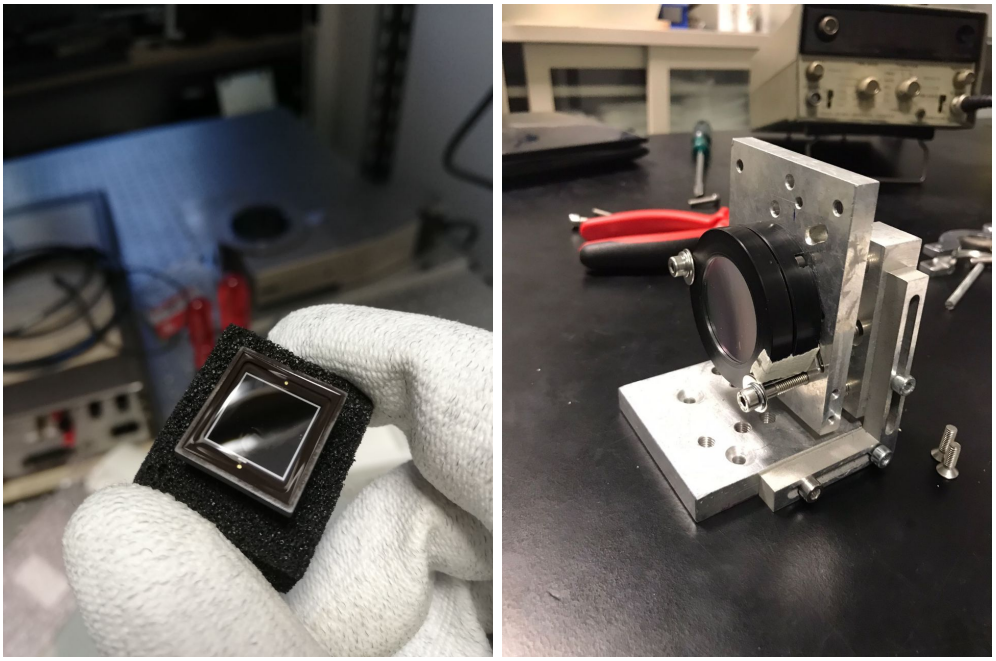

(a) (b)

Figure 6.10: a: one of the photodiodes used for the measurement. b: diffraction grating ready for the test

$$Eff(m,\lambda) = \frac{P_d(m,\lambda)}{P_i(m,\lambda)} = \frac{I_1(m,\lambda) - dark_1}{I_2(m,\lambda) - dark_2} \tag{6.1}$$

where m refers to the order of diffraction, the subscripts d,i to diffracted and incident respectively, I to the measured current and the subscripts *1,2* to the specific photodiode.

The measurement has been performed for three different cases: near-littrow, zero incidence angle and 40°incidence angle, the latter being the most representative of the grating operative configuration Each of the cases has also been simulated using PCGrate Demo. The profile shape selected for the simulation is sine-trapezoidal with a ridge (the upper plateau) of $0.15\mu m$, a land of $0.55\mu m$, a right frequency equal to left frequency (1.9033) and a groove depth of 77 nm. The used layer structure is an aluminium substrate with a coating of MgF2 (according to the component prescriptions). The depth of the MgF2 layer has been set to 25 nm. This parameter is not known and it has been derived in literature. In fact, according to Palmer 2020, to enhance the efficiency in the 120 nm-200 nm region of aluminium-coated diffraction gratings, an overcoating with aluminium followed by a coating of 25 nm of Magnesium Fluoride (MgF2) could be made. This also prevents the oxidation of the aluminium. Although the suggested spectral range for the specific diffraction gratings is 200 nm - 800 nm, without other information it is assumed that the MgF2 layer has a width of 25 nm and that the aluminium is optically thick. To simplify the simulation, it is assumed that the wavefront is plane (collimated beam), due

to the fact that the monochromator works at f/10.

Figure 6.11 shows the results of this analysis. Points refers to experimental data, solid lines to simulations and error bars to mean values along with standard deviation. Experimental data have been taken for m = -1, which is the diffraction order for HYPSOS. The efficiency derived from the datasheet is for order +1. It should be also noted that, as already said, it is provided in relative form and only for near-littrow condition. In general, the experimental trends are in agreement with the simulations, although not always the latter is inside the error bars, in particular for the near-littrow configuration for wavelengths higher than 500 nm. Due to mechanical constraints, the near-littrow has been measured adding a constant angle of 6°to both the experimental setup and analogously to the simulation. According to Palmer 2020, for the near-littrow it can be considered $\alpha \approx \beta$ (incidence and diffracted angle respectively), however, a simulation with that condition seems to be not so consistent with the datasheet curve; using instead the 6°angle of offset the datasheet and the simulation (for order +1) seems in agreement (see near-littrow case of Figure 6.11), catching for example particular features such as the "sinusoidal" trend around $\lambda = 550nm$. However, this type of measurement is extremely complex having many sources of error, so the results could be considered satisfactory. Probably, a better agreement could be found improving both the modeling and the experimental setup (along with the data analysis). A first source of error probably resides in the lack of a cross-calibration between the two photodiodes. Unfortunately, the computer where the data have been stored had a problem and the measurements of the currents were lost, so the cross-calibration to improve the reliability can not be applied. Another improvement could come from changing the readout circuit, selecting some option with higher degree of linearity, which is fundamental for this type of measurement. A good option is a transimpedance amplifier-based circuit. Another source of error could arise by the zone of the grating analyzed. The properties can change between different zones. However, these precautions are for highly specialized measurements which are out of the objectives of this work.

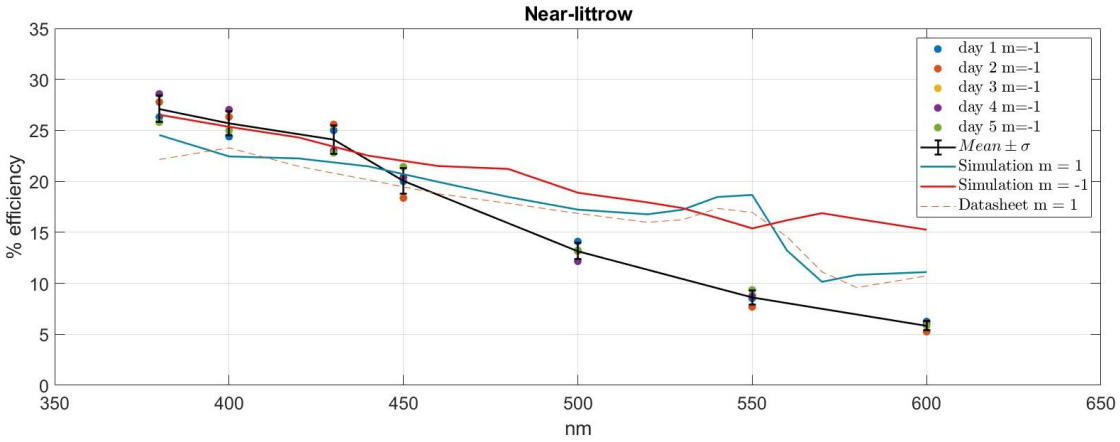

(a)

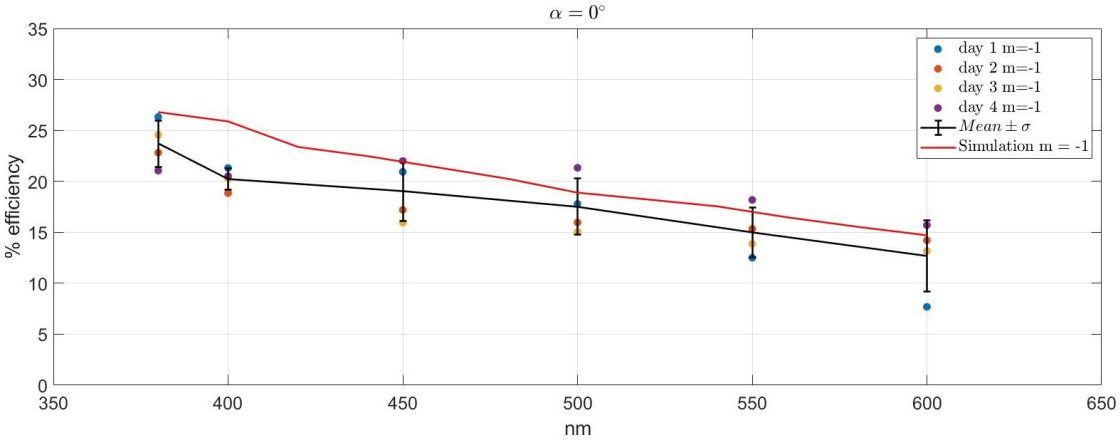

(b)

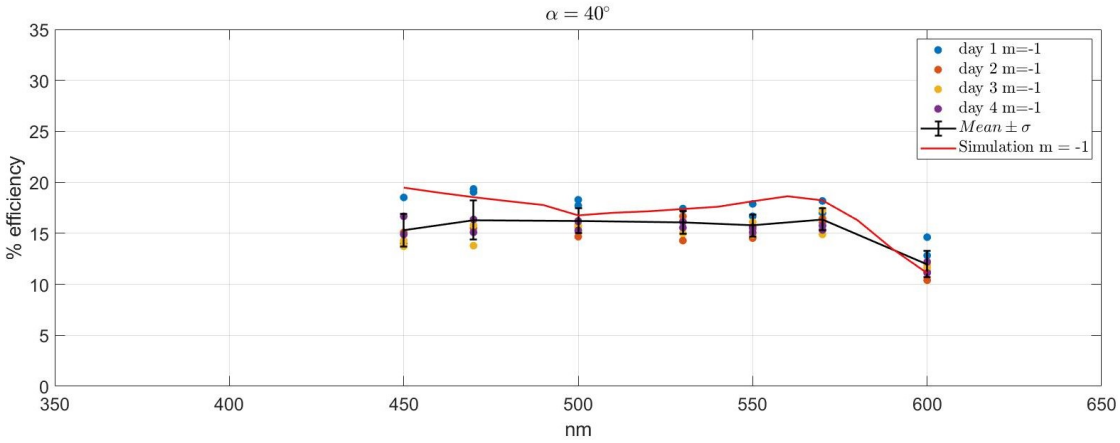

(c)

Figure 6.11: Diffraction grating efficiency at different configurations. Dots refer to experimental data, red solid line to simulation

Chapter 7

Alignment and performance verification

7.1 Spectrometer lens group assembly and verification

The first step of the spectrometer assembly has been the integration of the lenses into the dedicated barrel, which has been *ad hoc* designed (Faccioni 2020) for this experiment and realized in the workshop of INAF-OAPD (Observatory of Padua).

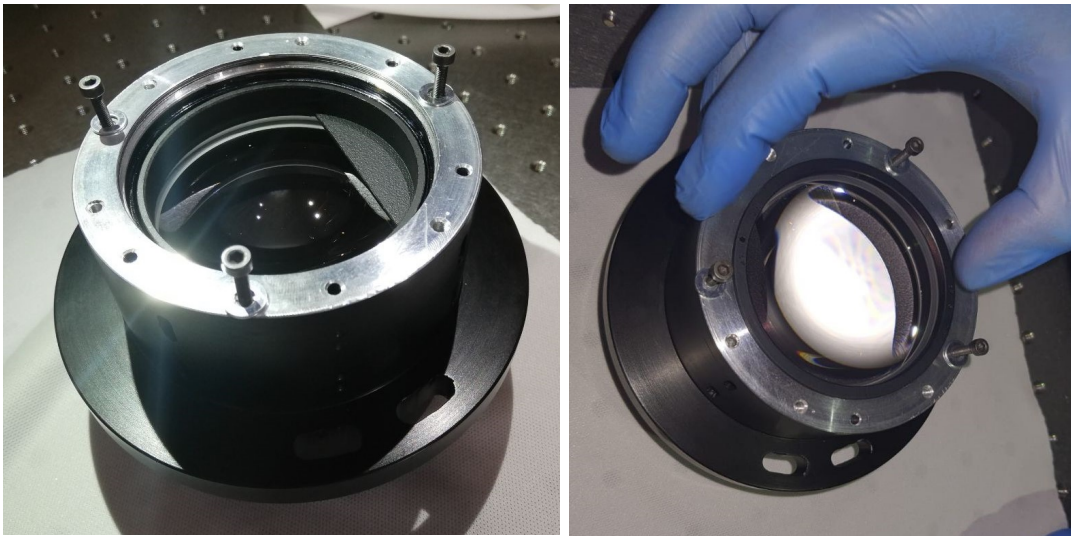

(a) (b)

Figure 7.1: Assembly of the spectrometer lens group. In Figure (a) it is also possible to see part of the light trap designed to stop the zero order path.

The structure is in black anodized aluminium. The lenses have been inserted in the barrel by simple mechanical tolerance (Figure 7.1). The lenses are kept in position thanks to a couple of retainers and of 3D printed structures which serve also for zero-order light

trap. The next step has been the verification of the assembly alignment. It should be considered that according to the tolerance analysis results, the spectrometer is quite tolerant to misalignments of the components, so it has been decided to execute few tests on the SLG. A parameter that has been considered useful to measure is the focal length of the assembly (actually, what it has been estimated is the back focal length of the system). To perform this measurement the barrel has been located on a vice and supported by a "V". The "V" avoids the barrel to tilt under its weight. The SLG is illuminated by a laser beam on a side and a camera positioned on a manual precision linear stage on the other side (Figure 7.2). To perform this measurement the barrel is positioned in "reverse" direction, that is the laser beam enters from the diffraction grating side, because the "nominal" side has not enough focal extraction to locate in a safety way the camera. Moreover, on that side it is possible to mount the diffraction grating support wall. This cover wall can be secured to the structure with mechanical tolerance. This ease to constraint the centre of the barrel. The SLG is aligned to the laser beam by means of back-reflections minimization, which can be observed on an iris suitably located in front of the barrel.

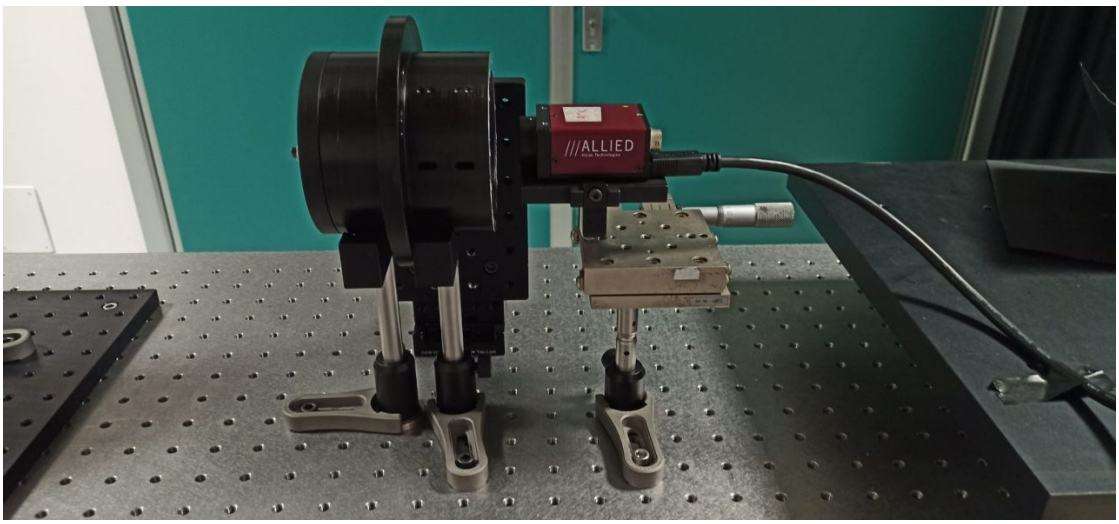

Figure 7.2: Spectrometer lens group characterization setup

Before the test, the position of the detector plane has been measured with respect to a convenient point of the detection assembly. When possible the distances are retrieved by datasheet, otherwise they are measured by means of a caliper. The caliper has also been used to measure the distance of last lens surface (which is plano-convex, with the plane surface towards the camera) from the barrel surface. The cameras is moved until the size of the spot is minimized. Then the distance between the barrel surface and the reference point of the camera has been measured with the caliper. This allows to evaluate the back-focal length of the system. This is compared with the back focal length from the optical model. The estimated value is 36.5 mm compared to the 36.48 mm of the optical model. The camera has been also used to perform a through focus acquisition

(Figure 7.3) which has been compared with the RMS spot radius of the optical model (red circle in the same figure).

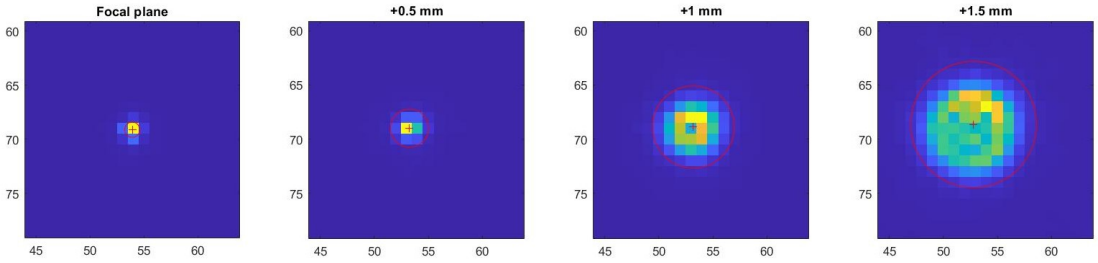

Figure 7.3: Spectrometer lens group characterization setup

7.2 Diffraction Grating alignment

The alignment of the diffraction grating has been performed taking advantage of the simmetry of the system. Although the spectrometer is not used in axialsymmetry when it is coupled to the telescope, its configuration is actually axial-symmetric. When the diffraction grating is in nominal position, if the spectrometer is illuminated by the laser beam along the optical axis, the orders +1 and -1 exit from the spectrometer symmetric with respect to the optical axis. The axisymmetric, anyway, leaves a free degree of freedom (the rotation around the z-axis, the optical axis) which requires to be defined. The orientation of the diffraction grating ruling defined the dispersion plane, which needs to be defined with respect to the slit, constraining the last degree of freedom. From Figure

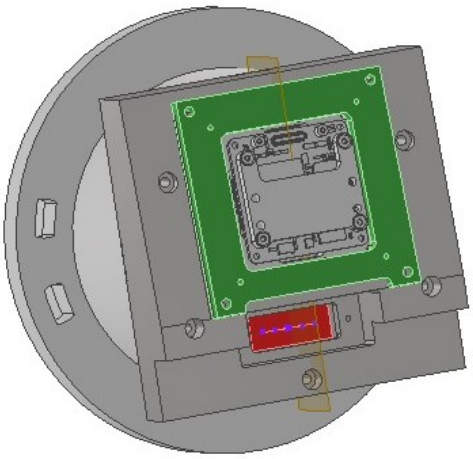

Figure 7.4: CAD rendering of the spectrometer. In green the 3D-printed support of the detector, in red the slit and in dark yellow a plane crossing the reference hole.

7.4 is possible to see that the slit (in red) is located over one of five holes which are used to fasten the rectangular flange to the barrel. The flange is the support for the detector and the slit. This series of holes is on a circumference centred on the axis of symmetry of the spectrometer. That hole has been selected as reference and together with the hole at 180°defines a line joining the spectrometer centre and the dispersion plane when the system is in aligned. A graph paper has been prepared and used it a target in front the spectrometer.

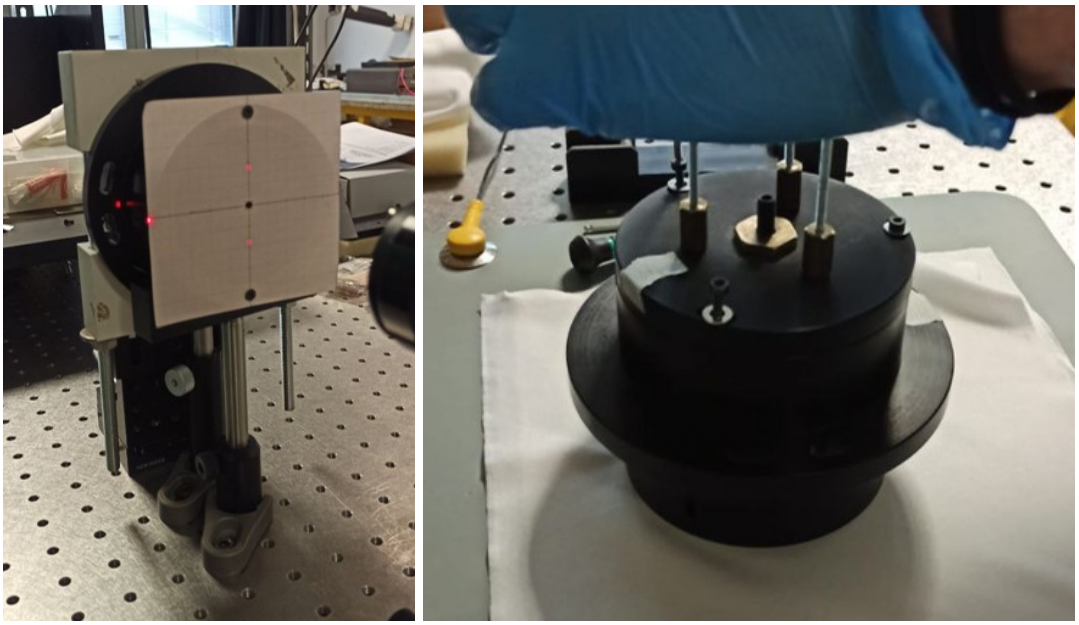

(a) (b)

Figure 7.5: a: graph paper target for diffraction grating alignment. b: spectrometer barrel with rear cover. The three threaded rods at 120° for the tip/tilt of the diffraction grating and the central pusher screw are visible.

The first step is the co-alignment of two laser beams. This allows to continuously check also the position of the rear side of the spectrometer illuminating the central threaded rod which should be mechanically aligned with the optical axis. The spectrometer is then aligned minimizing the back-reflection keeping the rear central rod illuminated by the secondary laser. The graph paper is fastened to the spectrometer using the reference holes (Figure 7.5a) and the diffraction grating support positioned in contact with the rear cover. The whole cover can be moved around the z-axis thanks to three eyelets. This allows to rotate also the two diffracted spots around the z-axis until they are on the vertical line of the target on the graph paper. The grating is then located at its nominal position 3 mm away from the cover wall using the central screw pusher. The right position is verified measuring with a caliper the length of the screw before and after the movement. The last step is the correction of the rotation around the x-axis and y-axis. This is executed with three threaded rods located at 120° around the midpoint, where is located the central

pusher screw. The effect of the misalignment on the graph paper target can be observed in Figure 7.6. The procedure is repeated until the the result is considered satisfactory.

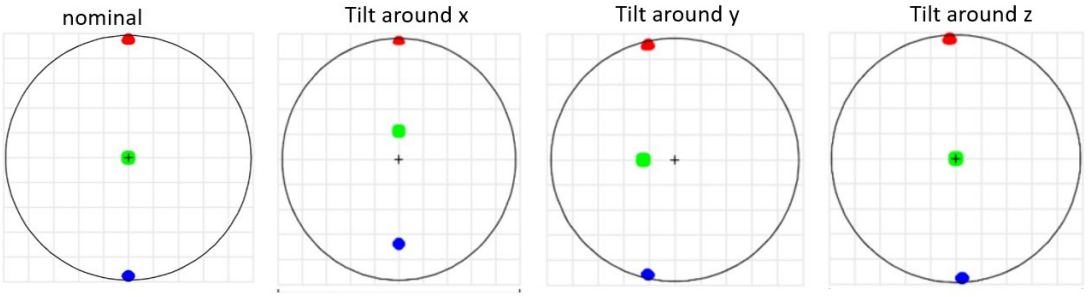

Figure 7.6: Effect of diffraction grating misalignment on graph paper target.

7.3 Spectral calibration

The objective of this measurement is to provide a curve which relates the pixel index (conventionally called *band*) with the wavelength. The relationship can be expressed as (Adriani et al. 2017):

$$\lambda(n) = \lambda_0 + SSI(n) \cdot n \tag{7.1}$$

where n is the band index, λ_0 is the central wavelength of the first sensitive band of the detector and SSI (Spectral Sampling Interval) is the spectral separation between two adjacent bands. This measurement could be important at different stages of the instrument integration. At the end it is required to generate the right spectral information, in earlier stages it provides an insight into the alignment, in particular verifying that the spectral range is all inside the detector. A simple and direct method to obtain this curve is through the use of a set of spectral lamps (e.g. Figure 7.7a). The spectral lamps are filled with different gases and generate emission spectra with narrow peaks. We used a set of spectral lamps available at CNR-IFN. The spectral calibration is performed in two steps: spectral registration and spectral calibration. The first step is required to generate couples of pixel index and related wavelengths, the second step is the identification of a functional form and the determination of the calibration parameters, such as the offset and the SSI. The pixel centroid is determined using a 2D gaussian fit. According to the optical design, it is expected a linear relationship, therefore the peaks are fitted with a simple line (Figure 7.7b).

From the fit it is possible to determine the linear dispersion of the spectrometer, which is a parameter easily comparable with the optical design prescriptions. The pixel size for the acquisitions of Figure 7.7b is 3.45 μm. Considering SSI = 0.1184 nm/pix the linear dispersion is 34.32 nm/mm, very close to the nominal 34.7 nm/mm. The test has been executed illuminating only the spectrometer and has been repeated after the preliminary integration of the barrel over the mechanical structure with the aligned telescope (the

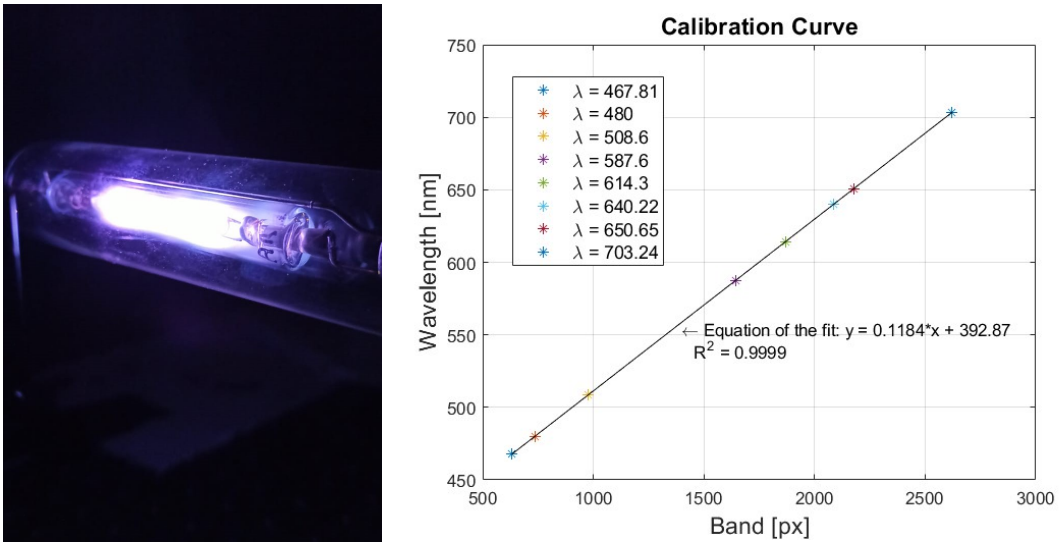

(a) (b)

Figure 7.7: a: Example of spectral lamp (Argon). b: HYPSOS preliminary spectral curve

lamp has then been located in the focal plane of the Collimator), with very similar results. This is a preliminary result because it is important, before determining this curve, to decide, for example, how to correct possible smile/keystone distortions.

7.4 Telescope Alignment

In this Section the procedure used to align the Three Mirror Anastigmat telescope of HYPSOS is described. The objective is to correctly located, along the optical path, the three mirrors plus the folding mirror. The mirrors are placed in custom cradles (as already described in Section 4.3). Figure 7.8a shows a sketch of a cradle. Four springs are located on the floor of the cradle and the mirror is inserted relying on that springs. The cradle is provided by four holes with set screws for the fine regulation of the mirror position. Each set screw couple opposes to springs which are properly inserted in the cradle and the regulation is achieved by pushing the mirror against the springs. The set screws are not in direct contact with the mirror substrate but a small metal plate is inserted in between to increase the contact surface. Figure 7.8b shows M1 inside its support. In the top right, close to the support, a couple of springs are visible.

The mirrors are then adjusted to their nominal position (centred with respect to the cradle) by means of the set screws and verifying the position with a caliper. After this procedure, the mask is fastened to the cradle and the alignment phase can start. The only mirror which is located decentered with respect to the cradle is M2. Due to a misunderstanding, its cradle has been designed considering the surface in the Zemax optical design file, where it is a decentered portion (1 mm) of an on-axis spherical mirror. The mirror has been purchased as a simple spherical surface having in mind to use only

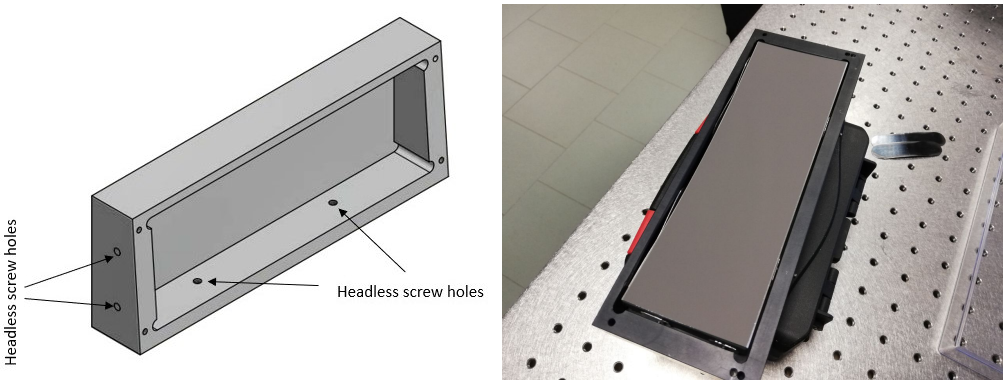

(a) (b)

Figure 7.8: a: CAD sketch of a cradle. b: M1 inside its support.

the off-axis portion. This means that mounting the mirror centred in the cradle introduces a decentering of the mirror itself of 1 mm when integrated in the instrument. Since the problem has been identified during the alignment, it has been fixed decentering the mirror by means of the bottom set screws. The screws are metric M3x0.5, thus we turned both the screw making two complete rotations. The cradles are positioned on the main structure inserting the threaded rods in the corresponding holes on the wall. For each mirror, the wall has four holes for the threaded rods and four holes for a set of springs (see Figure 7.9a). These springs have one side constrained at a corner of the mirror mask and the other side constrained to the structure wall by means of rod. The springs are not part of the original design and they have been added later: in fact, during the preliminary alignments it was understood that it was not possible to move these heavy mirrors in a reliable way, making the alignment procedure extremely difficult. The problem has been attributed to the gravity and a system of four symmetric springs has been introduced to improve the stability and to support the weight. For the same reason, a fourth threaded rod has been added in addition to the three foreseen at the beginning (it is possible to see the hole in the structure for M1 in Figure 7.9a). Actually, only three rods has been used to alignment. The spring system has been not implemented for M2 and the folding (Figure 7.9b) because it is mechanically difficult to realize.

The alignment has been divided into two main steps:

- coarse alignment
- fine alignment

The objective of the coarse alignment is to locate the optical elements in a near-nominal position, which is required by the fine alignment step. The mirrors are collocated following the order in which they reflect the light, thus M1, M2, M3 and the folding mirror. The procedure is almost the same for all of them.

First, the cradle is located at nominal distance from the supporting wall, that is, 3 mm for M1, M2 and M3 and 2.7 mm for the folding mirror (Figure 7.10).

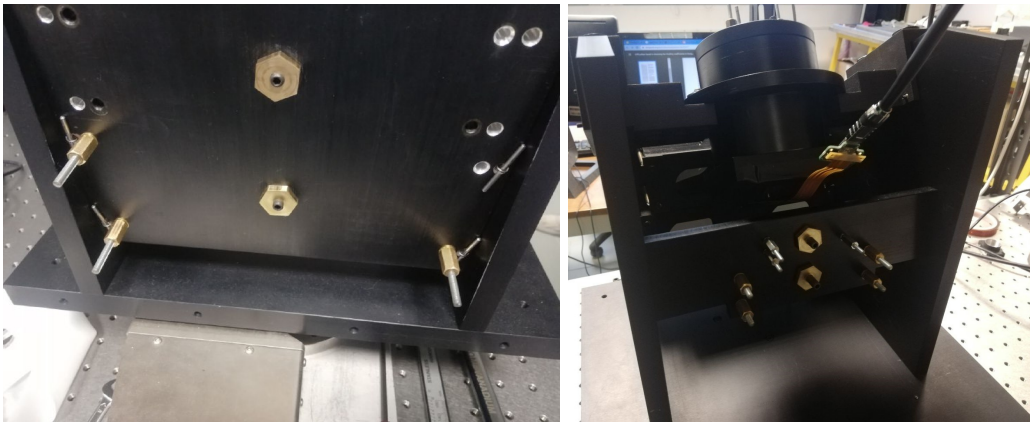

(a) (b)

Figure 7.9: a: CAD sketch of a cradle. b: M1 inside its support.

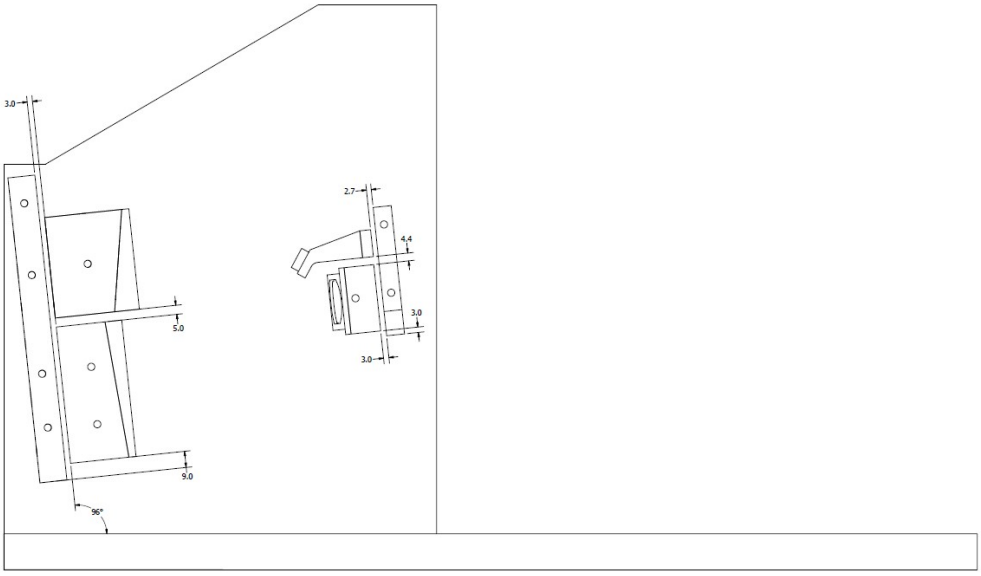

Figure 7.10: Nominal relative distances between elements of the TMA

This is achieved using a couple of calibrated shims which are located between the cradle and the wall. The position is fixed using a pusher set screw fitting a recess in the middle of the cradle, shaped like a spherical sector to fit the spherical head of the screw. As a further check, the length of the protruding part of the screw (out the wall) is measured with a caliper and verified against the expectation. The shims are then removed to allow regulating the orientation of the cradle. The screw is locked with a nut. A target graph paper is prepared and accurately placed in front of the mirror to be aligned. The

nuts on the threaded rods are used to move the spots coming from the AT towards the nominal position on the target. An example is shown in Figure 7.11; this figure refers to the spots after the folding mirror but the concept is the same for all mirrors.

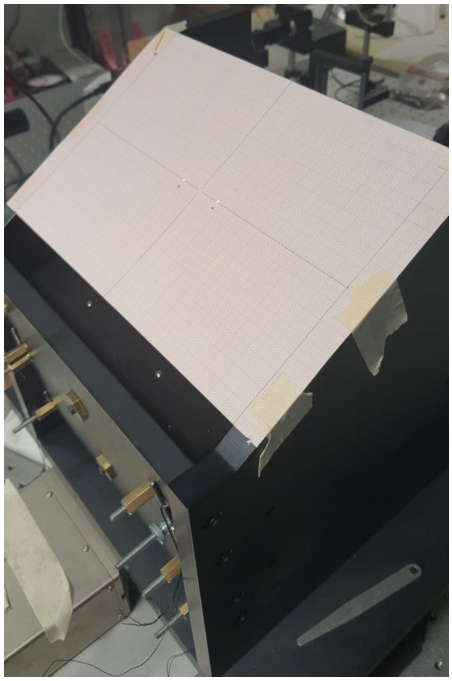

Figure 7.11: graph paper target after positioning of folding mirror

The graph paper target is prepared using the Zemax simulation of the system. The CAD (Autodesk Inventor) model of the instrument is used as support to precisely evaluate the nominal distances between the elements and to easily calculate them with respect to convenient points. The target indicates where the footprints of the laser beams should be without the next mirror (thus on the supporting wall). At every step, the spots coordinates are checked both in Zemax and Inventor as double check. This procedure is repeated also for M3. For M2 and the folding mirror it has been decided to fix them in nominal position by means of calibrated shims. This leads to a drawback: usually the alignment of a TMA is performed using M2 as compensator (Korsch 1977), but we found difficulties and poor reliability in the movement of M2 and the folding mirror, probably due to the lack of the springs, making very difficult the regulation of their position.

The procedure has been repeated several times trying to improve the results. It was found that the spots positions are in agreement with the nominal positions for M1, M2 and M3. Instead, after the folding mirror, the spots result to have a deviation from the expected, in particular along a specific direction. It was decided to perform a correction, operating manually on M1 and M3 in order to move the spots towards the target line, leaving to the fine alignment procedure the correction of the possible induced misalignment. In Figure 7.11 the crosses indicate where the spots are located before the

correction, and the horizontal line where they have expected to be; the deviation is about 4 mm.

The coarse alignment should provide a good starting point for the fine alignment phase. A camera has been placed on a precision micrometric manual linear stage and used to record the relative positions between the spots. The centroid of each spot is determined by fitting the intensity with a 2D gaussian. This information is used to start an optimization procedure. The spots distances are inserted in the merit function and the local optimization algorithm, starting from the nominal optical configuration, tries to reach the observed points changing the selected variables. We selected the x/y rotations of M1 and M3 as the most plausible. The opposite rotations are applied to the instrument to move the system from the misaligned configuration towards the nominal. The code performs a local optimization and thus it is important to provide a starting points near the local minimum. The Zemax simulation has been properly adapted to the laboratory condition, in particular, the rotation pivotal points have been located in the middle of mirrors cradles, since the cradles are kept in position by the central pusher set screws. The rotations are thus converted into rotations to give to the nuts of the cradles by means of the formula:

$$\theta[^\circ] = L \cdot \frac{\alpha_{Zemax} \cdot \pi}{180} \cdot \frac{1}{d} \cdot 360^\circ \tag{7.2}$$

where L is the distance between the middle of the cradle and the threaded rods (which depends from the considered rotation and the mirror). This is summarized in Table 7.1 where it is indicate what is used for the selected rotations. α is the angle retrieved from the optimization and d is the thread pitch. The threaded rods used have d equal to 0.7 mm.

L parameter for Equation 7.2

	x axis	y axis
M1	30 mm	95.5 mm
M3	20 mm	84.5 mm

Table 7.1: L parameter to be used in Equation 7.2.

During the fine alignment, we realized that the optimization procedure is capable to move the spots towards a desiderated relative position but this is not sufficient to guarantee an absolute positions of the spots on the focal plane (probably because in principle the merit function included only the relative spot positions), depending on the initial absolute position of the spots themselves. The merit function has been modified, constraining the optimizator to consider also the footprint coordinates on the folding mirror. We expect that this should improve the reliability of the fine alignment procedure. Due to stringent scheduling requirements the alignment has been considered satisfactory when the distances between the spots are nominal and the FWHM of the spots is within the 20% of the nominal one.

Figure 7.12 shows a mosaic image of a through focus acquisitions. The red dotted

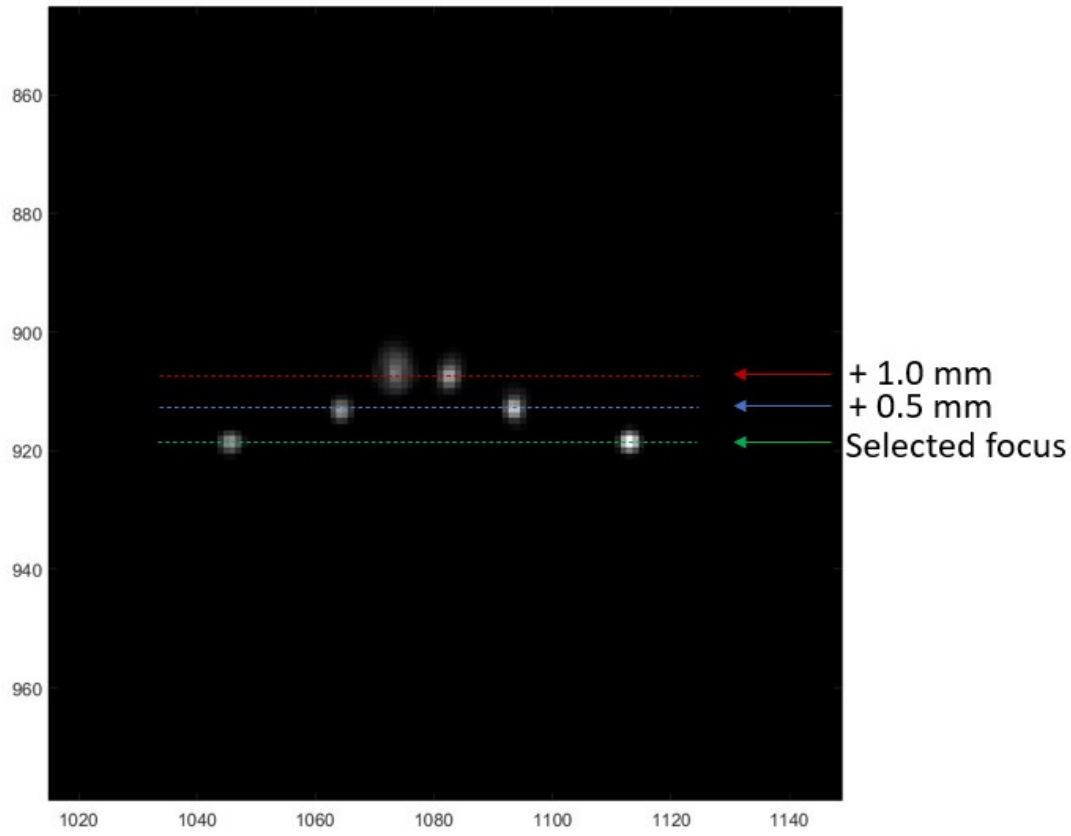

Figure 7.12: Through focus spots. *Left* and *Right* spots are from Channel1 and Channel2 in Section 5.2. The red dotted line indicate the focus according to the optical design, the green dotted lined the selected focus (best focus position).

line indicates the focus according to the optical design, the green line the selected focus position and the blue line an intermediate position between them. The estimated inter-spot positions are reported in Table 7.2, where it is possible also to compare them with that from simulations. There is a good agreement. However, due to some yet unexplained reason the best focus position is 1 mm towards the folding mirror (green dotted line).

	Inter-spot distance [μm]	
	Zemax	Obtained
+1mm	54	49.48
+0.5	159	160.28
Selected focus	371	370

Table 7.2: Comparison between nominal and obtained through focus positions

It is possible to observe the presence of a residual misalignment, in fact, the right

	FWHM [μm]	
	x	y
Left	14.74	14.18
Right	13.45	14.02
Airy	13.26	13.26

Table 7.3: FWHM values, focus position

channel is brighter than the left channel and the spread induced by aberration is more evident at the +1 mm line (red) from the selected focus position. The values of the FWHM (Full Width Half Maximum) at the focus are reported in Table 7.3. To have a comparison also the FWHM of the diffraction PSF (Point Spread Function) is reported. The latter is calculated as

$$FWHM_{Airy} = 1.028 \cdot \lambda \frac{f}{D} \tag{7.3}$$

with f the focal length of the instrument (assumed to be 244.5 mm), λ the wavelength (0.633 μm the wavelength of used HeNe laser) and D is the diameter of entrance pupil (here the laser beam diameter, 12 mm).

Part III

Conclusions

Chapter 8

Summary and conclusions

This PhD thesis is focused on the activities of characterization and calibration of two optical instruments, different both for type (JANUS is a high-resolution camera and the other a stereo imaging spectrometer) and for development phase (JANUS is ready to be launched in April 2023 and HYPSOS is a laboratory prototype). This work is therefore structured in two main themes: (i) the analysis of the data coming from the on ground calibration activities for JANUS and (ii) the description of the activities on the optical bench to develop the HYPSOS instrument prototype and its setup.

8.1 JANUS

A very large amount of data has been generated during the on ground calibration campaign of the JANUS instrument. The performed measurements cover, besides the "classic" aspects of an optical instrument (that is radiometric, geometric and spectral), also instrument-related behaviours (Agostini et al. 2023). The section of this thesis dedicated to JANUS is focused on the preliminary analysis of the radiometric, geometrical and spectral calibration sessions; on the analysis of the detector performance (such as offset stability and dark current) and a description of an effect (called *Offset Hollow effect*) observed on the experimental data is presented.

The first step has been to study the stability of the Offset (sometimes called Fixed Pattern Noise, FPN) at different temperatures and the possible impact of the dark current. It has been verified that the variation of the Offset is negligible in the temperature operative range and the dark current contribution is less than 6 DN at 100 s with no contribution with an exposure time lower than 10 s.

The objective of a radiometric calibration is to provide a mapping function between a traceable radiometric standard and the digital response of the instrument (DN). For JANUS, it could be achieved using a calibrated integrating sphere coupled to the thermo-vacuum chamber window. Two acquisition strategies have been used: (i) fixed radiance level and variable exposure time (namely ITFvsTEXPO) and (ii) fixed exposure time and variable radiance level (namely ITFvsRAD). The analysis shows that the shutter position (and therefore the radiance level evaluated using it) is not reliable and a more

appropriate way to determine the right spectral radiance level observed by the instrument is to use the photodiode current as parameter. Following the approach also used in Slemer et al. 2019 and Cremonese et al. 2020, the mean instrument response (in DN) has been plotted with respect to radiance multiplied the exposure time variable, allowing to combine the ITFvsTEXPO and ITFvsRAD measurements in the same plot, also at different temperatures. The result of this analysis is a set of (average) absolute radiometric calibration curves, one for each of the 13 filters which is possible to use in JANUS. The instrument shows very limited radiometric response variation with temperature, suggesting a very stable behaviour in this sense. Almost all the filters show a consistent behaviour, with the valuable exception of the panchromatic filter (F1) at low exposure time showing a divergence between the two types of measurements. An explanation is currently under study. A radiometric model has been developed using the most updated data and compared with the on ground measurements shows a good agreement, in particular up to half of the dynamic range, where the non-linearities of the detector have lower impact. The objective of the geometrical calibration is to provide a mapping between the 3D coordinates of the real "world" and the 2D image coordinates. For JANUS, the strategy used (called *Line Of Sight* or LOS) is to point a collimated beam in 63 known directions (in the JANUS FOV) with respect to a known reference system. In this thesis, the identification of the geometrical properties (focal length, FOV, IFOV and boresight direction) has been faced considered those of an ideal model which is determined minimizing the difference between the ideal model itself and the actual image data using a non-linear least squares optimization technique. Since JANUS is an axisymmetric on-axis telescope a pinhole mode has been considered a good option; another considered ideal model is the intrinsic one, making it possible to have different focal lengths for horizontal and vertical directions. In principle this method also provides the distortion map. Since the intrinsic high spatial resolution of the instrument it is very difficult to provide very reliable data with a ground-based setup. It has been not possible to derive a trustworthy set of geometrical parameters due to a not well understood pattern observed on the data. A suggested hypothesis is that the kinematic positioning system (the hexapod) introduced a "drift" in the angular orientation of the beam. An attempt to perform a relative correction has been made and a synthetic model of the JANUS-setup system has also been developed and used to guide this process. After the correction the expected pincushion distortion can be observed but with an amplitude slightly higher than the theoretical one. The estimated focal length (pinhole model: 468.3 mm; intrinsic model: 468 mm in y direction and 468.6 mm in x direction) is also slightly higher than expected (467 mm). Moreover, a focal length different if the horizontal/vertical direction is considered seems to be consistent with a simpler estimation based on the $\Delta x = f\ tan(\Delta\theta)$ formula (with Δx the distance between the spots on the focal plane, f the focal length and $\Delta\theta$ the angular separation between the spots). At this stage it is very difficult to separate the effects of the setup from the actual geometrical behaviour of the instrument. The analysis of specific measurement sessions (called *Boresight*), in which the hexapod has been kept fixed and the filter changed, seems to suggest the possibility that the boresight directions (potentially each filter has its own boresight direction) have very limited angular

separation.

The spectral calibration measurements have the main objective to verify the bandpass and the central wavelength of each filter. The measurement setup takes advantage of a monochromator coupled to an integrating sphere to illuminate a pinhole on the focal plane of a collimator. Although the filters response functions appear, to some extent, different from the expected ones in shape, in particular for filters at wavelength lower than 600 nm, the bandpass and the position in the spectrum appear to be in line with the expectation. The different shape is probably due to an incorrect normalization of the experimental data.

It has been observed on the experimental data that when the detector is illuminated by a source, no matter its shape, the signal level outside the image of the source is lowered with respect to the expected level and involves all the pixels having the same row index of the illuminated one. The magnitude of this effect, for each row, depends on the number of illuminated pixels in the same rows and on the signal level. Moreover a deep hollow is present in a region having pixels with higher column index. A complete comprehension of the effect is under study but a very recent paper (published during the writing of this thesis, Wocial et al. 2022) suggests an explanation.

The analysis performed on the on-ground calibration data allowed to achieve a preliminary, but solid, confidence on a significant portion of the dataset. A set of functions has been developed in MatLab tailored for the analysis of these data. The first direct result of the analysis presented in this thesis is its application to a first version of the calibration pipeline, in particular for the radiometric section and the offset/dark current behaviour. The radiometric curves, here presented only as an average response over the detector, could be easily extended to all pixels providing an absolute calibration of the instrument. The apparent different radiometric curve of F1 at low exposure time (a study on it is currently ongoing) could provide an insight into not yet understood behaviour of the instrument. The analysis of the geometrical calibration sessions revealed the mandatory requirement to perform one or more stellar field acquisitions during the interplanetary cruise in order to derive the geometrical information and the distortion map. The study performed in this context allowed us to develop a solid basis for the analysis of the in-flight calibrations.

8.2 HYPSOS

HYPSOS is a novel type of optical instrument able to provide contemporary 3D spatial information and spectral one (in a hyperspectral mode). The project started in April 2019 and it has required several different actions to implement the instrument on the optical bench. Since the main objective is the validation of the instrument concept, the integration of the instrument as a stand-alone unit is not sufficient and also the development of a suitable setup able to verify its working capabilities is required. This thesis summarizes the activities and the (preliminary) results achieved in the framework of this project. Before integrating the whole instrument several components have been singularly characterized including the two off-axis aspheric mirrors of the telescope (M1

and M3) and the diffraction grating. To test the mirrors and align the TMA (Three Mirror Anastigmat) telescope, a system able to generate three collimated parallel laser beams has been assembled and aligned (called Alignment Tool). The mirrors have been tested comparing a through focus acquisition with the expectation derived from the analogous ZEMAX model. In this way it has been possible to verify that the first sample of M3 had the wrong conic constant sign. The diffraction grating has been characterized using an Atomic Force Microscope, which allowed us to observe the average surface quality and to retrieve the main grooves parameters. After that, an analysis of the diffraction efficiency has been performed experimentally in the reflectometer facility of CNR-IFN in Padua using a custom readout circuit. The diffraction efficiency measurements at different angles have been compared with simulations developed in PCGrate, showing a general agreement in the trend, in particular at incidence angles 0° and 40°. The comparison in the case of the near-littrow condition seems to be less reliable for wavelengths higher than 450 nm. However, considering that this type of measurement is very complex and demanding, the results could be considered satisfactory. Some criticalities have been identified and could be used in a future to improve the reliability of the analysis. An important phase of this work has been the integration, verification and alignment of the telescope and the spectrometer. A procedure has been developed to align the diffraction grating in the spectrometer barrel, taking advantage of the symmetry of the diffraction orders and a procedure to align the telescope using the Alignment Tool. The latter is divided into two steps: a coarse alignment and a fine alignment. In the fine alignment phase, the optimization module of Zemax is used to determine the rotations to give to M1 and M3 in order to move two reference spots (images of the laser beams of the Alignment Tool) from the nominal position to the actual measured on the system. The FWHM of the on-axis spots are within the 20% of the nominal ones, although, due to unexplained reasons the best focus position is 1 mm away from the nominal one. A preliminary spectral calibration has been performed using a set of spectral lamps. The relationship between the central wavelength (of the spot) and the band (the pixel index) can be assumed to be linear and the measured dispersion is about 34.32 nm/mm very close to the nominal one of 34.7 nm/mm. Taking advantage of experience gained on STC (Naletto et al. 2012,Simioni et al. 2017) a dedicated setup has been developed. It is able to simulate dynamically a satellite pushbroom acquisition mode. This is achieved by means of a collimator, an illumination system with a linear stage allowing the relative movement of the target with respect to the instrument and a custom control software. A set of custom python modules has been developed and used to interface the control software with the setup hardware (rotator and linear stages and the detector). The pushbroom acquisition is simulated synchronizing the camera frame rate with the linear stage velocity. A preliminary test has been made to verify both the control software capabilities and the DTM generation method (Re et al. 2022) with very promising results.

The work conducted in the framework of the HYPSOS project posed a strong baseline for the future development of this instrument. The instrument has been prepared for the last part of the integration process (taht is the alignment of pechan prisms and the coupling of the spectrometer with the telescope). During the integration and the

alignment several criticalities have been identified (such as the sensibility of the mirrors cradles to gravity) and several problems have been faced (such as the identification of a wrong mirror conic constant). A setup has been studied and prepared, along with a dedicated control software able to manage the hardware and simulate (in scale) a dynamic pushbroom acquisition. This type of setup could be very useful to test both the performance of pushbroom-based instruments and the reconstruction algorithms in a controlled environment. An undesired effect, the Channel Crosstalk, has been identified and although it can be neglected for the laboratory-based implementation, it should be inevitably considered for a future spacecraft-oriented instrument. On the basis of the preliminary results obtained, the instrument is very promising about the achievement of its objective: providing 3D spatial and spectral information with a single instrument and avoiding problems of cross-calibration between different instruments, currently required to have the same information.

Part IV

Appendix

Appendix A

Radiometric calibration curves

The used convention is: the colours indicate the different filters. The different sessions are distinguished by different markers and the percentage deviations by different line styles.

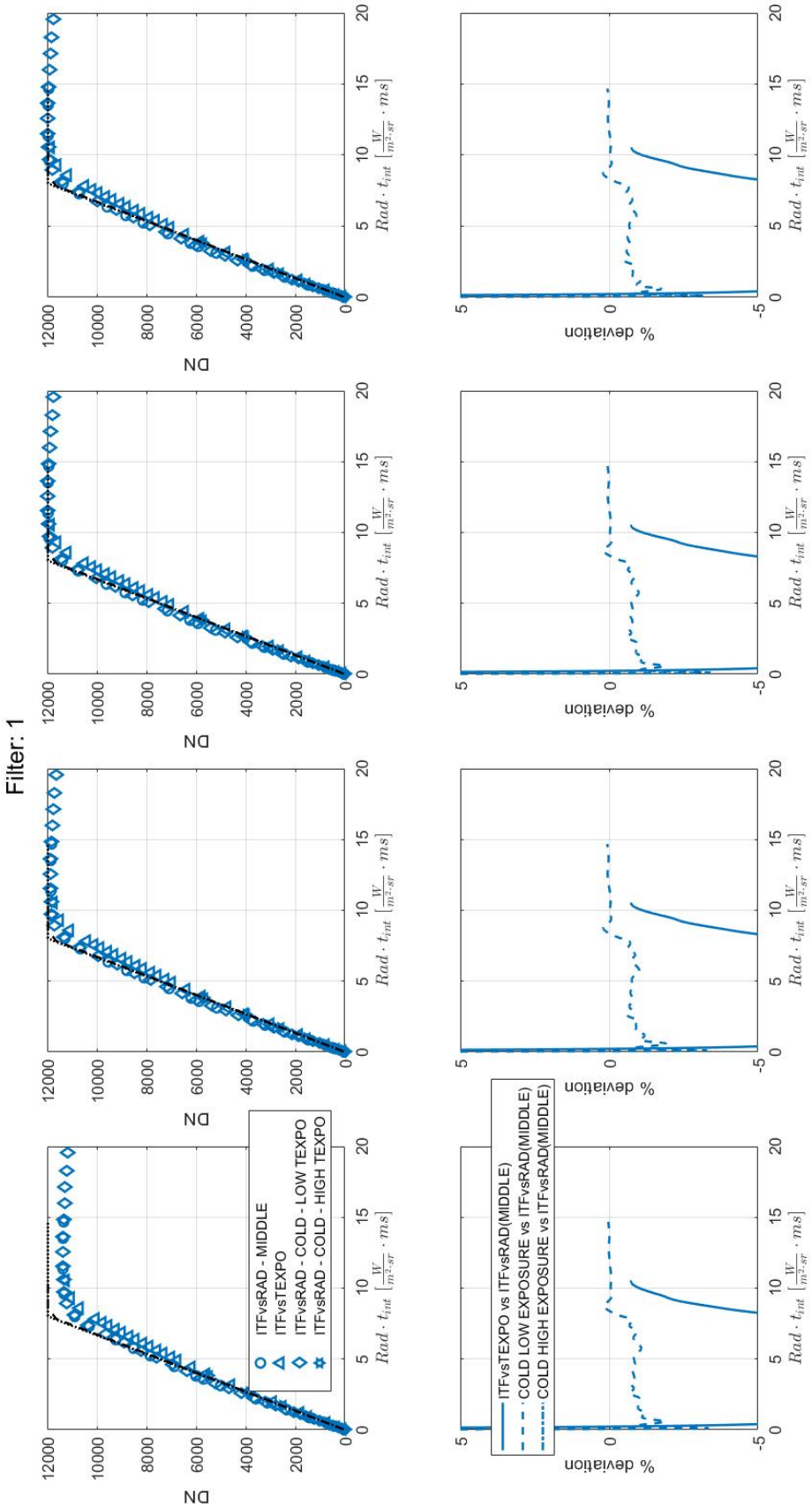
Filter: 1
DN
% deviation
$Rad \cdot t_{int}\ [\frac{W}{m^2 \cdot sr} \cdot ms]$
ITFvsRAD - MIDDLE
ITFvsTEXPO
ITFvsRAD - COLD - LOW TEXPO
ITFvsRAD - COLD - HIGH TEXPO
ITFvsTEXPO vs ITFvsRAD(MIDDLE)
COLD LOW EXPOSURE vs ITFvsRAD(MIDDLE)
COLD HIGH EXPOSURE vs ITFvsRAD(MIDDLE)

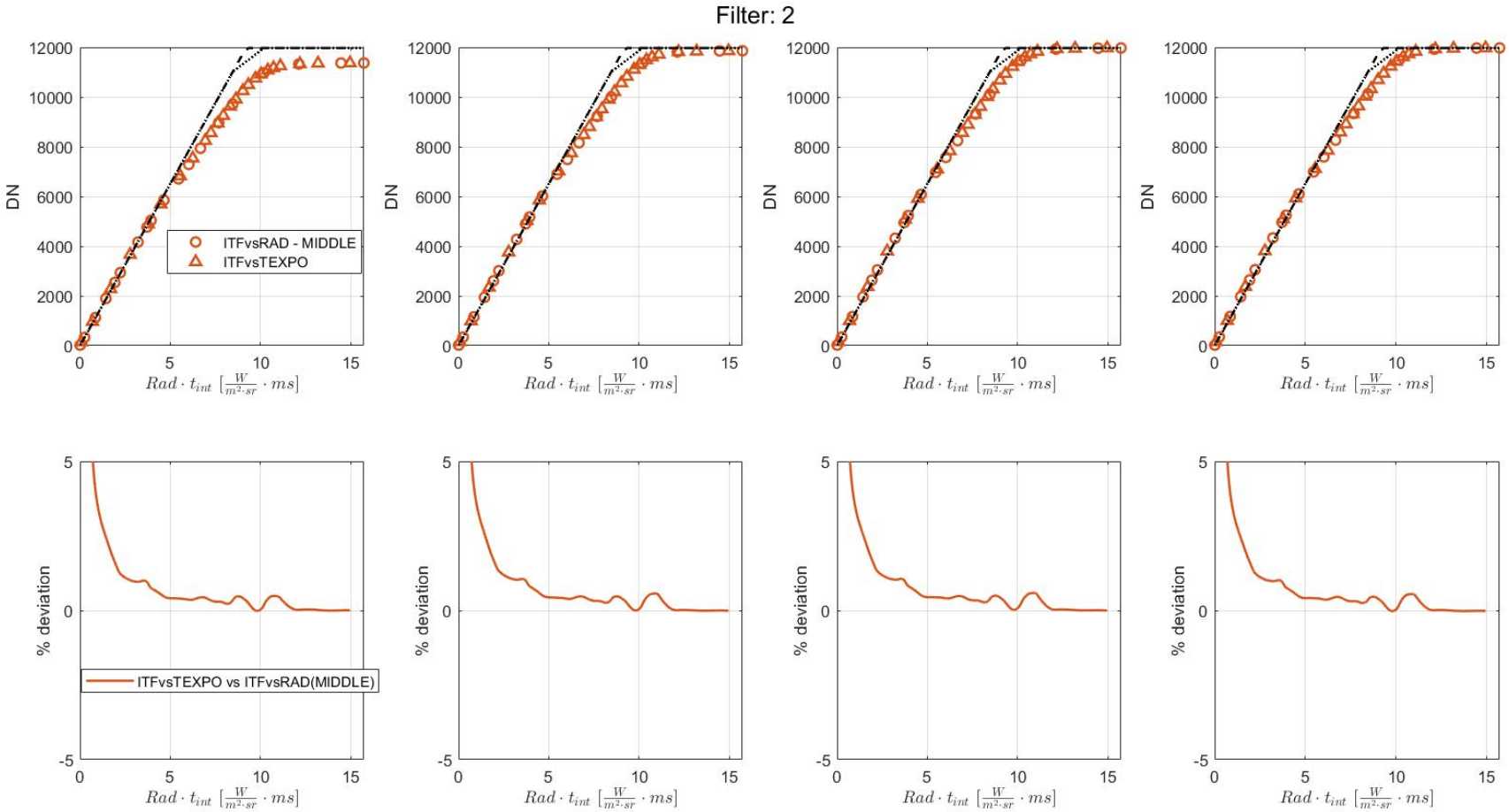
Filter: 2
DN
ITFvsRAD - MIDDLE
ITFvsTEXPO
$Rad \cdot t_{int}\ [\frac{W}{m^2 \cdot sr} \cdot ms]$
% deviation
ITFvsTEXPO vs ITFvsRAD(MIDDLE)

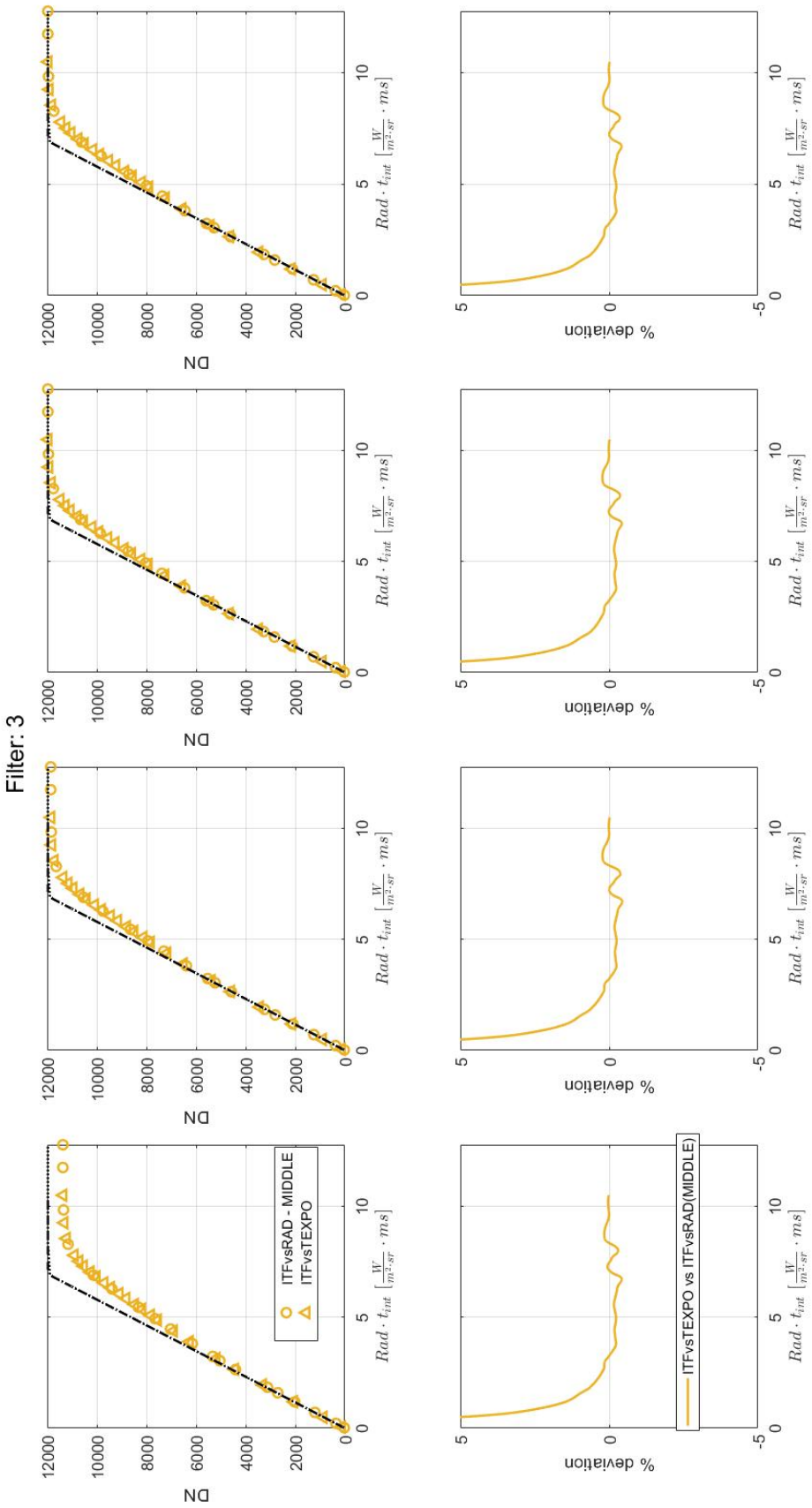
Filter: 3
DN
% deviation
$Rad \cdot t_{int}\ [\frac{W}{m^2 \cdot sr} \cdot ms]$
ITFvsRAD - MIDDLE
ITFvsTEXPO
ITFvsTEXPO vs ITFvsRAD(MIDDLE)

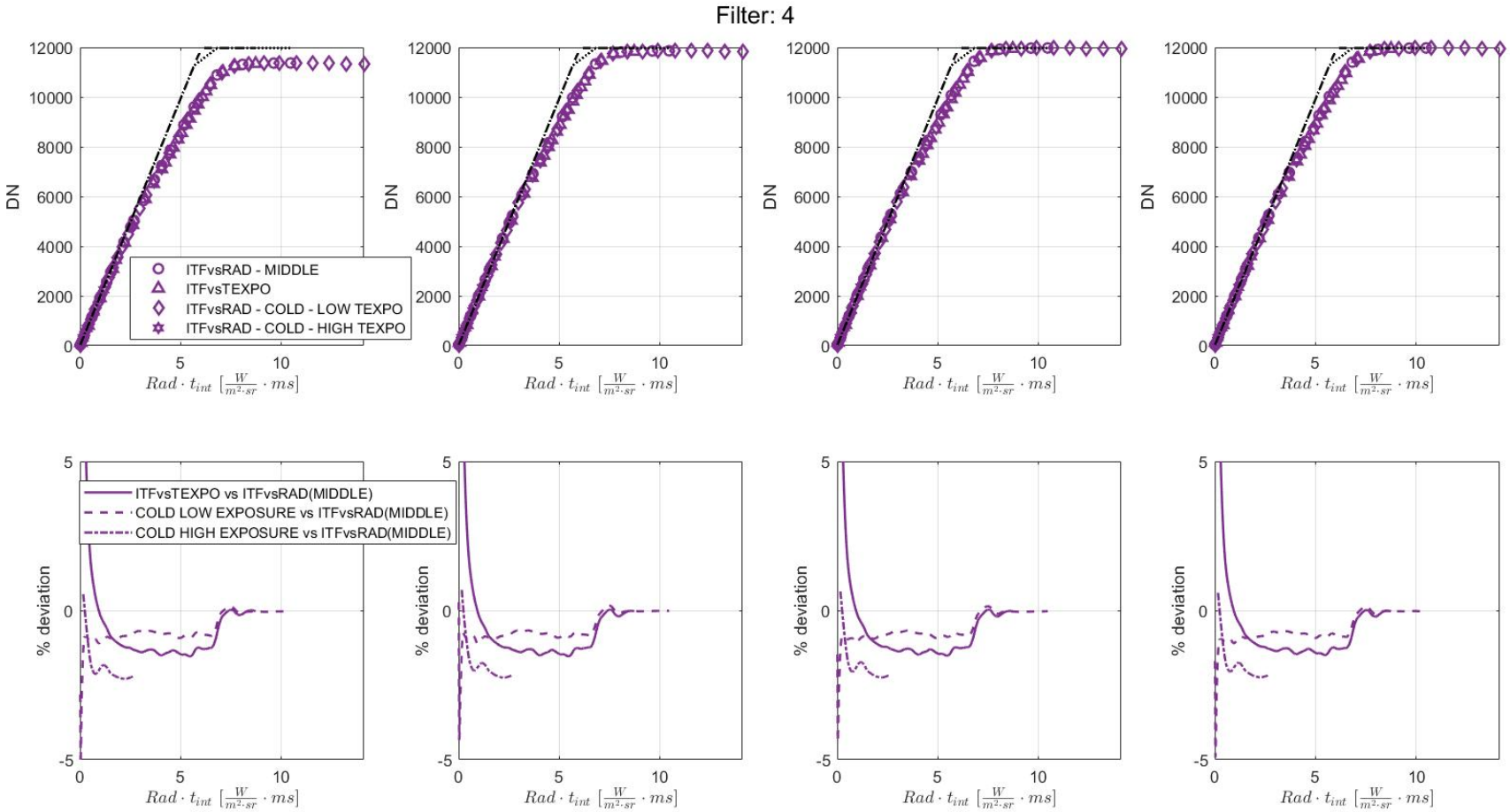
Filter: 4
DN
$Rad \cdot t_{int}\ [\frac{W}{m^2 \cdot sr} \cdot ms]$
ITFvsRAD - MIDDLE
ITFvsTEXPO
ITFvsRAD - COLD - LOW TEXPO
ITFvsRAD - COLD - HIGH TEXPO
% deviation
ITFvsTEXPO vs ITFvsRAD(MIDDLE)
COLD LOW EXPOSURE vs ITFvsRAD(MIDDLE)
COLD HIGH EXPOSURE vs ITFvsRAD(MIDDLE)

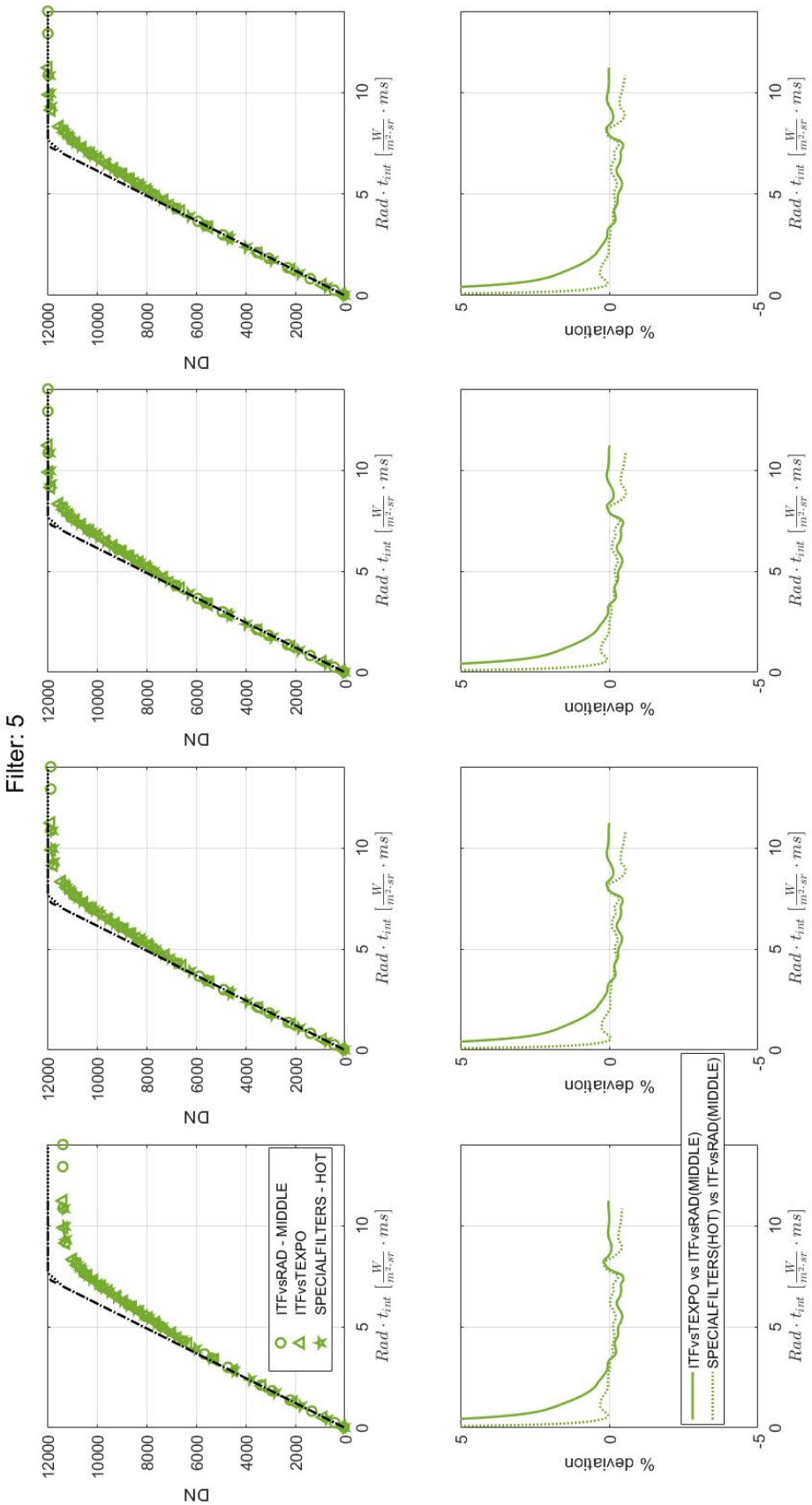
Filter: 5
DN
% deviation
$Rad \cdot t_{int}\ [\frac{W}{m^2 \cdot sr} \cdot ms]$
ITFvsRAD - MIDDLE
ITFvsTEXPO
SPECIALFILTERS - HOT
ITFvsTEXPO vs ITFvsRAD(MIDDLE)
SPECIALFILTERS(HOT) vs ITFvsRAD(MIDDLE)

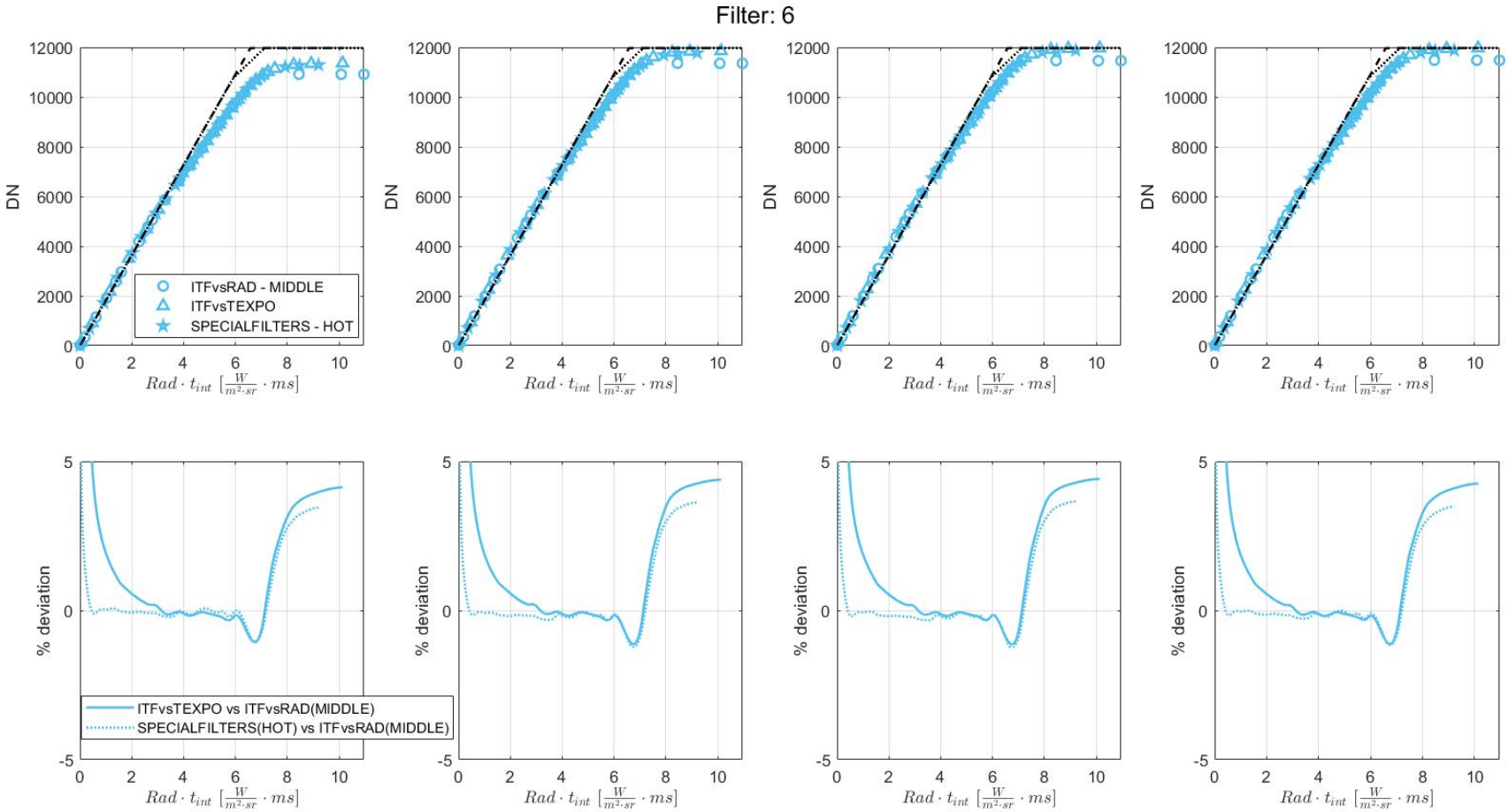
Filter: 6
DN
ITFvsRAD - MIDDLE
ITFvsTEXPO
SPECIALFILTERS - HOT
$Rad \cdot t_{int}\ [\frac{W}{m^2 \cdot sr} \cdot ms]$
% deviation
ITFvsTEXPO vs ITFvsRAD(MIDDLE)
SPECIALFILTERS(HOT) vs ITFvsRAD(MIDDLE)

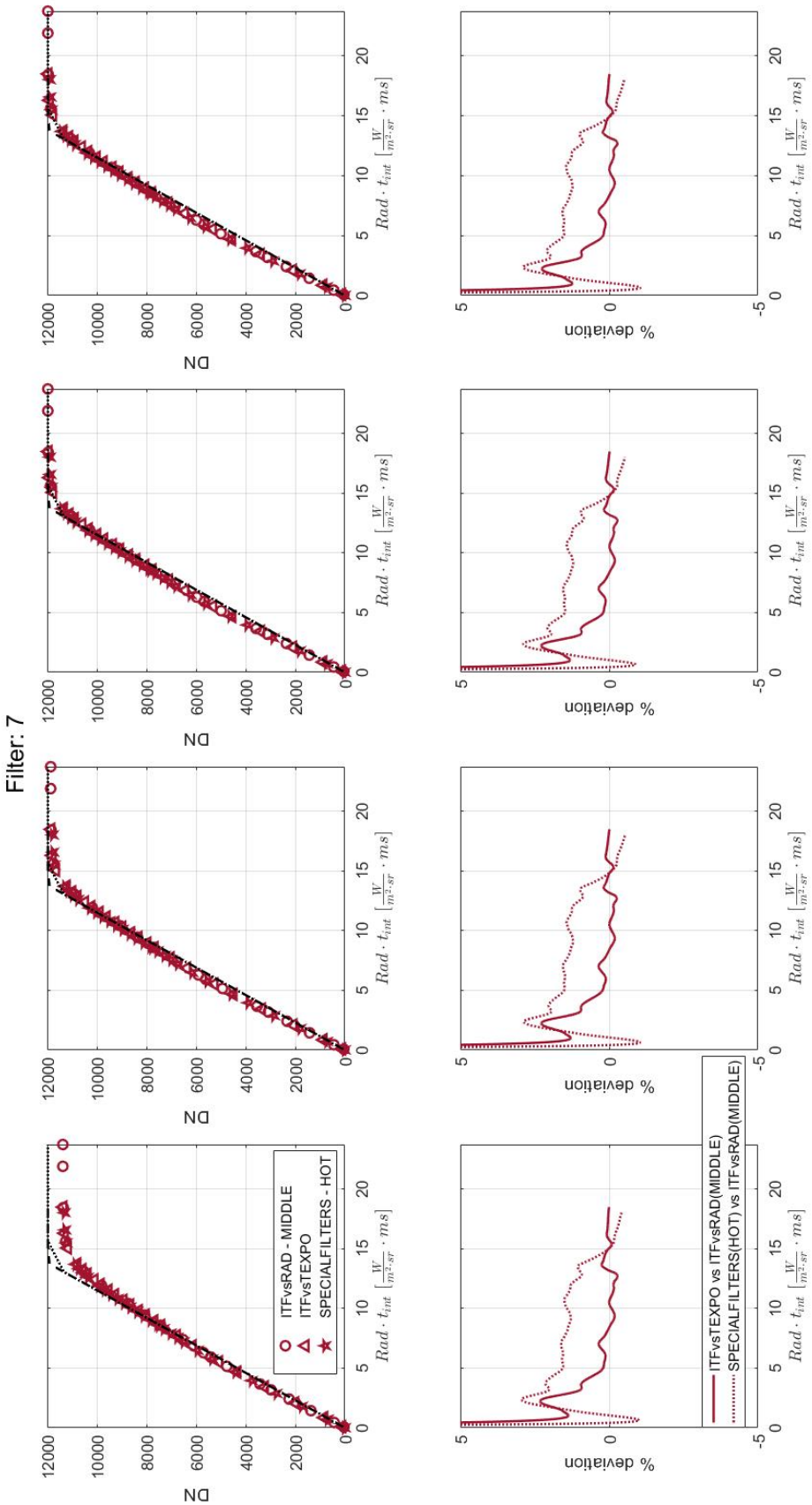
Filter: 7
DN
% deviation
$Rad \cdot t_{int}\ [\frac{W}{m^2 \cdot sr} \cdot ms]$
ITFvsRAD - MIDDLE
ITFvsTEXPO
SPECIALFILTERS - HOT
ITFvsTEXPO vs ITFvsRAD(MIDDLE)
SPECIALFILTERS(HOT) vs ITFvsRAD(MIDDLE)

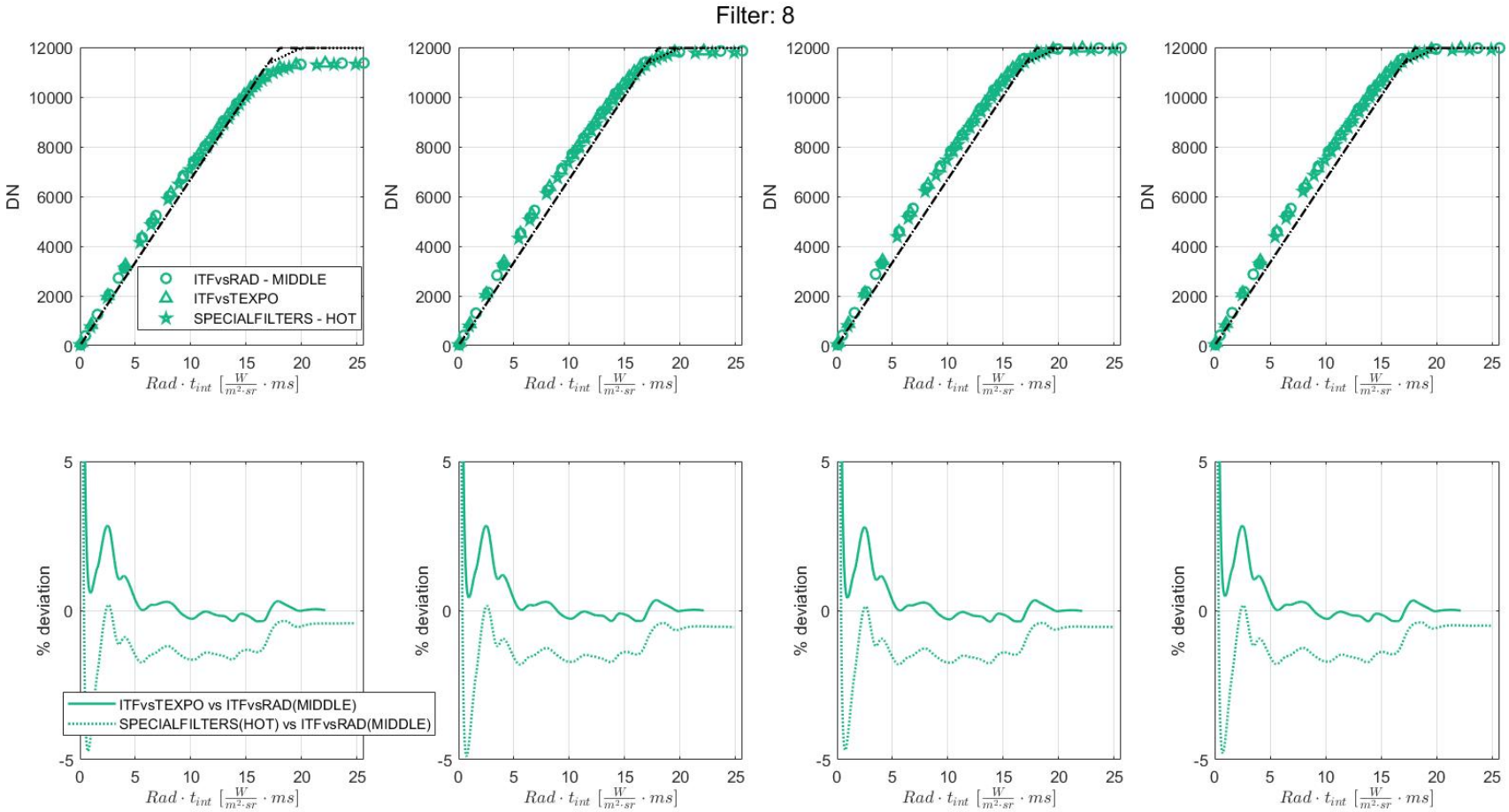
Filter: 8
DN
ITFvsRAD - MIDDLE
ITFvsTEXPO
SPECIALFILTERS - HOT
$Rad \cdot t_{int}\ [\frac{W}{m^2 \cdot sr} \cdot ms]$
% deviation
ITFvsTEXPO vs ITFvsRAD(MIDDLE)
SPECIALFILTERS(HOT) vs ITFvsRAD(MIDDLE)

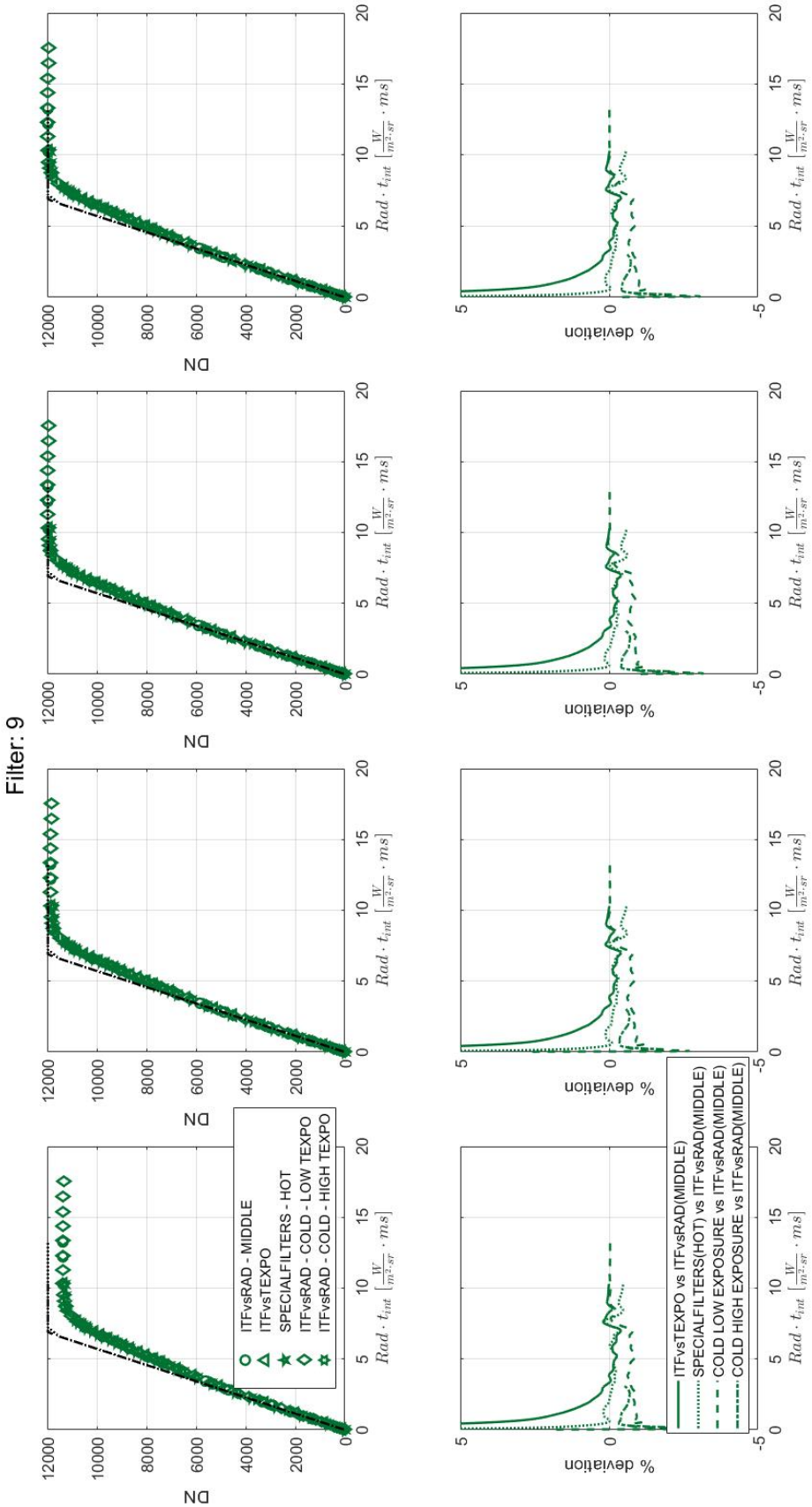
Filter: 9
DN
% deviation
$Rad \cdot t_{int}\ [\frac{W}{m^2 \cdot sr} \cdot ms]$
ITFvsRAD - MIDDLE
ITFvsTEXPO
SPECIALFILTERS - HOT
ITFvsRAD - COLD - LOW TEXPO
ITFvsRAD - COLD - HIGH TEXPO
ITFvsTEXPO vs ITFvsRAD(MIDDLE)
SPECIALFILTERS(HOT) vs ITFvsRAD(MIDDLE)
COLD LOW EXPOSURE vs ITFvsRAD(MIDDLE)
COLD HIGH EXPOSURE vs ITFvsRAD(MIDDLE)

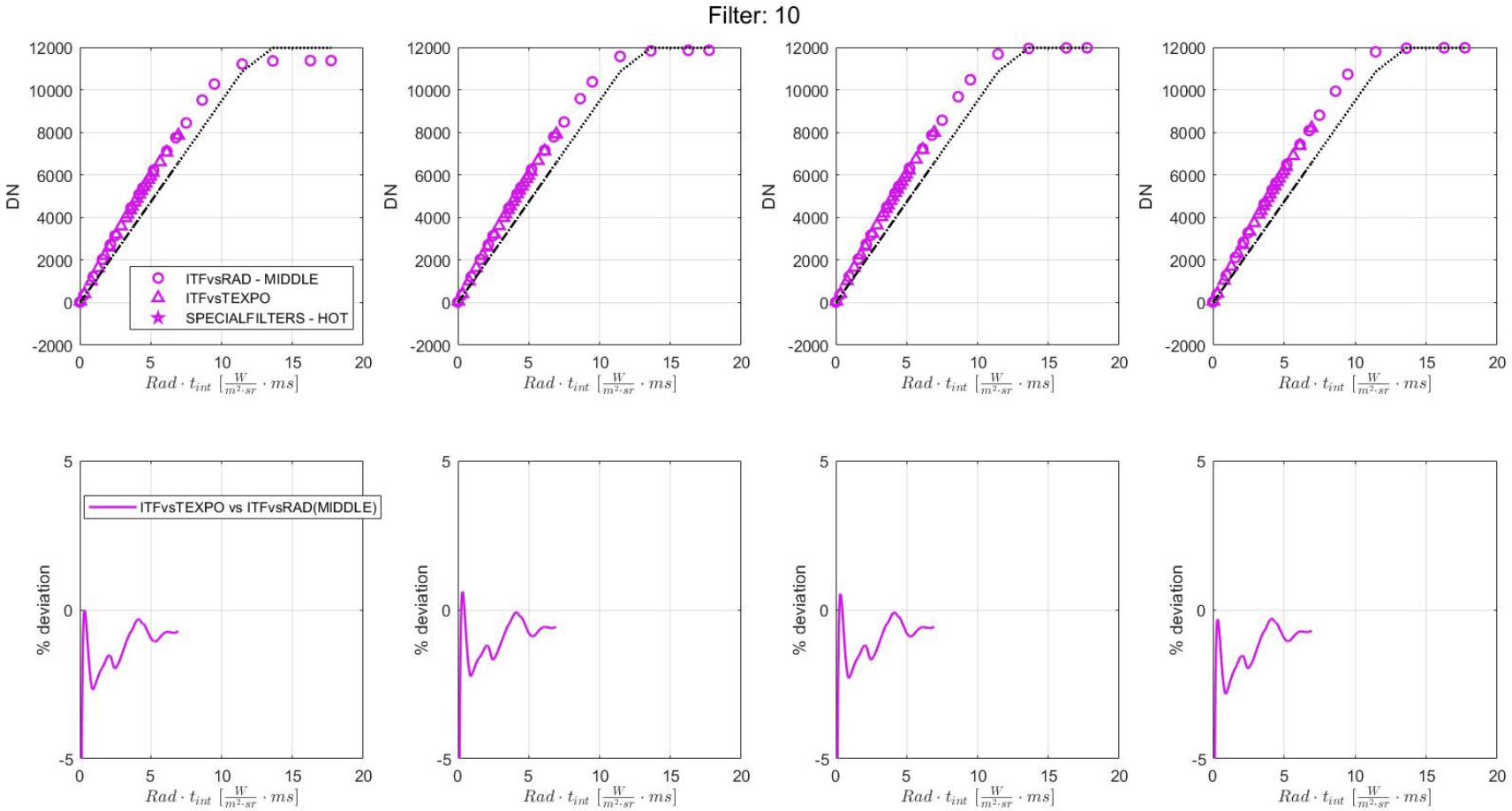
Filter: 10
DN
$Rad \cdot t_{int}\ [\frac{W}{m^2 \cdot sr} \cdot ms]$
ITFvsRAD - MIDDLE
ITFvsTEXPO
SPECIALFILTERS - HOT
% deviation
ITFvsTEXPO vs ITFvsRAD(MIDDLE)

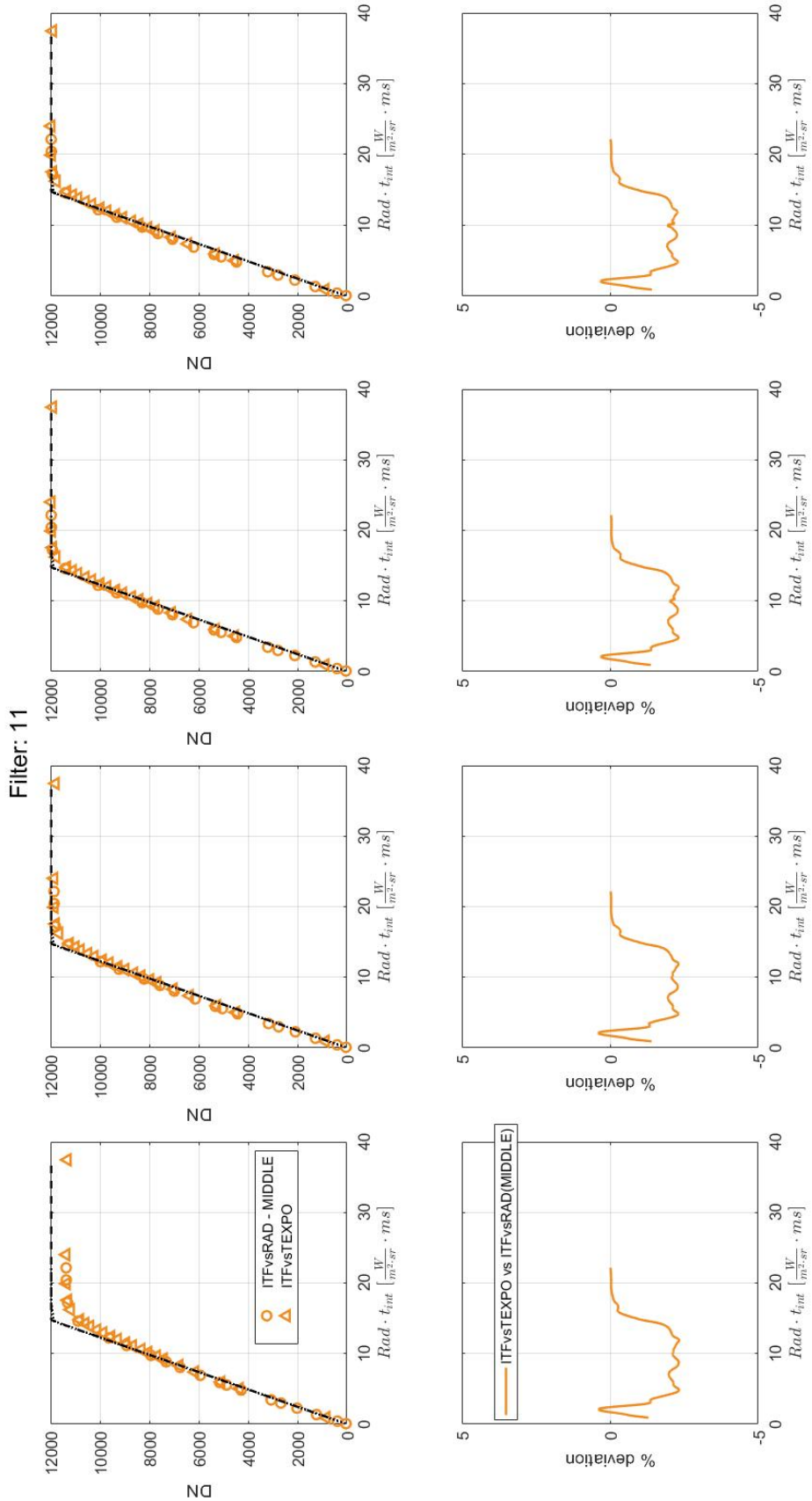
Filter: 11
DN
% deviation
$Rad \cdot t_{int}\ [\frac{W}{m^2 \cdot sr} \cdot ms]$
ITFvsRAD - MIDDLE
ITFvsTEXPO
ITFvsTEXPO vs ITFvsRAD(MIDDLE)

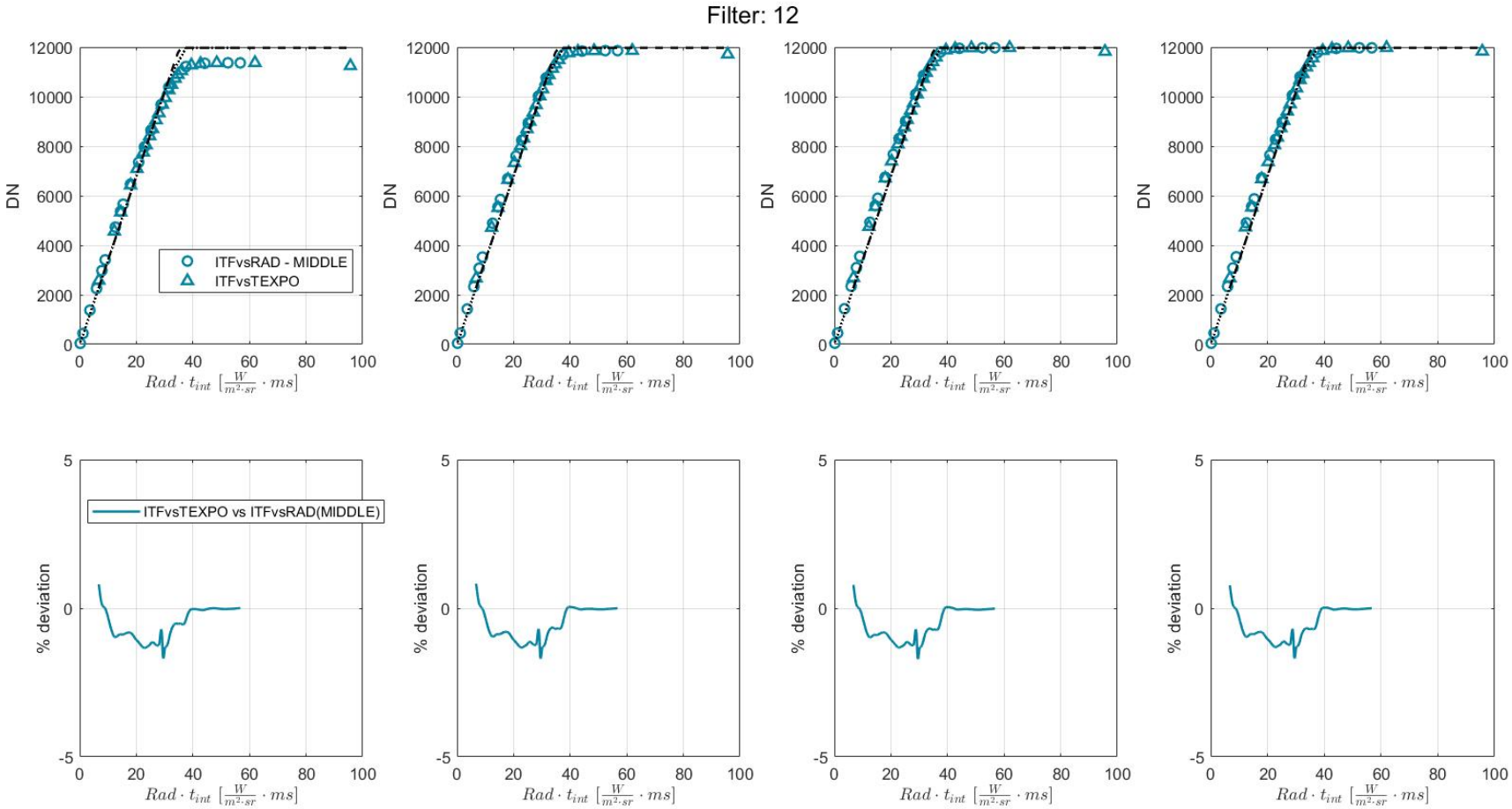
Filter: 12
DN
ITFvsRAD - MIDDLE
ITFvsTEXPO
$Rad \cdot t_{int}\ [\frac{W}{m^2 \cdot sr} \cdot ms]$
% deviation
ITFvsTEXPO vs ITFvsRAD(MIDDLE)

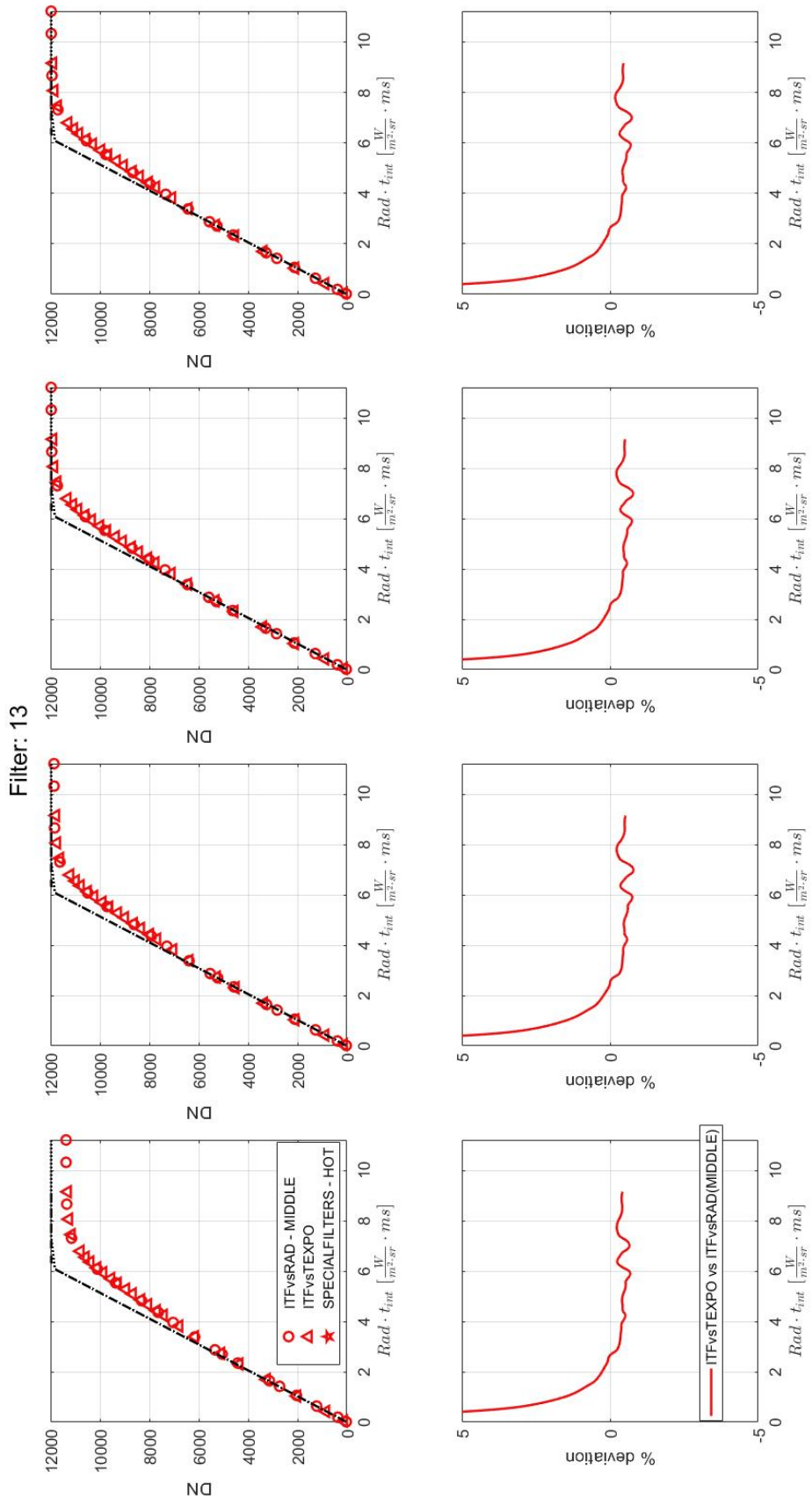
Filter: 13
DN
% deviation
$Rad \cdot t_{int}\ [\frac{W}{m^2 \cdot sr} \cdot ms]$
ITFvsRAD - MIDDLE
ITFvsTEXPO
SPECIALFILTERS - HOT
ITFvsTEXPO vs ITFvsRAD(MIDDLE)

Bibliography

Aboudan, Alessio et al. (2019). "Analysis of Ganymede rotational state using JANUS telescope". In: *2019 IEEE 5th International Workshop on Metrology for AeroSpace (MetroAeroSpace)*, pp. 13–16. DOI: 10.1109/MetroAeroSpace.2019.8869654.

Acton, C. H. (1996). "Ancillary data services of NASA's Navigation and Ancillary Information Facility". In: *Planetary and Space Science* 44.1. Planetary data system, pp. 65–70. ISSN: 0032-0633. DOI: https://doi.org/10.1016/0032-0633(95)00107-7. URL: https://www.sciencedirect.com/science/article/pii/0032063395001077.

Adriani, Alberto et al. (2017). "JIRAM, the Jovian infrared auroral mapper". In: *Space Science Reviews* 213.1, pp. 393–446.

Agostini, L. et al. (2022). "An analysis of possible asteroids flyby for the ESA JUICE mission". In: *Planetary and Space Science* 216, p. 105476. ISSN: 0032-0633. DOI: https://doi.org/10.1016/j.pss.2022.105476. URL: https://www.sciencedirect.com/science/article/pii/S0032063322000629.

Agostini, L. et al. (2023). "Making JANUS ready to launch: on ground calibration campaign". In: *Congresso Nazionale Scienze Planetarie*.

Avdellidou, C et al. (2021). "Characterisation of the main belt asteroid (223) Rosa". In: *Astronomy and Astrophysics-A&A* 656, p. L18.

Barilli, M. et al. (2012). "An unobscured four spherical mirrors based collimator as a tradeoff solution for the Optical Ground Support Equipment (OGSE) of the High Resolution Camera (HRIC) of Simbio-Sys". In: *Ground-based and Airborne Instrumentation for Astronomy IV*. Ed. by Ian S. McLean, Suzanne K. Ramsay, and Hideki Takami. Vol. 8446. International Society for Optics and Photonics. SPIE, 84463Z. DOI: 10.1117/12.925954. URL: https://doi.org/10.1117/12.925954.

Belton, M. J. S. et al. (1992). "Galileo Encounter with 951 Gaspra: First Pictures of an Asteroid". In: *Science* 257.5077, pp. 1647–1652. DOI: 10.1126/science.257.5077.1647. eprint: https://www.science.org/doi/pdf/10.1126/science.257.5077.1647. URL: https://www.science.org/doi/abs/10.1126/science.257.5077.1647.

Bowell, Edward et al. (1989). "Application of photometric models to asteroids." In: *Asteroids II*, pp. 524–556.

Bus, Schelte J. and Richard P. Binzel (2002). "Phase II of the Small Main-Belt Asteroid Spectroscopic Survey: A Feature-Based Taxonomy". In: *Icarus* 158.1, pp. 146–177. ISSN: 0019-1035. DOI: https://doi.org/10.1006/icar.2002.6856. URL: https://www.sciencedirect.com/science/article/pii/S0019103502968569.

Costa Sitjà, M., O. Witasse, and A. Escalante López (2020). "Surveying potential cruise fly-by opportunities for an Ice Giant mission". In: *Europlanet Science Congress 2020 - online*. Vol. EPSC2020-878. Europlanet Science Congress. DOI: https://doi.org/10.5194/epsc2020-878. URL: https://doi.org/10.5194/epsc2020-878.

Cremonese, G. et al. (June 2020). "SIMBIO-SYS: Scientific Cameras and Spectrometer for the BepiColombo Mission". In: *Space Science Reviews* 216.5, p. 75. ISSN: 1572-9672. DOI: 10.1007/s11214-020-00704-8. URL: https://doi.org/10.1007/s11214-020-00704-8.

Crews, C. et al. (Nov. 2019). "Predicting the effect of radiation damage on dark current in a space-qualified high performance CMOS image sensor". In: *Journal of Instrumentation* 14.11, p. C11008. DOI: 10.1088/1748-0221/14/11/C11008. URL: https://dx.doi.org/10.1088/1748-0221/14/11/C11008.

Crews, C. et al. (2020). "Quantum efficiency of the CIS115 in a radiation environment". In: *X-Ray, Optical, and Infrared Detectors for Astronomy IX*. Ed. by Andrew D. Holland and James Beletic. Vol. 11454. International Society for Optics and Photonics. SPIE, 114540E. DOI: 10.1117/12.2562202. URL: https://doi.org/10.1117/12.2562202.

Da Deppo, V. et al. (May 2010). "Optical design of the single-detector planetary stereo camera for the BepiColombo European Space Agency mission to Mercury". In: *Appl. Opt.* 49.15, pp. 2910–2919. DOI: 10.1364/AO.49.002910. URL: http://opg.optica.org/ao/abstract.cfm?URI=ao-49-15-2910.

Da Deppo, V. et al. (2014). "Characterization of the integrating sphere for the on-ground calibration of the SIMBIOSYS instrument for the BepiColombo ESA mission". In: *Space Telescopes and Instrumentation 2014: Optical, Infrared, and Millimeter Wave*. Ed. by Jacobus M. Oschmann Jr. et al. Vol. 9143. International Society for Optics and Photonics. SPIE, p. 914344. DOI: 10.1117/12.2057349. URL: https://doi.org/10.1117/12.2057349.

Da Deppo, V. et al. (2015). "Distortion definition and correction in off-axis systems". In: *Optical Systems Design 2015: Optical Design and Engineering VI*. Ed. by Laurent Mazuray, Rolf Wartmann, and Andrew P. Wood. Vol. 9626. International Society for Optics and Photonics. SPIE, p. 962634. DOI: 10.1117/12.2191332. URL: https://doi.org/10.1117/12.2191332.

Da Deppo, V. et al. (2016). "Radiometric model for the stereo camera STC onboard the BepiColombo ESA mission". In: *Modeling, Systems Engineering, and Project Management for Astronomy VII*. Ed. by George Z. Angeli and Philippe Dierickx. Vol. 9911. International Society for Optics and Photonics. SPIE, 99111T. DOI: 10.1117/12.2232130. URL: https://doi.org/10.1117/12.2232130.

Delbo, M. et al. (2015). *Asteroid thermophysical modeling*. University of Arizona Press Tucson, Arizona.

Della Corte, V. et al. (2014). "The JANUS camera onboard JUICE mission for Jupiter system optical imaging". In: *Space Telescopes and Instrumentation 2014: Optical, Infrared, and Millimeter Wave*. Ed. by Jacobus M. Oschmann Jr. et al. Vol. 9143. International Society for Optics and Photonics. SPIE, p. 91433I. DOI: 10.1117/12.2056353. URL: https://doi.org/10.1117/12.2056353.

Della Corte, V. et al. (2019). "Scientific objectives of JANUS Instrument onboard JUICE mission and key technical solutions for its Optical Head". In: *2019 IEEE 5th International Workshop on Metrology for AeroSpace (MetroAeroSpace)*, pp. 324–329. DOI: 10.1109/MetroAeroSpace.2019.8869584.

Duxbury, Thomas C et al. (2004). "Asteroid 5535 Annefrank size, shape, and orientation: Stardust first results". In: *Journal of Geophysical Research: Planets* 109.E2.

Ecale, Eric, Felice Torelli, and Ignacio Tanco (2018). "JUICE interplanetary operations design : drivers and challenges". In: *2018 SpaceOps Conference*. DOI: 10.2514/6.2018-2493. eprint: https://arc.aiaa.org/doi/pdf/10.2514/6.2018-2493. URL: https://arc.aiaa.org/doi/abs/10.2514/6.2018-2493.

ESA (2005). *BR-247 'Cosmic Vision'. Space Science for Europe 2015-2025*. ESA Publication Division.

ESA JUICE definition study report/Red Book (2014). *JUICE JUpiter ICy moons Explorer Exploring the emergence of habitable worlds around gas giants*. Tech. rep. ESA.

Faccioni, M. (2020). "The HYPSOS optomechanical bench design". MA thesis. https://thesis.unipd.it/bitstream/20.500.12608/28749/1/Faccioni_Matteo_1197599.pdf: University of Padova.

Fujiwara, A. et al. (2006). "The Rubble-Pile Asteroid Itokawa as Observed by Hayabusa". In: *Science* 312.5778, pp. 1330–1334. DOI: 10.1126/science.1125841. eprint: https://www.science.org/doi/pdf/10.1126/science.1125841. URL: https://www.science.org/doi/abs/10.1126/science.1125841.

Grasset, O. et al. (2013). "JUpiter ICy moons Explorer (JUICE): An ESA mission to orbit Ganymede and to characterise the Jupiter system". In: *Planetary and Space Science* 78, pp. 1–21. ISSN: 0032-0633. DOI: https://doi.org/10.1016/j.pss.2012.12.002. URL: https://www.sciencedirect.com/science/article/pii/S0032063312003777.

Greggio, D. et al. (2014). "A preliminary optical design for the JANUS camera of ESA's space mission JUICE". In: *Space Telescopes and Instrumentation 2014: Optical, Infrared, and Millimeter Wave*. Vol. 9143. SPIE, pp. 1216–1223.

Greggio, D. et al. (2016). "Trade-off between TMA and RC configurations for JANUS camera". In: *Space Telescopes and Instrumentation 2016: Optical, Infrared, and Millimeter Wave*. Vol. 9904. SPIE, pp. 1609–1614.

Greggio, D. et al. (2018). "Modeling the JANUS stray-light behavior". In: *Space Telescopes and Instrumentation 2018: Optical, Infrared, and Millimeter Wave*. Ed. by Makenzie Lystrup et al. Vol. 10698. International Society for Optics and Photonics. SPIE, p. 106984V. DOI: 10.1117/12.2313204. URL: https://doi.org/10.1117/12.2313204.

Gwinner, K. et al. (2016). "The High Resolution Stereo Camera (HRSC) of Mars Express and its approach to science analysis and mapping for Mars and its satellites". In: *Planetary and Space Science* 126, pp. 93–138. ISSN: 0032-0633. DOI: https://doi.org/10.1016/j.pss.2016.02.014. URL: https://www.sciencedirect.com/science/article/pii/S0032063316000490.

Hansen, Thomas C (2021). "The everlasting hunt for new ice phases". In: *Nature Communications* 12.1, pp. 1–3.

Harris, Alan W. and Alan W. Harris (1997). "On the Revision of Radiometric Albedos and Diameters of Asteroids". In: *Icarus* 126.2, pp. 450–454. ISSN: 0019-1035. DOI: https://doi.org/10.1006/icar.1996.5664. URL: https://www.sciencedirect.com/science/article/pii/S001910359695664X.

Hartley, Richard and Andrew Zisserman (2004). *Multiple View Geometry in Computer Vision*. 2nd ed. Cambridge University Press. DOI: 10.1017/CBO9780511811685.

Haruyama, Junichi et al. (Apr. 2008). "Global lunar-surface mapping experiment using the Lunar Imager/Spectrometer on SELENE". In: *Earth, Planets and Space* 60.4, pp. 243–255. ISSN: 1880-5981. DOI: 10.1186/BF03352788. URL: https://doi.org/10.1186/BF03352788.

Huang, Jiangchuan et al. (2013). "The ginger-shaped asteroid 4179 Toutatis: new observations from a successful flyby of Chang'e-2". In: *Scientific reports* 3.1, pp. 1–6.

Hussmann, H., C. Sotin, and J.I. Lunine (2015). "10.18 - Interiors and Evolution of Icy Satellites". In: *Treatise on Geophysics (Second Edition)*. Ed. by Gerald Schubert. Second Edition. Oxford: Elsevier, pp. 605–635. ISBN: 978-0-444-53803-1. DOI: https://doi.org/10.1016/B978-0-444-53802-4.00178-0. URL: https://www.sciencedirect.com/science/article/pii/B9780444538024001780.

Jalili, Nader and Karthik Laxminarayana (2004). "A review of atomic force microscopy imaging systems: application to molecular metrology and biological sciences". In: *Mechatronics* 14.8, pp. 907–945. ISSN: 0957-4158. DOI: https://doi.org/10.1016/j.mechatronics.2004.04.005. URL: https://www.sciencedirect.com/science/article/pii/S0957415804000455.

Keller, H. U. et al. (2007). "OSIRIS–The scientific camera system onboard Rosetta". In: *Space science reviews* 128.1, pp. 433–506.

Keller, H. U. et al. (2010). "E-Type Asteroid (2867) Steins as Imaged by OSIRIS on Board Rosetta". In: *Science* 327.5962, pp. 190–193. DOI: 10.1126/science.1179559. eprint: https://www.science.org/doi/pdf/10.1126/science.1179559. URL: https://www.science.org/doi/abs/10.1126/science.1179559.

Khorenko, V. et al. (2017). "BOL and EOL Characterization of Azur 3G Lilt Solar Cells for ESA Juice Mission". In: *E3S Web Conf.* 16, p. 03011. DOI: 10.1051/e3sconf/20171603011. URL: https://doi.org/10.1051/e3sconf/20171603011.

Korsch, Dietrich (Aug. 1977). "Anastigmatic three-mirror telescope". In: *Appl. Opt.* 16.8, pp. 2074–2077. DOI: 10.1364/AO.16.002074. URL: https://opg.optica.org/ao/abstract.cfm?URI=ao-16-8-2074.

Lamy, P. et al. (2010). "Multi-color, rotationally resolved photometry of asteroid 21 Lutetia from OSIRIS/Rosetta observations*". In: *A&A* 521, A19. DOI: 10.1051/0004-6361/201014452. URL: https://doi.org/10.1051/0004-6361/201014452.

Landis, ME et al. (2020). "The Science Case for a Themis Asteroid Family Mission". In: *51st Annual Lunar and Planetary Science Conference*. 2326, p. 1640.

Lauretta, DS et al. (2019). "The unexpected surface of asteroid (101955) Bennu". In: *Nature* 568.7750, pp. 55–60.

Levison, Harold F et al. (2021). "Lucy mission to the Trojan asteroids: Science goals". In: *The Planetary Science Journal* 2.5, p. 171.

Li, J.-Y. et al. (2015). "Asteroid photometry". In: *Asteroids IV* 86, pp. 277–326.

Licandro, J. et al. (2012). "5-14 itzer spectra of Themis family asteroids". In: *A&A* 537, A73. DOI: 10.1051/0004-6361/201118142. URL: https://doi.org/10.1051/0004-6361/201118142.

Lofthouse-Smith, D.-D. et al. (July 2018a). "Image lag optimisation in a 4T CMOS image sensor for the JANUS camera on ESA's JUICE mission to Jupiter". In: *SPIE 10709, High Energy, Optical, and Infrared Detectors for Astronomy VIII*. Ed. by Andrew D. Holland and James Beletic. URL: http://oro.open.ac.uk/56276/.

Lofthouse-Smith, D.-D. et al. (Mar. 2018b). "Thermal annealing response following irradiation of a CMOS imager for the JUICE JANUS instrument". In: *Journal of Instrumentation* 13.03, p. C03036. DOI: 10.1088/1748-0221/13/03/C03036. URL: https://dx.doi.org/10.1088/1748-0221/13/03/C03036.

Marchi, Simone et al. (2015). "Cratering on asteroids". In: *Asteroids Iv*, pp. 725–744.

Mattioli, F. et al. (2011). "A nanotechnology application for low energy neutral atom detection with high angular resolution for the BepiColombo mission to Mercury". In: *Microelectronic Engineering* 88.8. Proceedings of the 36th International Conference on Micro- and Nano-Engineering (MNE), pp. 2330–2333. ISSN: 0167-9317. DOI: https://doi.org/10.1016/j.mee.2011.02.092. URL: https://www.sciencedirect.com/science/article/pii/S016793171100219X.

Michel, P., F. E. DeMeo, and W. F. Bottke (2015). "Asteroids: Recent Advances and New Perspectives". In: *Asteroids IV*. Ed. by eds P. Michel et al. University of Arizona Press, pp. 3–10. DOI: 10.2458/azu_uapress_9780816532131-ch001.

Morbidelli, A. et al. (2015). "The dynamical evolution of the asteroid belt". In: *Asteroids IV*. Ed. by eds P. Michel et al. University of Arizona Press, pp. 493–507. DOI: 10.2458/azu_uapress_9780816532131-ch026.

Murdoch, Naomi et al. (2015). "Asteroid surface geophysics". In: *arXiv preprint arXiv:1503.01931*.

Naletto, G. et al. (1995). "Fluorescence of metachrome in the far- and vacuum-ultraviolet spectral region". In: *X-Ray and Ultraviolet Sensors and Applications*. Ed. by Richard B. Hoover and Mark Bennett Williams. Vol. 2519. International Society for Optics and Photonics. SPIE, pp. 31–38. DOI: 10.1117/12.211912. URL: https://doi.org/10.1117/12.211912.

Naletto, G. et al. (2012). "Innovative optical setup for testing a stereo camera for space applications". In: *Space Telescopes and Instrumentation 2012: Optical, Infrared, and Millimeter Wave*. Ed. by Mark C. Clampin et al. Vol. 8442. International Society for Optics and Photonics. SPIE, p. 84421M. DOI: 10.1117/12.926182. URL: https://doi.org/10.1117/12.926182.

Naletto, G. et al. (2021). "Laboratory characterization of HYPSOS, a novel 4D remote sensing instrument". In: *Sensors, Systems, and Next-Generation Satellites XXV*. Ed. by Sachidananda R. Babu, Arnaud Hélière, and Toshiyoshi Kimura. Vol. 11858. International Society for Optics and Photonics. SPIE, 118580E. DOI: 10.1117/12.2601091. URL: https://doi.org/10.1117/12.2601091.

Naletto, G. et al. (2022). "In-lab characterization of HYPSOS, a novel stereo hyperspectral observing system: first results". In: *International Conference on Space Optics — ICSO 2022 - in press*. International Society for Optics and Photonics. SPIE.

Nimmo, F and Robert T Pappalardo (2016). "Ocean worlds in the outer solar system". In: *Journal of Geophysical Research: Planets* 121.8, pp. 1378–1399.

Palmer, Christopher (Mar. 2020). *DIFFRACTION GRATING HANDBOOK, eighth edition*.

Palumbo, Pasquale et al. (2014). "JANUS: the visible camera onboard the ESA JUICE mission to the Jovian system". In.

Peyrou-Lauga, R. and S. Deschamps (2018). "JUICE (Jupiter Icy moons Explorer) Thermal design and early thermal verification". In: *48th International Conference on Environmental Systems, 8-11 July 2018, Albuquerque, New Mexico*. URL: http://hdl.handle.net/2346/74164.

Peyrou-Lauga, R. and P. Rouchit (2019). "JUICE (Jupiter Icy moons Explorer) Thermal control and interface". In: *49th International Conference on Environmental Systems, 7-11 July 2019, Boston, Massachusetts*.

Pinilla-Alonso, Noemí et al. (2016). "Portrait of the Polana–Eulalia family complex: Surface homogeneity revealed from near-infrared spectroscopy". In: *Icarus* 274, pp. 231–248. ISSN: 0019-1035. DOI: https://doi.org/10.1016/j.icarus.2016.03.022. URL: https://www.sciencedirect.com/science/article/pii/S0019103516300185.

Plaut, J. J. et al. (2014). "Jupiter Icy Moons Explorer (JUICE): science objectives, mission and instruments". In: *45th Lunar Planetary Science Congress*. Lunar Planetary Science Congress. EPSC. URL: https://elib.dlr.de/93869/1/2717.pdf.

Re, Cristina et al. (2022). "Calibration for the stereo hyperspectral pushbroom camera HYPSOS". In: *2022 IEEE 9th International Workshop on Metrology for AeroSpace (MetroAeroSpace)*, pp. 311–316. DOI: 10.1109/MetroAeroSpace54187.2022.9856258.

Reddy, Vishnu et al. (2015). "Mineralogy and surface composition of asteroids". In: *Asteroids IV* 2867.

Russell, CT et al. (2012). "Dawn at Vesta: Testing the protoplanetary paradigm". In: *Science* 336.6082, pp. 684–686.

Russell, CT et al. (2016). "Dawn arrives at Ceres: Exploration of a small, volatile-rich world". In: *Science* 353.6303, pp. 1008–1010.

Sarti, F. (2021). *JUI-FNM-JAN-RP-127 Iss A*. Tech. rep. Leonardo S.p.A.

Sarti, F. et al. (2022). "Results of JANUS integration and optical alignment". In: *International Conference on Space Optics — ICSO 2022*. International Society for Optics and Photonics. SPIE, in progress.

Scheeres, DJ et al. (2015). "Asteroid interiors and morphology". In: *Asteroids iv* 745766.

Schulz, R. (2010). "The Rosetta mission and its fly-by at asteroid 2867 Steins". In: *Planetary and Space Science* 58.9. Special Issue: Rosetta Fly-by at Asteroid (2867) Steins, p. 1057. ISSN: 0032-0633. DOI: https://doi.org/10.1016/j.pss.2010.04.026. URL: https://www.sciencedirect.com/science/article/pii/S0032063310001388.

Schulz, R. et al. (2012). "Rosetta fly-by at asteroid (21) Lutetia: An overview". In: *Planetary and Space Science* 66.1. Rosetta Fly-by at Asteroid (21) Lutetia, pp. 2–8.

ISSN: 0032-0633. DOI: https://doi.org/10.1016/j.pss.2011.11.013. URL: https://www.sciencedirect.com/science/article/pii/S0032063311003436.

Sierks, H. et al. (2011). "Images of Asteroid 21 Lutetia: A Remnant Planetesimal from the Early Solar System". In: *Science* 334.6055, pp. 487–490. DOI: 10.1126/science.1207325. eprint: https://www.science.org/doi/pdf/10.1126/science.1207325. URL: https://www.science.org/doi/abs/10.1126/science.1207325.

Simioni, E. et al. (2016). "Geometrical distortion calibration of the stereo camera for the BepiColombo mission to Mercury". In: *Space Telescopes and Instrumentation 2016: Optical, Infrared, and Millimeter Wave*. Ed. by Howard A. MacEwen et al. Vol. 9904. International Society for Optics and Photonics. SPIE, p. 990410. DOI: 10.1117/12.2232639. URL: https://doi.org/10.1117/12.2232639.

Simioni, E. et al. (2017). "Indoor calibration for stereoscopic camera STC: a new method". In: *International Conference on Space Optics — ICSO 2014*. Ed. by Zoran Sodnik, Bruno Cugny, and Nikos Karafolas. Vol. 10563. International Society for Optics and Photonics. SPIE, 105634E. DOI: 10.1117/12.2304188. URL: https://doi.org/10.1117/12.2304188.

Simioni, E. et al. (2018). "The pre-launch distortion definition of SIMBIO-SYS/STC stereo camera by rational function models". In: *Space Telescopes and Instrumentation 2018: Optical, Infrared, and Millimeter Wave*. Ed. by Makenzie Lystrup et al. Vol. 10698. International Society for Optics and Photonics. SPIE, p. 1069850. DOI: 10.1117/12.2313778. URL: https://doi.org/10.1117/12.2313778.

Simioni, E. et al. (2019). "SIMBIO-SYS/STC stereo camera calibration: Geometrical distortion". In: *Review of Scientific Instruments* 90.4, p. 043106. DOI: 10.1063/1.5085710. eprint: https://doi.org/10.1063/1.5085710. URL: https://doi.org/10.1063/1.5085710.

Simioni, E. et al. (2021). "3DPD: A photogrammetric pipeline for a PUSH frame stereo cameras". In: *Planetary and Space Science* 198, p. 105165. ISSN: 0032-0633. DOI: https://doi.org/10.1016/j.pss.2021.105165. URL: https://www.sciencedirect.com/science/article/pii/S0032063321000040.

Slemer, A et al. (2019). "Radiometric calibration of the SIMBIO-SYS STereo imaging Channel". In: *CEAS Space Journal* 11.4, pp. 485–496.

Soman, M. et al. (2014). "Design and characterisation of the new CIS115 sensor for JANUS, the high resolution camera on JUICE". In: *High Energy, Optical, and Infrared Detectors for Astronomy VI*. Ed. by Andrew D. Holland and James Beletic. Vol. 9154. International Society for Optics and Photonics. SPIE, p. 915407. DOI: 10.1117/12.2056810. URL: https://doi.org/10.1117/12.2056810.

Soman, M. et al. (Feb. 2015a). "Non-linear responsivity characterisation of a CMOS Active Pixel Sensor for high resolution imaging of the Jovian system". In: *Journal of Instrumentation* 10.02, p. C02012. DOI: 10.1088/1748-0221/10/02/C02012. URL: https://dx.doi.org/10.1088/1748-0221/10/02/C02012.

Soman, M. et al. (Sept. 2015b). "Proton irradiation of the CIS115 for the JUICE mission". In: *UV/Optical/IR Space Telescopes and Instruments: Innovative Technologies and Concepts VII*. Vol. 9602. URL: http://oro.open.ac.uk/44477/.

Soman, M. et al. (2016). "Electro-optic and radiation damage performance of the CIS115, an imaging sensor for the JANUS optical camera on-board JUICE". In: *High Energy, Optical, and Infrared Detectors for Astronomy VII*. Ed. by Andrew D. Holland and James Beletic. Vol. 9915. International Society for Optics and Photonics. SPIE, p. 991515. DOI: 10.1117/12.2234290. URL: https://doi.org/10.1117/12.2234290.

Sullivan, Donald L. (Sept. 1972). "Alignment of Rotational Prisms". In: *Appl. Opt.* 11.9, pp. 2028–2032. DOI: 10.1364/AO.11.002028. URL: https://opg.optica.org/ao/abstract.cfm?URI=ao-11-9-2028.

Symetrie (2020). *Software user manual*. Tech. rep. Symetrie.

Taylor, M. G. G. T. et al. (2017). "The Rosetta mission orbiter science overview: the comet phase". In: *Philosophical Transactions of the Royal Society A: Mathematical, Physical and Engineering Sciences* 375.2097, p. 20160262. DOI: 10.1098/rsta.2016.0262. eprint: https://royalsocietypublishing.org/doi/pdf/10.1098/rsta.2016.0262. URL: https://royalsocietypublishing.org/doi/abs/10.1098/rsta.2016.0262.

Tholen, David J (1989). "Asteroid taxonomic classifications". In: *Asteroids II*.

Tholen, David J and M Antonietta Barucci (1989). "Asteroid taxonomy." In: *Asteroids II*, pp. 298–315.

Thomas, N. et al. (Nov. 2017). "The Colour and Stereo Surface Imaging System (CaSSIS) for the ExoMars Trace Gas Orbiter". In: *Space Science Reviews* 212.3, pp. 1897–1944. ISSN: 1572-9672. DOI: 10.1007/s11214-017-0421-1. URL: https://doi.org/10.1007/s11214-017-0421-1.

Tordi, Massimiliano et al. (2020). "HYPSOS: a HYPerspectral stereo observing system for solar system exploration". In: *Space Telescopes and Instrumentation 2020: Optical, Infrared, and Millimeter Wave*. Vol. 11443. SPIE, pp. 1177–1187.

Veverka, J. et al. (1996). "Ida and Dactyl: Spectral Reflectance and Color Variations". In: *Icarus* 120.1, pp. 66–76. ISSN: 0019-1035. DOI: https://doi.org/10.1006/icar.1996.0037. URL: https://www.sciencedirect.com/science/article/pii/S0019103596900378.

Veverka, J. et al. (1997). "NEAR's flyby of 253 Mathilde: Images of a C asteroid". In: *Science* 278.5346, pp. 2109–2114.

Veverka, J. et al. (2000). "NEAR at Eros: Imaging and spectral results". In: *Science* 289.5487, pp. 2088–2097.

Watanabe, S. et al. (2019). "Hayabusa2 arrives at the carbonaceous asteroid 162173 Ryugu—A spinning top–shaped rubble pile". In: *Science* 364.6437, pp. 268–272. DOI: 10.1126/science.aav8032. eprint: https://www.science.org/doi/pdf/10.1126/science.aav8032. URL: https://www.science.org/doi/abs/10.1126/science.aav8032.

Winstone, G. P. et al. (Sept. 2015). "Proton-induced Random Telegraph Signal in the CMOS imaging sensor for JANUS, the visible imaging telescope on JUICE". In: *UV/Optical/IR Space Telescopes and Instruments: Innovative Technologies and Concepts VII*, 96020N. URL: http://oro.open.ac.uk/44479/.

Witasse, O. et al. (2019). "JUICE (Jupiter Icy Moon Explorer): A European mission to explore the emergence of habitable worlds around gas giants". In: *EPSC-DPS2019-400-*

1. Vol. 13. European Planetary Science Congress. EPSC. URL: https://meetingorganizer.copernicus.org/EPSC-DPS2019/EPSC-DPS2019-400-1.pdf.

Witasse, O. et al. (2021). *JUICE (Jupiter Icy Moon Explorer): Plans for the cruise phase*. Tech. rep. Copernicus Meetings.

Witasse, O. et al. (2022). "JUICE (Jupiter Icy Moons Explorer): status report for 2022". In: *EGU22-1876*. European Planetary Science Congress. EPSC. URL: https://meetingorganizer.copernicus.org/EPSC-DPS2019/EPSC-DPS2019-400-1.pdf.

Wocial, T. et al. (2022). "A Method to Achieve High Dynamic Range in a CMOS Image Sensor Using Interleaved Row Readout". In: *IEEE Sensors Journal* 22.22, pp. 21619–21627. DOI: 10.1109/JSEN.2022.3211152.

Wyatt, Clair L. (1978). "CHAPTER I - Introduction and Objectives". In: *Radiometric Calibration: Theory and Methods*. Ed. by CLAIR L. WYATT. Academic Press, pp. 1–6. ISBN: 978-0-12-766150-6. DOI: https://doi.org/10.1016/B978-0-12-766150-6.50004-9. URL: https://www.sciencedirect.com/science/article/pii/B9780127661506500049.

Zuppella, P et al. (Oct. 2012). "Optical subsystems calibration and derived radiometric instrument response of the PHEBUS spectrometer on board of the BepiColombo Mission". In: *Journal of Instrumentation* 7.10, P10023. DOI: 10.1088/1748-0221/7/10/P10023. URL: https://dx.doi.org/10.1088/1748-0221/7/10/P10023.

Zusi, M. (2009). "The High Resolution Imaging Channel of the SIMBIO-SYS suite aboard the BepiColombo mission to Mercury". PhD thesis. University of Naples - Federico II.